

# Parameter Identification and Analysis of Synchronous Machines Incorporating Magnetic Saturation and Iron Effects

Sascha Kühl

Vollständiger Abdruck der von der TUM School of Engineering and Design der Technischen Universität München zur Erlangung des akademischen Grades eines

Doktors der Ingenieurwissenschaften (Dr.-Ing.)

genehmigten Dissertation.

Vorsitzender: Prof. Dr.-Ing. habil. Gerhard Rigoll  
Prüfer der Dissertation: 1. Prof. Dr.-Ing. Dr. h. c. Ralph M. Kennel  
2. Prof. Silverio Bolognani

Die Dissertation wurde am 28.09.2021 bei der Technischen Universität München eingereicht und durch die TUM School of Engineering and Design am 26.04.2022 angenommen.



# PREFACE

---

Electric synchronous machines are affected by magnetic saturation as well as magnetic hysteresis and eddy currents – so-called iron effects. This work analyzes the influence of these effects on the motor characteristics with special emphasis on anisotropy-based sensorless control schemes. Two different measurement techniques along with an optimization algorithm that ensures physical validity of the results are proposed and employed to identify accurate motor models.

This thesis bases on my work at the Institute for Electrical Drive Systems and Power Electronics of the Technical University of Munich. It would not have been possible without the supervision of Prof. Dr.-Ing. Ralph Kennel, to whom I would like to express my sincere gratitude.

I wish to also thank the co-assessor of this work, Prof. Silverio Bolognani from the University of Padova, for his time and the valuable feedback.

Finally, I would like to thank all my colleagues at the Institute for Electrical Drive Systems and Power Electronics for the fruitful discussions and the pleasant atmosphere, making the time at the university unforgettable.

My special thanks are due to Dr.-Ing. Peter Landsmann and Dr.-Ing. Dirk Paulus for their support during our time together at the university and especially during the exciting and intense phase in which we founded our start-up company Bitflux.

Munich, July 2022

Sascha Kühl



# CONTENTS

---

PREFACE .....	III
CONTENTS .....	V
CHAPTER 1 INTRODUCTION .....	1
1.1 MOTIVATION.....	1
1.2 OUTLINE.....	2
CHAPTER 2 THEORETICAL BACKGROUND .....	5
2.1 ELECTROMAGNETIC FIELDS AND FERROMAGNETISM.....	5
2.1.1 Electromagnetic Fields in Free Space .....	5
2.1.2 Electromagnetic Fields in Matter .....	7
2.2 DESCRIPTION OF SYNCHRONOUS MACHINES .....	22
2.2.1 Preliminaries on Synchronous Machines .....	22
2.2.2 Space Vector Notation .....	27
2.2.3 General Mathematical Model .....	33
2.3 TWO-LEVEL VOLTAGE SOURCE INVERTERS .....	53
2.3.1 Topology .....	53
2.3.2 Space Vector Modulation.....	53
2.4 FOURIER ANALYSIS OF SPACE VECTORS.....	57
2.4.1 Fourier Series of Space Vectors .....	57
2.4.2 Leakage Effect of Fourier Coefficients.....	58
2.4.3 The Aliasing Effect in Sampled Signals .....	60
CHAPTER 3 TEST BENCH DESCRIPTION.....	63
3.1 RAPID PROTOTYPING SYSTEM .....	64
3.2 POWER ELECTRONICS .....	65
3.2.1 DC Source.....	65
3.2.2 Load Inverter .....	65
3.2.3 Test Inverter .....	65
3.3 USED SENSOR SYSTEMS .....	68
3.3.1 Current Measurement .....	68
3.3.2 Voltage Measurement.....	68
3.3.3 Speed and Position Measurement .....	68
3.4 TESTED MACHINES.....	68

CHAPTER 4 ON MAGNETIC CHARACTERISTICS OF SYNCHRONOUS MACHINES .....	71
4.1 THE SYNCHRONOUS RELUCTANCE MACHINE .....	71
4.1.1 The Relation between Magnetic Energy, Flux Linkage and Stator Current .....	71
4.1.2 Torque Generation and Associated Control Strategies .....	76
4.1.3 Affine Model Parameters.....	78
4.1.4 Characteristics for Sensorless Control.....	82
4.2 THE INTERIOR PERMANENT MAGNET SYNCHRONOUS MACHINE.....	89
4.2.1 The Relation between Magnetic Energy, Flux Linkage and Stator Current .....	89
4.2.2 Torque Generation, MTPA and MTPV .....	94
4.2.3 Affine Model Parameters.....	95
4.2.4 Characteristics for Sensorless Control.....	98
4.3 THE SURFACE PERMANENT MAGNET SYNCHRONOUS MACHINE.....	103
4.3.1 The Relation between Magnetic Energy, Flux Linkage and Stator Current .....	103
4.3.1 Torque Generation, MTPA and MTPV .....	106
4.3.2 Affine Model Parameters.....	107
4.3.3 Characteristics for Sensorless Control.....	110
CHAPTER 5 OPTIMIZING MEASURED INDUCTANCE MAPS .....	115
5.1 MOTIVATION .....	115
5.2 SYMMETRY AND PHYSICAL CONSTRAINTS .....	116
5.2.1 Symmetry Considerations .....	116
5.2.2 Physical Considerations .....	117
5.3 THE OPTIMIZATION PROBLEM .....	119
CHAPTER 6 MEASURING FLUX LINKAGE IN SYNCHRONOUS MACHINES .....	121
6.1 STATE OF THE ART MEASUREMENT TECHNIQUES .....	121
6.1.1 Preliminaries: Distinguishing Between EMF, BEMF and HF Based Methods.....	121
6.1.2 EMF Based Techniques.....	122
6.1.3 BEMF Based Techniques .....	123
6.1.4 HF Based Techniques.....	125
6.2 ENSURING A COMPARABLE MEASUREMENT ENVIRONMENT .....	126
6.3 BEMF BASED MEASUREMENT METHOD.....	128
6.3.1 Measurement Scheme and Algorithm.....	128
6.3.2 Measurement Results .....	130
6.4 SMALL-SIGNAL HF BASED MEASUREMENT METHOD .....	144
6.4.1 Measurement Scheme and Algorithm.....	144
6.4.2 Measurement Results .....	164
6.5 DISCUSSIONS .....	186
6.5.1 Sensorless Control .....	186
6.5.2 Differences in Torque .....	199
CHAPTER 7 CONCLUSIONS AND OUTLOOK .....	205
7.1 SUMMARY .....	205
7.2 OUTLOOK .....	207
APPENDIX A NOMENCLATURE .....	211
A.1 LIST OF SYMBOLS .....	211
A.1.1 Roman Characters .....	211
A.1.2 Greek Characters .....	214
A.1.3 Special Characters.....	215

A.2	LIST OF ABBREVIATIONS .....	216
APPENDIX B	CALCULATIONS .....	219
B.1	ENERGY BALANCE OF SYNCHRONOUS MACHINES .....	219
B.2	ALTERNATIVE MACHINE MODEL IN STATOR COORDINATES .....	220
B.3	ROTATIONAL TRANSFORMATIONS OF MATRICES .....	221
B.4	EIGENVALUES AND EIGENVECTORS OF A (2×2) MATRIX .....	223
B.5	DEFINITION OF ATAN2(Y,X) .....	224
B.6	RESPONSE OF LINEAR STATE SPACE MODELS TO ROTATING INPUT SIGNALS .....	225
B.7	CURRENT RESPONSE OF SYNCHRONOUS MACHINES TO ROTATING VOLTAGES .....	227
B.8	FOURIER ANALYSIS OF PIECEWISE CONSTANT VECTOR FUNCTIONS .....	229
APPENDIX C	RELATED WORKS .....	231
C.1	ADVISED STUDENT THESIS .....	231
C.2	LIST OF PUBLICATIONS .....	231
BIBLIOGRAPHY	.....	233



# CHAPTER 1

---

## Introduction

---

### 1.1 Motivation

---

Electric motors play an important role in our daily lives. On the consumer market, their fields of application range from the vibration alert in cell phones to washing machines or high-power drives in electric cars. Many modern industrial sectors such as intra logistics, transportation, pumps and fans, or fabrication base on the use of electric machines.

One type of electric motors are *synchronous machines* (SM). They play an important role, whenever the focus is on torque or power density or on efficiency. With increasing use of *variable frequency drives* (VFD) in combination with the political implementation of energy efficiency directives, their importance grows.

VFDs are electrical energy converters that provide electric power at variable frequency and amplitude. With respective control techniques, it is thus possible to operate electric motors at optimal speeds and torques for the actual application.

Many control strategies, such as the widely applied *field-oriented control* (FOC), or the more sophisticated *predictive control* require accurate mathematical models of the motor to be operated. While in FOC the motor parameters are mainly needed to tune the PI-type current controllers and for observing the magnetic field of the motor [1, 2], predictive control applies the model to predict the motor behavior and use the results to derive optimal control actions [3–5]. Applying inaccurate models can lead to non-ideal operation, to unwanted oscillations, or to instability of the drive system at worst. Deadbeat control as a special type of predictive control aiming at maximal control bandwidth is known for becoming instable rather quickly, when the time constants of the underlying model are incorrect [6].

Control methods with focus on energy efficiency do also require parameter knowledge of the operated motor in order to find the operating points with minimal losses. Here, it should be obvious that model errors directly lead to efficiency reductions.

Another important field of control techniques for synchronous motors is *sensorless control* [7–17]. It aims at reducing system costs and improving robustness and reliability of the drive system by avoiding sensors that measure the rotor position, such as rotary encoders or resolvers. Instead of the sensor, position estimates based on motor currents and voltages are employed. Especially at low speed operation down to standstill, these control methods are challenging and their control performance strongly depends on the quality and accuracy of the motor model they base on [8, 18–30].

Many control schemes base on simplified, linear models in order to reduce mathematical complexity or algorithmic and computational effort. In practice, however, synchronous machines are nonlinear. The main reason for that are magnetic effects such as saturation, hysteresis, and eddy currents in ferromagnetic material. Being able to identify and model these effects is thus a prerequisite to improve the control performance in a variety of control schemes and applications and motivates the present work.

## 1.2 Outline

---

The focus of this work lies on identifying the magnetic characteristics of synchronous machines without knowledge about the employed material properties, the windings schemes or the design of rotor or stator sheets. In practice, only basic information such as motor type, rated voltage and current, rated torque and speed is typically available. We thus aim at obtaining accurate motor models by appropriate measurement techniques rather than by analytical techniques such as, for instance, *finite element analysis* (FEA).

The key elements of this work are two measurement techniques, one basing on evaluating the *back electromotive force* (BEMF) and the other on *high frequency* (HF) signal injection. Along with a state-of-the-art analysis, both methods are described and compared in Chapter 6. The sensitivities of both methods to a variety of disturbances are extensively analyzed and discussed. Major effort is put on reducing the known sources of error as good as possible, such that only iron effects remain. This allows us to ideally analyze the influence of these effects that are mathematically difficult to address and also difficult to measure.

In Chapter 6 too, the results are discussed in the context of anisotropy-based sensorless control and of an efficient control strategy named *maximum torque per ampere* (MTPA).

In order to being able to obtain best results and to ideally compare the measurement results of both methods, an optimization algorithm is proposed in Chapter 5. With minimal corrections, it enforces symmetry and guarantees physical validity of the measurement results.

Chapter 2 sets the theoretical basis of this work. It presents the state-of-the-art of the theory needed in the following chapters. The detailed and unified descriptions shall enable the reader to better understand and validate the present work without referring to further literature.

In Chapter 3, the tested motors and the test bench that are used to transfer the theory to practice are described. Special emphasis is placed on nonlinear effects of the voltage source inverter, that can influence the proposed measurement schemes. In order to identify those effects, a measurement technique is proposed, and the results are presented and discussed.

In an attempt to introduce the tested motors and also to motivate the following chapters, the results of the BEMF-based measurements refined by the optimization algorithm are presented already in Chapter 4. The results presented here are used as reference in the later discussions of measurement results. From magnetic (co-) energy to torque, flux linkages and inductances, the influence of magnetic saturation is extensively analyzed. Additionally, its relevance for mathematically accurately linearized models and for anisotropy-based sensorless control schemes is discussed.



# CHAPTER 2

---

## Theoretical Background

---

This chapter sets the theoretical basis of the complete work. The relevant theory known from literature is collected and presented here in a unified form in the context of synchronous machines. Special emphasis is put on magnetic saturation and how this typically nonlinear effect influences the electrical as well as mechanical behavior of the machines.

In literature, usually linear or linearized models of synchronous machines are applied. The purpose of this chapter is twofold: first, to justify the validity of the derived mathematical model, even when nonlinearities caused by magnetic saturation play an important role; second, to have all relevant well-known theory collected here for reference, such that the later chapters with new contributions do not have to be interrupted, when the results are discussed.

### 2.1 Electromagnetic Fields and Ferromagnetism

---

#### 2.1.1 Electromagnetic Fields in Free Space

Electric charges and its relative movements are the source of electromagnetic fields. Our today's knowledge about the interaction between electric and magnetic fields bases on the work of *James Clerk Maxwell* [31], who is therefore considered one of the most influential physicists of the 19<sup>th</sup> century. The set of four equations describing electromagnetic fields is hence named after him. In the free, three-dimensional space, for a system at rest, they are given in integral form as follows [32 pp. 38–42 (Ch. 1)].

$$\oiint_S \epsilon_0 \vec{E} \cdot d\vec{a} = \iiint_V \rho \cdot dv \quad (\text{a})$$

$$\oint_C \vec{H} \cdot d\vec{s} = \iint_S \vec{j} \cdot d\vec{a} + \frac{d}{dt} \iint_S \epsilon_0 \vec{E} \cdot d\vec{a} \quad (\text{b})$$

$$\oint_C \vec{E} \cdot d\vec{s} = -\frac{d}{dt} \iint_S \mu_0 \vec{H} \cdot d\vec{a} \quad (\text{c})$$

$$\oiint_S \mu_0 \vec{H} \cdot d\vec{a} = 0 \quad (\text{d})$$

The fundamental assumption in *Maxwell's equations* is that electric charges and their movements can be considered as continuous charge and current distributions. Although this is not true on atomic scale, it is a convenient simplification to describe electromagnetic fields of interest on *mesoscopic* and *macroscopic* view [32 pp. 10–11 (Ch. 1)]. The charge density,  $\rho$ , is thus defined as net charge per mesoscopic unit volume,  $\Delta V$ , whereas its movement at the velocity  $\vec{v}$  is denoted as current density,  $\vec{j}$

$$\rho = \frac{\text{net charge in } \Delta V}{\Delta V} \quad (2.2)$$

$$\vec{j} = \rho \vec{v} \quad (2.3)$$

Equation (2.1)(a) is also known as *Gauss' law*. It states that any electric net charge expressed in terms of the charge density in an arbitrary volume,  $V$ , that is enclosed by a surface,  $S$ , is a source of electric displacement flux. The latter is described by the electric displacement flux density,  $\epsilon_0 \vec{E}$ , which for its part consists of the electric field intensity,  $\vec{E}$ , times the *permittivity of free space*,  $\epsilon_0 = 8.854 \cdot 10^{-12}$  F/m. The closed surface is described on each infinitesimal point by corresponding normal vectors,  $d\vec{a}$ , whereas the volume can be divided into infinitesimal volume elements,  $dv$ .

While Gauss' law reveals that the electric field intensity can be a conservative (or source) field, *Faraday's law*, (2.1)(c), states that it can also be a solenoidal (or vortex) field [33 p. 15], as its circulation around a contour,  $C$ , is proportional to the time rate of change of the magnetic flux piercing the surface,  $S$ , enclosed by that contour. Each point of the contour is described by corresponding differential line segments,  $d\vec{s}$ . The magnetic flux is expressed in terms of the magnetic flux density,  $\mu_0 \vec{H}$ , that consists of the magnetic field intensity,  $\vec{H}$ , and the *permeability of free space*,  $\mu_0 = 4\pi \cdot 10^{-7}$  H/m.

*Ampère's law*<sup>1</sup>, (2.1)(b), expresses the circulation of the magnetic field intensity along a contour enclosing an arbitrary surface as superposition of the current density piercing that surface and the time rate of change of the electric displacement flux density through the same surface.

The last of Maxwell's equations, (2.1)(d), is *Gauss' law for magnetic flux*. It reveals that magnetic flux has no sources, as the net flux out of any closed volume is zero. We can directly

---

<sup>1</sup> What Ampère defined in his law was in fact only the relation between magnetic field intensity and current density. Complementing this expression with the time rate of change of the electric displacement flux density was the achievement of Maxwell

derive from here that no magnetic monopoles can exist and that the magnetic flux density field is always solenoidal [33 p. 15].

Maxwell's equations, (2.1), provide a closed mathematical description of electric and magnetic fields and their interaction as electromagnetic fields. The link between electric and magnetic fields is found to be dependent on the time-derivatives of both, the electric and magnetic flux. Under certain conditions at high frequencies, this link lets magnetic fields arise from electric fields and vice versa – energy is radiated by electromagnetic waves. However, in many technical processes, electromagnetic radiation is unwanted. In consequence, they are designed in such a way that the time rate of change of either the electric or the magnetic flux can be neglected, thus leading to considering the processes as *electroquasistatic* (EQS) or *magnetoquasistatic* (MQS) systems.

Except for some special applications in micro-mechanical systems [34], electromechanical energy converters base on that part of the *Lorentz force* that is due to moving charges in magnetic fields. Consequently, synchronous machines have windings to generate magnetic flux, and are constructed such that the condition  $\sqrt{\mu_0\epsilon_0}l \ll 1/f$  is satisfied, where  $l$  is the largest length of the motor and  $f$  are the frequencies of interest of the electrical quantities. We can hence consider the machine as MQS system in good approximation [32 pp. 8–20 (Ch. 3)]. Equation (2.1)(b) then simplifies to

$$\oint_C \vec{H} \cdot d\vec{s} \approx \iint_S \vec{j} \cdot d\vec{a}. \quad (2.4)$$

### 2.1.2 Electromagnetic Fields in Matter

Maxwell's equations, as discussed so far, are valid for charge distributions in free space. In material medium, however, atoms or molecules are densely packed. As they consist of negatively charged electrons orbiting positive nuclei, they are sources of electromagnetic fields. The effort to describe fields of engineering interest by superposition of the atomic field contributions is generally tremendous and would also require the consideration of quantum mechanical laws. Consistently with the mesoscopic definition of charge distributions (which are technically seen also matter), a more expedient approach is to approximate the electromagnetic processes inside a medium in a mesoscopic or macroscopic view. Therefore, we introduce equations describing material with respect to their averaged magnetic and electric characteristics over a distance of order of a few nanometers (mesoscopic view) to distances including whole bodies of matter (macroscopic view). In these regions, the local fields are assumed homogeneous [35 p. 25].

#### 2.1.2.1 Electrical Conductivity

An important property of electromagnetic material is the electric conductivity, i.e. the ability of the material to transport free charges. The availability of free (i.e. unpaired or unbound) charges is thus a prerequisite for electric conductors. In presence of magnetic or electric fields, the charged particles are accelerated by the Lorentz force. The resulting kinetic energy of the particles is equivalent to their magnetic energy [36]. In contrast to free space, the particles collide with the atomic or molecular constituents in the conductor, leading to a comparably

low average velocity [32 pp. 3–4 (Ch. 7)]. The collisions transform the kinetic energy of the particles into thermal energy of the material and therefore produce *Ohmic losses*, often also referred to as *Joule losses*.

The mesoscopic conduction law is a generalization of *Ohm's law* [37] and is given by

$$\vec{j}_f \approx \sigma \vec{E}, \quad (2.5)$$

where  $\vec{j}_f$  is the free current density and  $\sigma$  is the electrical conductivity. The latter is typically depending on the local temperature of the conductor. For inhomogeneous temperature distributions, the conductivity will therefore become directional dependent, i.e. *anisotropic*. Mathematically, this would have to be taken into account by defining  $\sigma$  as a *tensor* depending on temperature and location [38 p. 18]. Equation (2.5), where  $\sigma$  is considered as constant and scalar, is hence an averaging approximation.

In synchronous machines, where typically copper conductors are applied, the approximation is convenient, if the temperature distribution of the wires is homogeneous and the conducting cross-sectional areas remain constant. In practice, the validness of these assumptions is impaired by the occurrence of Ohmic losses in combination with inhomogeneous heat conduction and the *proximity effect* (similar to the *skin effect* [32 pp. 35–42 (Ch. 10)]) at high frequencies [38 pp. 18 and 51–57]. This is taken up again in the later sections, where the measurement schemes are described and the results are discussed.

### 2.1.2.2 Saturation in Ferromagnetic Material

In *ferromagnetic material*, we must consider the *magnetic dipole moment*. It is associated with the spin of electrons and their orbital motion around the nucleus of atoms<sup>2</sup>. The quantum mechanical exchange interaction between or among the electronic spins and orbits in single atoms or molecules typically lead to cancelled net contributions to the molecular magnetic moment. Only in case of electrons orbiting the nucleus in unfilled shells<sup>3</sup>, a non-zero net magnetic moment occurs [32 pp. 15–19 (Ch. 9)]. In ferromagnetic solids, the mutual magnetic moment interaction of densely packed atoms leads to *spontaneous magnetization*, i.e. domains where the magnetic moments of all atoms are parallelly aligned. Typical volumes of *magnetic domains* range from  $10^{-9}$  to  $1 \text{ mm}^3$  [39 p. 548]. In common synchronous machines, we therefore have a large number of domains with different magnetic orientations. The overall domain structure of a given ferromagnetic specimen is a result of the minimization of the free energy due to the magnetic dipole moments [35 p. 231].

In an unmagnetized or virgin state, the magnetizations of all domains cancel. The ferromagnet thus has no net macroscopic *magnetization density*  $\vec{M}$  [32 pp. 3–4 and 17, 35 pp. 8 and 258–260]. When, however, an external magnetic field,  $\vec{H}$ , is applied to the ferromagnetic material, the magnetic dipole moments tend to align with that field. As a result, domains with a similarly

---

<sup>2</sup> Note that the spin of the nucleus can usually be neglected, since the corresponding nuclear moment is three orders of magnitude smaller than the one associated with electrons [35 p. 24]

<sup>3</sup> The theory of electrons orbiting an atomic nucleus on discrete shells is a concept of quantum mechanics that has its origin in Bohr's atomic model

oriented magnetization grow at the expense of other domains. The resulting imbalance between the magnetic dipole moments within the specimen leads to an overall magnetization. This is exemplarily shown in Figure 2.1 for a circular specimen with four magnetic domains. Starting from the initial demagnetized state, an increasing field in direction of the axes of abscissae is applied. The lower left domain has the closest orientation to the applied field and thus enlarges the most, resulting in an increasing magnetization. When the material is isotropic, the overall magnetization is in the same direction as the  $\vec{H}$  field. With increasing external field, the domains with opposed orientations disappear one after each other and the relative growth of the lower left domain lessens – the ferromagnetic material begins to saturate. The phase of domain growth is characterized by *domain wall motion*. The following phase is predominated by the so-called *coherent rotation* or magnetic moment rotation [35 p. 246, 40 p. 101], where the magnetic moments of the remaining domains start to rotate in order to align with the applied field.

In the final state for high applied fields, all magnetic moments are in alignment with that field. As a result, no further increase of the magnetization density can be obtained – the ferromagnetic specimen is saturated. The corresponding value is denoted as saturation magnetization,  $M_s$ .

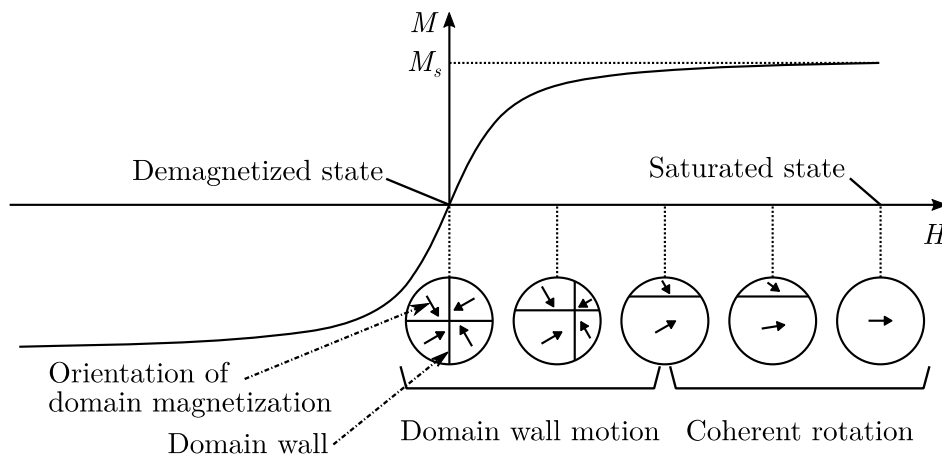


Figure 2.1: Magnetic saturation as result of domain wall motion and magnetic moment rotation in ferromagnetic material

It is important to note that the spontaneous magnetization depends on the temperature of the ferromagnetic media [35 pp. 9–11]. With increasing temperature, the value of  $M_s$  continuously decreases until it falls precipitously to zero at the *Curie temperature*. At this temperature and above, the ferromagnetic order collapses.

### 2.1.2.3 MQS Approximations of Maxwell's Equations in Ferromagnetic Material

In order to account for the influence of ferromagnetic material on MQS systems, Ampere's law (2.4), Faraday's law (2.1)(c) and Gauss' law for magnetic flux (2.1)(d) are rewritten as

$$\oint_C \vec{H} \cdot d\vec{s} \approx \iint_S \vec{j}_f \cdot d\vec{a} \quad (\text{a})$$

$$\oint_C \vec{E} \cdot d\vec{s} = -\frac{d}{dt} \iint_S \vec{B} \cdot d\vec{a} \quad (\text{b}) \quad (2.6)$$

$$\oiint_S \vec{B} \cdot d\vec{a} = 0 \quad (\text{c})$$

with the aforementioned free current density  $\vec{j}_f$  and  $\vec{B}$  as *magnetic flux density*, which is given by the superposition of external magnetic field intensity and magnetization density [32 pp. 4–6 (Ch. 9), 39 p. 694]

$$\vec{B} = \mu_0(\vec{H} + \vec{M}) \quad (2.7)$$

Equation (2.7) is typically rewritten in a compacter form that is analogous to Ohm's law (2.5). Before we can do this, however, we must introduce *magnetic anisotropy* and *magnetic hysteresis*, which is done in the following two subsections.

#### 2.1.2.4 Magnetic Anisotropy

As mentioned before, the magnetic samples in Figure 2.1 are assumed to be isotropic, which results in perfect alignment of  $\vec{H}$  and  $\vec{M}$ . Without loss of information, we can thus only consider the magnitudes of both fields, as expressed by the scalar axis labeling. In actual ferromagnetic material, however, we do have magnetic anisotropy. According to the formal definition, the latter requires a change in the internal energy of a magnetic specimen, when the magnetization in that material changes its direction [41 p. 266]. Another interpretation of this definition is that the magnetization has one or more easy axes, along which it prefers to lie [41 p. 247]. This leads to misalignment between applied field and magnetization, unless the direction of the applied field is along an easy or hard axis, as shown in Figure 2.2. Note that for a constant magnitude of  $\vec{H}$ , the resulting magnitude of  $\vec{M}$  is maximal, when oriented along the easy axis (a) and minimal, when oriented along the hard axis (c).

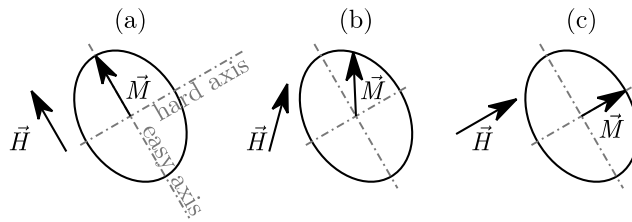


Figure 2.2: Influence of magnetic anisotropy on the relation between applied field,  $\vec{H}$ , and magnetization,  $\vec{M}$ ; (a) applied field along easy axis; (b) applied field between easy and hard axis; (c) applied field along hard axis

Magnetic anisotropy has different origins [35 p. 168]. On microscopic view, the crystal structure and the micro-scale texture of a magnetic specimen are the main sources. The corresponding *magnetocrystalline* and *induced magnetic anisotropies* depend on the chemical composition and on the manufacturing processes of the magnetic material. A macroscopic source of anisotropy is the shape of the sample. In [40 pp. 224–226], it is demonstrated that the demagnetizing

energy density is a function of the angle between the magnetization and the long axis of a spheroidal body. This means that *shape anisotropy* is inherent in every non-spherical magnetic sample [40 p. 205].

### 2.1.2.5 Magnetic Hysteresis

The concepts of domain wall motion and coherent rotation can sufficiently explain the occurrence of magnetic saturation. In real ferromagnetic material, however, another effect is observed. When the external  $\vec{H}$  field, applied to a given specimen, is linearly increased with time (i.e.  $H \sim t$ ), the resulting increasing magnetization presents small-scaled discontinuities. This effect was discovered first by *Heinrich Barkhausen* in 1919 and is hence named after him [35 pp. 257–258].

*Barkhausen jumps* result from the interplay between domain wall motion, domain rotation and microscopic or mesoscopic magnetic anisotropy [42]. *Stoner-Wolfarth particles* do explain them as irreversible catastrophic discontinuities due to jumps from one energy minimum to another, leading to a sudden change of magnetization of a domain [35 pp. 247–252]. In real material, we have impurities, i.e. voids, or crystallographic defects, which can be seen as induced magnetic anisotropies or small-scale shape anisotropies. These impurities impede the domain wall motion, as they act as *pinning sites* for the domain walls. Figure 2.3 illustrates an emerging Barkhausen jump due to domain wall motion over a single pinning site. Beginning with a given domain distribution, an increasing external field in direction of the axis of abscissae is applied. As the increase of the field is linear in time, the axis of abscissae qualitatively represents both, the applied magnetic field and the time. Between the first and second depicted snapshot of the domain distributions in the magnetic discs, the domain wall bows around the pinning site. With further increasing field, the force on the wall reaches a critical value and the internal energy minimum becomes unstable [42]. As a result, a switching process to a new, stable energy minimum occurs – a Barkhausen jump happens. In Figure 2.3, this is shown between the second and third depicted quasistationary domain wall distributions. For comparison, also a magnetization curve with the same relative domain sizes but without pinning site is shown in grey.

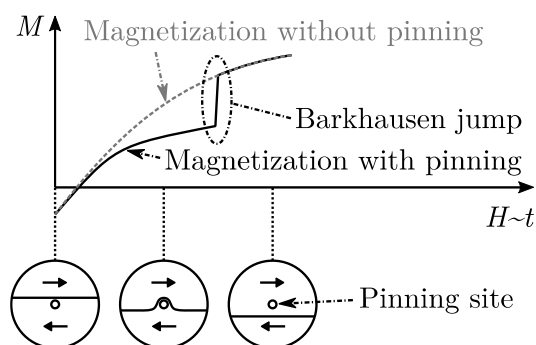


Figure 2.3: Occurrence of Barkhausen jumps due to domain wall motions over pinning sites

When repeating the experiment shown in Figure 2.3 in reverse order, i.e. starting from the right domain configuration and successively decreasing the applied field, it is obvious that a

Barkhausen jump is irreversible. The domain wall would again bend around the pinning site, this time, however, from bottom to top. When falling below a critical external field, another Barkhausen jump will occur. The irreversible transitions between both jumps cause an effect known as magnetic hysteresis [35 pp. 244–260].

Figure 2.4 shows a typical major hysteresis loop for ferromagnetic material (grey plot). The initial curve with predominating pinning processes is plotted in black [35 pp. 259–260, 43 p. 359]. Starting from an initial unmagnetized state, a segment with low gradient follows, where the domain walls bow out from the pinning sites. Since no Barkhausen jumps occur, the magnetization is reversible. The following line segment with high slope is characterized by irreversible domain wall motions with Barkhausen jumps, leading to beginning saturation obeying the same mechanisms as described before (c.f. Figure 2.1). In this phase, some of the initial domain walls vanish, as indicated by the corresponding snapshot of the domain distribution. As a result, the initial state cannot be recovered by external magnetic fields [35 p. 8].

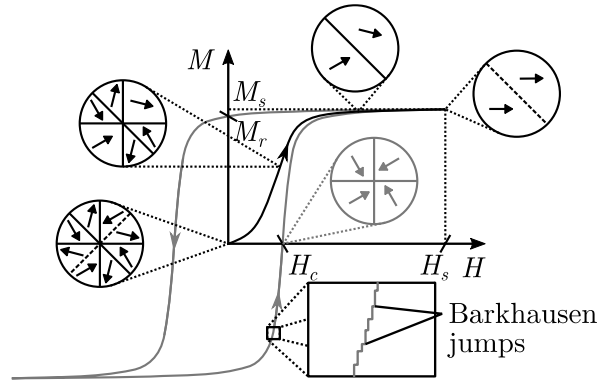


Figure 2.4: Initial magnetization (black) and magnetic hysteresis loop (grey) and as a result of impurities and crystallographic defects in ferromagnetic material

The last line segment of the initial magnetization curve approaches the saturation magnetization,  $M_s$ , and its slope approaches zero. This phase is dominated by coherent rotation, which is reversible again. When, beginning from here, the applied field is cycled between  $\pm H_s$ , the grey hysteresis curve will occur. It presents the same reversible and irreversible saturation effects as the initial curve, i.e. erratic domain wall motion for segments with high slope and coherent rotation when the magnetization saturates. It is worth noting that the hysteresis curve, as well as the ideal magnetization curve (see Figure 2.1) are symmetric to the origin.

The characteristic points of a hysteresis curve are the remanent or residual magnetization,  $M_r$ , and the intrinsic coercive field intensity,  $H_c$  [40 p. 100]. The remanence is the magnetization left behind after the external field is completely removed. It describes the state of magnetization, where the internal energy is stuck in a local minimum, which can be significantly larger than the absolute minimum energy from the initial state [35 p. 244]. The coercivity is the external magnetic field that is necessary to completely demagnetize a magnetic specimen, after it has been maximally magnetized. The value of  $H_c$  varies over a wide range for

ferromagnetic material and is used to distinguish between *soft* and *hard magnetic material*. Typical hard magnetic applications are permanent magnets, where values between 50 to 770 kA/m are obtained at room temperature for the most important magnet materials [40 p. 352]. Unless for permanent magnets, wide hysteresis loops are usually unwanted, as the area of a loop corresponds to losses associated with one magnetization cycle (see also the following subsection at p. 14). In applications where ferromagnets are dynamically magnetized in a wide range, soft magnetic material is employed. Permalloys typically applied as core material in transformers and electric machines have typical values of 8 A/m or less for the coercivity [41 p. 13].

Magnetic hysteresis is mathematically difficult to handle, since its description must incorporate discontinuities. As described above, hysteresis is dominated by irreversible highly dynamic events occurring in high numbers all over the magnetic specimen, where each of the events is restricted to small areas near pinning sites. As a result, even smallest changes in the applied field cause discontinuities that must be taken into account. In non-ideal processes, we must rely on measurements that are superimposed by noise. It is therefore difficult to distinguish between measurement noise and small-scale field changes that cause hysteretic effects.

Another problem with hysteresis is that it relies on the magnetic history of the material. Any point within the major loop can be reached by nearly infinite ways. This means that for any applied field,  $H_1$ , within the non-saturated region, the corresponding values of  $M$  can lie in the range between  $M_{1,min}$  and  $M_{1,max}$ , as is shown in Figure 2.5 [44 p. 299]. Expressed in a mathematical point of view, the relation between  $M$  and  $H$  is not *bijective*.

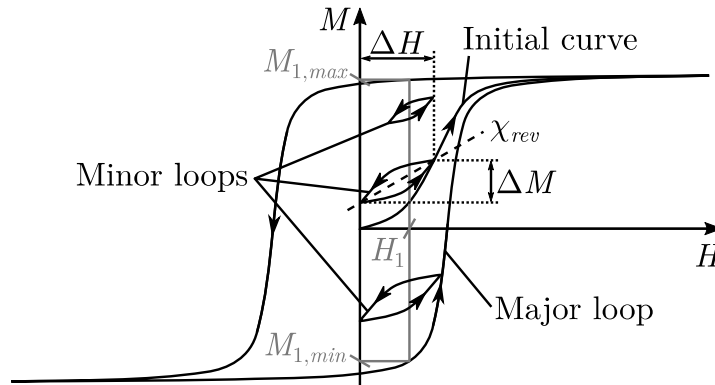


Figure 2.5: Minor loops in comparison with the initial magnetization curve and the major loop; depending on the starting points and the applied fields, all values of  $M$  lying between  $M_{1,min}$  and  $M_{1,max}$  are accessible.

The *minor loops* as depicted in Figure 2.5 occur when one or both of the extrema of  $H$  defining that loop is not either  $+H_s$  or  $-H_s$  [45]. Their average slope is given by

$$\chi_{rev} = \frac{\Delta M}{\Delta H} \quad (2.8)$$

and is a measure for the local relation between magnetization and applied field due to reversible processes [41 p. 11, 44 pp. 225–229]. It is called *reversible susceptibility* and denoted by  $\chi_{rev}$ .

In order to simplify the mathematical descriptions following in the next sections, we will henceforward neglect magnetic hysteresis. For the narrow loops of soft magnetic material, the approximation error is usually small when only the *anhysteretic* (i.e. hysteresis-free) curve is considered. It represents the globally optimal macroscopic state for the magnetization caused by an applied field in a given magnetic body [44 pp. 229–230, 46]. It thus corresponds to the ideal saturation curve already presented in Figure 2.1. It is usually close to the average of both branches of the major loop [47 p. 8]. We should keep in mind at this point that the slope of the anhysteretic curve, i.e. the *differential susceptibility*,

$$\chi_{dif} = \frac{\partial M}{\partial H}, \quad (2.9)$$

will always be larger than  $\chi_{rev}$ , since it also contains the changes in  $M$  due to irreversible processes [41 p. 11]. We will take this up again later when discussing the measurement results in Chapter 6.

The simplification of using the anhysteretic curve allows us to express the general relation between  $\vec{M}$  and  $\vec{H}$  as bijective function, i.e.

$$\vec{M} = \chi(\vec{H}) \cdot \vec{H}. \quad (2.10)$$

As mentioned before, magnetic anisotropy can cause misalignments between the vectors  $\vec{M}$  and  $\vec{H}$  (see Figure 2.2). In order to account for possible anisotropies, the *magnetic susceptibility*,  $\chi$ , thus has to be a symmetric second-rank tensor [35 p. 40]. In a given coordinate system, it can be expressed as  $3 \times 3$  matrix [44 p. 39]. Since the influence of magnetic saturation renders the relation between magnetization and magnetic field intensity nonlinear,  $\chi$  is a generic likewise nonlinear and bijective function of  $\vec{H}$ .

With (2.10), we are now able to simplify the definition of the flux density (2.7) by introducing the permeability matrix,  $\boldsymbol{\mu}$ , and the relative permeability matrix,  $\boldsymbol{\mu}_r$ , respectively [44 p. 39]. By this means, we can directly relate  $\vec{B}$  and  $\vec{H}$  as

$$\vec{B} = \mu_0 \underbrace{(\mathbf{I} + \chi(\vec{H}))}_{\boldsymbol{\mu}_r(\vec{H})} \vec{H} = \mu_0 \underbrace{\boldsymbol{\mu}_r(\vec{H})}_{\boldsymbol{\mu}(\vec{H})} \vec{H}, \quad (2.11)$$

where  $\mathbf{I}$  is the unity matrix.

### 2.1.2.6 Energy and Losses in MQS Systems

The most important fundamental law in physics is the *law of energy conservation*. It states that the total energy of an isolated system is conserved, i.e. energy can neither be created nor destroyed. It can only be transformed from one form of energy to another. Mathematically, this can be expressed in terms of generalized field theory as

$$-\oint_S \vec{p} \cdot d\vec{a} = \frac{d}{dt} \iiint_V w \cdot dv, \quad (2.12)$$

where  $w$  denotes the volume density of energy and the vector  $\vec{p}$  represents the flow of power density [32 pp. 5–6 (Ch. 11)]. The term on the *left-hand-side* (LHS) of (2.12) is the net power flowing into an arbitrary volume,  $V$ , enclosed by the surface  $S$ . Since the norm vector,  $\vec{a}$ , of

that surface is per definition positive and points out of the volume, the minus sign guarantees that a positive  $\vec{p}$  pointing towards the volume is counted as power flowing into that volume. The term on the *right-hand-side* (RHS) is the time rate of change of the total energy within the volume.

By means of the Lorentz force and the definition of mechanical work, we obtain *Joule's law*, describing the transformation from electromagnetic energy to thermal energy [32 pp. 6–7 (Ch. 11)]. The latter corresponds to the aforementioned Joule losses and will be denoted by  $p_J$ . Joule's law in terms of field theory is given as

$$p_J = \vec{j}_f \cdot \vec{E}. \quad (2.13)$$

Combining (2.13) with the MQS approximation of Maxwell's equations in matter (2.6) gives

$$-\oint_S (\vec{E} \times \vec{H}) \cdot d\vec{a} = \iiint_V \vec{H} \cdot \frac{\partial \vec{B}}{\partial t} dv + \iiint_V \vec{j}_f \cdot \vec{E} dv, \quad (2.14)$$

which is the MQS version of *Poynting's theorem* [39 pp. 751–752].

The comparison of (2.12) and (2.14) gives the *Poynting vector*,  $\vec{p}$ , defining the flow of electromagnetic power density as

$$\vec{p} = \vec{E} \times \vec{H}. \quad (2.15)$$

We can further see that the terms on the RHS of (2.14) represent the time rate of change of net electromagnetic energy in a closed volume. The second term on the RHS is obviously that part of electromagnetic energy that is transformed to thermal energy according to (2.13). Since the closed system is considered from an electromagnetic point of view, the thermal energy is always leaving the system and is thus generally regarded as dissipated energy.

Due to the fact that only MQS systems are considered, the first term on the RHS of (2.14) describes the rate of change of magnetic energy density, i.e.

$$p_\mu = \vec{H} \cdot \frac{\partial \vec{B}}{\partial t}. \quad (2.16)$$

From (2.16), the magnetic energy density can be directly given as integral of  $p_\mu$  over a time interval  $\Delta t$ , or as integral of  $\vec{H}$  vs.  $\vec{B}$  along a contour line,  $C$ , describing the progression of  $\vec{H}(t)$  within that time interval.

$$w_\mu = \int_{\Delta t} p_\mu dt = \int_C \vec{H} \cdot d\vec{B}. \quad (2.17)$$

Figure 2.6 illustrates the definition of  $w_\mu$  acc. to (2.17) for an isotropic example, where the contour line is chosen from zero to  $B_1$  in order to obtain the absolute magnetic energy density. From the example in (a), it becomes apparent that for linear material, the energy is given by  $0.5 \vec{H} \cdot \vec{B}$ . In saturating material as shown in (b), however, only the general definition (2.17) is valid. It is clear that the areas above and below the saturation curve are different. This circumstance led to the definition of *magnetic co-energy* [32 pp. 22–24 (Ch. 11)],  $w_{\mu,co}$ , which is given by

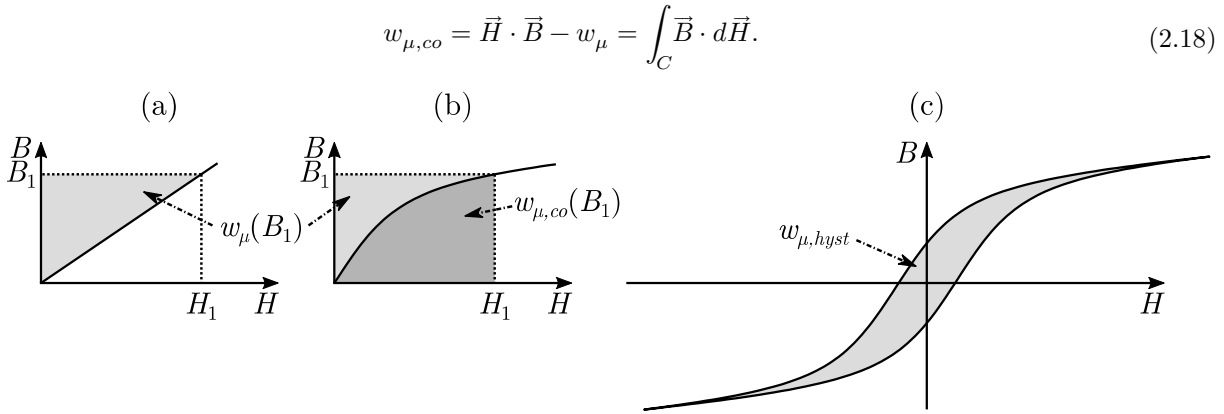


Figure 2.6: Graphical interpretation of magnetic energy and co-energy; (a) linear material; (b) saturating material; (c) dissipated energy in hysteresis loop

Figure 2.6(c) shows a major hysteresis loop, where, in contrast to the loops shown before,  $\vec{B}$  is the ordinate. When performing the integration from (2.17) along the closed contour of the hysteresis loop, we become aware that the area of the loop corresponds to the energy dissipated during one cycle,  $w_{\mu,hyst}$ . Hysteresis loops are thus inseparably linked with dissipated energy. The losses associated with it are often referred to as *hysteresis losses*.

Hysteresis losses are typically one of the two main contributors to the so-called *iron losses*, i.e. losses associated with iron, or ferromagnetic material in general, in magnetic systems. The other main part of iron losses is due to *eddy currents*.

Eddy currents occur, when the magnetic flux changes in conducting material [39 pp. 661–666]. Mathematically, they are described by the *diffusion equation* and thus have the same origin as the aforementioned proximity and skin effects [32 pp. 27–30 (Ch. 10)]. Since the diffusion equation has no general solution, when no specific body with defined boundary values is given, this work will only qualitatively deal with eddy currents.

When assuming a changing  $\vec{B}$  field, a rotational  $\vec{E}$  field will be induced in accordance with Faraday’s law, (2.6)(b). In conducting media, this so-called *electromotive force* (EMF) will cause an electric current acc. to Ohm’s law, (2.5) – Eddy currents are circulating within the material and dissipate energy by producing Joule losses acc. to (2.13).

When taking a step back again to the hysteresis losses, we can now address the origin of these losses. Knowing that changes in  $\vec{B}$  cause eddy currents, it becomes obvious that domain wall motions in conducting ferromagnetic material must be related to eddy currents. In fact, the speed of the wall motion is damped by eddy currents in a viscous manner [48 p. 95]. In [49], in reference to prior published works [50–54], it is pointed out that the physical origins of hysteresis losses are eddy currents and spin relaxation. Especially, when reminding the fact that Barkhausen jumps are local quasi-discontinuous changes of the magnetization and thus of the flux density, local eddy currents close to domain wall pinning sites can be identified to be the main source of hysteresis losses [50].

Although eddy currents are typically seen as dynamic losses, their connection with Barkhausen jumps makes them relevant also in macroscopically quasistatic re- or demagnetization processes. The hysteresis loops resulting from infinitely slow magnetization cycles are referred to as *quasistatic hysteresis loops*.

When we turn around the former statement that hysteresis loops are linked with losses, we arrive at the conclusion that losses are the reason for hysteresis<sup>4</sup>. Moreover, we can state that *all* types of losses associated with a remagnetization cycle are necessarily expressed in terms of the area enclosed by the corresponding  $\vec{B}$  vs.  $\vec{H}$  trajectory during that cycle. These losses depend on the remagnetization frequency, but also on specific properties of the material such as stress, temperature, micro- and macrostructure. In technical processes with frequencies in a range allowing the usage of the MQS approximations, the losses will mainly occur due to global and local eddy currents [50], but in literature also other effects like *magnetostriction* are identified [41 pp. 343–349]. The latter describes the mechanic deformation of material under the influence of changing magnetization. It can cause acoustic noise emissions and hence must also be a drain for electromagnetic energy.

With increasing remagnetization frequency, we can expect an increasing influence of global eddy currents and, in consequence, the shape of the resulting hysteresis loop will differ from that of the quasistatic loop. This can be seen, for instance in the works of Jiles [46], or, in the context of electrical machines, in the work of Cordier [55]. The complex interaction of global and local eddy currents, however, influences the domain wall motions [54, 56] and makes it difficult to predict the forms of the loops.

### 2.1.2.7 Equivalent Current Density

The magnetization density is measured in the same unit as the magnetic field intensity and has the same origin, i.e. moving (or spinning) electrical charges. In accordance with Ampere’s MQS law (2.4), we can thus define an intrinsic equivalent current density that causes the magnetization of a given specimen [35 pp. 43–44, 39 pp. 534–540, 41 pp. 8–10]. Technically seen, the *magnetizing current density*,  $\vec{j}_M$ , is that part of charges bound to atoms or molecules that contributes on microscopic scale to the net molecular magnetic moment and on macroscopic scale to the net magnetization  $\vec{M}$ .

$$\oint_C \vec{M} \cdot d\vec{s} \approx \iint_S \vec{j}_M \cdot d\vec{a}. \quad (2.19)$$

Figure 2.7 shows a graphical interpretation of (2.19) in a magnetized solenoid. In the left drawing, (a), slices with volumetric current density loops are shown. It emerges that the current densities at neighboring loops are always in opposed direction at their closest distances – within

---

<sup>4</sup> It was stated before that irreversible processes are causing hysteresis. In fact, the dissipation of energy is the reason for those processes to be irreversible. When reminding the statement that hysteresis results from the internal energy being stuck in a local minimum, it should be clear that the internal energy must have approached that minimum from a higher energy level (i.e. a local maximum) and that the difference energy between local maximum and minimum has to be dissipated in order to let the internal energy come to rest at that minimum.

the solenoid, they tend to cancel. Only in case of inhomogeneous magnetizations, they are relevant [39 pp. 538–539].

In homogeneous magnetization fields, the loops are uniformly distributed and have the same current densities. Within the body, they hence cancel completely, having only a net contribution along the circumference of the slices. For the representation of uniform magnetizations or when, in macroscopic view, only the net magnetization of the body shall be considered, it is sufficient to introduce a surface current density,  $\vec{j}_{MS}$ , as shown in Figure 2.7(b) [39 pp. 539–540]. Mathematically, it is given by the cross product of the uniform magnetization density and a norm vector,  $\vec{n}$ , in radial direction of the solenoid on the respective point on the surface.

$$\vec{j}_{MS} = \vec{M} \times \vec{n} \tag{2.20}$$

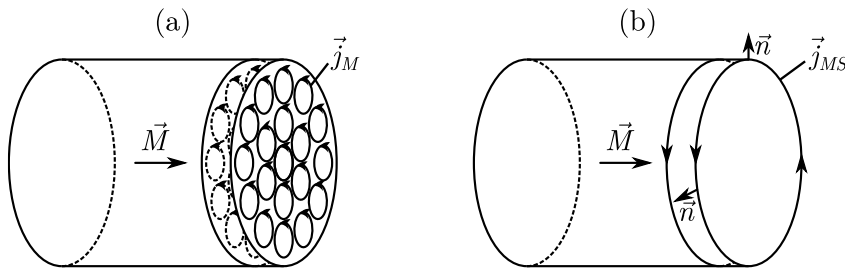


Figure 2.7: Illustration of the concept of equivalent current density for magnetized bodies; (a) slices with magnetization volume current density loops for inhomogeneous magnetizations; (b) slices with magnetization surface current density loops for both, homogeneous and inhomogeneous magnetizations

We can conclude that the macroscopic magnetization of a specimen can be considered as the result of an intrinsic current loop with such a spacial orientation and current density that the resulting field intensity corresponds to that magnetization. We will take this concept up again in section 2.2.3.1, where we discuss the virtual magnetic origin of synchronous machines.

### 2.1.2.8 Macroscopic Approximations: Circuit Theoretical Approach

Up to now, the electromagnetic processes were considered in a mesoscopic volume average. From a control engineering point of view, however, we are basically interested in the macroscopic electromagnetic repercussions, which can be measured and influenced via the electric terminals of synchronous machines. As mentioned before, the latter are MQS systems and as such, they are characterized by coils with ferromagnetic cores.

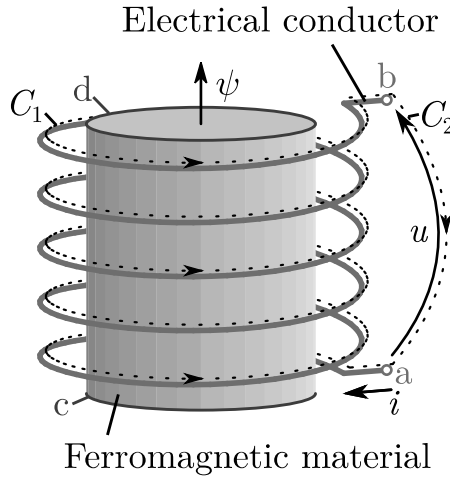


Figure 2.8: Definition of macroscopic electromagnetic field repercussions for an electric coil with ferromagnetic core and electric terminals a and b and magnetic terminals c and d; dashed lines represent integration paths  $C_1$  and  $C_2$

Figure 2.8 sketches a coil as such an element known from *circuit theory* with two electric and two magnetic terminals [57 pp. 353–422]. The terminals a and b are the electric interfaces of the coil, where we can measure the *voltage*  $u$  between the terminals and the *electrical current*  $i$  flowing into terminal a and out of terminal b.

According to the formal definition, voltage is the difference between *electric potentials* at two different points in a conservative electric field [32 pp. 2–3 (Ch. 4)]. The terminal voltage is hence given by

$$u \approx - \int_{C_2} \vec{E} \cdot d\vec{s}, \quad (2.21)$$

where  $d\vec{s}$  is an infinitesimal segment of the path  $C_2$  from terminal a to b well outside the coil, where the electric field can be assumed to be conservative [32 pp. 24–25 (Ch. 8)]. The minus sign in (2.21) takes care of the fact that the path  $C_2$  is defined in opposite direction to the voltage  $u$ . The current through a conductor is determined from the free current density integrated over the cross-sectional area,  $S$ , of that conductor. The terminal current is thus

$$i \approx \iint_S \vec{j}_f \cdot d\vec{a}, \quad (2.22)$$

where  $\vec{a}$  is the norm vector of  $S$  pointing in direction of the path  $C_1$  along the conductor from terminal a to b. Note that (2.22) gives a sufficiently accurate solution for  $i$  independent from the position of  $S$  as long as the conductor is surrounded by isolators with very low conductivity.

With a given terminal current,  $i$ , the voltage along the conductor obeys Ohm's law in its original, i.e. macroscopic form [37]. Hence,

$$\int_{C_1} \vec{E} \cdot d\vec{s} \approx R \cdot i, \quad (2.23)$$

where the *resistance*,  $R$ , is a material-specific parameter describing the conductor's resistivity against the movement of electric charges averaged over the complete conductor. Note that in contrast to the mesoscopic form of Ohm's law (2.5) the macroscopic equivalent usually applies resistivity instead of conductivity, whose relation is reciprocal. Note further that the same statements made with respect to the approximate character of (2.5) also hold for (2.23).

The third quantity introduced in Figure 2.8 is the *magnetic flux linkage*,  $\psi$ , where the term 'linkage' indicates that the superposed flux of a coil with multiple windings is considered. It is hence given by integration of the flux density over the surface  $S$ , which is enclosed by the paths  $C_1 + C_2$ .

$$\psi \approx \iint_S \vec{B} \cdot d\vec{a} \quad (2.24)$$

As long as the ferromagnetic core is not saturated and surrounded by paramagnetic media (i.e. media with  $\chi \approx 0$ ), the flux linkage 'flows' into the magnetic terminal c, through the ferromagnet and out of d. That part of the magnetic flux not passing the terminals is typically referred to as *leakage flux* and is neglected in (2.24).

The three macroscopic quantities current, voltage und flux linkage as defined in (2.21)-(2.23) are related to each other by Faraday's law for MQS systems (2.6)(b). When the closed integration path is again  $C_1 + C_2$ , we get

$$-\frac{d\psi}{dt} \approx \oint_{C_1+C_2} \vec{E} \cdot d\vec{s} = \int_{C_1} \vec{E} \cdot d\vec{s} + \int_{C_2} \vec{E} \cdot d\vec{s}. \quad (2.25)$$

Substituting (2.21) and (2.23) into (2.25) finally leads to

$$u \approx R \cdot i + \frac{d\psi}{dt}. \quad (2.26)$$

Equation (2.26) is the basis for the mathematical model of synchronous machines, or electrical machines in general. It is an approximate solution since it was derived by applying several assumptions that are repeated below for clarity:

1. The system is assumed to be MQS, i.e. the electric energy within the system is negligible compared to the magnetic energy and the maximal length of the system is small compared to the wavelengths of occurring frequencies ( $\rightarrow \frac{d}{dt} \iint_S \epsilon_0 \vec{E} \cdot d\vec{a} \approx 0$ )
2. The occurring frequencies are assumed to be low enough such that no relevant reduction of the effective cross-sectional area of the conductor due to proximity or skin effects has to be taken into account ( $\rightarrow R \approx \text{const.}$ )
3. The temperature of the system is assumed to be constant such that its influence on the resistance can be neglected ( $\rightarrow R \approx \text{const.}$ )
4. The terminal voltage is defined assuming the electrical terminals and the integration path between them to be located in a conservative electric field ( $\frac{d\psi}{dt} \approx 0$  outside the coil in the area between the electric terminals)
5. Leakage flux, i.e. flux not passing the magnetic terminals, is negligible

6. The conductor is assumed to be perfectly isolated such that the same amount of electric charges flowing into terminal a flows out of terminal b, or vice versa ( $i_a = -i_b$ ); due to the MQS assumptions, which involve that the conductor is non-capacitive, that condition must be valid at any time

When all these assumptions are applicable, (2.26) describes the macroscopic repercussions of the electromagnetic processes in a winding. It seems to be linear – at least at first sight. In fact, we must remind that the current produces a magnetic field acc. to Ampere’s law (2.6)(a). This field is amplified by the magnetization within the ferromagnetic core acc. to (2.7) and as extensively discussed in the former subsections, the relation between  $\vec{H}$  and  $\vec{M}$  is determined by saturation and hysteresis and is thus nonlinear. The superposition of  $\vec{H}$ - and  $\vec{M}$ -fields leads to the magnetic flux density and for a given geometry to the flux linkage. We can thus state that (2.26) is nonlinear in all applications, where ferromagnetic material is (re-)magnetized in such magnitudes that it saturates or desaturates. In common synchronous machines, this is usually the case, as they are designed to be as compact and material-saving as possible.

At this point, it shall be emphasized that – regardless of all assumptions listed above – Equation (2.26) is explicitly valid also in case of *nonlinear relations between current and flux linkage*, because it was derived without any constraints requesting linearity.

When considering the nonlinear relation between current and flux linkage, (2.26) can be rewritten by applying the chain rule of differential calculus [58 p. 437] such that only the quantities related with the electrical terminals occur. Hence,

$$u \approx R \cdot i + \frac{\partial \psi}{\partial i} \frac{di}{dt}, \quad (2.27)$$

with

$$L = \frac{\partial \psi}{\partial i} \quad (2.28)$$

as the formal definition of the *inductance*  $L$ .

It is important to note that in many applications, an affine or even linear relation between flux linkage and current is assumed for convenience. In the affine case, the differential quotient from (2.28) simplifies to a difference quotient, and in the linear case to an absolute quotient. Hence,

$$L_{affine} = \frac{\Delta \psi}{\Delta i} \quad (2.29)$$

and

$$L_{linear} = \frac{\psi}{i}. \quad (2.30)$$

Figure 2.9(a) and (b) illustrate the definitions of affine and linear inductances. The linear inductance acc. to (2.30) is found very often in literature. It is, however, important to note that it is only applicable when no flux linkage offset is present and no magnetic saturation occurs.

In applications where magnetic saturation must be taken into account, the inductance value acc. to (2.28) is depending on the actual operating point as shown in Figure 2.9(c). Whenever it is necessary to linearize a system at a given operating point, it is crucial to properly distinguish between the different definitions of inductances acc. to (2.28) to (2.30). As shown in (c), where the slopes of the grey, dashed lines correspond the inductances at the operating point, all three inductances have different values.

Generally, (2.28) is the formal correct definition, whereas (2.29) is an approximation that can be used for linearization. For sufficiently small  $\Delta i$ , we obtain the *small-signal inductance*, which is a good approximation for the actual *differential inductance* acc. to (2.28). For  $\Delta i = i_{op}$ , as it is shown in Figure 2.9(c), we obtain the *large-signal inductance*, often also referred to as *absolute inductance*. It corresponds to the average slope of the flux linkage curve in the range from  $i = 0$  to  $i = i_{op}$ .

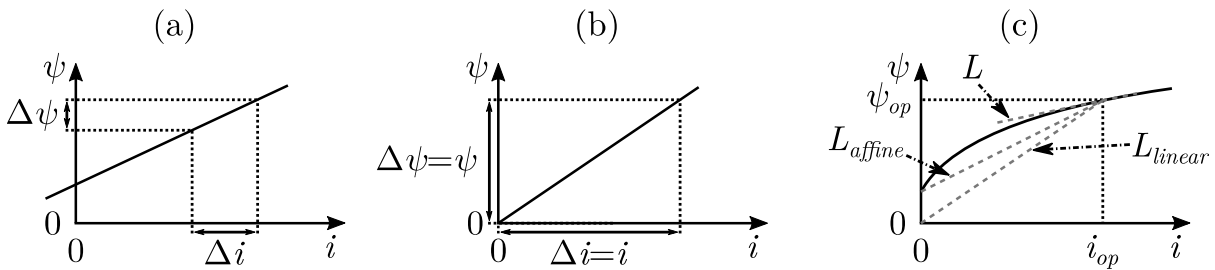


Figure 2.9: Graphical interpretations of inductances; (a) affine relation between flux linkage and current; (b) linear relation between flux linkage and current; (c) nonlinear relation between flux linkage and current

In terms of circuit theory, (2.27) can be interpreted as lumped element model as shown in Figure 2.10. Each term on the RHS of (2.27) is considered as discrete element linking voltage and current (Resistor) or current derivative (Inductor), respectively.

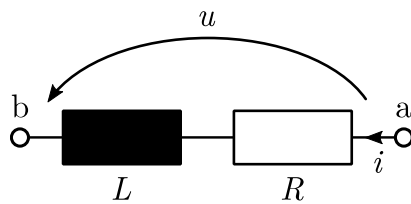


Figure 2.10: Lumped element model of the electric part of a coil as shown in Figure 2.8

## 2.2 Description of Synchronous Machines

### 2.2.1 Preliminaries on Synchronous Machines

Synchronous machines exist in several variants. They all have in common that the stator windings produce a rotating magnetic field. As the name indicates, the rotor tends to follow this stator field, such that a synchronous rotation occurs.

In order to produce a rotational magnetic field, at least two non-parallel windings are necessary. The simplest configuration with two orthogonal windings is shown in Figure 2.11. In the depicted cross-sectional view, a stator-fixed *Cartesian coordinate system* with the perpendicular axes  $\alpha$  and  $\beta$  is introduced.

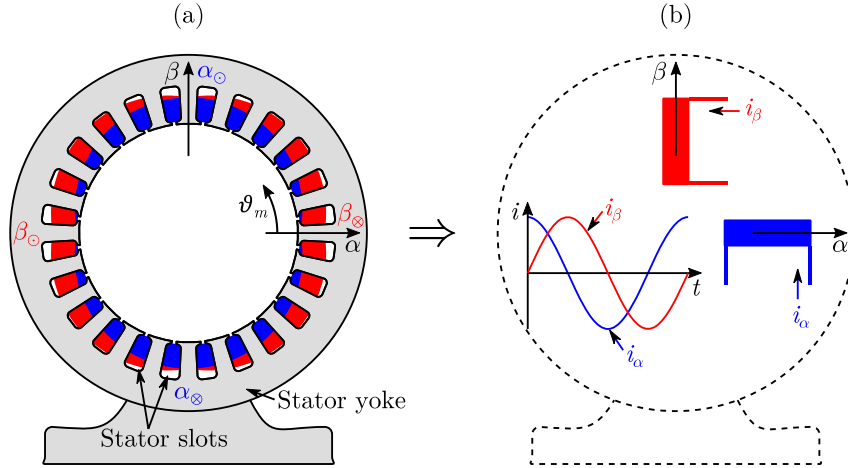


Figure 2.11: Example of a stator in cross-sectional view with a winding configuration, which allows the generation of rotational fields by two orthogonal windings with idealized sinusoidal distribution along the circumference

A useful definition in order to simplify the field calculations is the *current loading*. In the same manner as magnetization can be interpreted as surface current density acc. to (2.20) (see Figure 2.7(b)), the current density in axial direction in the windings is interpreted as linear current density, or current loading at an infinitesimal layer in the air gap between stator and rotor [38 p. 6]. It is defined as axial current per differential length  $\partial l$  along the middle of the air gap.

$$a = \frac{\partial}{\partial l} \iint_S \vec{j} \cdot d\vec{a} \approx \frac{\Delta}{\Delta l} \iint_S \vec{j} \cdot d\vec{a} \quad (2.31)$$

The approximate solution in (2.31) corresponds to the mean current loading over a finite circumferential section  $\Delta l$  and helps to further simplify calculations. The surface  $S$  is typically chosen as the area of a stator slot and  $\Delta l$  is the corresponding slot opening. As a result, we will get a discrete current loading distribution along the circumference, which has the value of the mean current loading in the areas of the corresponding slots and which is zero elsewhere [59 p. 61].

By means of *Fourier analysis*, the discrete current loading can be expressed in terms of harmonic components. For the moment, we will neglect the fact that stators are slotted in order to host the windings and only consider the fundamental wave of the current loading. This is analogue to assuming the windings to be sinusoidally distributed along the circumference of the stator, as indicated in Figure 2.11(a). In this case, the superposition of the current loadings of both coils give a joint, likewise sinusoidal current loading distribution (cf. superposition of harmonic functions [58 p. 83]).

When, as shown in Figure 2.11(b), sinusoidally alternating currents (AC) with a phase difference of  $\pm 90^\circ$  flow through both coils, the joint current loading moves along the circumference. In accordance with the MQS approximation of Ampere’s Law, a synchronously rotating magnetic field is the result. The direction of rotation is determined by the sign of the phase delay between both currents. In the shown case, where  $i_\alpha$  leads  $90^\circ$  in phase, a mathematically positive or counter-clockwise rotation occurs.

Additionally to the Cartesian system, it is useful to introduce also a polar coordinate system with the *mechanical angle*  $\vartheta_m$ , whose reference direction is the  $\alpha$ -axis, as shown in Figure 2.11(a).

In practice, most synchronous machines have three symmetrical, star-connected<sup>5</sup> phases as shown in Figure 2.12. This has the advantage that only three power lines are necessary to supply the motor instead of the obligatory four lines a two phase machine would need. The assumptions from the definition of the lumped element model (especially numbers 1 and 6, see p. 20) allow the application of *Kirchhoff’s current law* [60]. Employing it in the given case with star-connection without neutral conductor directly leads to

$$i_a + i_b + i_c = 0, \tag{2.32}$$

which reduces the degrees of freedom for the three stator currents to two.

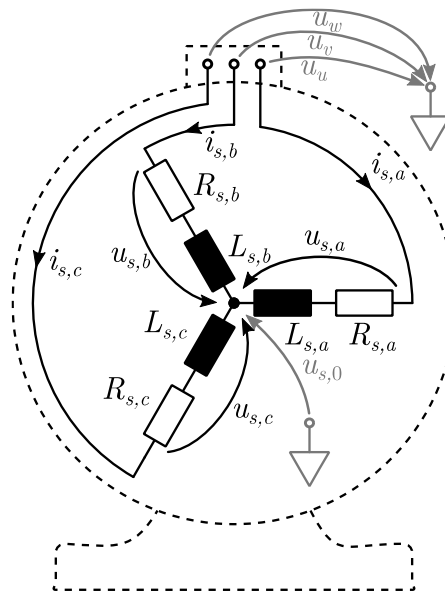


Figure 2.12: Stator configuration of a star-connected three-phase synchronous machine

<sup>5</sup> Star connection is the standard for three-phase synchronous machines, since the alternative delta connection would allow circular short circuit currents, which occur in the case of third harmonic components (e.g. due to magnetic saturation, see Section 2.2.3) in the electromotive force (EMF) of the machine [2 p. 429].

The three stator coils are wound such that their spatial orientations are exactly  $\pm 120^\circ/p$  displaced from each other, whereat  $p$  denotes the *number of pole pairs*.

Provided that assumption number 4 (see p. 20) is applicable, the phase voltages  $u_{s,a}$ ,  $u_{s,b}$  and  $u_{s,c}$  are linked with the applied terminal voltages  $u_u$ ,  $u_v$  and  $u_w$  by *Kirchhoff's voltage law* [60].

$$\begin{bmatrix} u_u - u_v \\ u_v - u_w \\ u_w - u_u \end{bmatrix} = \begin{bmatrix} 1 & -1 & 0 \\ 0 & 1 & -1 \\ -1 & 0 & 1 \end{bmatrix} \begin{bmatrix} u_{s,a} \\ u_{s,b} \\ u_{s,c} \end{bmatrix} \quad (2.33)$$

Since the rank of the matrix in (2.33) is two, we can state that the degree of freedom for the terminal voltages is also two, whereas the phase voltages have three degrees of freedom [61 p. 53]. It is thus not possible to determine the phase voltages from the terminal voltages without knowing the star point potential  $u_0$ .

Due to the symmetry of the windings and when we assume an equal temperature distribution in the machine, we get the following relations for the *stator resistances*.

$$R_{s,a} = R_{s,b} = R_{s,c} = R_s \quad (2.34)$$

The *phase inductances* of the stator windings,  $L_{s,a}$ ,  $L_{s,b}$  and  $L_{s,c}$ , however, can differ, since they depend not only on the stator but also on the magnetic coupling with the rotor and the level of magnetic saturation.

At this point, we get to the main distinguishing criterion of standard sine-wave commutated synchronous machines – the rotor design. It determines the way the rotor field is produced and how the inductances change during a rotor turn. Figure 2.13 shows three examples of brushless synchronous machines, i.e. machines without field windings in the rotor. The advantage of omitting rotor windings is that no electric current and, in consequence, no *direct current* (DC) power supply and no carbon brushes are necessary. Unless superconductors are employed (as, for instance, in high-power marine applications [62]), the rotor current is associated with Ohmic losses. For this reason, *permanent magnet* (PM) synchronous machines generally present higher efficiency than the electrically excited ones, however, at increased raw material costs due to the higher price of PM material. The absence of brushes, on the other hand, reduces the maintenance costs and increases the drive's robustness. Additionally, the construction process of electrically excited rotors is more complex [63]. For those reasons, this work addresses only the three main types of brushless synchronous motors, as exemplarily shown in Figure 2.13.

Common PM materials in synchronous machines are *ferrites* in low cost applications, *Samarium-Cobalt* (SmCo) in high-performance applications and *Neodymium-Iron-Boron* (NdFeB) in small-size or high-performance applications with low operating temperature [48 p. 28].

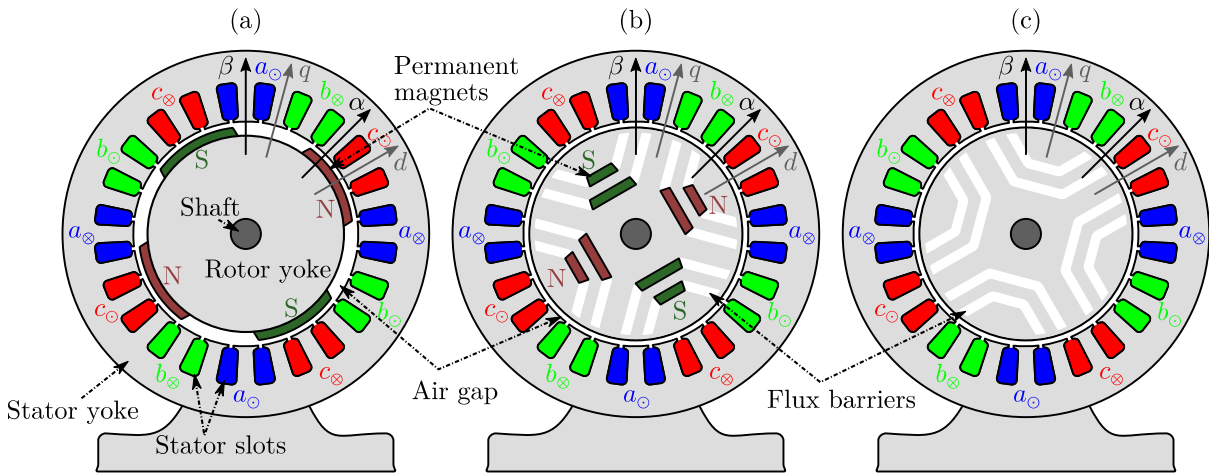


Figure 2.13: Cross-sectional views of three-phase brushless synchronous machines with four poles each; (a): surface permanent magnet synchronous motor (SPMSM); (b): interior permanent magnet synchronous motor (IPMSM); (c): synchronous reluctance motor (SynRM)

The subfigures (a) and (b) show *permanent magnet synchronous machines* (PMSMs). In (a), the field of the internal rotor is produced by *surface (mounted) permanent magnets* (SPM), whereas in (b) *interior permanent magnets* (IPM) are employed. Subfigure (c) shows a *synchronous reluctance machine* (SynRM<sup>6</sup>), where no PMs are used. All three machines have the same three-phase stators. They have four poles each at the stator and the rotor, i.e.  $p = 2$ . The magnetic stator field or – in case of the PMSMs – the joint field as superposition of stator and rotor field passes along both yokes and crosses the air gap. Here, Lorentz forces arise and sum up to a torque that is applied to external processes via the shaft of the machine.

As indicated, stator and rotor are constructed rotationally symmetric in order to maximally utilize the ferromagnetic material and to avoid torque fluctuations during operation.

In Figure 2.11, the stator-fixed  $\alpha\beta$  coordinate system has already been introduced. It is also depicted in Figure 2.13. Note that the angle between the axes in the real spatial interpretation is  $90^\circ/p = 45^\circ$ , since  $p = 2$ . For the mathematical interpretation, however, an *electrical rotor angle* is introduced as

$$\vartheta_r = \vartheta_m \cdot p. \quad (2.35)$$

Due to this definition, we can mathematically describe the electrical processes in the machine in terms of a stator-fixed system with orthogonal axes. This is further described in the following section 2.2.2.

<sup>6</sup> In literature also referred to as reluctance synchronous machine and abbreviated by RSM. In German literature, however, RSM is reserved for ‘Reihenschlussmaschine’, i.e. series-wound DC machine. Additionally, the abbreviation SRM is typically used for ‘switched reluctance machine’. We will hence use the abbreviation SynRM within this work in order to avoid confusion.

In order to simplify the mathematical representation of the rotor's magnetic properties, it is useful to define a rotor-fixed Cartesian coordinate system. It is also drawn in Figure 2.13 in dark grey. Per common definition, it has a  $d$ -axis (direct axis) that is aligned with the rotor flux and a corresponding (in terms of the electrical angle) perpendicular  $q$ -axis. In case of the SynRM, where no flux is produced in the rotor, the  $d$ -axis is aligned with the magnetically easy axis of the rotor, i.e. with direction of the flux path with the least air gap. This definition has the advantage that for all types of synchronous machines, the stable operating point under no load condition is obtained, when the  $d$ -axis is aligned with the stator field.

Rotors with SPMs are usually easier and hence cheaper to produce. Common PM materials have a relative permeability of  $\mu_r \approx 1$  (SmCo and NdFeB magnets have both  $\mu_r = 1.05$ , Barium-Iron ferrites have  $\mu_r = 1.1$  [39 p. 552], since at remanence magnetization they are almost completely saturated). They can thus be considered as an increase of the effective air gap for the magnetic flux traversing the magnets. In case of the *surface permanent magnet synchronous machine* (SPMSM), it can be stated that both, the  $d$ - and the  $q$ - axis flux linkage traverse an equidistant air gap. An SPM motor hence does not have an easy axis. In practice, however, it nevertheless exhibits a magnetic anisotropy, which results from pre-saturation of the  $d$ -axis due to the permanent magnets, as will be shown later in section 4.3.

As the name indicates, in *interior permanent magnet synchronous machines* (IPMSM) the magnets are embedded into the rotor. This is advantageous, because the PMs are removed from the air gap, which, in consequence, can be significantly reduced. By this means, the magnetic utilization of the rotor yoke can be improved. When the magnets, however, are surrounded by ferromagnetic material, flux barriers are necessary in order to prevent the PM flux from directly closing on the shortest way within the rotor. The typically air-filled flux barriers cause a strict separation between the  $d$ - and the  $q$ -flux paths. Since the  $d$ -path has an increased effective air gap due to the PMs and the flux barriers, both paths have different magnetic resistances, or *reluctances*, i.e. the rotor exhibits magnetic shape anisotropy. This reluctance difference can be exploited in order to generate an additional so-called *reluctance torque*. The superposition with the torque originating from the PM field allows higher torque and power densities than non-reluctant machines have [2 p. 866]. As in SPM motors, the PMs pre-saturate the  $d$ -flux path and thus enhance the magnetic anisotropy due to the salient rotor design.

Another use of salient rotor designs with flux barriers is in synchronous reluctance machines. Here, the only torque produced is the reluctance torque and the magnets are consequently omitted. This leads to cheaper and more temperature resistant motors, however, at the expense of lower torque and power densities [59 p. 775].

### 2.2.2 Space Vector Notation

An efficient and common mathematical description of synchronous machines applies the *space vector* notation. Here, the idea is to express the magnetic field distributions of an  $n$ -phase motor in terms of the simple two-dimensional case as depicted in Figure 2.11. A space vector is, accordingly, a two-dimensional vector with a spatial orientation in the cross-sectional view of a motor. It should be noted that in this cross-sectional interpretation, only currents in axial

direction and related fields in radial direction are considered, or, with other words, the end windings are neglected. This is a valid simplification for standard radial flux machines, where the length of the machine is significantly larger than its diameter. For all machines used within this work, this condition is fulfilled.

### 2.2.2.1 Current Space Vector

The Figures 2.14 to 2.16 illustrate an example of the space vector theory for currents in the stator windings of three-phase motors with two stator poles.

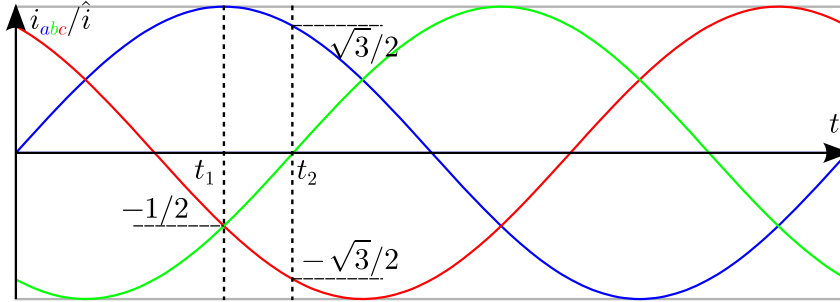


Figure 2.14: Symmetrical three-phase alternating current in the phases  $a$ ,  $b$  and  $c$  over time

Figure 2.14 shows the currents in a symmetrical three-phase alternating current (AC) system. Within the diagram, the times  $t_1$  and  $t_2$  and the corresponding instantaneous line currents are defined as they are shown in the following Figures 2.15 and 2.16. For simplicity, the stators in Figure 2.15 are drawn without stator slots and with non-sinusoidally distributed windings, which would lead to rectangular shaped current density distributions along the circumference as shown in Figure 2.16. However, the problem of harmonic distortions due to slotting, non-sinusoidal winding schemes, air gap geometries or magnetic saturation shall be neglected for the moment. We thus only consider the fundamental wave of the current loading as indicated, which would correspond to a motor with sinusoidally distributed windings [64 p. 182] as in Figure 2.11. From Figure 2.16, we can see that the fundamental component of the current loading has a constant amplitude and thus describes a propagating wave traveling along the stator in positive direction of the angle  $\vartheta$ .

As depicted in Figure 2.15, a stator current space vector for each phase is defined as the projection of the generic instantaneous line current on the respective winding axis. This might seem unusual, since it is defined orthogonal to the extrema of the current loading. However, space vectors shall describe the magnetic couplings between the phases and also between the rotor and stator fields and thus point into the direction of the magnetic field produced by the electrical current of each winding. The superposition of the three windings' fields consequently leads to an overall stator current space vector  $\mathbf{i}_\Sigma^s$  as summation of the three phase current vectors.

$$\mathbf{i}_\Sigma^s = \mathbf{i}_a^s + \mathbf{i}_b^s + \mathbf{i}_c^s \quad (2.36)$$

In order to not confuse space vectors with the field vectors from section 2.1, space vectors are written in bold letters. The distinction from matrices is made by only using small letters for

space vectors and capital letters for matrices. For both, space vectors and matrices, the superscript  $s$  denotes the reference coordinate system of the space vectors, which is in this case a stator-fixed Cartesian system with the two perpendicular axes  $\alpha$  and  $\beta$ , respectively. Per definition, the abscissa of the stator-oriented system is aligned with the phase  $a$  winding's axis, as shown in Figures 2.13 and 2.15.

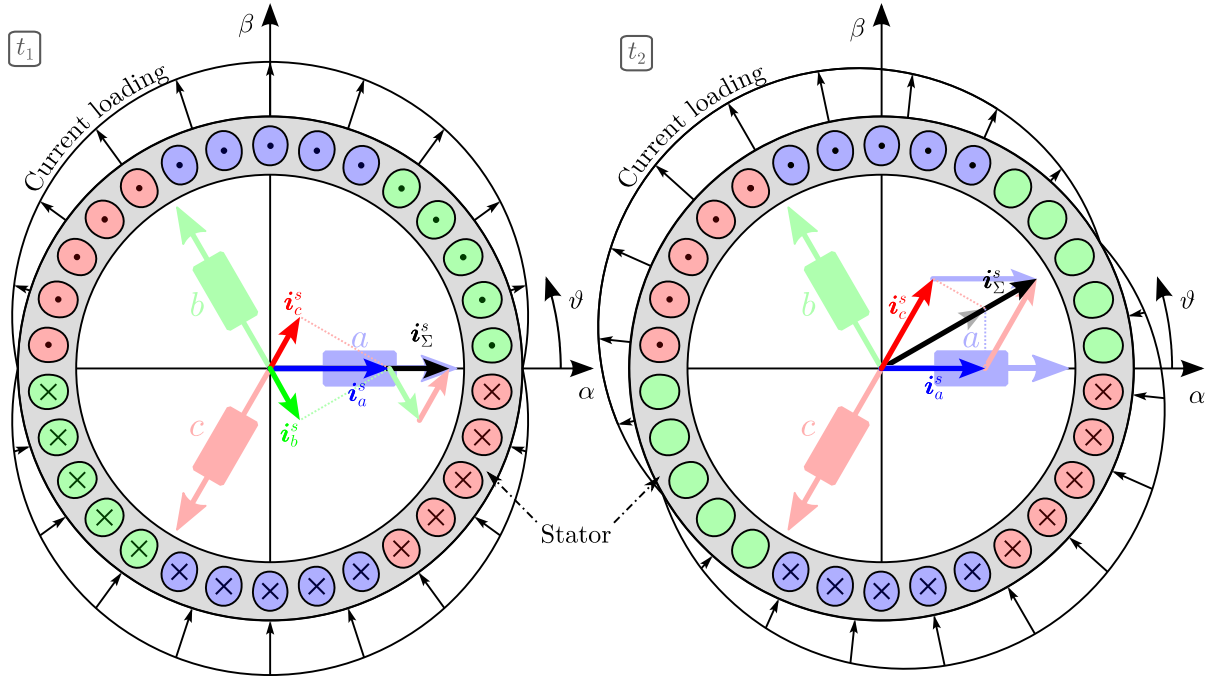


Figure 2.15: Graphical interpretation of stator current space vectors for three-phase AC motors at two different times  $t_1$  and  $t_2$  defined in Figure 2.14 with the fundamental component of the current loading

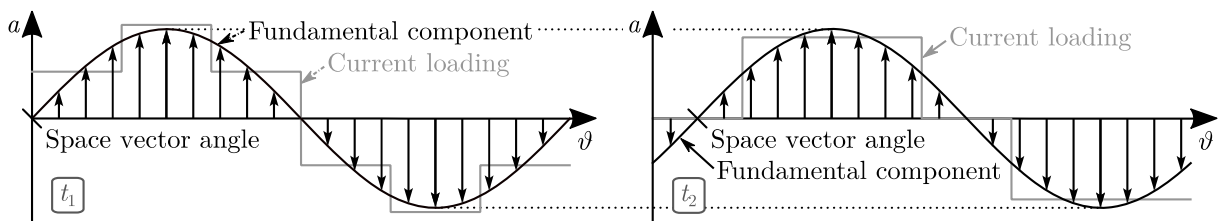


Figure 2.16: Current density distribution along the circumference of the stators from Figure 2.15 at the times  $t_1$  and  $t_2$  as defined in Figure 2.14

By considering the information about the spatial distribution of the windings, we can write the phase current vectors as

$$\begin{aligned} \mathbf{i}_a^s &= \begin{bmatrix} i_a \\ 0 \end{bmatrix}, \\ \mathbf{i}_b^s &= \mathbf{T} \left( \frac{2\pi}{3} \right) \begin{bmatrix} i_b \\ 0 \end{bmatrix}, \\ \mathbf{i}_c^s &= \mathbf{T} \left( -\frac{2\pi}{3} \right) \begin{bmatrix} i_c \\ 0 \end{bmatrix}, \end{aligned} \quad (2.37)$$

where  $\mathbf{T}(\vartheta)$  is the rotation matrix, which – when multiplied with a given two-dimensional column vector – gives a new vector that is rotated by the angle  $\vartheta$  in mathematically positive sense [58 p. 299, 65 p. 66].

$$\mathbf{T}(\vartheta) = \begin{bmatrix} \cos \vartheta & -\sin \vartheta \\ \sin \vartheta & \cos \vartheta \end{bmatrix} \quad (2.38)$$

With (2.37)-(2.38), we can rewrite (2.36) as

$$\begin{aligned} \mathbf{i}_{\Sigma}^s &= \begin{bmatrix} i_a \\ 0 \end{bmatrix} + \begin{bmatrix} -1/2 & -\sqrt{3}/2 \\ \sqrt{3}/2 & -1/2 \end{bmatrix} \begin{bmatrix} i_b \\ 0 \end{bmatrix} + \begin{bmatrix} -1/2 & \sqrt{3}/2 \\ -\sqrt{3}/2 & -1/2 \end{bmatrix} \begin{bmatrix} i_c \\ 0 \end{bmatrix} \\ &= \begin{bmatrix} 1 \\ 0 \end{bmatrix} i_a + \begin{bmatrix} -1/2 \\ \sqrt{3}/2 \end{bmatrix} i_b + \begin{bmatrix} -1/2 \\ -\sqrt{3}/2 \end{bmatrix} i_c. \end{aligned} \quad (2.39)$$

By collecting the scalar phase currents in a three-dimensional column vector, we can further simplify (2.39) to

$$\mathbf{i}_{\Sigma}^s = \begin{bmatrix} 1 & -1/2 & -1/2 \\ 0 & \sqrt{3}/2 & -\sqrt{3}/2 \end{bmatrix} \begin{bmatrix} i_a \\ i_b \\ i_c \end{bmatrix}. \quad (2.40)$$

When applying (2.40) to the steady state three-phase AC system with the line current amplitude  $\hat{i}$  as shown in Figures 2.14 to 2.16, we see that  $\mathbf{i}_{\Sigma}^s$  rotates at the AC frequency with a constant amplitude of  $3/2 \cdot \hat{i}$ . It is therefore common practice to define a space vector with a scaling factor of  $2/3$  in order to normalize it to the phase amplitude [2, 66–68]. This so-called *non-power-invariant form* has the advantage that the orthogonal projections of the current space vector on the phase axes yields the instantaneous values of the respective line current [66 p. 35] as indicated by the dotted lines in Figure 2.15. It is worth noting that this is only valid, if no zero-sequence components are present, which is guaranteed in our case due to the star connection of the windings (see Equation (2.36)).

In steady-state, the electrical behavior of AC machines can be described by single-phase equivalent circuits [59 pp. 223–225 and 516]. It is due to this fact that space vectors are most commonly defined as complex vectors, so-called space phasors [2, 59, 66–69] in analogy to the phasors used for the analysis of AC equivalent circuits [70 p. 18, 71 pp. 33–42]. It is important, however, not to confuse both phasors, since space phasors have a spatial orientation (the  $\beta$ -axis is defined as imaginary axis) and can also describe non-sinusoidal variables [66 p. 33]. For that reason and also because of limitations in describing the magnetic anisotropy of synchronous machines, the mathematically equivalent generic vector notation will be used within this work.

Concluding above considerations, we get an expression for calculating the stator current (denoted by index  $_s$ ) space vector  $\mathbf{i}_s^s$  from the generic instantaneous line currents by the bijective transformation function

$$\mathbf{i}_s^s = \begin{bmatrix} i_{s,\alpha} \\ i_{s,\beta} \end{bmatrix} = \frac{2}{3} \begin{bmatrix} 1 & -1/2 & -1/2 \\ 0 & \sqrt{3}/2 & -\sqrt{3}/2 \end{bmatrix} \begin{bmatrix} i_a \\ i_b \\ i_c \end{bmatrix}. \quad (2.41)$$

Equation (2.41) is the vectorial equivalent of the *Clarke transformation* (with the difference that the applied scaling factor there is  $1/3$ ) [69 pp. 54–70]. Its inverse can be obtained by means of the *pseudo-inverse* of the transformation matrix. Hence,

$$\begin{bmatrix} i_a \\ i_b \\ i_c \end{bmatrix} = \frac{3}{2} \begin{bmatrix} 2/3 & 0 \\ -1/3 & \sqrt{3}/3 \\ -1/3 & -\sqrt{3}/3 \end{bmatrix} \begin{bmatrix} i_{s,\alpha} \\ i_{s,\beta} \end{bmatrix}. \quad (2.42)$$

### 2.2.2.2 Voltage Space Vector

In *voltage source inverter* (VSI) driven applications, as exclusively considered within this thesis, the terminal voltages are the actuation variables for controlling synchronous machines. For a complete mathematical model, also a space vector for the stator voltages must be defined. Therefore, we collect the terminal equations (2.26) for the three phase windings and rewrite them in matrix notation as

$$\begin{bmatrix} u_a \\ u_b \\ u_c \end{bmatrix} = R_s \cdot \begin{bmatrix} i_a \\ i_b \\ i_c \end{bmatrix} + \frac{d}{dt} \begin{bmatrix} \psi_a \\ \psi_b \\ \psi_c \end{bmatrix}, \quad (2.43)$$

where the stator resistance is scalar, since we assumed it to have the same value for each phase acc. to (2.34).

From (2.41), we know that the Clarke transformation is the result of a linear matrix multiplication. We can thus apply the transformation also to (2.43) without loss of generality. In this particular case, however, we shall extend the transformation matrix by a third line accounting for a potential zero-sequence component. For the current space vector (2.41), this line was omitted, since star connection without neutral conductor suppresses zero-sequence currents (see (2.32)). The phase voltages in unbalanced<sup>7</sup> star-connected machines, however, can have a zero-sequence component,  $u_{s,\gamma}$ . In accordance with the *theory of symmetrical components*, the zero-sequence voltage is defined as the mean value of the instantaneous phase voltages [72 pp. 6–12]. We can thus transform (2.43) by matrix multiplication and obtain

$$\begin{aligned} & \frac{2}{3} \begin{bmatrix} 1 & -1/2 & -1/2 \\ 0 & \sqrt{3}/2 & -\sqrt{3}/2 \\ 1/2 & 1/2 & 1/2 \end{bmatrix} \begin{bmatrix} u_a \\ u_b \\ u_c \end{bmatrix} \\ &= R_s \cdot \frac{2}{3} \begin{bmatrix} 1 & -1/2 & -1/2 \\ 0 & \sqrt{3}/2 & -\sqrt{3}/2 \\ 1/2 & 1/2 & 1/2 \end{bmatrix} \begin{bmatrix} i_a \\ i_b \\ i_c \end{bmatrix} + \frac{d}{dt} \left( \frac{2}{3} \begin{bmatrix} 1 & -1/2 & -1/2 \\ 0 & \sqrt{3}/2 & -\sqrt{3}/2 \\ 1/2 & 1/2 & 1/2 \end{bmatrix} \begin{bmatrix} \psi_a \\ \psi_b \\ \psi_c \end{bmatrix} \right), \end{aligned} \quad (2.44)$$

which can be rewritten compacter in extended space vector notation as

$$\begin{bmatrix} u_{s,\alpha} \\ u_{s,\beta} \\ u_{s,\gamma} \end{bmatrix} = R_s \begin{bmatrix} i_{s,\alpha} \\ i_{s,\beta} \\ 0 \end{bmatrix} + \frac{d}{dt} \begin{bmatrix} \psi_{s,\alpha} \\ \psi_{s,\beta} \\ \psi_{s,\gamma} \end{bmatrix}. \quad (2.45)$$

<sup>7</sup> Reminding the fact that the three phase inductances can differ due to salient rotor geometry and magnetic saturation (see Section 2.2.1)

It was mentioned before that the factor  $2/3$  in the Clarke transformation scales the space vector to the instantaneous phase values of the respective quantities (see p. 30). It is worth noting that in consequence, the resistance of a single phase can be applied without scaling in the space vector model.

From (2.44) and (2.45), we can see that the extended voltage space vector is given by

$$\begin{bmatrix} u_{s,\alpha} \\ u_{s,\beta} \\ u_{s,\gamma} \end{bmatrix} = \frac{2}{3} \begin{bmatrix} 1 & -1/2 & -1/2 \\ 0 & \sqrt{3}/2 & -\sqrt{3}/2 \\ 1/2 & 1/2 & 1/2 \end{bmatrix} \begin{bmatrix} u_a \\ u_b \\ u_c \end{bmatrix}. \quad (2.46)$$

The inverse transformation of (2.46) can be obtained by matrix inversion. Hence,

$$\begin{bmatrix} u_a \\ u_b \\ u_c \end{bmatrix} = \frac{3}{2} \begin{bmatrix} 2/3 & 0 & 2/3 \\ -1/3 & \sqrt{3}/3 & 2/3 \\ -1/3 & -\sqrt{3}/3 & 2/3 \end{bmatrix} \begin{bmatrix} u_{s,\alpha} \\ u_{s,\beta} \\ u_{s,\gamma} \end{bmatrix}. \quad (2.47)$$

For cost effectiveness, most star-connected synchronous machines do not have an accessible star point. It is thus not possible to directly measure its potential  $u_{s,0}$  (see Figure 2.12). By means of Kirchhoff's voltage law, however, we can relate it with the zero-sequence voltage by

$$u_{s,\gamma} = \frac{u_a + u_b + u_c}{3} = u_{s,0} + \frac{u_u + u_v + u_w}{3}. \quad (2.48)$$

The zero-sequence voltage is thus the sum of the (unknown) star point potential and the zero-sequence component of the supply voltage. The latter depends on the voltage source topology and the modulation scheme [73]. Both are not in the scope of this work and thus will be taken as given (see description of the test rig in Chapter 3). We will therefore assume that we cannot freely influence the zero-sequence component of the supply voltage.

When we remind the equation for the terminal voltages (2.33) and substitute the phase voltages by (2.47), we get

$$\begin{bmatrix} u_u - u_v \\ u_v - u_w \\ u_w - u_u \end{bmatrix} = \frac{3}{2} \begin{bmatrix} 1 & -\sqrt{3}/3 & 0 \\ 0 & 2\sqrt{3}/3 & 0 \\ -1 & -\sqrt{3}/3 & 0 \end{bmatrix} \begin{bmatrix} u_{s,\alpha} \\ u_{s,\beta} \\ u_{s,\gamma} \end{bmatrix}. \quad (2.49)$$

From (2.49), we can see that the terminal voltages do not depend on the zero-sequence component  $u_{s,\gamma}$ , or vice versa. The two  $\alpha$  and  $\beta$  components of the voltage space vector do thus have the same content of information as the terminal voltages, which corroborates the statement from section 2.2.1 that the terminal voltages have two degrees of freedom.

We can conclude that we can neither measure, nor freely influence the zero-sequence voltage. For that reason and also due to the fact that  $u_{s,\gamma}$  does not influence the mechanical behavior of the machine, we will henceforth consequently calculate with two-dimensional ( $\alpha\beta$ ) voltage space vectors. We can thus remove the redundant information in (2.49) and give its inverse transformation as

$$\begin{bmatrix} u_u - u_v \\ u_w - u_u \end{bmatrix} = \frac{3}{2} \begin{bmatrix} 1 & -\sqrt{3}/3 \\ -1 & -\sqrt{3}/3 \end{bmatrix} \begin{bmatrix} u_{s,\alpha} \\ u_{s,\beta} \end{bmatrix}, \quad (2.50)$$

$$\mathbf{u}_s^s = \begin{bmatrix} u_{s,\alpha} \\ u_{s,\beta} \end{bmatrix} = \frac{2}{3} \begin{bmatrix} 1/2 & -1/2 \\ -\sqrt{3}/2 & -\sqrt{3}/2 \end{bmatrix} \begin{bmatrix} u_u - u_v \\ u_w - u_u \end{bmatrix}. \quad (2.51)$$

### 2.2.2.3 Flux Linkage Space Vector

The last missing space vector needed for a complete mathematical model is the flux linkage space vector. It can be obtained in the same manner as the voltage space vector from multiplying (2.43) with the Clarke transformation matrix. Since the transformation matrix is time-invariant, it can be included into the time-derivative of the flux linkage, leading directly to

$$\boldsymbol{\psi}_s^s = \begin{bmatrix} \psi_\alpha \\ \psi_\beta \end{bmatrix} = \frac{2}{3} \begin{bmatrix} 1 & -1/2 & -1/2 \\ 0 & \sqrt{3}/2 & -\sqrt{3}/2 \end{bmatrix} \begin{bmatrix} \psi_a \\ \psi_b \\ \psi_c \end{bmatrix} \quad (2.52)$$

and its inverse,

$$\begin{bmatrix} \psi_a \\ \psi_b \\ \psi_c \end{bmatrix} = \frac{3}{2} \begin{bmatrix} 2/3 & 0 \\ -1/3 & \sqrt{3}/3 \\ -1/3 & -\sqrt{3}/3 \end{bmatrix} \begin{bmatrix} \psi_{s,\alpha} \\ \psi_{s,\beta} \end{bmatrix}. \quad (2.53)$$

In (2.52) and (2.53), the zero-sequence component,  $\psi_{s,\gamma}$ , was also omitted, since we cannot measure it, we cannot freely influence it by applying a voltage  $u_{s,\gamma}$  and we cannot relate it to the current as its zero-sequence component is always zero.

## 2.2.3 General Mathematical Model

### 2.2.3.1 The Electric Model

In the previous section, the space vector notation was introduced. Combining it with the electromagnetic field theory from section 2.1.2 leads to the stator (index  $_s$ ) voltage balance in a stator-oriented (superscript  $^s$ ) reference frame [2 p. 761, 66 p. 60].

$$\mathbf{u}_s^s = R_s \mathbf{i}_s^s + \frac{d}{dt} \boldsymbol{\psi}_s^s \quad (2.54)$$

The first term on the RHS of (2.54) is the Ohmic voltage drop caused by the current space vector  $\mathbf{i}_s^s$  at the phase resistances  $R_s$ . The second term is the time derivative of the flux linkage vector  $\boldsymbol{\psi}_s^s$ .

As already discussed in the end of section 2.1.2, the relation between current and flux linkage is typically nonlinear in synchronous machines. Additionally, the shape of the rotor can cause a magnetic anisotropy. In order to account for that shape anisotropy, it is useful to transform the current and flux linkage space vectors into a rotor-oriented coordinate system and describe their nonlinear relation by a general vector function,  $\mathbf{f}^r$ . Hence,

$$\boldsymbol{\psi}_s^r = \mathbf{f}^r(\mathbf{i}_s^r). \quad (2.55)$$

Note that  $\mathbf{f}^r$  can only be bijective, when magnetic hysteresis is neglected. In this case,  $\mathbf{f}^r$  is invertible and we can write

$$\mathbf{i}_s^r = \mathbf{f}^{r-1}(\boldsymbol{\psi}_s^r). \quad (2.56)$$

When the stator is magnetically isotropic and the effects of discrete winding distributions and slotting are neglected,  $\mathbf{f}^r$  does not depend on the rotor angle.

The transformation of any space vector quantity,  $\mathbf{x}$ , from a stator- into a rotor-oriented reference frame is done by means of the rotation matrix,  $\mathbf{T}$ , which was given in (2.38). In (2.35), the angle between the stator  $\alpha$ - and the rotor  $d$ -axis was introduced as  $\vartheta_r$ . The transformation is thus done by

$$\mathbf{x}^r = \mathbf{T}(-\vartheta_r)\mathbf{x}^s. \quad (2.57)$$

Note that  $\mathbf{T}$  is a skew-symmetric  $2 \times 2$  matrix. In combination with its trigonometric character, we can state that

$$\mathbf{T}^{-1}(\vartheta) = \mathbf{T}^T(\vartheta) = \mathbf{T}(-\vartheta) = \begin{bmatrix} \cos \vartheta & \sin \vartheta \\ -\sin \vartheta & \cos \vartheta \end{bmatrix}, \quad (2.58)$$

where  $\mathbf{T}^T$  denotes the transpose of  $\mathbf{T}$ . With (2.58), we can give the inverse transformation of (2.57), i.e. the transformation of a vector in rotor coordinates into stator coordinates, as

$$\mathbf{x}^s = \mathbf{T}(\vartheta_r)\mathbf{x}^r. \quad (2.59)$$

The time-derivative of  $\mathbf{T}(\vartheta_r)$  is given by

$$\frac{d}{dt}\mathbf{T}(\vartheta_r) = \omega_r \mathbf{J}\mathbf{T}(\vartheta_r), \quad (2.60)$$

where  $\omega_r$  is the electrical angular velocity of the rotor and  $\mathbf{J}$  is the matrix analogon to the complex operator  $j$  in phasor analysis, i.e. a vector rotation by  $\pi/2$ . Hence,

$$\omega_r = \frac{d}{dt}\vartheta_r \quad (2.61)$$

and

$$\mathbf{J} = \mathbf{T}\left(\frac{\pi}{2}\right) = \begin{bmatrix} 0 & -1 \\ 1 & 0 \end{bmatrix}. \quad (2.62)$$

With (2.57)-(2.62), the transformation of (2.54) into rotor coordinates gives us

$$\mathbf{u}_s^r = R_s \mathbf{i}_s^r + \omega_r \mathbf{J}\boldsymbol{\psi}_s^r + \frac{d}{dt}\boldsymbol{\psi}_s^r. \quad (2.63)$$

In (2.63), we can now eliminate either the current or the flux linkage by means of (2.55) and (2.56), respectively. The first case is straightforward and results in

$$\mathbf{u}_s^r = R_s \mathbf{f}^{r-1}(\boldsymbol{\psi}_s^r) + \omega_r \mathbf{J}\boldsymbol{\psi}_s^r + \frac{d}{dt}\boldsymbol{\psi}_s^r. \quad (2.64)$$

The second case can be done in a similar manner as in (2.27), which led to the definition of the inductance acc. to (2.28). This time, however, we must take into account that the machine windings are magnetically coupled with each other as well as with the permanent magnetic flux linkage. What this means is exemplarily shown in Figure 2.17. In case (a), where two coils are coupled by a ferromagnetic toroid, the flux linkage produced by one coil will also flow through

the other coil (when leakage flux is neglected). In consequence, the flux linkage  $\psi_{12}$  will depend on both,  $i_1$  and  $i_2$ .

The second example, (b), shows two coils with perpendicular winding axes. In free space, their magnetic coupling would be negligible. When wound around a ferromagnetic sphere, however, the fields of both coils are applied to the same material and thus cause magnetic saturation. The changing level of saturation caused by one coil in turn influences the magnetic properties of the other coil. This effect is called *magnetic cross-saturation* and is illustrated in Figure 2.17(c) and (d).

We assume that the ferromagnetic material is isotropic. When we further assume that the current  $i_y$  is zero, the resulting flux linkage space vector,  $\psi_x(i_x, 0)$ , is aligned with the current space vector  $i_x$  in  $x$ -direction. When we now let a current  $i_y$  flow in the other coil while  $i_x$  is hold constant, the resulting current space vector  $i_{xy} = i_x + i_y$  will cause a likewise aligned flux linkage space vector, as shown in Figure 2.17(d). In linear material, the flux linkage vector would correspond to  $\psi_{xy}$ , which would have the same  $x$ -component as  $\psi_x(i_x, 0)$ . In case of saturating material, however, the resulting flux linkage vector,  $\psi'_{xy}$ , will be smaller, depending on the level of saturation as indicated in Figure 2.17(c). The corresponding  $x$ -component,  $\psi'_x(i_x, i_y)$  will hence be smaller than  $\psi_x(i_x, 0)$  although the current  $i_x$  was not changed.

In synchronous machines, typically, both types of magnetic coupling between the three phase windings occur. The direct coupling as described in the first example, (a), is inherently considered in the space vector notation, which allows to express the three coils as two

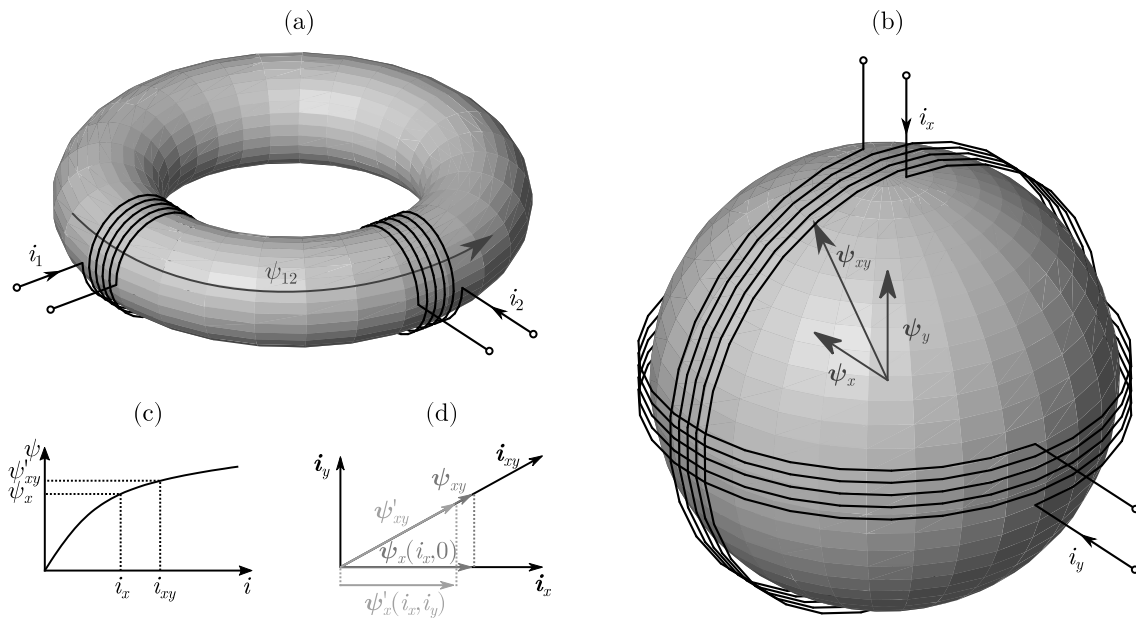


Figure 2.17: Examples of magnetically coupled coils; (a) two coils on a ferromagnetic toroid; (b) two perpendicular coils around a ferromagnetic sphere; (c) anhyseretic saturation curve of ferromagnetic material; (d) effect of cross-saturation in a two-dimensional winding system

perpendicular coils. Since this corresponds to the second example, (b-d), we will only have to consider magnetic cross-saturation, when working with space vectors. Additionally, in case of PM machines, the coupling between the PM flux linkage and the virtual space vector coils must be incorporated in  $\mathbf{f}^r$ .

As a consequence of the magnetic couplings, we can conclude that both components of the flux linkage space vector are depending on both current vector components. In this case, the flux linkage can be eliminated in (2.63) by means of (2.55) and the chain rule of differential calculus. Hence,

$$\mathbf{u}_s^r = R_s \mathbf{i}_s^r + \omega_r \mathbf{J} \mathbf{f}^r(\mathbf{i}_s^r) + \mathbf{L}_s^r \frac{d}{dt} \mathbf{i}_s^r. \quad (2.65)$$

where  $\mathbf{L}_s^r$  is the *Jacobian matrix* of  $\mathbf{f}^r$ ,

$$\mathbf{L}_s^r = \begin{bmatrix} \frac{\partial \psi_d}{\partial i_d} & \frac{\partial \psi_d}{\partial i_q} \\ \frac{\partial \psi_q}{\partial i_d} & \frac{\partial \psi_q}{\partial i_q} \end{bmatrix} = \begin{bmatrix} L_{dd} & L_{dq} \\ L_{qd} & L_{qq} \end{bmatrix}. \quad (2.66)$$

Note that  $\mathbf{L}_s^r$  contains the information of the magnetic susceptibility tensor,  $\boldsymbol{\chi}$ , as it was defined in (2.10) in section 2.1.2. It was stated that  $\boldsymbol{\chi}$  is a symmetric second-rank tensor and for that reason,  $\mathbf{L}_s^r$  has the same properties. In the given rotor coordinate system, it will again be written in matrix notation. Since in space vectors only two dimensions are considered, it has the dimension  $2 \times 2$ . The symmetry requirements enforce that the mutual inductances (for conciseness denoted with the index  $m$  in the following) must be equal at any time, i.e.

$$L_{dq} = L_{qd} = L_m. \quad (2.67)$$

When reminding the formal definition of an inductance acc. to (2.28) as the differential quotient from flux linkage and current, the entries of  $\mathbf{L}_s^r$  can be identified to be differential inductances and  $\mathbf{L}_s^r$  will consequently referred to as (*differential*) *inductance matrix*.

In many applications, it is useful to work with affine or linear machine models at given operating points. A convenient way of linearization in technical processes splits the nonlinear model up into two models – one for the large signal behavior at a given operating point and one for the small signal dynamics around that operating point [74 p. 860]. This basically corresponds to the *Taylor series expansion* of the nonlinear model up to the first term of the *Taylor polynomial*. [58 pp. 452–453 and 707].

As it is easier to measure, the electric current is typically chosen as state variable rather than the flux linkage. We then can write

$$\begin{aligned} \mathbf{u}_s^r &= \mathbf{u}_{s,op}^r + \Delta \mathbf{u}_s^r, & (a) \\ \mathbf{i}_s^r &= \mathbf{i}_{s,op}^r + \Delta \mathbf{i}_s^r, & (b) \end{aligned} \quad (2.68)$$

where the first terms on the RHS describe the large signal and the second terms the small signal behavior. For the large signal model, we assume steady states and thus can rewrite (2.65) as

$$\mathbf{u}_{s,op}^r = R_s \mathbf{i}_{s,op}^r + \omega_{r,op} \mathbf{J} \mathbf{f}^r(\mathbf{i}_{s,op}^r), \quad (2.69)$$

where the index *op* indicates the constant machine states and inputs at the actual operating point.

The current or voltage vector progressions for sufficiently small changes around that operating point are approximated by

$$\Delta \mathbf{u}_s^r = R_s \Delta \mathbf{i}_s^r + \omega_{r,op} \mathbf{J} \mathbf{L}_{s,op}^r \Delta \mathbf{i}_s^r + \mathbf{L}_{s,op}^r \frac{d}{dt} \Delta \mathbf{i}_s^r, \quad (2.70)$$

where the inductance matrix  $\mathbf{L}_{s,op}^r$  is given by

$$\mathbf{L}_{s,op}^r = \mathbf{L}_s^r |_{\mathbf{i}_{s,op}^r}. \quad (2.71)$$

Note that in (2.70) the rotor speed at the operating point,  $\omega_{r,op}$ , is assumed constant, which is typically a good approximation except for machines with very low moments of inertia.

By vector addition acc. to (2.68) of the two models, (2.69) and (2.70), we obtain the affine SM model in rotor coordinates,

$$\mathbf{u}_s^r = R_s \mathbf{i}_s^r + \omega_{r,op} \mathbf{J} \left( \underbrace{\mathbf{f}^r(\mathbf{i}_{s,op}^r) - \mathbf{L}_{s,op}^r \mathbf{i}_{s,op}^r}_{\boldsymbol{\psi}_{s,ls}^r} + \underbrace{\mathbf{L}_{s,op}^r \mathbf{i}_{s,op}^r + \mathbf{L}_{s,op}^r \Delta \mathbf{i}_s^r}_{\boldsymbol{\psi}_{s,ss}^r = \mathbf{L}_{s,op}^r \mathbf{i}_s^r} \right) + \mathbf{L}_{s,op}^r \frac{d}{dt} \mathbf{i}_s^r. \quad (2.72)$$

It shall be emphasized at this point that (2.72) is the formally correct affine approximation that can be applied to model the current or voltage vector progressions for sufficiently small changes around the operating point. In many recent publications dealing with the nonlinear effect of magnetic saturation (e.g. [75–79]), it is observed that the authors do not properly distinguish between the operating point dependent absolute flux linkage term,  $\boldsymbol{\psi}_{s,ls}^r$ , describing the large-signal behavior, and the differential component,  $\boldsymbol{\psi}_{s,ss}^r$ , taking into account the small-signal current progressions. A common mistake is that the absolute flux linkage in PMSMs is written as

$$\boldsymbol{\psi}_s^r |_{\mathbf{i}_{s,op}^r} = \mathbf{L}_{abs}^r |_{\mathbf{i}_{s,op}^r} \mathbf{i}_s^r + \boldsymbol{\psi}_{PM}^r, \quad (2.73)$$

where  $\mathbf{L}_{abs}^r |_{\mathbf{i}_{s,op}^r}$  is a matrix containing the absolute inductances at the given operating point (see, for instance, [75]) and

$$\boldsymbol{\psi}_{PM}^r = \begin{bmatrix} \psi_{PM} \\ 0 \end{bmatrix} \quad (2.74)$$

is the PM flux linkage space vector, which is treated as constant.

When looking at the overall flux linkage vector as given in (2.72), i.e.

$$\boldsymbol{\psi}_s^r |_{\mathbf{i}_{s,op}^r} = \boldsymbol{\psi}_{s,ls}^r + \mathbf{L}_{s,op}^r \mathbf{i}_s^r, \quad (2.75)$$

we see – at a given operating point – a constant offset term,  $\boldsymbol{\psi}_{s,ls}^r$ , and a linear term consisting of the likewise operating point depending constant,  $\mathbf{L}_{s,op}^r$ , multiplied with the variable stator current vector.

Comparing offset and linear terms in (2.73) and (2.75) directly leads to

$$\mathbf{L}_{abs}^r |_{\mathbf{i}_{s,op}^r} = \mathbf{L}^r |_{\mathbf{i}_{s,op}^r} \quad (2.76)$$

and

$$\boldsymbol{\psi}_{PM}^r = \boldsymbol{\psi}_{s,ls}^r = \mathbf{f}^r(\mathbf{i}_{s,op}^r) - \mathbf{L}^r |_{\mathbf{i}_{s,op}^r} \mathbf{i}_{s,op}^r. \quad (2.77)$$

We see that applying absolute inductances in the sense of  $L = \psi/i$  (see section 2.1.2 at page 22) is wrong and that  $\boldsymbol{\psi}_{PM}^r$  must indeed be operating point dependent. Furthermore, we should be aware that  $\boldsymbol{\psi}_{PM}^r$  acc. to (2.77) does not only contain the PM flux linkage but also the large-signal flux linkage associated with the stator currents and is thus a misleading choice of name.

We can conclude that absolute inductances could be used to describe  $\mathbf{f}^r$  in a form of, for instance,

$$\mathbf{f}^r(\mathbf{i}_{s,op}^r) = \begin{bmatrix} \psi_{PM} \\ 0 \end{bmatrix} + \mathbf{L}_{abs}^r |_{\mathbf{i}_{s,op}^r} \mathbf{i}_{s,op}^r, \quad (2.78)$$

where the underdetermined matrix  $\mathbf{L}_{abs}^r$  can be defined by means of the *Moore-Penrose inverse* [65 p. 29] of the current vector,  $(\mathbf{i}_{s,op}^r)^+$ , as

$$\mathbf{L}_{abs}^r |_{\mathbf{i}_{s,op}^r} = \left( \mathbf{f}^r(\mathbf{i}_{s,op}^r) - \begin{bmatrix} \psi_{PM} \\ 0 \end{bmatrix} \right) (\mathbf{i}_{s,op}^r)^+. \quad (2.79)$$

According to that definition,  $\mathbf{L}_{abs}^r$  contains non-equal mutual inductance values, which is necessary to properly account for cross-saturation of the permanent magnetic flux linkage.

It is however – from a strictly mathematical point of view – not valid to apply the absolute inductances as quasi-constant parameters to be multiplied with variable stator currents,  $\mathbf{i}_s^r$ , in order to model the dynamic interrelation of stator voltage and stator current space vectors. This fact makes the use of absolute inductances generally questionable. Despite the problem, that absolute inductances tend to  $\pm\infty$  for small currents and are thus sensitive to measurement errors around zero-currents, it seems more expedient to directly evaluate  $\mathbf{f}^r(\mathbf{i}_{s,op}^r)$  from appropriate models or look-up tables (LUTs) instead of multiplying  $\mathbf{i}_{s,op}^r$  with absolute inductances, which are itself functions of  $\mathbf{i}_{s,op}^r$ . For that reason, this work hereinafter discusses the relation between flux linkage and stator current only in the general form of look-up data describing  $\mathbf{f}^r$ .

From (2.78), we can see that, if the magnetic influence of the PM shall be described by a constant, scalar parameter,  $\psi_{PM}$ , it must be part of  $\mathbf{f}^r$ , such that

$$\mathbf{f}^r(\mathbf{i}_s^r = \mathbf{0}) = \begin{bmatrix} \psi_{PM} \\ 0 \end{bmatrix}. \quad (2.80)$$

Another way of describing the PM influence with a single parameter is to take up the concept of equivalent current density from section 2.1.2.7 again and introduce the stator current space vector equivalent of the PM flux linkage as

$$\mathbf{i}_{s,PM}^r = \begin{bmatrix} i_{PM} \\ 0 \end{bmatrix}. \quad (2.81)$$

It is thus a space vector aligned with the  $d$ -axis, that would – seen from the stator windings – produce the same magnetic flux linkage space vector as the permanent magnet does. The latter could be physically replaced by a  $d$ -axis current of magnitude  $i_{PM}$ .

In the inverse view, this means that a negative  $d$ -axis current of value  $-i_{PM}$  would exactly compensate the PM flux linkage, such that the overall flux linkage is zero. This *point of magnetic origin* is thus characterized by

$$\boldsymbol{\psi}_{s,0}^r = \begin{bmatrix} 0 \\ 0 \end{bmatrix} \quad (2.82)$$

and

$$\boldsymbol{i}_{s,0}^r = \begin{bmatrix} -i_{PM} \\ 0 \end{bmatrix}. \quad (2.83)$$

It should be obvious, that in case of SynRMs, the equivalent current is zero, while it is positive for PMSMs.

It is worth noting at this point that assigning a PM equivalent current to the stator windings is a simplification, which allows to superimpose virtual PM current and real electrical current vectors. In this simplified view, we cannot distinguish between the overall magnetic states of machines, where the PM field is actively weakened by a negative  $d$ -axis current and where no electrical current is present but weaker permanent magnets are employed.

In reality, however, both cases lead to different magnetic states in the rotor. This becomes clear, when considering a more accurate model, where the permanent magnets are replaced by virtual windings at their exact positions in the rotor. Assuming that we are not permanently demagnetizing the PMs leads us to constant equivalent currents in those windings. With a negative  $d$ -axis current, we do thus have stator windings and rotor windings that produce counteracting electromagnetic fields. Depending on the actual rotor and stator geometry, those fields do not exactly cancel each other everywhere in the machine. Instead, the magnetic field of the negative  $d$ -axis stator current influences the permanent magnetic field paths to close within the rotor rather than interacting with the stator windings. We thus have regions within the rotor, where the fields of both, permanent magnet and stator current superimpose and lead to strong saturation effects. Those effects are not present in the case of weaker magnets and zero stator currents.

We can thus state that the magnetic origin as defined by (2.82) and (2.83) is a simplification, or a virtual magnetic origin. It is, nevertheless, a good approach to discuss the general similarities and differences between the different PM and PM free machine types, as it is done in Chapter 4. It is also useful, when addressing the magnetic energy and co-energy in synchronous machines, as it defines the point, where energy and co-energy are zero. This is taken up again in the following section.

### 2.2.3.2 Energy and Torque – The Mechanic Model

In the macroscopic description of synchronous machines, the flux linkage and current densities become their integral counterparts. The local energy densities accordingly are condensed to the absolute values of the overall energy within the machine at a certain point of time. Analogously

to the mesoscopic case as described in section 2.1.2, the energy balance of a synchronous machine can be obtained, when (2.43) is multiplied by the transpose of the phase current vector, transformed into rotor-oriented space vectors and integrated over time [80]. For conciseness, the individual calculation steps are moved to Appendix B.1. Hence,

$$W_{el} = \int_{\Delta t} \frac{3}{2} \mathbf{i}_s^{rT} \mathbf{u}_s^r dt = \int_{\Delta t} \frac{3}{2} R_s \mathbf{i}_s^{rT} \mathbf{i}_s^r dt + \int_C \frac{3}{2} \mathbf{i}_s^{rT} d\boldsymbol{\psi}_s^r + \int_{\Delta t} \frac{3}{2} \omega \mathbf{i}_s^{rT} \mathbf{J} \boldsymbol{\psi}_s^r dt, \quad (2.84)$$

where  $W_{el}$  is the electric energy of the synchronous machine exchanged with an external system via the electric terminals during a time interval  $\Delta t$ . It is worth noting the occurrence of the factor  $3/2$ , which justifies the former statement that the chosen scaling factor leads to non-power-invariant space vectors (see p. 30).

The first term on the RHS of (2.84) denotes the dissipated energy due to Ohmic losses in the winding resistances, while the second term on the RHS is the change of magnetic energy in the machine during that time. The integration path  $C$  hereby describes the corresponding trajectory of the flux linkage space vector. Analogously to the energy and co-energy definitions acc. to (2.17) and (2.18), we can thus determine the exchanged magnetic energy and co-energy of the stator windings by

$$\Delta W_\mu|_C = \frac{3}{2} \int_C \mathbf{i}_s^{rT} d\boldsymbol{\psi}_s^r \quad (2.85)$$

and

$$\Delta W_{\mu,co}|_C = \frac{3}{2} \int_C \boldsymbol{\psi}_s^{rT} d\mathbf{i}_s^r = \frac{3}{2} \boldsymbol{\psi}_s^{rT} \mathbf{i}_s^r - \Delta W_\mu|_C \quad (2.86)$$

It is important to note, that the definition of co-energy acc. to (2.86) can be problematic in case of PM machines. In order to illustrate that problem, Figure 2.18 shows the graphical interpretations of (2.85) and (2.86), when exemplarily selecting integration trajectories from  $\mathbf{i}_s^{rT} = [0 \ 0]$  and  $\boldsymbol{\psi}_s^{rT} = [\psi_{PM} \ 0]$  towards an operating point on the  $d$ -axis. In subfigure (a), the operating point is defined by a positive current. We see that the PM flux linkage leads to additional co-energy. In subfigure (b), we see that for a negative-valued current operating point, the co-energy along with the sum of energy and co-energy can also become negative (note that the product of positive flux linkage and negative current is negative).

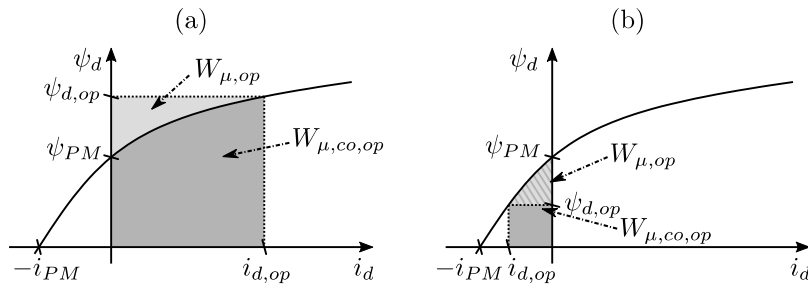


Figure 2.18: Graphical interpretation of magnetic energy and co-energy in the  $d$ -axis of a PM machine

The reason for this behavior is, that the flux linkages in (2.85) and (2.86) include the influence of the permanent magnet, while the stator currents do not. In order to improve the comparability of PMSMs and SynRMs, where no negative co-energies can occur, we define the absolute stored magnetic energy and co-energy within any type of synchronous machine as

$$W_\mu = \frac{3}{2} \int_{\psi_{s,0}^r}^{\psi_{s,op}^r} (\mathbf{i}_s^r + \mathbf{i}_{s,PM}^r)^T d\boldsymbol{\psi}_s^r \quad (2.87)$$

and

$$W_{\mu,co} = \frac{3}{2} \int_{\mathbf{i}_{s,0}^r}^{\mathbf{i}_{s,op}^r} \boldsymbol{\psi}_s^{rT} d\mathbf{i}_s^r = \frac{3}{2} \boldsymbol{\psi}_s^{rT} (\mathbf{i}_s^r + \mathbf{i}_{s,PM}^r) - W_\mu, \quad (2.88)$$

where the integration paths are the trajectories of currents and flux linkages from the virtual magnetic origin acc. to (2.82) and (2.83) to a given operating point. The above definitions imply that magnetic energy and co-energy are zero at the point of origin, i.e.

$$W_\mu|_{\psi_{s,0}^r} = W_{\mu,co}|_{\mathbf{i}_{s,0}^r} = 0. \quad (2.89)$$

At any other point, they must be positive. We thus also get a positive-valued magnetic energy at zero stator current. This is the energy associated with the permanent magnetic field.

Rewriting (2.87) and (2.88) in differential form and solving for flux linkage and current space vectors gives

$$\mathbf{i}_s^r + \mathbf{i}_{s,PM}^r = \frac{2}{3} \nabla W_\mu \quad (2.90)$$

and

$$\boldsymbol{\psi}_s^r = \frac{2}{3} \nabla W_{\mu,co}, \quad (2.91)$$

where  $\nabla$  is the nabla operator denoting the gradient of  $W_\mu$  in a flux linkage plane and of  $W_{\mu,co}$  in a stator current plane, respectively.

An inherent part of the law of energy conservation is that the magnetic energy in the flux linkage plane as given by (2.87) cannot jump, i.e. that the magnetic energy scalar field is *continuously differentiable*. Due to that condition, the integration paths in (2.87) and (2.88) can be arbitrarily chosen, or, with other words,  $\mathbf{i}_s^r$  and  $\boldsymbol{\psi}_s^r$  are conservative vector fields. From (2.90) or (2.91), it can easily be shown that the following conditions must apply at any time [32 pp. 44–45 (Ch. 11)]:

$$\frac{\partial i_d}{\partial \psi_q} = \frac{\partial^2 W_\mu}{\partial \psi_d \partial \psi_q} = \frac{\partial^2 W_\mu}{\partial \psi_q \partial \psi_d} = \frac{\partial i_q}{\partial \psi_d} \quad (2.92)$$

$$\frac{\partial \psi_d}{\partial i_q} = \frac{\partial^2 W_{\mu,co}}{\partial i_d \partial i_q} = \frac{\partial^2 W_{\mu,co}}{\partial i_q \partial i_d} = \frac{\partial \psi_q}{\partial i_d} \quad (2.93)$$

Note that (2.92) and (2.93) are in accordance with the former statement that  $\boldsymbol{\chi}$  as well as  $\mathbf{L}_s^T$  have to be symmetrical (see p. 14).

As described before, all energy dissipating effects associated with the re- or demagnetization of the ferromagnetic material in the machine (e.g. global and local eddy currents or acoustic noise emissions) are expressed in terms of the areas of resulting hysteresis loops (see 2.1.2, pp. 14-17). Further losses cannot be represented by the electric machine model (2.63) in the present form, since they are excluded due to the assumptions made in order to derive that circuit theoretical model (see p. 20). In consequence, the third term on the RHS of (2.84) can only be the mechanic energy exchanged with an external system via the shaft of the synchronous machine.

In combination with the relation between electric and mechanic angular velocity (2.35) and with the well-known equation describing the relationship between *mechanical work*,  $P_{mech}$ , and *torque*,  $M$ , in rotary systems [59 p. 12],

$$P_{mech} = M \cdot \omega_m, \quad (2.94)$$

the torque of the machine can be derived from (2.84) as

$$M = \frac{3}{2} p \mathbf{i}_s^T \mathbf{J} \boldsymbol{\psi}_s^r = \frac{3}{2} p (\psi_{s,d} i_{s,q} - \psi_{s,q} i_{s,d}). \quad (2.95)$$

Note that by transforming the space vectors in (2.84) into stator coordinates, a quite similar expression is found, namely

$$M = \frac{3}{2} p (\psi_{s,\alpha} i_{s,\beta} - \psi_{s,\beta} i_{s,\alpha}). \quad (2.96)$$

Comparing (2.95) and (2.96) shows that the torque is independent of the coordinate system, as long as both, current and flux linkage space vectors, are written in the same reference frame. In fact, the torque is determined by the relative positions of both vectors, or, more precisely, their cross product.

In order to complete the mechanic model, the relation between torque and angular velocity of the machine shaft can be given by

$$\frac{d}{dt} \omega_m = \frac{1}{\Theta} (M - M_L), \quad (2.97)$$

where  $\Theta$  is the *moment of inertia* of the rotor and the coupled load and  $M_L$  is the *load torque*. Note that  $M_L$  is typically depending on the speed  $\omega_m$  due to friction.

### 2.2.3.3 Sensorless Control Based on Magnetic Anisotropy

When transforming the machine model in rotor coordinates (2.65) back into stator coordinates, we get

$$\mathbf{u}_s^s = R_s \dot{\mathbf{i}}_s^s + \omega_r (\mathbf{J} \boldsymbol{\psi}_s^s - \mathbf{L}_s^s \mathbf{J} \dot{\mathbf{i}}_s^s) + \mathbf{L}_s^s \frac{d}{dt} \dot{\mathbf{i}}_s^s, \quad (2.98)$$

which, solved for the current derivative, gives

$$\frac{d}{dt} \dot{\mathbf{i}}_s^s = \underbrace{\mathbf{L}_s^{s-1}}_{\mathbf{\Gamma}_s^s} \underbrace{(\mathbf{u}_s^s - R_s \dot{\mathbf{i}}_s^s - \omega_r (\mathbf{J} \boldsymbol{\psi}_s^s - \mathbf{L}_s^s \mathbf{J} \dot{\mathbf{i}}_s^s))}_{\mathbf{u}_{s,L}^s}, \quad (2.99)$$

where

$$\mathbf{L}_s^s = \mathbf{T}(\vartheta_r) \mathbf{L}_s^r \mathbf{T}(-\vartheta_r) = \mathbf{L}_s^{s-1}, \quad (2.100)$$

$$\mathbf{L}_s^s = \mathbf{T}(-\vartheta_r)^{-1} \mathbf{L}_s^{r-1} \mathbf{T}(\vartheta_r)^{-1} = \mathbf{T}(\vartheta_r) \mathbf{L}_s^r \mathbf{T}(-\vartheta_r), \quad (2.101)$$

and

$$\mathbf{L}_s^r = \begin{bmatrix} \frac{\partial i_d}{\partial \psi_d} & \frac{\partial i_d}{\partial \psi_q} \\ \frac{\partial i_q}{\partial \psi_d} & \frac{\partial i_q}{\partial \psi_q} \end{bmatrix} = \begin{bmatrix} \Gamma_{dd} & \Gamma_{dq} \\ \Gamma_{qd} & \Gamma_{qq} \end{bmatrix} = \mathbf{L}_s^{r-1}. \quad (2.102)$$

A detailed derivation of above equations can be found in Appendix B.2.

The ability to provide position information also at standstill is a key characteristic of anisotropy based sensorless control (see for instance [7–16]). We are therefore only interested in the third term on the RHS of (2.98), which is the only term that contains extractable position information, even when  $\omega_r = 0$ . We thus focus on the differential inductance (2.100) or its inverse (2.102), respectively. By means of trigonometric calculus (see Appendix B.3), we can rewrite both matrices as

$$\mathbf{L}_s^s = \underbrace{\frac{1}{2}(L_{dd} + L_{qq})}_{L_\Sigma} \mathbf{I} + \underbrace{\frac{1}{2}(L_{qd} - L_{dq})}_0 \mathbf{J} + \left( \underbrace{\frac{1}{2}(L_{dd} - L_{qq})}_{L_\Delta} \mathbf{I} + \underbrace{\frac{1}{2}(L_{qd} + L_{dq})}_{L_m} \mathbf{J} \right) \mathbf{S}(\vartheta_r) \quad (2.103)$$

and

$$\mathbf{L}_s^s = \underbrace{\frac{1}{2}(\Gamma_{dd} + \Gamma_{qq})}_{\Gamma_\Sigma} \mathbf{I} + \underbrace{\frac{1}{2}(\Gamma_{qd} - \Gamma_{dq})}_0 \mathbf{J} + \left( \underbrace{\frac{1}{2}(\Gamma_{dd} - \Gamma_{qq})}_{\Gamma_\Delta} \mathbf{I} + \underbrace{\frac{1}{2}(\Gamma_{qd} + \Gamma_{dq})}_{\Gamma_m} \mathbf{J} \right) \mathbf{S}(\vartheta_r), \quad (2.104)$$

where

$$\mathbf{S}(\vartheta) = \begin{bmatrix} \cos(2\vartheta) & \sin(2\vartheta) \\ \sin(2\vartheta) & -\cos(2\vartheta) \end{bmatrix}. \quad (2.105)$$

The fact that the mutual inductances have to be equal as stated in (2.67) leads directly to

$$\Gamma_{dq} = \Gamma_{qd} = \Gamma_m, \quad (2.106)$$

and is taken into account in (2.103) and (2.104).

When comparing the definitions of  $\mathbf{S}(\vartheta)$  acc. to (2.105) and  $\mathbf{T}(\vartheta)$  acc. to (2.38), we can see that  $\mathbf{S}$  comprises of a double angle rotation following a vertical flip of the vector it is multiplied with, i.e.

$$\mathbf{S}(\vartheta) = \mathbf{T}(2\vartheta) \mathbf{X}, \quad (2.107)$$

where

$$\mathbf{X} = \begin{bmatrix} 1 & 0 \\ 0 & -1 \end{bmatrix} \quad (2.108)$$

is the analogon to the complex conjugate operation in complex calculus [81 pp. 10–24].

With (2.98)-(2.108), we are able to graphically interpret the current progression for a given inductive voltage vector  $\mathbf{u}_{s,L}^s$ . As shown in Figure 2.19, the time rate of change of the current comprises of an isotropic component, which is aligned with  $\mathbf{u}_{s,L}^s$  and an anisotropic component with constant amplitude that rotates with twice the rotor position.

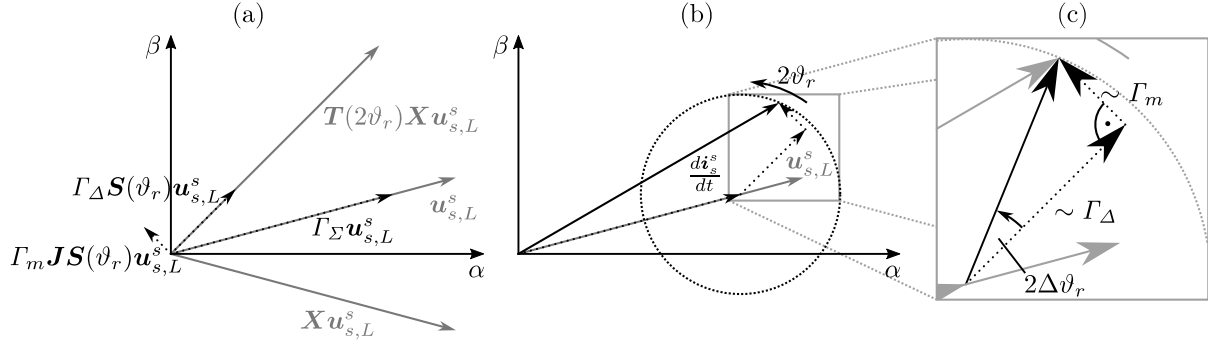


Figure 2.19: Vector diagram of the time rate of change of the stator current space vector in stator coordinates; (a): graphical interpretation of (2.99), (2.104) and (2.107) for a given voltage vector  $\mathbf{u}_{s,L}^s$  and a rotor position of  $\vartheta_r = 30^\circ$ ; (b): time rate of change of the current as vector sum and its progression with increasing rotor position  $\vartheta_r$ ; (c): magnification of the rotational component of the current derivative vector

All anisotropy based sensorless control algorithms are extracting the position information from that rotating component of the current derivative vector. The main distinguishing criterions of the algorithms are the way that a current change is enforced (e.g. by phase voltage pulse injection [14], rotating [10], elliptic [15], alternating [11, 82, 83] or arbitrary [84] voltage injection), and by the way the rotational component is separated from the rest of the current derivative.

Many sensorless algorithms neglect the effect of magnetic cross-saturation by applying the simplifying assumption that  $L_m = \Gamma_m = 0$ . This allows comparably simple derivations of the position signal without extensive parameter knowledge. The main drawback, however, is that the estimated position inherits an error depending on the actual level of magnetic cross-saturation.

Several publications analyze this error for certain position estimation schemes. Independently from the injection scheme, the error is found to be the same (e.g. in [23] for elliptic voltage injection and in [19] for alternating injection), which corroborates the former statement that all algorithms have the same source of position information.

From Figure 2.19(c), it can almost instantly be seen that the angle difference of the rotational component for  $\Gamma_m \neq 0$  compared to those with  $\Gamma_m = 0$  is exactly

$$\Delta\vartheta_r = \frac{1}{2} \text{atan2}(\Gamma_m, \Gamma_\Delta), \quad (2.109)$$

which is the result of the error analysis in mentioned publications. The definition of the atan2 function can be found in Appendix B.5.

From a mathematical point of view, it is interesting to note that neglecting the mutual (inverse) inductances means to assume an (inverse) inductance matrix that decouples the  $d$ - and  $q$ -axes of the respective vector it is multiplied with. This decoupling of a linear system of equations is subject of the well-established *eigenvalue problem* [58 pp. 318–325].

It is known that the *eigendecomposition* of a square ( $n \times n$ ) matrix,  $\mathbf{A}$ , with  $n$  linearly independent eigenvectors is given by

$$\mathbf{A} = \mathbf{V}\mathbf{D}\mathbf{V}^T, \quad (2.110)$$

where  $\mathbf{V}$  is a square matrix, whose columns are the eigenvectors of  $\mathbf{A}$ , and  $\mathbf{D}$  is a diagonal matrix, whose diagonal elements are the corresponding eigenvalues. Furthermore, if  $\mathbf{A}$  is real and symmetric, its eigenvectors are orthogonal and so is  $\mathbf{V}$ .

Knowing that  $\mathbf{L}_s^r$  is real and symmetric, we can see that the diagonal matrix of its respective eigendecomposition is an inductance matrix, where the mutual inductances are zero and the respective eigenvalues are the diagonal elements that can be written as (see Appendix B.4 for details)

$$L_{D/Q} = L_\Sigma \pm \sqrt{L_\Delta^2 + L_m^2}. \quad (2.111)$$

The indices  $D$  and  $Q$  indicate the axes of a new coordinate system, which we will refer to as *anisotropy coordinate system* in the following. It describes the easy and the hard axes of the magnetic anisotropy (cf. Figure 2.2 in section 2.1.2). An overview of the different coordinate systems and their relative angles is given in Figure 2.20 exemplarily under saturated conditions. Note that the  $D$  axis is aligned with the easy axis of the anisotropy for SynRMs, whereas it is aligned with the hard axis for PMSMs (cf. Figure 2.13). Note further that even SPMSMs typically develop a magnetic anisotropy as shown in Figure 2.20 (b) due to the permanent magnetic presaturation of the  $d$  path. We do thus have to distinguish the anisotropy inductance definitions in the following way:

$$\begin{aligned} \text{SynRM:} \quad L_D &= L_\Sigma + \sqrt{L_\Delta^2 + L_m^2}, & (a) \\ L_Q &= L_\Sigma - \sqrt{L_\Delta^2 + L_m^2}, & (b) \\ \text{PMSM:} \quad L_D &= L_\Sigma - \sqrt{L_\Delta^2 + L_m^2}, & (c) \\ L_Q &= L_\Sigma + \sqrt{L_\Delta^2 + L_m^2}. & (d) \end{aligned} \quad (2.112)$$

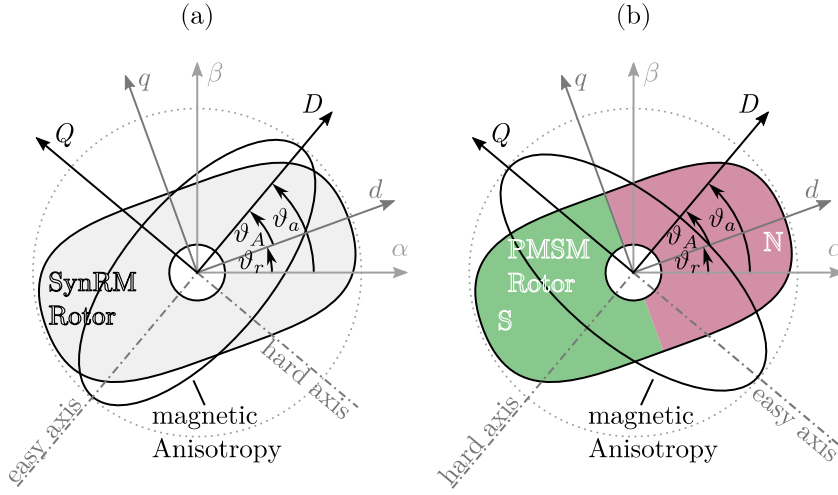


Figure 2.20: Introduction of the anisotropy coordinate system in comparison to the known rotor and stator fixed coordinate systems for SynRMs (a) and for PMSMs (b)

Besides the anisotropy inductances,  $L_{D/Q}$ , we can also determine the orientation of the anisotropy's easy and hard axes. The detailed derivations can be found in Appendix B.4. The result is

$$\vartheta_{D/Q} = \frac{1}{2} \text{atan2}(\pm L_m, \pm L_\Delta), \quad (2.113)$$

where we have to consider again the differences between SynRMs and PMSMs in the same manner as written above.

Note that we are only able to determine the easy or hard axes of the magnetic anisotropy, which means that we are not necessarily able to distinguish between positive or negative  $D$  or  $Q$  axis. This is a problem especially for PMSMs, where the direction of the positive  $d$  or  $D$  axis is determined by the PM north pole. Here, an initialization procedure is necessary to avoid  $180^\circ$  errors in the position estimate [13].

When considering the different definitions of the  $D$  and  $Q$  axis for SynRMs and PMSMs and the fact that the anisotropy position,  $\vartheta_A$ , is defined relative to the  $D$  axis, we can conclude that

$$\text{SynRM:} \quad \vartheta_A = \frac{1}{2} \text{atan2}(L_m, L_\Delta), \quad (a) \quad (2.114)$$

$$\text{PMSM:} \quad \vartheta_A = \frac{1}{2} \text{atan2}(-L_m, -L_\Delta). \quad (b)$$

Since the eigendecomposition can be done analogously for the inverse inductance matrix,  $\mathbf{I}_s^r$ , we can also write

$$\text{SynRM:} \quad \Gamma_D = \Gamma_\Sigma - \sqrt{\Gamma_\Delta^2 + \Gamma_m^2}, \quad (a) \quad (2.115)$$

$$\Gamma_Q = \Gamma_\Sigma + \sqrt{\Gamma_\Delta^2 + \Gamma_m^2}, \quad (b)$$

$$\text{PMSM:} \quad \Gamma_D = \Gamma_\Sigma + \sqrt{\Gamma_\Delta^2 + \Gamma_m^2}, \quad (\text{c})$$

$$\Gamma_Q = \Gamma_\Sigma - \sqrt{\Gamma_\Delta^2 + \Gamma_m^2} \quad (\text{d})$$

and

$$\text{SynRM:} \quad \vartheta_A = \frac{1}{2} \text{atan2}(\Gamma_m, \Gamma_\Delta), \quad (\text{a})$$

$$\text{PMSM:} \quad \vartheta_A = \frac{1}{2} \text{atan2}(-\Gamma_m, -\Gamma_\Delta). \quad (\text{b})$$

From the comparison of (2.116) and (2.109), we can see that the estimation error of anisotropy based sensorless algorithms that neglect magnetic cross-saturation corresponds to the anisotropy angle,  $\vartheta_A$ , or, with other words, they do not track the rotor position but rather the orientation of the magnetic anisotropy,  $\vartheta_a$ . For that reason, it is essential to know  $\boldsymbol{\psi}_s^r = \mathbf{f}^r(\mathbf{i}_s^r)$  for each valid operating point in order to understand error and stability issues of anisotropy based sensorless control algorithms.

Another aspect worth noting is that calculating the  $\Delta$  and  $\Sigma$  components of the (inverse) inductances in anisotropy coordinates,  $L_A$  (or  $\Gamma_A$ , respectively), analogously to those defined in (2.103) and (2.104) gives us

$$L_{A,\Sigma} = \frac{1}{2}(L_D + L_Q) = L_\Sigma, \quad (2.117)$$

$$\Gamma_{A,\Sigma} = \frac{1}{2}(\Gamma_D + \Gamma_Q) = \Gamma_\Sigma, \quad (2.118)$$

$$\text{SynRM:} \quad L_{A,\Delta} = \frac{1}{2}(L_D - L_Q) = \sqrt{L_\Delta^2 + L_m^2}, \quad (\text{a})$$

$$\text{PMSM:} \quad L_{A,\Delta} = \frac{1}{2}(L_D - L_Q) = -\sqrt{L_\Delta^2 + L_m^2}, \quad (\text{b})$$

and

$$\text{SynRM:} \quad \Gamma_{A,\Delta} = \frac{1}{2}(\Gamma_D - \Gamma_Q) = \sqrt{\Gamma_\Delta^2 + \Gamma_m^2}, \quad (\text{a})$$

$$\text{PMSM:} \quad \Gamma_{A,\Delta} = \frac{1}{2}(\Gamma_D - \Gamma_Q) = -\sqrt{\Gamma_\Delta^2 + \Gamma_m^2}. \quad (\text{b})$$

The  $\Sigma$  components describing the isotropic current progression do thus not change, while the  $\Delta$  components now represent the absolute value (or the length) of the anisotropic current derivative vector (cf. Figure 2.19(c)).

We can thus write the (inverse) inductance matrix in stator coordinates independently from the SM type as

$$\mathbf{L}_s^s = \underbrace{\frac{1}{2}(L_D + L_Q)}_{L_\Sigma} \mathbf{I} + \underbrace{\frac{1}{2}(L_D - L_Q)}_{L_{A,\Delta}} \mathbf{S}(\vartheta_a). \quad (2.121)$$

$$\mathbf{\Gamma}_s^s = \underbrace{\frac{1}{2}(\Gamma_D + \Gamma_Q)}_{\Gamma_\Sigma} \mathbf{I} + \underbrace{\frac{1}{2}(\Gamma_D - \Gamma_Q)}_{\Gamma_{A,\Delta}} \mathbf{S}(\vartheta_a). \quad (2.122)$$

It becomes clear that the (inverse) inductance matrixes contain three independent variables, i.e. an isotropic component, an anisotropic component and the orientation of the anisotropy. When assessing the suitability of SMs for sensorless control, the anisotropic component is the most relevant parameter. In practice, however, it is also important to assess the relation between anisotropic and isotropic components, as it is a measure for sensorless signal content in the current derivative vector. This so-called *saliency ratio* (SR) is defined by

$$r_S = \frac{L_{A,\Delta}}{L_\Sigma} = \frac{\Gamma_{A,\Delta}}{\Gamma_\Sigma}. \quad (2.123)$$

An important aspect in the discussion of position errors in sensorless control schemes is the differentiation between *open-loop* (OL) and *closed-loop* (CL) errors. The OL case starts with a given stator current vector in rotor coordinates. For this operating point, a set of inductance parameters ( $L_\Sigma$ ,  $L_{A,\Delta}$  and  $\vartheta_A$ ) can be identified. So far, we thus discussed OL errors (namely  $\vartheta_A$ ) for sensorless control schemes that neglect magnetic (cross-) saturation.

A CL error occurs, if the erroneous position estimate is applied in order to control the stator current vector in an estimated rotor reference frame (as it is done in FOC, for instance). The estimation error leads to a misalignment of the resulting current space vector and thus to a new operating point with different inductance parameters. The CL current control continuously adapts the current vector angle, until a possibly stable operating point is reached.

A stable CL operating point is characterized by two conditions:

1. The angle difference between the OL and the CL current vectors must be exactly the anisotropy angle at the given CL operating point

$$\vartheta_{i,CL} - \vartheta_{i,OL} = \vartheta_{A,CL} \quad (2.124)$$

2. The gradient of anisotropy angle over current vector angle in a sufficiently large area around the CL operating point must be smaller than one

$$\frac{\partial \vartheta_{A,CL}}{\partial \vartheta_{i,CL}} < 1 \quad (2.125)$$

Equation (2.124) identifies potentially stable operating points and allows to determine the resulting CL current angle,  $\vartheta_{i,CL}$ , for a given reference angle,  $\vartheta_{i,OL}$ . Whether or not this point is stable is decided by (2.125). It ensures that the CL current angle does not drift away, if small perturbations occur.

An exemplary illustration of the transition from OL to CL operation is shown in [85] but is not repeated here for conciseness. A more detailed analysis with focus on condition two can be found in [86]. For the purpose of discussing the measured flux linkage maps in Chapter 4, the above mathematical characterization is sufficient.

The differences between OL and CL controlled current vectors with the corresponding angle definitions are shown in Figure 2.21. The OL current vector is the resulting vector, when the correct rotor position is applied in the current controller. The angle  $\vartheta_{i,OL}$  can thus be seen as the reference angle for the current in order to obtain the desired torque.

When the estimated rotor position is used for current control, the CL current vector is the result (given, that a stable CL operating point exists). It can be seen that the difference between the desired and the actual current angle is exactly  $\vartheta_{A,CL}$ , as requested by (2.124).

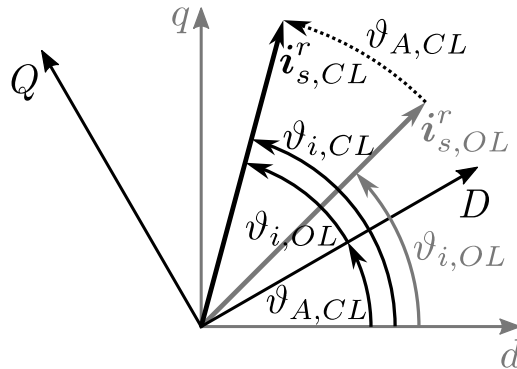


Figure 2.21: Vector diagram of current space vector resulting from open-loop (grey) and closed-loop (black) sensorless current control

#### 2.2.3.4 Sources of Harmonic Distortions

In section 2.2.2, it was stated that the Clarke transformation gives the phase quantities a spatial interpretation. The resulting space vectors point into the direction of the superimposed magnetic fields associated with the phase currents and voltages. For this spatial interpretation, however, it is necessary to assume sinusoidal field distributions along the circumference of the machine, as in this case the *superposition principle for harmonic signals* of same frequency or wavelength can be applied [58 pp. 83–84]. All phase components of same wavelength superimpose to a likewise sinusoidal signal of that wavelength and the direction of the space vector describes the spatial orientation of that wave.

Space vectors were derived by considering only the fundamental components of the circumferential current and flux density distributions, although several sources of harmonic distortions were identified. *Non-sinusoidal winding schemes* and *slotting* belong together and cannot be avoided completely in machines with ferromagnetic stator yokes (see simplified example from Figure 2.16). *Salient rotor geometries* can be avoided but are often designed intentionally in order to obtain reluctance torque. These sources of harmonics can be seen as linear in the sense that the spectrum of the current loading can be found also in the flux density with the same relative harmonic components.

In contrast to these linear harmonic sources, harmonic distortions can also arise from *magnetic saturation*. This is illustrated in the following example, where the linear sources are neglected.

Figure 2.22 shows two examples of sinusoidal current loadings (d) and the resulting flux densities (a) under the influence of saturation (b). The amplitude of the blue current loading is ten times bigger than the orange signal’s amplitude. As a result, the orange current loading only interacts with the linear part of the saturation curve in (b), leading to a likewise sinusoidal flux density distribution along the circumference. The spectral analysis of the orange flux density shown in (c) states that no harmonic distortions of the flux density occur in the linear case. When, however, the ferromagnetic material is driven into magnetic saturation as exemplarily demonstrated by the blue current loading, the resulting flux density distribution results in a flattened sine function. The spectral analysis of the saturated signal shows that relevant third, fifth and seventh harmonic components occur, while the fundamental wave’s amplitude is reduced to only ca. 37% of the amplitude it would have in the linear case.

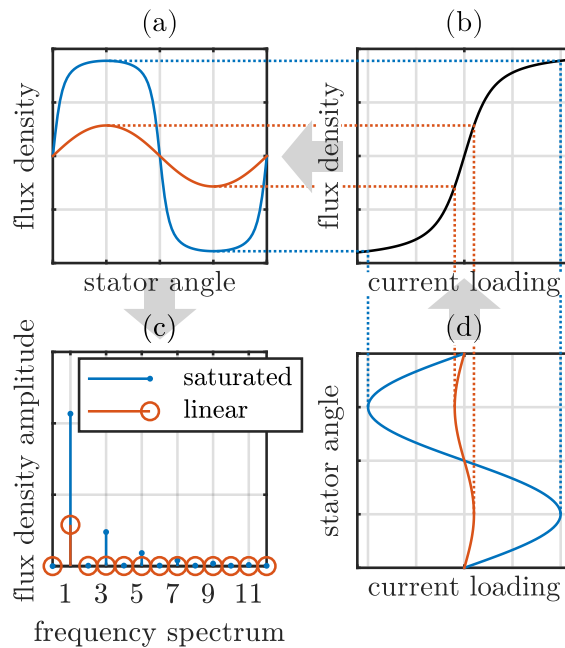


Figure 2.22: Harmonic distortion of the circumferential flux density distribution due to magnetic saturation

In case of highly saturated machines, the sigmoidal saturation curve as shown in Figure 2.22(b) approaches a signum function and, in consequence, the flattened sine function approaches a square wave function, whose *Fourier series expansion* is given by (see [58 p. 1071] and also section 2.4)

$$y_{square}(t) = \frac{4}{\pi} \sum_{k=1}^{\infty} \frac{\sin(2\pi(2k-1)ft)}{2k-1}. \quad (2.126)$$

The fundamental component of a square wave function is thus  $4/\pi$  times the amplitude of the square signal. When only considering the fundamental waves along the circumference, the observed saturation curve describing the relation between current loading and flux density will be stretched accordingly. This is shown in Figure 2.23(a), where the blue line shows the same saturation curve as in Figure 2.22(b) and the orange curve is the ratio of the amplitudes of sinusoidal current loading and the fundamental flux density component. In Figure 2.23(b),

where the ratio between the blue and orange curves is plotted, it can be seen that both curves are identical in the linear region of the saturation curve. For larger amplitudes, however, the fundamental components become larger and tend to the aforementioned value of  $4/\pi \approx 1.27$ .

It is also worth noting from (2.126) that a square wave function does only consist of odd-ordered harmonic components. Without further quantitative analysis, we can thus conclude from the above considerations that the upper limit in harmonic distortions due to magnetic saturation is an increase of approximately 27% in the fundamental component and the occurrence of odd-ordered harmonics, whose amplitudes decrease with the inverse of their order.

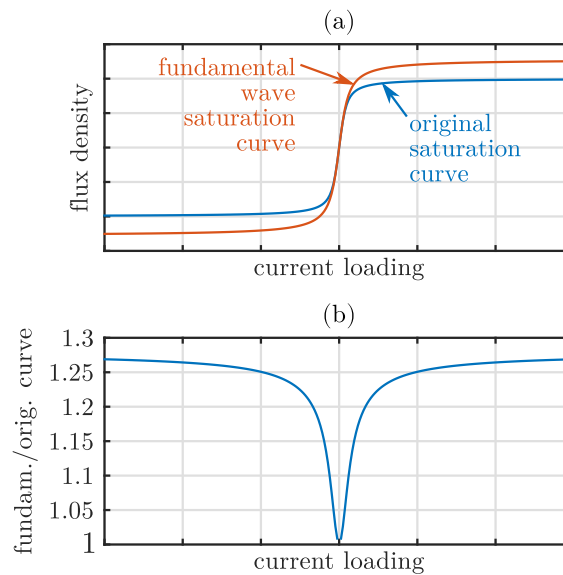


Figure 2.23: Influence of magnetic saturation on the fundamental wave components in the circumferential flux density distribution, when excited by sinusoidal current loadings

Another source of harmonic distortions is *magnetic hysteresis*. This is exemplarily shown in Figure 2.24. When only reversible magnetizing processes are considered as indicated by the orange signals, no hysteresis occurs in (b) and thus the sinusoidal current signal (d) produces a likewise sinusoidal flux linkage (a) without harmonic distortions (c). Note that the given example assumes small current amplitudes, as in this case magnetic saturation is negligible and thus the flux linkage is linearly related to the current.

As discussed in section 2.1.2, small-signal magnetic excitation of ferromagnetic material leads to minor hysteresis loops as a result of irreversible magnetization changes. Such a minor loop is depicted in blue in subfigure (b). When excited with the same current signal as the orange signals, the hysteresis distorts the resulting flux linkage signal as shown in (a). The spectral analysis of that signal reveals a slight increase of the fundamental component as well as third and fifth harmonics.

Again, we can analyze the upper limits of the harmonic distortions by considering the most extreme form the nonlinear effect can show. In this case, the hysteresis loop cannot widen up to more than a square, a so-called *relay hysteron*, which is the basis for the *Preisach model of*

*hysteresis* [87], leading again to a square wave function of the flux linkage. We can thus state that magnetic hysteresis is quite similar to magnetic saturation in its influence on harmonic distortions. It increases the fundamental component by maximal 27% and only causes odd-ordered harmonics with amplitudes that are inverse proportional to their orders.

It is worth noting, however, that the 27% increase of the fundamental small-signal amplitude is related to the anhysteretic susceptibility or inductance. The latter are not necessarily depending only on the operating point of the fundamental current space vector but also on the frequency of the small-signal current due to the occurrence of eddy currents (cf. section 2.1.2).

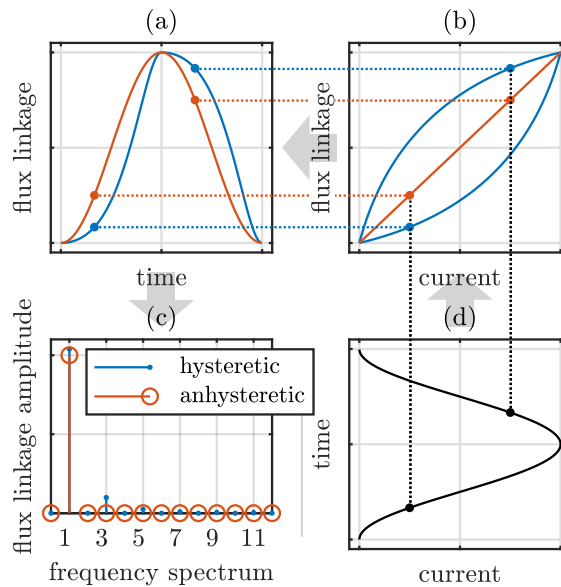


Figure 2.24: Harmonic distortion of flux linkage due to magnetic hysteresis

### 2.2.3.5 Remarks on Model Validity

The derivation of space vectors bases on vector addition (see (2.36) - (2.41)). Since flux density and current loading must be periodic along the circumference, they can be described as Fourier series, i.e. as sum of sinusoidal functions [58 pp. 477–479] (see also section 2.4). For that reason, harmonic space vectors can be defined, whereas their vector sum gives the overall space vector. Except for the fundamental space vector, however, the harmonic vectors will rotate asynchronously to the mechanical velocity of the machine or do not rotate at all. They can therefore be seen as additional flux leakage, i.e. flux linkage not contributing to the intended synchronous torque generation [38 pp. 42–45].

We can conclude that the electric and mechanic models derived above are valid also in case of relevant harmonic components in the current loading and flux density. It must be kept in mind that the fundamental behavior we are interested in is superposed by harmonic distortions that can cause torque ripples and acoustic noise. The harmonic content is influenced by the geometric design of the machine, but also depends on the level of magnetic saturation and hysteresis. When operated in highly saturated states, the fundamental saturation curve will differ from the actual one but will still be sigmoidal.

## 2.3 Two-Level Voltage Source Inverters

Two-level *voltage source inverters* (VSI) are a standard way to control electrical machines in industrial applications. They convert a fixed DC voltage into an AC voltage with variable frequency and amplitude. More precisely, they are switching devices and as such they can only generate discrete output voltages. Due to the low pass characteristic of the connected motors, the resulting currents are comparable to those coming from an ideal analog AC voltage source. The lower the switching frequency of the inverter, however, the more harmonic distortions occur in the currents.

### 2.3.1 Topology

The topology of an ideal two-level VSI is shown in Figure 2.25. The DC voltage from an external source,  $u_{DC}$ , is sustained by a large capacitor. The switching devices are power semiconductors. Although the symbol of a bipolar junction transistor is used here, various transistor types can be used depending on the switching frequency and power of the target application. The antiparallel diodes are so-called freewheeling diodes that are necessary to avoid high voltage peaks, when a transistor switches off an inductive current.

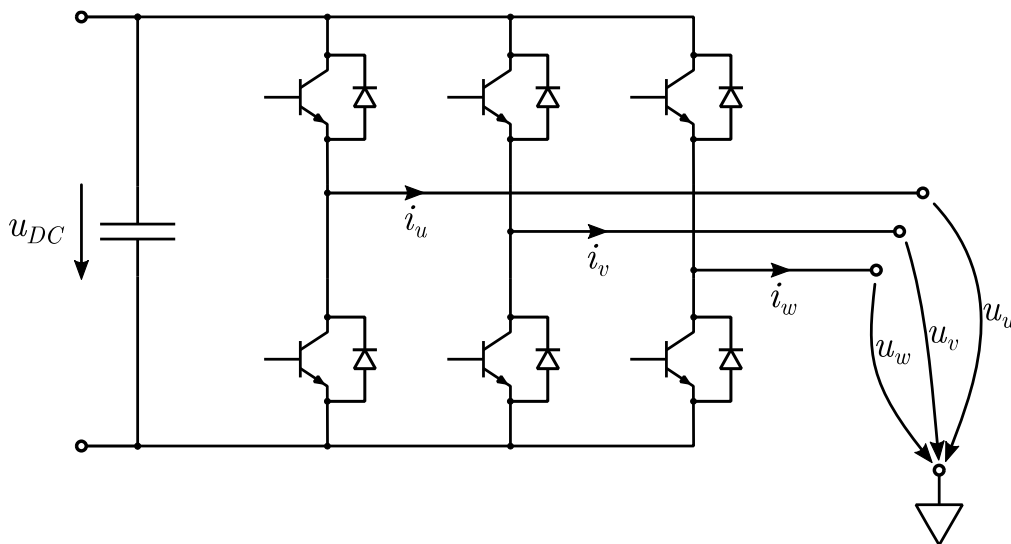


Figure 2.25: Topology of a three-phase two-level voltage source inverter

### 2.3.2 Space Vector Modulation

As depicted in Figure 2.25, a VSI consists of three half-bridges, one for each phase. The bridges itself consist of two series transistors each. In order to avoid short circuits, only one of the two bridge transistors can be switched on at a time. We can thus describe the actual state of a half-bridge with a binary parameter. Per common definition, this parameter has the value one, when the upper transistor is switched on and the lower off, and the value zero vice versa. For the three phases, we thus get eight possible switching combinations which result in a set of terminal voltages. When now assuming a three-phase AC machine connected to the inverter outputs, we can apply the space vector notation from section 2.2.2 and transform the terminal voltages into voltage space vectors in stator coordinates by means of (2.51). Table 1 lists all possible discrete

voltages and Figure 2.26(a) gives the graphical representation of the voltage space vectors in the  $\alpha\beta$  plane.

Table 1: Possible switching states and resulting terminal and space vector voltages

#	Switching states			Terminal voltages		Voltage space vector	
	$U$	$V$	$W$	$u_u - u_v$	$u_w - u_u$	$u_\alpha$	$u_\beta$
0	0	0	0	0	0	0	0
1	1	0	0	$u_{DC}$	$-u_{DC}$	$2/3 u_{DC}$	0
2	1	1	0	0	$-u_{DC}$	$1/3 u_{DC}$	$1/\sqrt{3} u_{DC}$
3	0	1	0	$-u_{DC}$	0	$-1/3 u_{DC}$	$1/\sqrt{3} u_{DC}$
4	0	1	1	$-u_{DC}$	$u_{DC}$	$-2/3 u_{DC}$	0
5	0	0	1	0	$u_{DC}$	$-1/3 u_{DC}$	$-1/\sqrt{3} u_{DC}$
6	1	0	1	$u_{DC}$	0	$1/3 u_{DC}$	$-1/\sqrt{3} u_{DC}$
7	1	1	1	0	0	0	0

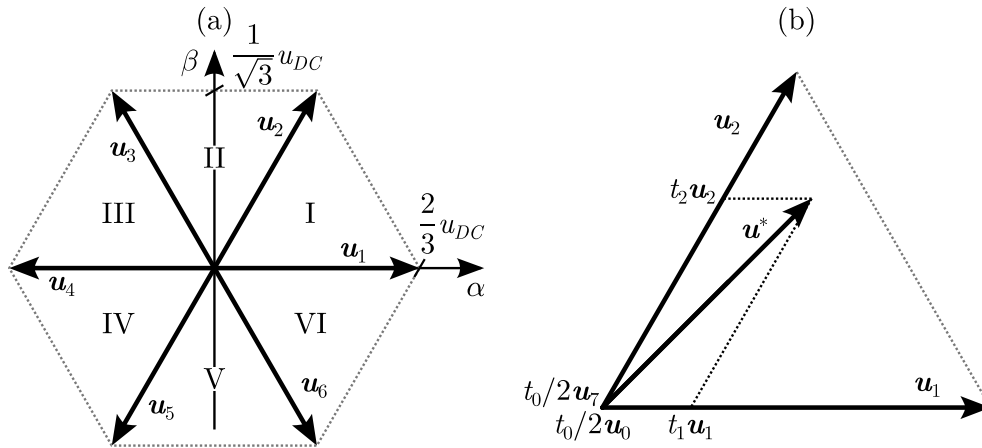


Figure 2.26: (a) Set of active voltage space vectors and the respective sectors (roman numerals) for a two-level VSI; (b) example of SVM for a voltage reference  $u^*$  in sector I

We see that the output voltages are restricted to six active ( $u_1..u_6$ ) and two zero vectors ( $u_0, u_7$ ). It is also worth noting that a transition between two adjacent active vectors requires only one switching operation. Furthermore, one commutation of a half-bridge is necessary for a transition from an active to a zero vector, or vice versa. All even active vectors form a set with  $u_7$  and all odd with  $u_0$ .

In drive systems, where the motor is controlled by a VSI, we can distinguish between direct control algorithms and those who require a modulator. A well-known example of direct algorithms is *direct torque control* (DTC) that was developed in the 1980s by Takahashi and Noguchi [88] and Depenbrock [89]. It considers the discrete nature of the inverter and gives pulse commands directly to the inverter.

Conventional *field oriented control* (FOC), as it is applied within this work, belongs to the class of algorithms that calculate continuous voltage references. The discrete voltages of the inverter do thus have to be modulated. In literature, a wide range of different modulation techniques exists. They are optimized with respect to different criteria such as algorithmic complexity, current harmonics, or switching losses. A good overview is given in the survey paper from Holtz [73].

This work applies the so-called *space vector modulation* (SVM), a special form of *pulse width modulation* (PWM) techniques. It is easy to implement and causes comparably low harmonic distortions, especially in the low and medium voltage range [73 pp. 1200–1202]. Its basic idea is to average the desired reference vector over a fixed time period by the vectorial sum of the two adjacent active vectors and one or both of the zero vectors. Figure 2.26(b) demonstrates this exemplarily for a reference vector  $\mathbf{u}^*$  in sector I. The closest active vector to the right,  $\mathbf{u}_1$ , is applied for a time  $t_1$ , and the left vector,  $\mathbf{u}_2$ , for a time  $t_2$ , respectively. For an arbitrary reference vector in sector number  $S$ , this can be expressed mathematically as

$$T_S \mathbf{u}^* = t_r \mathbf{u}_r + t_l \mathbf{u}_l, \quad (2.127)$$

where  $T_S$  is the SVM cycle time and the left (subscript  $l$ ) and right (subscript  $r$ ) voltage vectors are given by

$$\mathbf{u}_r = \frac{2}{3} u_{DC} \mathbf{T}((S-1) \cdot 60^\circ) \begin{bmatrix} 1 \\ 0 \end{bmatrix}, \quad (a) \quad (2.128)$$

$$\mathbf{u}_l = \frac{2}{3} u_{DC} \mathbf{T}(S \cdot 60^\circ) \begin{bmatrix} 1 \\ 0 \end{bmatrix}. \quad (b)$$

By substituting (2.128) into (2.127), we can find the switching times

$$\begin{bmatrix} t_r \\ t_l \end{bmatrix} = \frac{\sqrt{3} T_S}{u_{DC}} \begin{bmatrix} \sin(S \cdot 60^\circ) & -\cos(S \cdot 60^\circ) \\ -\sin((S-1) \cdot 60^\circ) & \cos((S-1) \cdot 60^\circ) \end{bmatrix} \begin{bmatrix} u_\alpha^* \\ u_\beta^* \end{bmatrix} \quad (2.129)$$

and

$$t_0 = T_S - t_r - t_l. \quad (2.130)$$

It should be obvious that  $t_0$  must not be negative. This, however, occurs, when the given reference vector exceeds the limiting hexagon as shown in Figure 2.26(a). In this case, the reference vector is cut at its intersection point with the hexagon. For that reason, a saturation factor is introduced as

$$k_{sat} = \frac{T_S}{t_l + t_r}. \quad (2.131)$$

Feasible vector times are then calculated by

$$t_{0,sat} = 0, \quad (a)$$

$$\begin{bmatrix} t_{r,sat} \\ t_{l,sat} \end{bmatrix} = k_{sat} \begin{bmatrix} t_r \\ t_l \end{bmatrix} \quad (b) \quad (2.132)$$

and the reference vector that is actually modulated is given by

$$\mathbf{u}_{sat}^* = k_{sat} \mathbf{u}^*. \quad (2.133)$$

From Figure 2.26(a), we can see that the maximal feasible reference voltages are directed along the  $u, v, w$  axes and are of length  $2/3 u_{DC}$ . When, however, a reference vector is oriented along a sector middle, its maximal length is  $1/\sqrt{3} u_{DC}$ . This corresponds to the maximal length a rotating reference vector can have without being saturated.

After the vector times are computed, it is necessary to determine the exact switching times and the order in which the discrete inverter voltage vectors are applied. In literature, different strategies are discussed with respect to harmonic distortions, switching losses and maximum modulation indices [73]. A common technique with relatively good characteristics is to arrange the switching times symmetrically around the middle of an SVM cycle and to share the time  $t_0$  equally among both zero vectors,  $\mathbf{u}_0$  and  $\mathbf{u}_7$ . Additionally, the active vectors are ordered in such a way that only one commutation occurs at the transition from one vector to the following one. The switching sequence for a complete SVM cycle with an exemplary reference vector in sector I is then as follows:

$$\mathbf{u}_0 \left\langle \frac{t_0}{4} \right\rangle \rightarrow \mathbf{u}_1 \left\langle \frac{t_1}{2} \right\rangle \rightarrow \mathbf{u}_2 \left\langle \frac{t_2}{2} \right\rangle \rightarrow \mathbf{u}_7 \left\langle \frac{t_0}{2} \right\rangle \rightarrow \mathbf{u}_2 \left\langle \frac{t_2}{2} \right\rangle \rightarrow \mathbf{u}_1 \left\langle \frac{t_1}{2} \right\rangle \rightarrow \mathbf{u}_0 \left\langle \frac{t_0}{4} \right\rangle$$

Typically, the vector times are translated into *duty cycles*,  $d_{u,v,w}$ , which determine the times, where the respective half-bridge is in state ‘1’, i.e. where the upper switch is closed. Depending on the actual sector, they are calculated as listed in Table 2.

Table 2: Duty cycles for each sector

$S$	$d_u$	$d_v$	$d_w$
<b>I</b>	$\frac{t_r + t_l + t_0/2}{T_S}$	$\frac{t_l + t_0/2}{T_S}$	$\frac{t_0/2}{T_S}$
<b>II</b>	$\frac{t_l + t_0/2}{T_S}$	$\frac{t_r + t_l + t_0/2}{T_S}$	$\frac{t_0/2}{T_S}$
<b>III</b>	$\frac{t_0/2}{T_S}$	$\frac{t_r + t_l + t_0/2}{T_S}$	$\frac{t_l + t_0/2}{T_S}$
<b>IV</b>	$\frac{t_0/2}{T_S}$	$\frac{t_l + t_0/2}{T_S}$	$\frac{t_r + t_l + t_0/2}{T_S}$
<b>V</b>	$\frac{t_r + t_l + t_0/2}{T_S}$	$\frac{t_0/2}{T_S}$	$\frac{t_l + t_0/2}{T_S}$
<b>VI</b>	$\frac{t_r + t_l + t_0/2}{T_S}$	$\frac{t_0/2}{T_S}$	$\frac{t_l + t_0/2}{T_S}$

In practice, the exact duty cycles usually cannot be processed as calculated due to hardware limitations (e.g. time quantization effects in digital systems; see description of the test bench in Chapter 3). In order to be as accurate as possible, it is thus useful, to calculate the applied voltage space vector from the exact duty cycles as processed by the real time system.

By means of Kirchhoff’s voltage law, we can directly obtain the output voltages from the VSI circuit diagram in Figure 2.25. Thus,

$$\begin{aligned} u_u - u_v &= u_{DC}(d_u - d_v), & (a) \\ u_w - u_u &= u_{DC}(d_w - d_u). & (b) \end{aligned} \quad (2.134)$$

Substituting (2.134) into (2.51), then leads to the desired expression,

$$\begin{bmatrix} u_\alpha^* \\ u_\beta^* \end{bmatrix} = u_{DC} \frac{2}{3} \begin{bmatrix} 1/2 & -1/2 \\ -\sqrt{3}/2 & -\sqrt{3}/2 \end{bmatrix} \begin{bmatrix} d_u - d_v \\ d_w - d_u \end{bmatrix}. \quad (2.135)$$

## 2.4 Fourier Analysis of Space Vectors

When dealing with synchronous machines at steady states, we have to deal with constantly rotating and thus time periodic space vectors. The theory dealing with periodic signals is named after *Jean Baptiste Joseph Fourier*, who approximated arbitrary (continuous) functions by trigonometric series in order to simplify his analysis of heat distribution and heat movement [90, 91]. This section gives a short introduction to the Fourier analysis of space vectors.

### 2.4.1 Fourier Series of Space Vectors

A space vector describing the periodic progressions of voltages, currents and flux linkages in time can be written as sum of multiple space vectors, each rotating constantly at unique combinations of speed and amplitude. Taking, for instance, voltage space vectors, we can write

$$\mathbf{u}(t) = \sum_{k=-\infty}^{\infty} u_k \mathbf{T}(\omega_k t + \phi_k) \mathbf{e}_1, \quad (2.136)$$

where  $u_k$  is the amplitude of the voltage space vector rotating with a speed of  $\omega_k$  with an initial orientation given by the angle  $\phi_k$  with respect to the axis of abscissae of the given reference coordinate system. The vector  $\mathbf{e}_1$  is the unit vector of that respective axis and  $\mathbf{T}(\phi)$  is the rotation matrix as introduced in section 2.2.2 (see (2.38)).

Equation (2.136) is the space vector form of the classical Fourier series in complex notation [92 p. 85], where

$$\mathbf{u}_k = u_k \mathbf{T}(\phi_k) \mathbf{e}_1 \quad (2.137)$$

corresponds to the complex Fourier coefficients and

$$\omega_k = 2\pi \frac{k}{T_1} \quad (2.138)$$

is describing the discrete radian frequencies of the overall signal with a period length of  $T_1$ . The corresponding frequency is thus given by

$$f_k = \frac{k}{T_1} = kf_1. \quad (2.139)$$

Equations (2.138) and (2.139) involve that all occurring frequencies have to be  $k$  times periodic to the overall signal and that also negative frequencies can occur, where

$$-\omega_k = \omega_{-k} \quad (2.140)$$

and

$$-f_k = f_{-k}. \quad (2.141)$$

For  $k > 0$  we thus have rotating vectors in mathematically positive direction and in negative direction for  $k < 0$ , accordingly.

In section 2.2.3, it was shown that splitting up the overall signal  $\mathbf{u}(t)$  into its spectral components can be useful to simplify the analysis of the underlying physical processes in synchronous machines. The transformation of the machine model from stator to rotor fixed coordinates allows to separate out the torque producing current space vector components at rotor synchronous frequencies and making them easy to handle for standard control techniques.

The same procedure can be generally applied at arbitrary frequencies, leading to a signal transformed into a coordinate system that is constantly rotating at  $\omega_x$ . Hence,

$$\mathbf{u}^x(t) = \mathbf{T}(-\omega_x t) \mathbf{u}(t) = \sum_{k=-\infty}^{\infty} u_k \mathbf{T}((\omega_k - \omega_x)t + \phi_k) \mathbf{e}_1. \quad (2.142)$$

From (2.142), we can see that the frequencies of all spectral components in  $\mathbf{u}(t)$  are shifted to the new frequencies  $\omega_k - \omega_x$ , whereas only that signal component with  $\omega_k = \omega_x$  is constant in that respective coordinate system. For this reason, we can determine that specific Fourier coefficient by eliminating all oscillating signal components. When we consider a period of  $T_1$  or integer multiples thereof, this can be easily done by calculating the arithmetic mean of (2.142). We thus get

$$\mathbf{u}_x = u_x \mathbf{T}(\phi_x) \mathbf{e}_1 = \frac{1}{T_1} \int_{(T_1)} \mathbf{T}(-\omega_x t) \mathbf{u}(t) dt, \quad (2.143)$$

where  $u_x$  is the Euclidean norm of  $\mathbf{u}_x$  and  $\phi_x$  is the analogon to the argument of complex numbers,

$$\begin{aligned} u_x &= \|\mathbf{u}_x\|_2, & (a) \\ \phi_x &= \angle(\mathbf{u}_x, \mathbf{e}_1). & (b) \end{aligned} \quad (2.144)$$

### 2.4.2 Leakage Effect of Fourier Coefficients

When analyzing integrable periodic functions, the Fourier coefficients can be precisely determined by (2.143). In practice, however, it is often difficult to consider complete periodic time ranges of  $\mathbf{u}(t)$ , especially when  $\mathbf{u}(t)$  is not a known function but a series of measurements. This might be, for instance, due to combinations of occurring frequencies that would require impracticable long periods of times to be analyzed. Also, measurements are typically impaired by measurement noise, which makes it difficult to identify the exact period length, since the identity  $\mathbf{u}(t) = \mathbf{u}(t + nT_1)$  cannot be found.

If a spectral component is not precisely periodic in the evaluated time range, its arithmetic mean is not zero and thus causes an error when determining in the Fourier coefficients acc. to (2.143) – the non-periodic signals ‘leak’ into neighboring frequencies.

The error due to the leakage effect can be determined, when we substitute the sum expression from (2.142) into (2.143) and solve the integral from the arithmetic mean operation for a non-periodic time range,  $T_{avg}$ . For each transformed frequency component, we can now define a factor,  $n_{kx}$ , that describes the (not necessarily integer) number of periods of that specific frequency within the time range  $T_{avg}$ . Thus,

$$T_{avg} = n_{kx} \frac{2\pi}{\underbrace{\omega_{kx}}_{T_{kx}}}, \quad \forall n_{kx} \in \mathbb{R}^+. \quad (2.145)$$

For conciseness, we introduce the transformed angular frequencies

$$\omega_{kx} = \omega_k - \omega_x \quad (2.146)$$

and then solve

$$\bar{\mathbf{u}}_x = \frac{1}{T_{avg}} \int_{(T_{avg})} \sum_{k=-\infty}^{\infty} u_k \mathbf{T}(\omega_{kx}t + \phi_k) \mathbf{e}_1 dt. \quad (2.147)$$

When we denote the starting point of the evaluated time range as  $t_0$ , we can solve the integral and further simplify the result, ending up with

$$\bar{\mathbf{u}}_x = \sum_{k=-\infty}^{\infty} u_k \operatorname{sinc}(n_{kx}) \mathbf{T}(\omega_{kx}t_0 + n_{kx}\pi + \phi_k) \mathbf{e}_1, \quad (2.148)$$

where

$$\operatorname{sinc}(n_x) = \frac{\sin(\pi n_x)}{\pi n_x} \quad (2.149)$$

is the normalized Sinus cardinalis, or *cardinal sine function* [92 p. 105], as shown in Figure 2.27.

When we, as in the former section, assume that we are looking for a specific, existing frequency component, we get  $\omega_{kx} = 0$  and hence  $n_{kx} = 0$ . Equation (2.148) thus contains the information we are interested in, namely  $\mathbf{u}_x$ . It is, however, distorted by all other frequency components. When we rewrite (2.148) as

$$\bar{\mathbf{u}}_x = \mathbf{u}_x + \sum_{k \in \mathbb{Z}, k \neq x} u_k \operatorname{sinc}(n_{kx}) \mathbf{T}(\omega_{kx}t_0 + n_{kx}\pi + \phi_k) \mathbf{e}_1, \quad (2.150)$$

we see that the distortion amplitude depends on the amplitude  $u_k$  and the term  $\operatorname{sinc}(n_{kx})$ . As shown in Figure 2.27, the Fourier coefficient of interest is only distorted by frequency components with  $n_{kx} \notin \mathbb{N}$ . We further see that the amplitude of the disturbance decreases with increasing  $n_{kx}$ . When determining the extrema of the sinc function, we can state that the maximal disturbance amplitude for  $n_{kx} > 32.5$  is less than 1% of  $u_k$  and for  $n_{kx} > 63.5$  it is less than 0.5%.

We can thus conclude that if we cannot guarantee  $n_{kx} \in \mathbb{N}^+$  for all nonzero spectral components, the measurement period should be as long as possible and as close as possible to the roots of the corresponding sinc function.

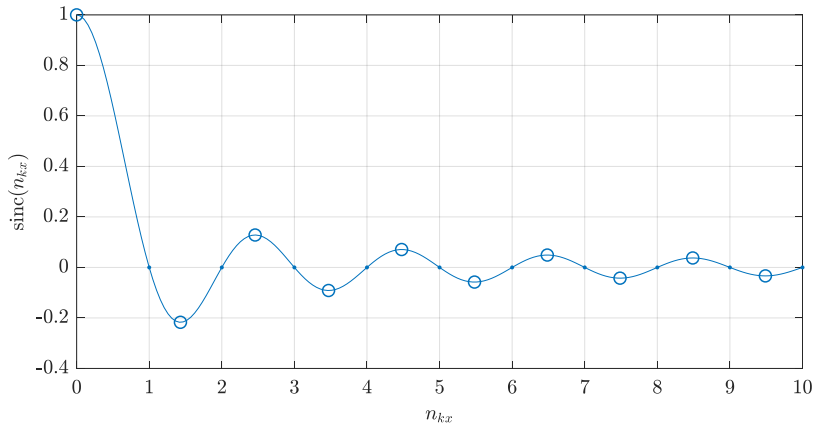


Figure 2.27: The cardinal sine function with its roots marked by dots and its extrema marked by circles

### 2.4.3 The Aliasing Effect in Sampled Signals

In digital signal processing, analogue signals are generally sampled at certain times. Typically, the time  $T_S$  between the samples is constant, such that we get a sampling frequency of

$$f_S = \frac{1}{T_S}. \tag{2.151}$$

Without further knowledge about the general properties of the sampled signal, we have no information about the signal during that time between the samples. When attempting to analyze the spectral components of sampled data, we face the problem that the trigonometric functions are periodic and thus non-injective. For a given set of equidistant, periodic samples, we can find an infinite set of frequencies that would result in the same set of sampled data. This is illustrated exemplarily for two cosine functions in Figure 2.28(a). It can thus happen that one signal, for instance at  $f = 5/4 f_S$ , is interpreted as a signal of same phase and amplitude at  $f = 1/4 f_S$ . We can say that one frequency appears to be another – they are *alias frequencies* of each other.

In Figure 2.28(a), we can see that alias frequencies are intersecting at the sampling times. Mathematically and in accordance with the space vector notation applied within this work, we can thus find the definition of alias frequencies from the expression

$$\mathbf{T}(2\pi f T_S) \mathbf{e}_1 = \mathbf{T}(2\pi f_{an} T_S + 2\pi n) \mathbf{e}_1, \quad \forall n \in \mathbb{N}, n \neq 0, \tag{2.152}$$

where  $f_{an}$  is the  $n$ th alias frequency of  $f$  and the term  $2\pi n$  takes into account the fact that there is an infinite number of solutions.

When solving (2.152) for  $f_{an}$ , we get an infinite set of alias frequencies,

$$f_{an} = f - n f_S, \quad \forall n \in \mathbb{N}, n \neq 0. \tag{2.153}$$

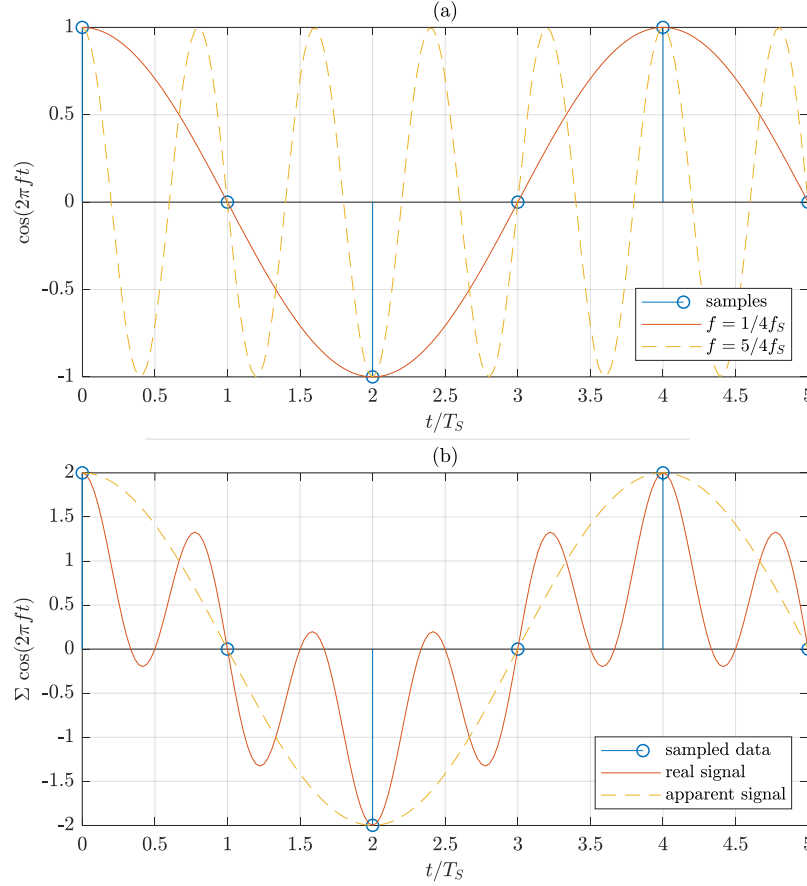


Figure 2.28: (a): Example of two cosine functions with same amplitude and phase but at different frequencies that produce the same set of sampled data; (b): sum of both functions from (a) and how its samples could be misinterpreted in Fourier analysis

If we now assume a real signal that consists solely of the sum of spectral components at alias frequencies and that is sampled at the discrete times  $t = n_S T_S, \forall n_S \in \mathbb{N}$ , we can write

$$\mathbf{u}(n_S T_S) = \left( u \mathbf{T}(2\pi f n_S T_S + \phi) + \sum_{n \in \mathbb{N}, n \neq 0} u_{an} \mathbf{T}(2\pi f_{an} n_S T_S + \phi_{an}) \right) \mathbf{e}_1. \quad (2.154)$$

Substituting (2.153) into (2.154) and determining the Fourier coefficient acc. to (2.143) at  $f$  or any other of the alias frequencies, we obtain

$$\mathbf{u}(f) = \mathbf{u}(f_{a1}) = \dots = \left( u \mathbf{T}(\phi) + \sum_{n \in \mathbb{N}, n \neq 0} u_{an} \mathbf{T}(\phi_{an}) \right) \mathbf{e}_1. \quad (2.155)$$

We see that it is impossible to correctly determine the amplitudes and phases of each spectral component from the sampled data. Instead, the Fourier coefficient for each of the alias frequencies appears to be the sum of all respective Fourier coefficients. This is exemplarily shown in Figure 2.28(b), where the sum of both functions from (a) is sampled. When

determining the Fourier coefficient of this sampled data for  $f = 1/4 f_S$ , we obtain a result with twice the amplitude (i.e. the sum of both amplitudes) of the actual component.

The aliasing effect motivated the *sampling theorem*, first formulated in 1933 by *Vladimir Kotelnikov* [93], which states that a sampled signal can only be correctly reconstructed, if the sampling frequency is higher than twice the highest occurring frequency in a signal, usually called the *Nyquist frequency*.

We can conclude that the aliasing effect can only be avoided, when a signal has a finite bandwidth, and the sampling frequency is chosen high enough to guarantee that no alias components can disturb the Fourier analysis.

## CHAPTER 3

### Test Bench Description

The test rig, as used for all measurements within this work, is shown in Figure 3.1. In order to have full flexibility, the motor under test is always coupled with a load motor. The latter is controlled by an industrial inverter, which can be set to torque or speed control mode.

The motor under test is driven by a modified industrial inverter. Its control unit is replaced by an interface that provides current and DC voltage measurement signals and accepts three-phase PWM commands. The latter are directly fed to the original power electronics module, which contains over-current protection and ensures proper switching dead times in order to avoid bridge short-circuits.

Both inverters are coupled at their DC links, which allows the optimal use of electrical energy during the tests. Typically, one motor is operated in generator mode and can thus provide the

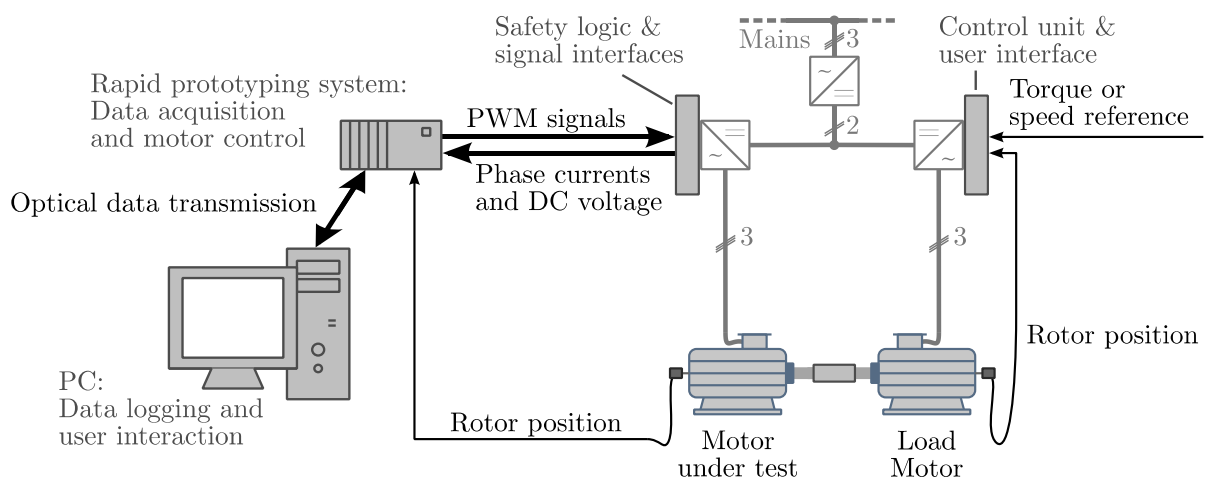


Figure 3.1: Graphical overview of the complete test bench

energy for the other motor. The DC source supplying both inverters does only have to provide sufficient energy during acceleration periods and for compensating the overall losses. Since the DC source actively controls the voltage and is capable of recuperating brake energy into the supply grid, no braking chopper is necessary.

The control algorithms for the motor under test run on a rapid prototyping system, which also acquires all available measurement signals, i.e. phase currents, DC voltage and rotor position. The rapid prototyping system has an optical communication module that is connected with a standard PC, where the measurements can be visualized, and user commands can be processed and forwarded to the motor controller.

It is worth noting that all measurement raw data are logged on the PC. The evaluation of the flux linkage information as discussed in Chapter 6 is done during post processing. This has the advantage that the results obtained with different methods can be optimally compared to each other.

In the following sections, the specifications of each of the described components are given. As we will show later, the switching characteristics of the test inverter are important for the measurement results. Therefore, this issue is addressed in detail.

### **3.1 Rapid Prototyping System**

---

The rapid prototyping system consists of a *dSPACE DS1005 PowerPC Board* with a one GHz *real-time processor* (RTP) and 128 MByte SDRAM. For generation of the symmetric PWM pulse patterns, a *DS4002 Timing and Digital IO Board* is employed. The rotor position is acquired by a *DS3002 Incremental Encoder Board*. The other sensors deliver analogue voltages, which are fed to a *DS2001 High-Speed ADC Board* with five 16-Bit *analog-to-digital converter* (ADC) channels with a sample and hold unit each for synchronous data acquisition.

The timing of data acquisition, control and PWM generation is shown in Figure 3.2. From top downwards, the PWM signals as they are passed to the test inverter are shown. At bottom, the sequential working steps of the real-time system are shown. With the beginning of each PWM cycle, the DS4002 board generates an interrupt. The resulting *interrupt service routine* (ISR) starts with sampling all measurement signals. As the sampling takes place in the middle of the zero vector  $\mathbf{u}_0$ , the sampling frequency corresponds to the PWM frequency, which is in this case  $f_S = 10$  kHz. The sampling time is thus  $T_S = 1/f_S = 100$   $\mu$ s.

After the simultaneous data acquisitions of all available signals, the ISR processes the field-oriented control algorithm. Its outcome is the reference signal of the stator voltage vector  $\mathbf{u}_s^{s*}$ . As indicated, the updated reference does not influence the actual PWM. Only after finishing a complete cycle, the duty-cycles are updated. This leads to a dead time in the voltage commands that must be taken into account when evaluating the measurements.

The different lengths of both ISRs in Figure 3.2 indicates that the processing times can differ from one call to another. In order to guarantee real-time processing, the ISR has to be completely processed before the next interrupt occurs. This is monitored by a watch dog routine, which turns off the test inverter, if not regularly reset at the end of each ISR.

The time between two ISRs is used by the system for a background routine, which mainly consists of data exchange with the connected PC. Updated user commands are received and the measurements buffered during the ISR are transmitted.

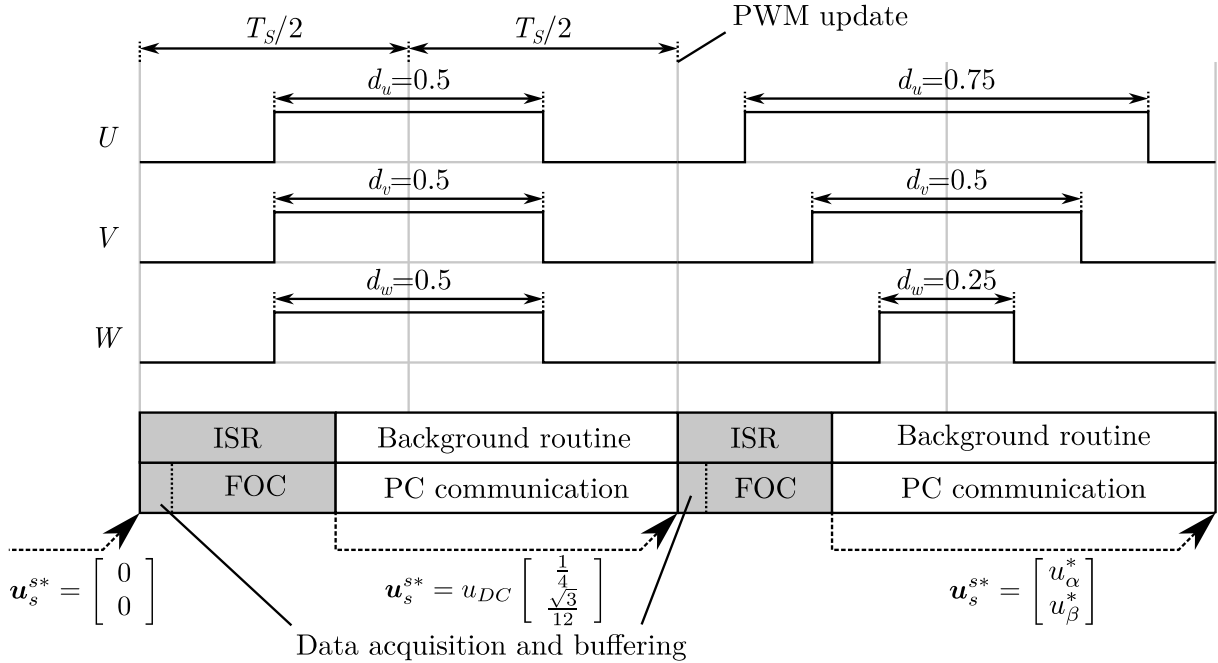


Figure 3.2: Timing diagram of data acquisition, control routine, communication and three-phase PWM signal generation

### 3.2 Power Electronics

#### 3.2.1 DC Source

The DC link voltage is supplied by an industrial inverter for elevators. The RPI 5.5 from ThyssenKrupp has an input power of 7 kVA and controls the DC voltage to remain within a range between 570 V and 630 V.

#### 3.2.2 Load Inverter

The load motor is driven by an *FC302 industrial two-level VSI from Danfoss*. It has a nominal power of 11.1 kVA and is manually commanded by the user via a control panel.

#### 3.2.3 Test Inverter

The motor under test is driven by a *modified MDX60A0074 two-level VSI from SEW*. It provides phase current and DC link voltage measurements as described below in section 3.3. Its nominal output power is 11.2 kVA with a nominal output phase current of 16 A (AC). The integrated over-current protection turns off the power module, when the phase current exceeds 120% of the nominal current (i.e. 27.15 A).

As the given test bench does not provide possibilities to measure the inverter output voltages (which is common in industrial applications), the later flux linkage measurements must rely on

the DC voltage measurements. However, the switching elements, in this case *insulated gate bipolar transistors* (IGBTs), are not ideal. They have typical forward voltage drops of 2-3 V [94 p. 690] and different turn-on and -off times, depending on the currents they switch. Additionally, the inverter enforces a switching dead time of *800 ns*. All these effects lead to errors in the assumed phase voltages.

While the voltage drops and the constant dead times could be compensated for easily, the nonlinear dependency of the switching times from the currents requires more effort. For that reason, the holistic voltage distortions caused by the inverter are measured according to the following procedure:

1. Initialization:
  - a. An appropriate motor (in terms of nominal voltage and current) is connected to the inverter. The motor shaft can be free or fixed. This has no influence on the measurements as we only need the motor as typical RL load.
  - b. The motor is operated in current control mode. A slowly rotating nominal stator current vector is applied in order to uniformly heat up the stator windings and the IGBTs.
  - c. When the motor temperature arrives at a steady state, the inverter is turned off and the exact motor and cable resistances are measured with an Ohmmeter.
2. Measurements:
  - a. The motor is operated again in current control mode. A set of gridded stator currents in the  $\alpha\beta$  plane is chosen as reference for the current controller. One after each other, all current references are applied and the resulting steady state phase currents and the DC voltage are logged for a time interval of two seconds. In order to account for limitations regarding the minimal and maximal pulse width and time quantization due to the DS4002 PWM board, also the exact duty-cycle times as they are processed by the board are logged.
  - b. In between each measurement, a simple resistance estimation is performed. Since the usually employed copper wires in AC motors have a positive temperature coefficient (i.e. the resistance increases with increasing temperature), the winding temperature can be hold in a defined range by either heating up the motor again or pausing the measurements. In this way, we can ensure that the measured resistance value from step 1.c remains valid.
3. Post-processing:
 

After finishing the measurements, the stator current and voltage space vectors are computed acc. to (2.41) and (2.135), respectively. Now, the voltage distortion caused by the inverter can be calculated by  $\mathbf{u}_{s,inv}^s = \mathbf{u}_s^{s*} - R_{cal}\mathbf{i}_s^s$ . This should be zero and the fact that it is not, must be due to the inverter as all other sources of error are eliminated as good as possible.

Figure 3.3 shows the results of described method. While the 3D plots of the inverter distortion voltages in  $\alpha$ - and  $\beta$ -axis, shown in (a) and (c), shall give a more qualitative overview, the respective contour plots, (b) and (d), improve the quantitative readability.

As expected, we see a nonlinear dependency of the voltage errors on the currents. The diode or IGBT forward voltage drops, the switching dead time and the different turn-on and -off times are all contained in the plots and sum up at maximum to an absolute value of ca. 8.2 V in the  $\alpha$ , and ca. 7.5 V in the  $\beta$ -axis. The differences between both axes can be explained by the asymmetric coupling between the phase  $abc$  axes and the space vector  $\alpha\beta$  axes.

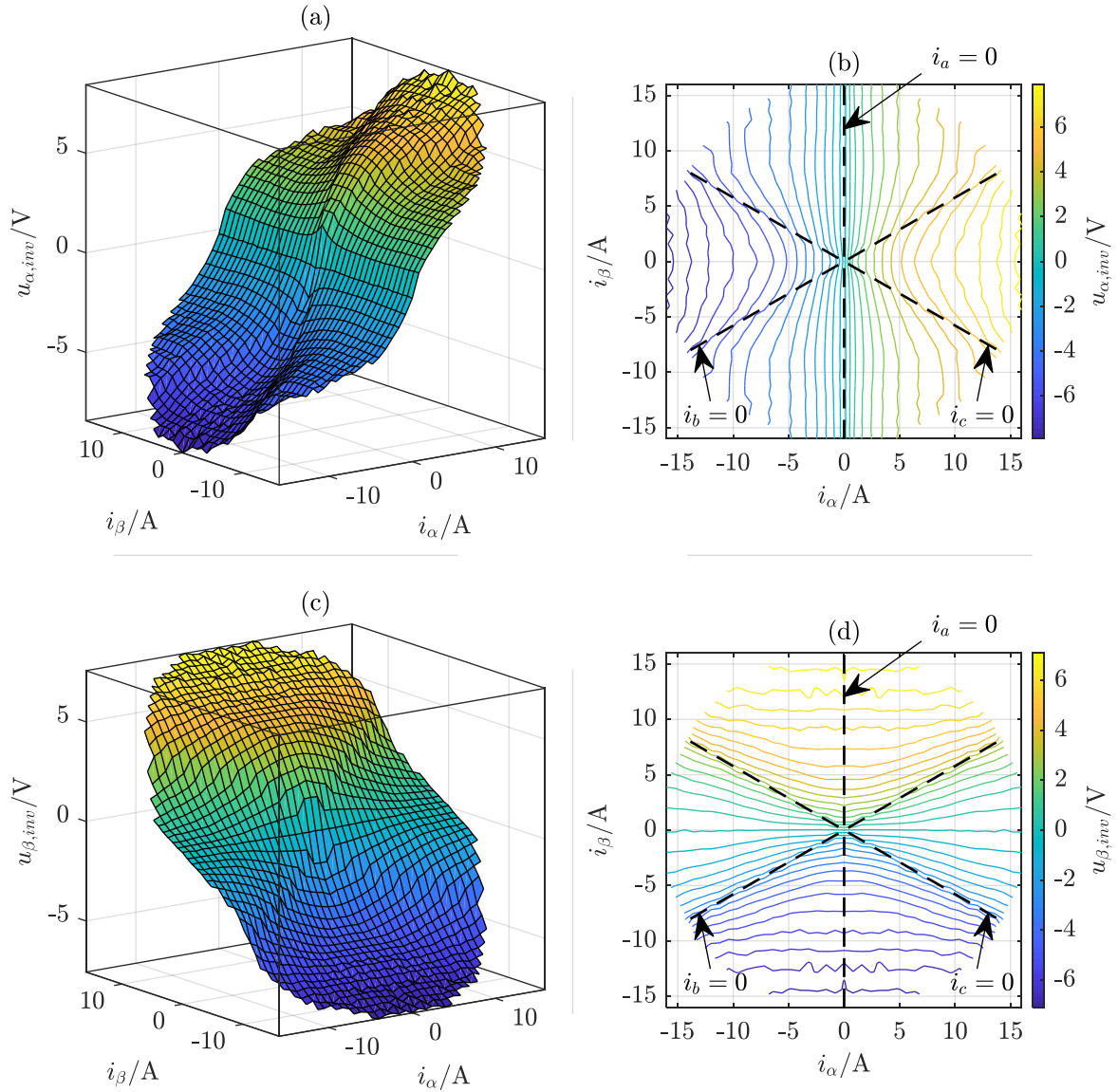


Figure 3.3: Voltage perturbation caused by the inverter plotted over stator currents in  $\alpha\beta$  plane; (a): 3D view of the  $\alpha$ -axis voltage perturbation, color represents  $z$ -axis value, see color bar from (b); (b): corresponding  $xy$  contour plot, black dotted lines depict points, where phase currents are zero; (c): 3D view of the  $\beta$ -axis voltage perturbation, color represents  $z$ -axis value, see color bar from (d); (d): corresponding  $xy$  contour plot, black dotted lines depict points, where phase currents are zero

Another effect that is slightly<sup>8</sup> observable in Figure 3.3 is the occurrence of discontinuities in the disturbance voltages along the phase axes. The latter are plotted in dotted lines in the subplots (b) and (d). During each commutation phase, the switching delays and dead times lead to a period, where both IGBTs of a half-bridge are insulating. During this time, the direction of the current driven by its own magnetic energy determines whether the upper or the lower freewheeling diode is conducting. The potential of the respective phase then corresponds to the high- or low-side DC voltage potential, accordingly. In consequence, the potential instantly changes with a change in the direction of the phase current [95, 96].

### 3.3 Used Sensor Systems

---

#### 3.3.1 Current Measurement

The phase currents are measured with the internal current transducers of the test inverter. Their technology bases on the closed-loop Hall effect principle.

Two sensors are applied to measure the currents of the phases  $U$  and  $V$ , while the current of phase  $W$  is calculated acc. to (2.32) by means of an analog circuit. All three signals are also analogously low pass filtered with a filter time constant of  $T_{fi} = 5 \mu\text{s}$ .

#### 3.3.2 Voltage Measurement

A measurement signal for the DC voltage,  $u_{DC}$ , is also provided by the test inverter. The signal is low-pass filtered with a second order filter, whose time constants are  $T_{fu1} = 1.1 \mu\text{s}$  and  $T_{fu2} = 4.7 \mu\text{s}$ .

#### 3.3.3 Speed and Position Measurement

The rotor position,  $\vartheta_m$ , is measured with an optical incremental encoder with 1024 pulses per revolution. With quadruple evaluation, we thus get a resolution of  $2\pi/4096 = 5.5''$ .

From the position information, the speed is approximated from

$$\omega_m = \frac{d\vartheta_m}{dt} \approx \frac{\Delta\vartheta_m}{\Delta t}, \quad (3.1)$$

where  $\Delta\vartheta_m$  is the position difference between two subsequent samples and  $\Delta t$  is the sampling time. With  $T_S = 100 \mu\text{s}$ , we get a speed resolution of  $15.3 \text{ }^\circ/\text{s} = 146.5 \text{ rpm}$ . In order to reduce these discretization effects, the speed signal is low-pass filtered with a filter that averages the past ten speed values. In this way, the resolution of the speed signal can be improved by the factor ten, however at the expense of a time lag in the signal.

### 3.4 Tested Machines

---

Three different types of synchronous motors are tested within this work:

- A synchronous reluctance motor (SynRM)
- A permanent magnet synchronous motor with buried magnets (IPMSM)

---

<sup>8</sup> The discontinuities would be better visible with smaller step sizes in the measurement grid, however at the cost of exponentially increasing measurement effort.

- A permanent magnet synchronous motor with surface magnets (SPMSM)

Their relevant parameters are given in Table 3.

Table 3: Parameters of the tested motors according to manufacturer (italic formatting indicates values that are not directly given but could be derived from the information given)

					
SM type			SynRM	IPMSM	SPMSM
Manufacturer			Stellenbosch University, EM Lab	Yaskawa Electric Corporation	Merkes GmbH
Type			Prototype	SSR1-43P7AFN	MT5-1050-30-560/P
Nominal voltage (RMS)	$U_N$	V	400	369	330
Nominal current (RMS)	$I_N$	A	3.5	6.8	6.3
Nominal power	$P_N$	kW	1.5	3.7	2.76
Nominal torque	$M_N$	Nm	<i>9.55</i>	<i>20.2</i>	8.8
Nominal speed	$\omega_{m,N}$	rpm	1500	1750	3000
Nominal phase resistance	$R_{s,N}$	$\Omega$		1.798	<i>0.85</i>
Nominal phase inductance	$L_{s,N}$	mH		32.93 ( <i>d</i> -axis) 37.70 ( <i>q</i> -axis)	<i>7.6</i>
PM flux linkage	$\psi_{PM}$	mVs	0	498.7	<i>226.3</i>
Number of pole pairs	$p$		2	3	3



# CHAPTER 4

---

## On Magnetic Characteristics of Synchronous Machines

---

Before the following chapters address how to identify the magnetic characteristics of synchronous machines, this chapter explains the basic interrelations between magnetic energy, flux linkage and inductances in the context of synchronous machines and discusses, how this information can improve practical control tasks. Presenting now already the final results of the following chapters shall motivate and simplify understanding the hereinafter presented theory.

### 4.1 The Synchronous Reluctance Machine

---

#### 4.1.1 The Relation between Magnetic Energy, Flux Linkage and Stator Current

In the description of synchronous machines in Chapter 2.2, a detailed analysis came to the conclusion that the relation between the flux linkage and stator current space vectors is essential for modelling and controlling SMs. The mathematical translation of this relation was found in (2.55) to be

$$\boldsymbol{\psi}_s^r = \boldsymbol{f}^r(\boldsymbol{i}_s^r), \quad (4.1)$$

where  $\boldsymbol{f}^r$  is a bijection that maps each current space vector with a flux linkage vector. We further found in (2.91) that the flux linkage is a conservative vector field derived from the gradient of the magnetic co-energy scalar field, i.e.

$$\boldsymbol{\psi}_s^r = \frac{2}{3} \nabla W_{\mu,co}(\boldsymbol{i}_s^r). \quad (4.2)$$

We can thus state that all information describing the magnetic characteristics of synchronous machines is contained in the co-energy field. The same statement holds analogously for the inverse of  $\boldsymbol{f}^r$  and the magnetic energy acc. to (2.56) and (2.90), i.e.

$$\boldsymbol{i}_s^r = \boldsymbol{f}^{r-1}(\boldsymbol{\psi}_s^r) \quad (4.3)$$

and

$$\mathbf{i}_s^r + \mathbf{i}_{s,PM}^r = \frac{2}{3} \nabla W_\mu(\psi_s^r). \quad (4.4)$$

Figure 4.1 presents the magnetic energy and co-energy maps as final result of measurements described in section 6.3 for the SynRM introduced in Table 3. We can see that both, energy and co-energy, are zero in the origin of the respective planes and that they are symmetric with respect to the respective  $d$  and  $q$  axes. As discussed in section 2.1.2.4, the different energy levels along both axes are expressing the magnetic anisotropy of the machine.

We can clearly see that the magnetic energy and co-energy maps are not equal as it would be in non-saturating (linear) material. In fact, the co-energy is larger than the energy at any point except the origin, which is clearly indicating that the ferromagnetic material of the SynRM is saturating in the expected way, i.e. that the magnetization versus the magnetic field is characterized by a sigmoid function (cf. Figure 2.1 and Figure 2.6).

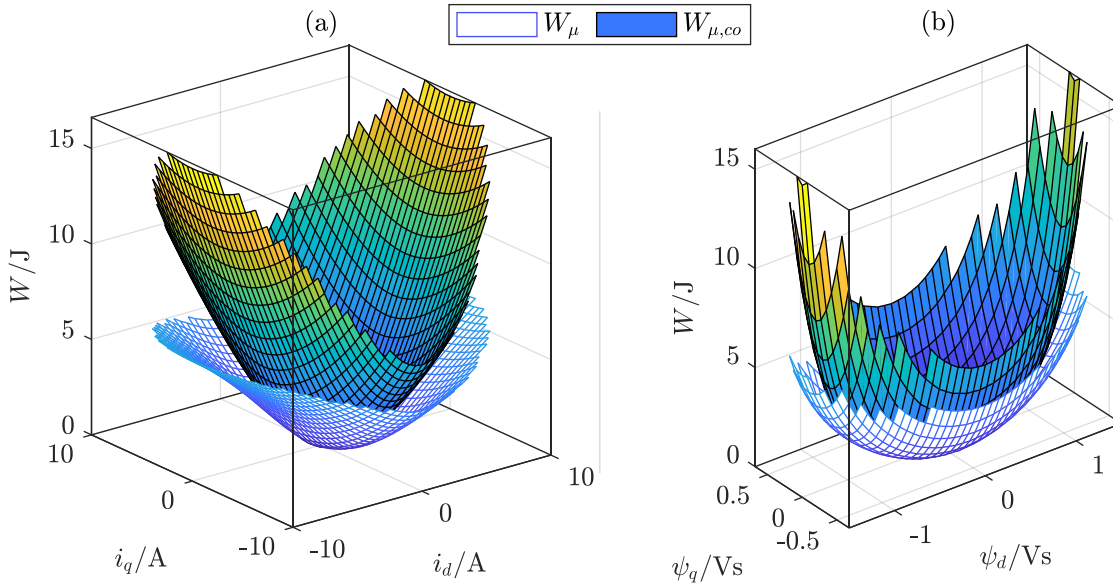


Figure 4.1: Magnetic energy and co-energy maps of the SynRM plotted as surfaces over stator current (a) and flux linkage (b) planes

With this information, we can obtain both,  $\mathbf{f}^r$  and  $\mathbf{f}^{r-1}$ , by applying (4.2) and (4.4), respectively. The corresponding visualizations are presented in Figure 4.2 and Figure 4.3. The black contour lines indicate loci of constant magnetic (co-)energy. The blue arrows represent the flux linkage and current space vectors as gradient of the respective (co-)energy fields (i.e. they are always orthogonal to their corresponding (co-)energy lines). The arrow lengths are proportionally correct but only of qualitative nature as a graphical comparison of the arrow length at a given point with a map scale would be difficult. The starting points of each arrow indicate the actual current (cf. Figure 4.2) or flux linkage (cf. Figure 4.3) points they are valid for.

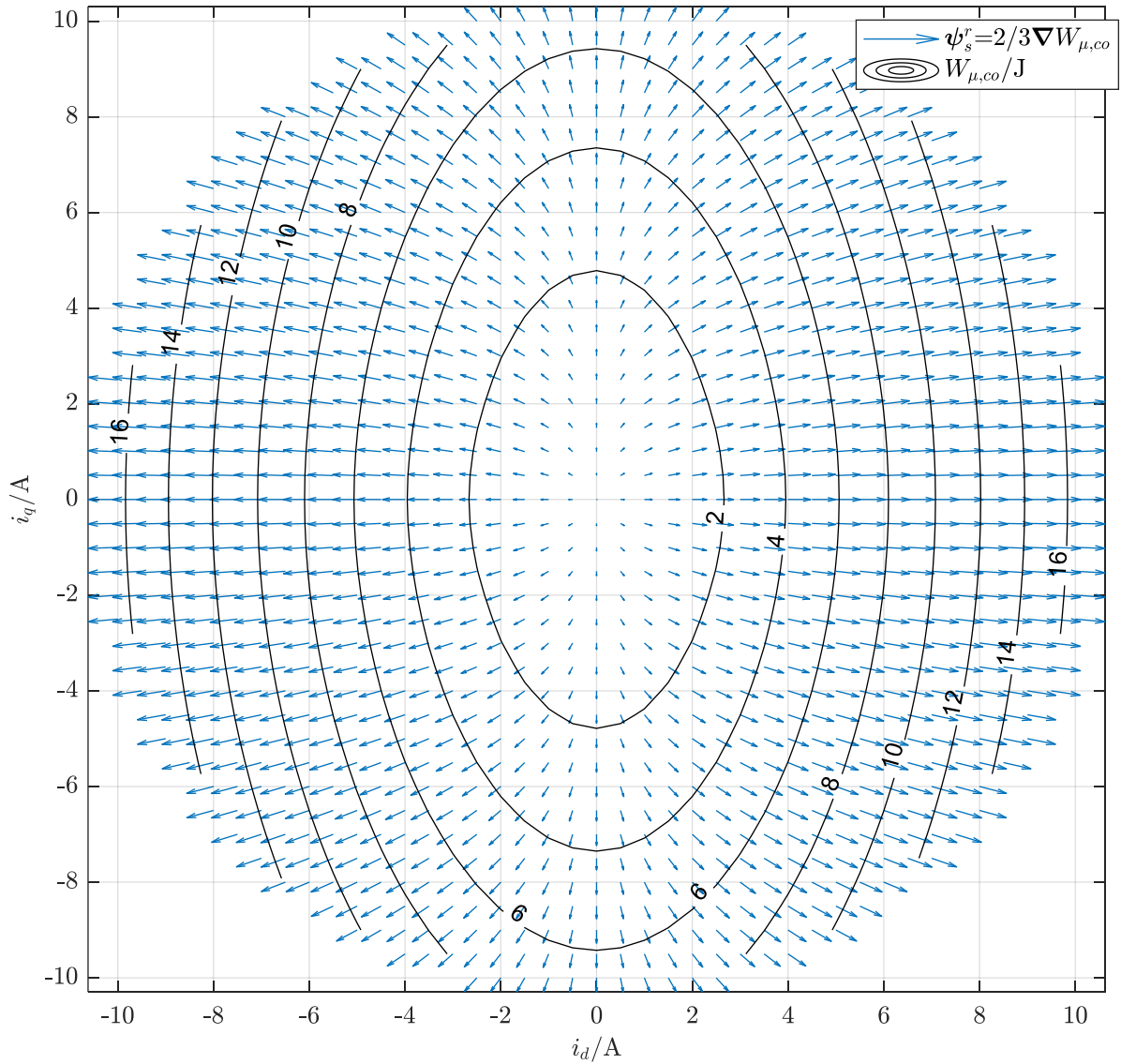


Figure 4.2: SynRM flux linkage space vector field derived from the magnetic co-energy scalar field in the  $dq$  current plane

Since this work only considers the fundamental components of flux linkage and stator current space vectors and since all measurements are performed at a rotor speed well above standstill, the magnetic anisotropy observable in Figure 4.2 is a shape anisotropy due to the specific rotor geometry, i.e. it results from different amounts of ferromagnetic material along  $d$  and  $q$  axis enforced by flux barriers (cf. Figure 2.13). The additional amount of magnetic material along the  $d$  axis path leads to faster increasing magnetic co-energy in that axis.

Regarding the magnetic energy, the inverse effect is seen in Figure 4.3. When reminding the graphical interpretation from Figure 2.6 (b), where the energy is interpreted as area between  $\mathbf{f}^r$  and the flux linkage axis, it is obvious that the most energy is stored in the axis with a lower slope of  $\mathbf{f}^r$ , i.e. the  $q$  axis which has more air in its path.

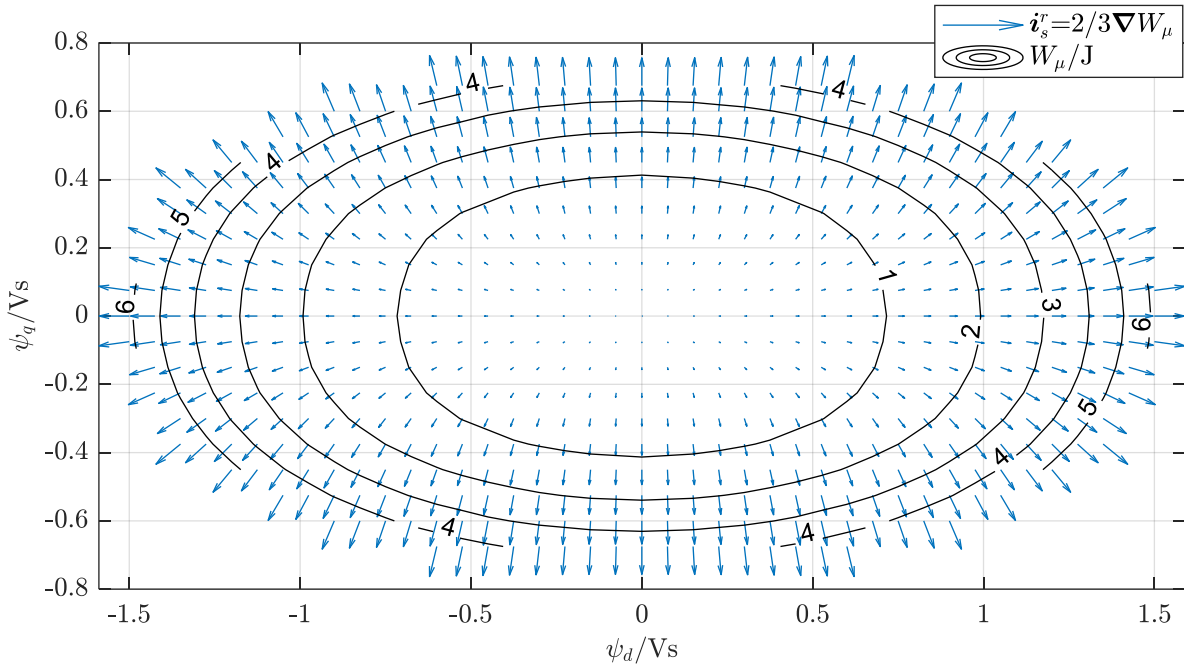


Figure 4.3: SynRM stator current space vector field derived from the magnetic energy scalar field

From now on, we could continue to parallelly analyze  $\mathbf{f}^r$  in a current and  $\mathbf{f}^{r-1}$  in a flux linkage plane. For brevity, however, we will henceforward focus on  $\mathbf{f}^r$  only. Since the stator currents are directly measured, they seem to be the natural choice as reference plane.

As a quantitative analysis of  $\mathbf{f}^r$  is difficult in the form presented in Figure 4.2, it is necessary to interpret the  $d$  and  $q$  components of  $\mathbf{f}^r$  separately. This is done in Figures 4.4 and 4.5, where the  $d$  flux map (Figure 4.4) and the  $q$  flux map (Figure 4.5) are plotted versus the  $d$  and  $q$  currents.

The 3D plots in the subfigures (a) shall give a qualitative impression of  $f_d$  and  $f_q$ , whereas the subfigures (b)-(d) allow also quantitative analysis. The (b) plots show contour lines of the flux linkages for constant  $q$  currents and thus correspond to the view on (a) from the front right. The (c) subfigures accordingly correspond to a view on (a) from the front left along the  $d$  current axis and the (d) subfigures show the contour lines of constant flux linkage, when we look at (a) from the top.

In Figure 4.4(b) and Figure 4.5(c), we see the expected, typical sigmoidal saturation curves in accordance with the theoretical conclusions from section 2.2.3.5. Around the origin, the material is nearly linear, beginning to saturate with increasing currents. The  $d$  axis flux linkage shows a higher increase than its counterpart in the  $q$  axis. Additionally, the saturation begins at a point farther away from the origin and the cross-saturation effect is less significant around the origin.

The latter statement is confirmed by the comparison of Figure 4.4(c) and Figure 4.5(b). While the  $d$  flux linkage shows only few and nearly linear decrease with increasing  $q$  current, the  $q$

axis flux linkage develops a quite nonlinear decrease with increasing  $d$  current, especially around the origin.

When analyzing the cross-saturation effects of both axes, it should be noted that best comparability is given for subfigures (d) of Figure 4.4 and Figure 4.5, as both are plotted on the same equidistant current plane. Here, the influence of cross-saturation is expressed by the additional current that is necessary to hold the flux linkage constant, when the current in the orthogonal axis is increasing.

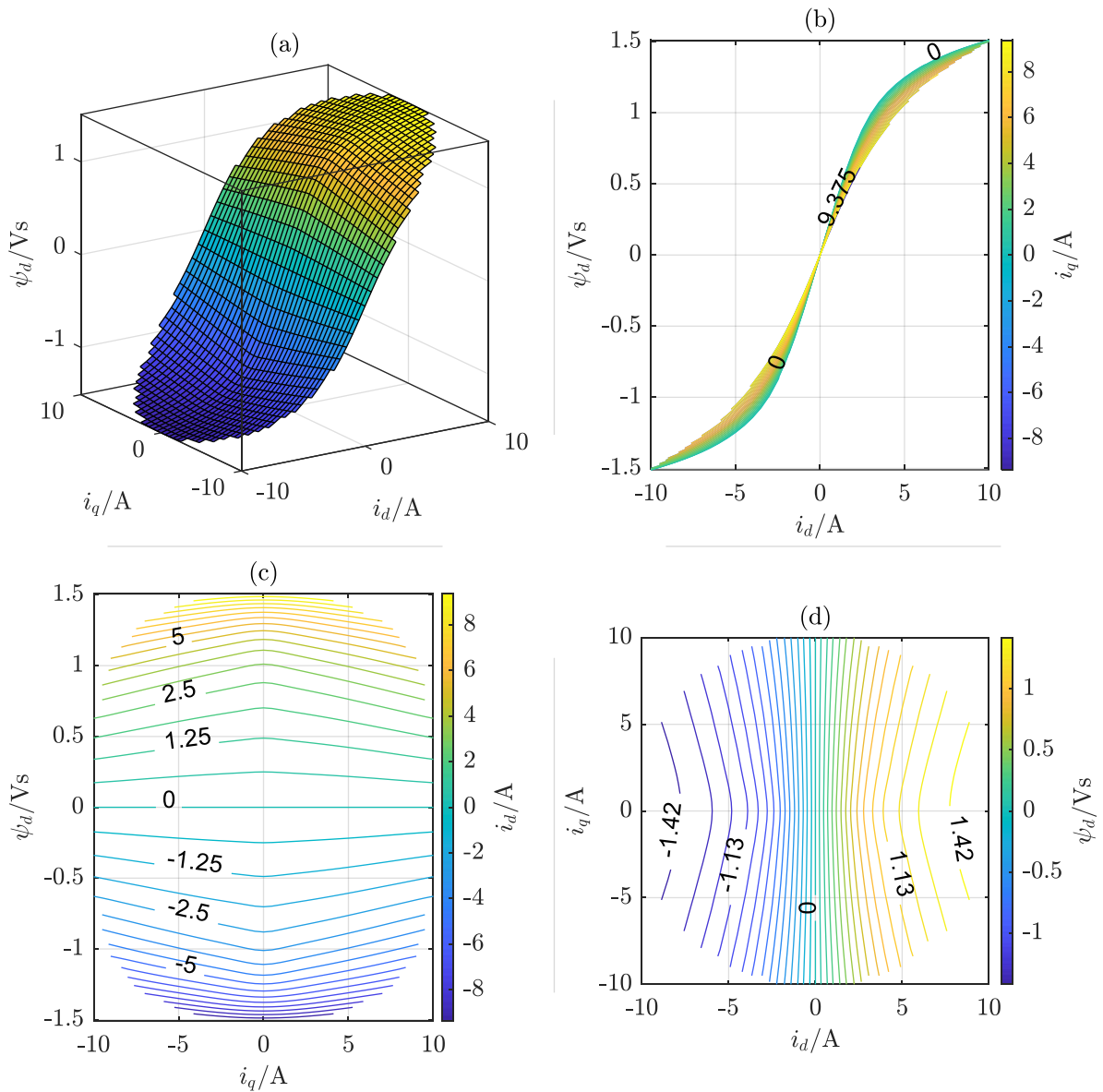


Figure 4.4: SynRM  $d$ -axis flux linkage maps plotted over stator currents in  $dq$  plane; (a): 3D view of flux linkage surface, color represents flux linkage value, see color bar from (d); (b): corresponding  $xz$  contour plot; (c): corresponding  $yz$  contour plot; (d): corresponding  $xy$  contour plot

All subfigures in Figures 4.4 and 4.5 demonstrate the symmetry of both flux linkage surfaces with respect to the origin. This symmetry is an obvious result from the geometric symmetry of the rotor yoke.

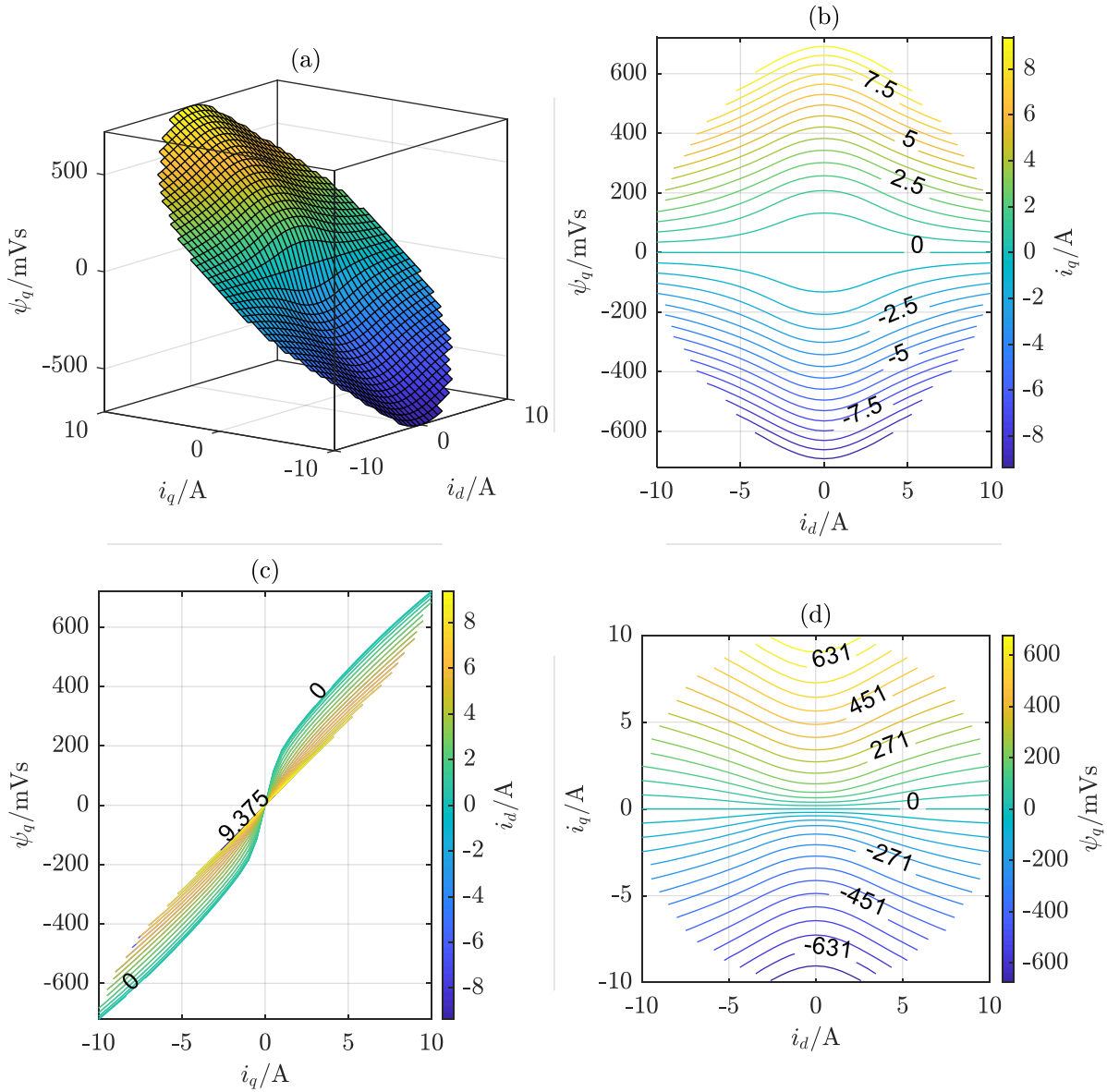


Figure 4.5: SynRM  $q$ -axis flux linkage maps plotted over stator currents in  $dq$  plane; (a): 3D view of flux linkage surface, color represents flux linkage value, see color bar from (d); (b): corresponding  $xz$  contour plot; (c): corresponding  $yz$  contour plot; (d): corresponding  $xy$  contour plot

#### 4.1.2 Torque Generation and Associated Control Strategies

In section 2.2.3.2, the torque was defined in (2.95) as

$$M = \frac{3}{2} p \mathbf{i}_s^T \mathbf{J} \boldsymbol{\psi}_s^r = \frac{3}{2} p (\psi_d i_q - \psi_q i_d). \quad (4.5)$$

With the measured pairs of flux linkage and stator current space vectors as presented above, we are thus able to calculate the torque at all feasible operating points. Figure 4.6 shows the SynRM torque over both, current and flux linkage planes in rotor coordinates.

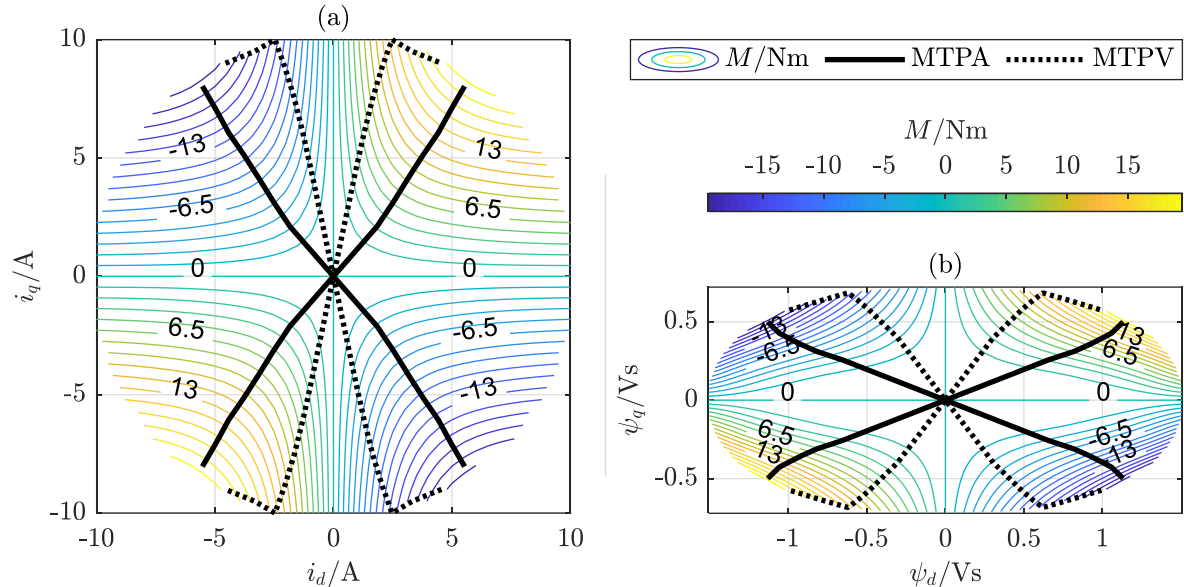


Figure 4.6: SynRM torque contour lines plotted over stator currents (a) and flux linkage in  $dq$  plane; legend and color bar are valid for both subfigures

We see that the torque is symmetric with respect to the origin, as it could be expected due to the symmetry of flux linkage and current surfaces. The torque in first and third quadrants is positive, whereas it is negative in the quadrants two and four. Along both axes, no torque is produced, which means that both axes must be simultaneously magnetized to generate torque.

The loci of constant torque indicate that a certain torque can be produced by a variety of operating points. This degree of freedom leads to the introduction of optimization criteria in order to develop advantageous control strategies. In many cases, optimizing the machine losses is the primary goal. An important role in loss minimization strategies play the so-called *maximum torque per Ampere* (MTPA) and the *maximum torque per Volts*<sup>9</sup> (MTPV) trajectories. As their names indicate, they aim at finding the maximum torque for a given current or flux linkage space vector of constant length.

They are seen as advantageous, because both, current and flux linkage space vectors are associated with losses. The electric current produces Ohmic losses in the stator windings, whereas the flux linkage is associated with iron losses. However, only when the motor is

<sup>9</sup> In fact, this strategy aims at maximizing the torque for a given flux linkage and hence should be abbreviated by MTPVs (“per Volt seconds”). However, besides minimizing the associated iron losses, this strategy also minimizes the back electromotive force (BEMF), which is measured in Volts. In literature, this strategy is also referred to as maximum torque per flux, which is, however, inconsistent with the naming of MTPA

operated at a certain speed, the resulting remagnetization cycles of the stator yoke produce relevant hysteresis and eddy current losses.

In practice, operating points in between both trajectories or intelligent switching procedures between the strategies have to be applied. Independent from the actual implementation, however, both trajectories enclose the areas of relevant operating points for efficient control strategies.

The MTPA and MTPV current and flux linkage trajectories in Figure 4.6 indicate that the optimal current angles for the analyzed SynRM lie between approximately 50 to 80 degrees for positive and between -50 to -80 degrees for negative torques.

It is worth noting that both trajectories are comparably linear. Only at the borders of the measured area, the MTPV trajectories show a sharp curve towards the MTPA trajectories. Under those limited conditions, the torque is maximal along the border. Without limitations, however, the MTPV trajectories would proceed relatively linear. Note that a quite similar effect can be seen for the MTPA moving towards the MTPV trajectory, when considering voltage limitations. This, however, only happens at high speeds and is thus not indicated in Figure 4.6.

Also note that both, MTPA and MTPV, are not only relevant for efficiency but also to optimally deal with current and voltage constraints. MTPA allows maximal torque at a given current limit (determined by thermal heating in the stator windings and power electronics). MTPV allows to obtain maximal torque, when at high speed the BEMF approaches the maximum voltage of the inverter.

### 4.1.3 Affine Model Parameters

An affine model of synchronous machines was discussed in section 2.2.3.1 and mathematically described by (2.72), i.e.

$$\mathbf{u}_s^r = R_s \dot{\mathbf{i}}_s^r + \omega_{r,op} \mathbf{J}(\boldsymbol{\psi}_{s,ls}^r(\mathbf{i}_{s,op}^r) + \mathbf{L}_{s,op}^r \mathbf{i}_s^r) + \mathbf{L}_{s,op}^r \frac{d}{dt} \mathbf{i}_s^r. \quad (4.6)$$

In the context of magnetic saturation, we can identify to sets of parameters, that can be considered constant for small changes around given operating points – the differential inductance matrix  $\mathbf{L}_s^r$  and the large-signal flux linkage vector  $\boldsymbol{\psi}_{s,ls}^r$ , where

$$\boldsymbol{\psi}_{s,ls}^r = \boldsymbol{\psi}_s^r(\mathbf{i}_{s,op}^r) - \mathbf{L}_{s,op}^r \mathbf{i}_{s,op}^r. \quad (4.7)$$

The inductance matrix parameters are plotted in Figure 4.7 as maps in the  $dq$  stator current plane. They are derived by computing the mean gradients of the flux linkage maps, which were shown in section 4.1.1. Especially in the contour plots on the right side of Figure 4.7, we can note a higher level of noise in the maps, which is a direct consequence of the numerical differentiation of the (at least slightly) noisy flux linkage data. The borders of the maps show the most noise. This is due to two effects. Firstly, at the borders no mean gradients can be computed. Instead, the gradients to the inner points are taken, which halves the evaluation distance and thus doubles the effect of noise on the numerical differentiation. The second effect results from the optimization process that is used to polish the measured data. That process is described in detail in Chapter 5. For the moment, it is only important, that it reduces noise by

solving an optimization problem involving all measurement points simultaneously. For that reason, neighboring points contribute to reducing the noise on each center point. In the border region, however, each point only has a reduced number of valid neighbors.

All subfigures of Figure 4.7 demonstrate the highly non-linear behavior of the SynRM as a consequence of magnetic saturation. In a perfectly linear machine, both,  $L_{dd}$  and  $L_{qq}$ , would be positive valued constants and the coupling inductance,  $L_m$ , would always be zero. Instead,  $L_{dd}$  is decreasing very fast along the  $d$ -axis, whereas  $L_{qq}$  decreases along the  $q$ -axis. The influence of cross-saturation is observable in both,  $L_{dd}$  and  $L_{qq}$ , and is also demonstrated by mutual inductances that reach up to  $\pm 60\%$  of the main axes' inductance values in the border regions of the measured area.

It is worth noting that the mutual inductance values change their signs, when entering from one quadrant to its neighbor. The consequences of this sign changes at the  $dq$  axes are important in anisotropy-based sensorless control schemes, which are addressed in the following section.

Due to less ferromagnetic material along the  $q$ -axis flux linkage paths,  $L_{qq}$  is generally smaller and faster saturating than  $L_{dd}$ . Furthermore,  $L_{qq}$  seems to be maximally saturated in the border regions of the measured area, since it does not relevantly change with increasing  $d$ - or  $q$ -currents. Note, however, that this does not necessarily mean that the  $q$ -axis is generally maximally saturated. As already mentioned, the mutual inductances have a relevant influence on the overall flux linkages in the border region. This was already observed in the  $q$ -axis flux linkage measurements in Figure 4.5.

A similar point can be made for the  $d$ -axis, where  $L_{dd}$  begins to desaturate with increasing  $q$ -currents for inductance values smaller than 200mH. With regard to the flux linkage maps in Figure 4.4, we can state that increasing  $q$ -currents always led to cross-saturation, which is again a result of the mutual inductances.

In the global perspective, we cannot identify any region of relevant size, where the machine could be considered linear. This underlines the necessity to distinguish between large- and small-signal behavior of synchronous machines, as it was discussed in section 2.2.3.1.

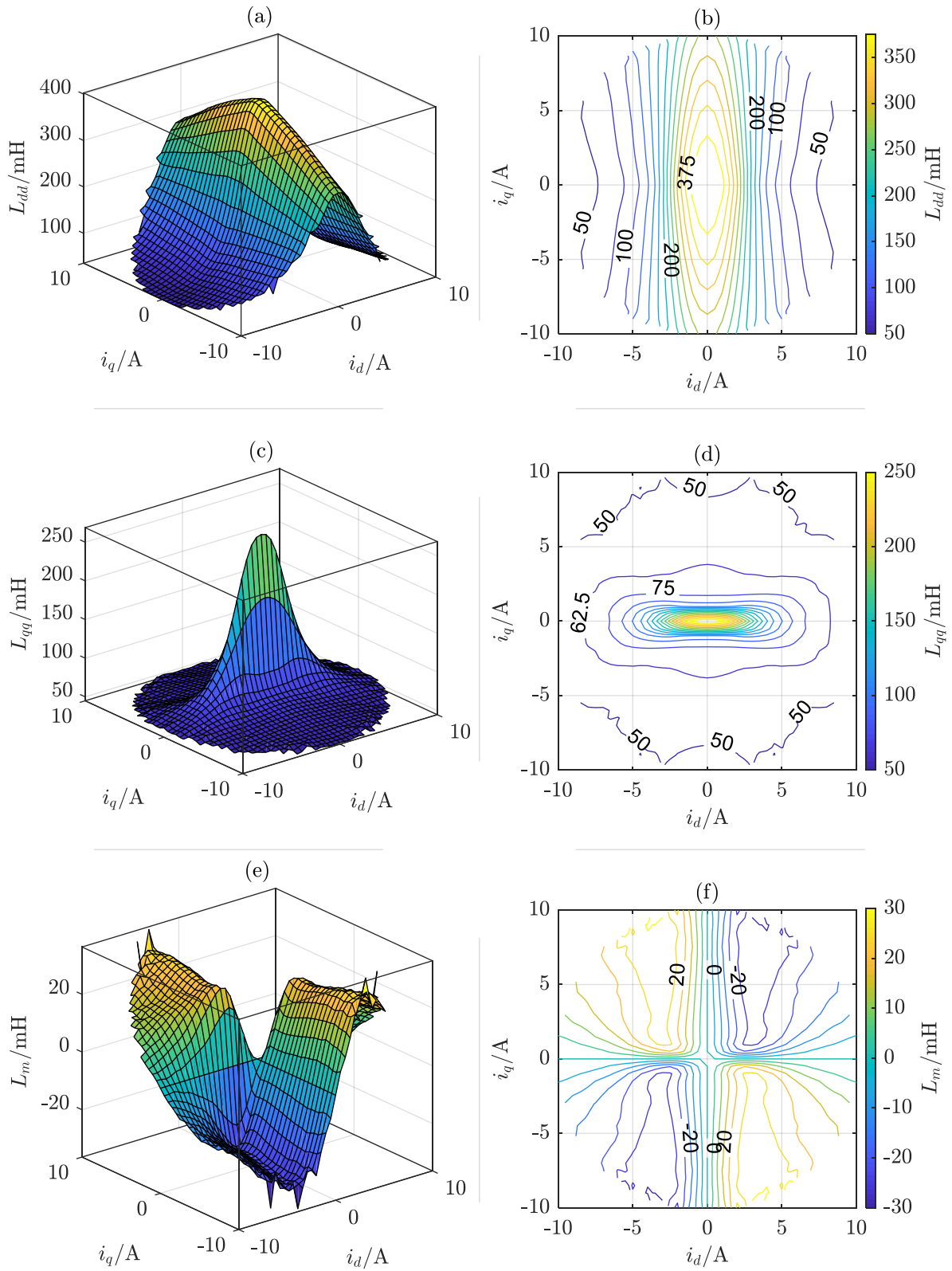


Figure 4.7: SynRM inductances plotted over stator currents in  $dq$  plane; (a)&(b):  $d$  axis inductance; (c)&(d):  $q$  axis inductance (e)&(f): mutual inductance

The large-signal flux linkages, that determine the offsets in the affine SM model acc. to (4.6), are shown in Figure 4.8. It is worth noting that  $\psi_{d,ls}$  reaches values of about four times of  $\psi_{q,ls}$ , which is significantly more than the ratio between the maximal values of the flux linkages ( $\approx 2.1$ , cf. Figures 4.4 and 4.5) Also note, that the maps are comparably curvy, making it difficult to approximate by simple mathematical models.

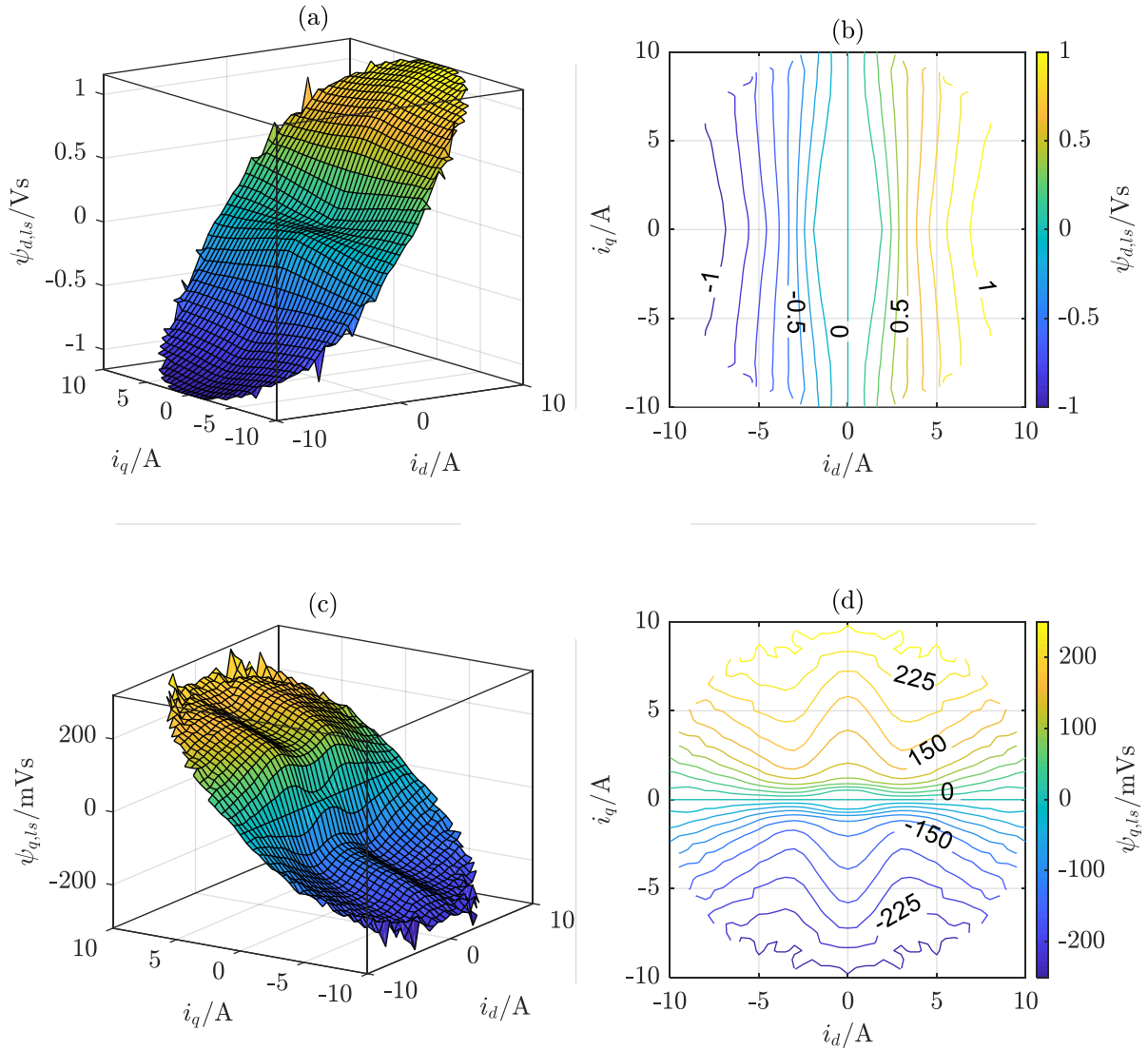


Figure 4.8: SynRM large-signal flux linkages for linearized models plotted over stator currents in  $dq$  plane; (a)&(b):  $d$  axis flux linkage; (c)&(d):  $q$  axis flux linkage

#### 4.1.4 Characteristics for Sensorless Control

In section 2.2.3.3, it was discussed that the suitability of synchronous machines for anisotropy based sensorless control depends on the ratio of anisotropic and isotropic components in the inductance matrix,  $\mathbf{L}_s^r$ . In Figure 4.9, this saliency ratio acc. to (2.123) is plotted over the stator current plane in rotor coordinates in subfigures (a) and (b). With up to 70%, it reaches comparably high values, indicating that this machine should be well suited for sensorless control. Only for current vectors along the  $d$  axis and especially at  $i_d \approx \pm 4A$ , comparably low anisotropic current derivatives of less than 10% of the overall current change are observable. As stated above in section 4.1.2, however, these regions are not of interest for typical control strategies.

In subfigures (c) and (d), the half-differences between the  $d$ - and  $q$ - axis inductances are shown. Here, it is interesting to note that for large  $d$ -currents the inductance difference becomes negative. This means that in these regions, the current saturates the  $d$ -axis inductance to a point, where it is smaller than the  $q$ -axis inductance. For the anisotropy, this means that the easy and hard axes are interchanged.

It should be emphasized that even at points, where  $L_{dd} = L_{qq}$  (i.e. along the zero-locus in subfigure (d) ), there is still an anisotropic component. This can easily be seen when comparing subfigures (b) and (d). According to (2.119), the coupling inductance,  $L_m$ , thus solely contributes to the anisotropic behavior of the machine at these points. Figure 4.7 (f) confirms this statement. Only the specific points at the  $d$ -axis, where  $L_m = L_\Delta = 0$ , show no magnetic anisotropy. For sophisticated sensorless control schemes, however, this is not generally problematic, since a bijective assignment of rotor position and actual operating point should still be possible (see, for instance, [17, 97]).

The subfigures (e) and (f) in Figure 4.9 show the orientation of the magnetic anisotropy. We see that along the  $q$ -axis, the anisotropy axes are exactly aligned with the rotor axes. Along the  $d$ -axis, beginning from the points, where  $L_\Delta \leq 0$ , a misalignment of  $\pm 90^\circ$  can be observed, which means that a standard anisotropy based sensorless control scheme would interpret the  $d$ - as  $q$ - axis and vice versa. The discontinuities in the anisotropy angle indicate that the directions of the interpreted anisotropy axes are ambiguous (i.e. the  $d$ -axis could be interpreted as positive or negative  $q$ -axis). They result from the combination of small  $L_\Delta$  and a change of sign in  $L_m$  (see Figure 4.7 (f)), which lead to a large quotient  $L_m/L_\Delta$  and a change of sign when passing the  $q$ -axis. These large values with changing signs substituted into the definition of the anisotropy angle acc. to (2.114)(a) explain the observed discontinuities.

The regions, where  $L_\Delta \leq 0$  generally lead to  $|\vartheta_A| \geq 45^\circ$ , which lets the estimated  $d$ -axis be closer to the  $q$ -axis than the real  $d$ -axis. As mentioned before, the MTPA and MTPV trajectories demarcate the typical operating areas of the SynRM. We can thus conclude that the critical areas discussed above are not within that region. The maximal open-loop errors that can occur here, are at approximately  $\pm 22.5^\circ$ .

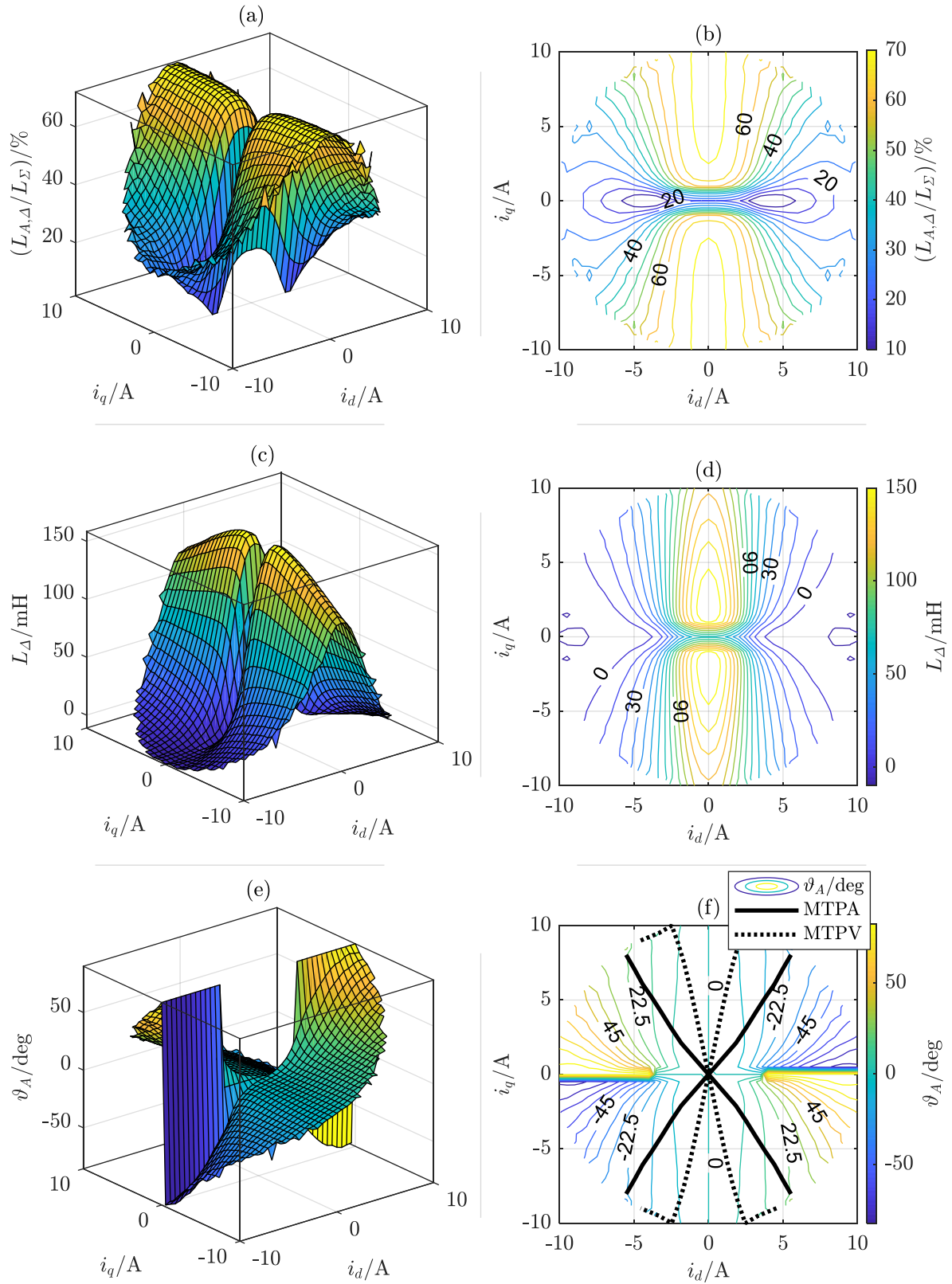


Figure 4.9: SynRM anisotropy characteristics plotted over stator currents in  $dq$  plane; (a)&(b): saliency ratio; (c)&(d): half difference between  $d$  and  $q$  axis inductances; (e)&(f): angle difference between  $D$  and  $d$  axis, MTPA and MTPV trajectories for reference

As discussed in section 2.2.3.3, we have to distinguish between open-loop (OL) and closed-loop (CL) sensorless control errors. Of course, CL control is the main purpose of sensorless control and thus we must further analyze the predictable CL behavior of the SynRM. Figure 4.10 (a) shows the top view and (b) the side view of the anisotropy angle. In contrast to subfigures (e) and (f) in Figure 4.9, it is plotted over the stator currents in an anisotropy-oriented reference frame. In order to obtain best result for visualization, a polar grid has been chosen and all points along the  $d$ -axis, where  $|\vartheta_A| > 89^\circ$  are eliminated. We can see that there are relevant operating points in the regions between the MTPA and MTPV trajectories, where the relation between current vector and anisotropy angle is non-bijective. For that reason, it seems not reasonable to compute the relevant current trajectories from the measured flux linkage maps and simply operate the SynRM in an anisotropy reference frame. Taking, for instance, a reference point on the MTPA trajectory with  $i_D = 2.3\text{A}$  and  $i_Q = 6\text{A}$  would lead to two possible anisotropy positions at  $\vartheta_A \approx -15^\circ$  or  $\vartheta_A \approx -60^\circ$ . In consequence, a simple position estimator that tracks the anisotropy angle should fail in assigning an unambiguous rotor position without further parameter knowledge.

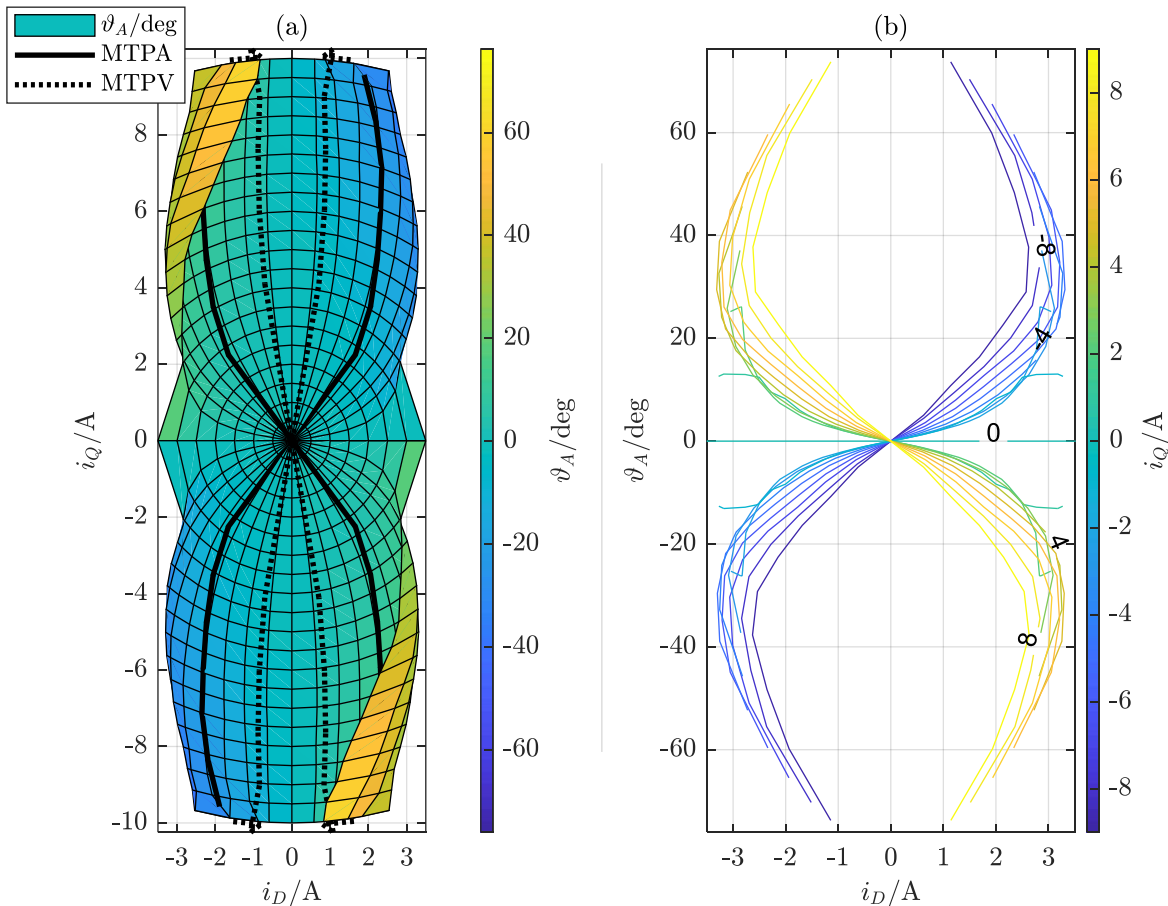


Figure 4.10: SynRM anisotropy angle plotted over stator current in  $DQ$  plane; (a): top view of 3D surface plot; (b): corresponding  $xz$  contour plot

Figure 4.10 thus indicates that sensorless CL operation might be instable in certain relevant operating regions, when only the anisotropy orientation is tracked, and no further parameters are applied. We thus analyze the CL stability acc. to the conditions (2.124) and (2.125) in the following Figures 4.11 and 4.12.

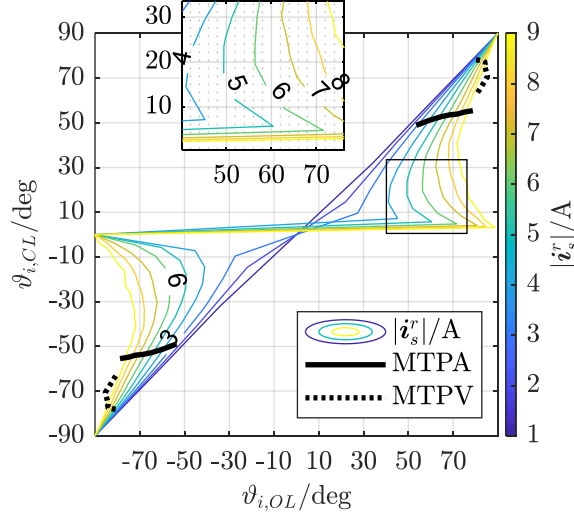


Figure 4.11: SynRM potentially stable CL operating points plotted over OL stator current angle reference in rotor-oriented coordinate system

In Figure 4.11, the CL current angle is plotted over the corresponding OL (or reference) current angle. It is obtained by solving (2.124) for  $\vartheta_{i,OL}$ , i.e.

$$\vartheta_{i,OL} = \vartheta_{i,CL} - \vartheta_{A,CL}, \quad (4.8)$$

and applying this to all combinations of apparent CL stator currents and corresponding anisotropy angles, which were shown in Figure 4.9 (e) and (f). For a given reference current vector in rotor coordinates, we can find the potentially stable corresponding CL current angle. Taking up the former example of  $i_D = 2.3\text{A}$  and  $i_Q = 6\text{A}$  leads us to the MTPA point of  $i_d = 3.8\text{A}$  and  $i_q = 5.2\text{A}$  (transformed into rotor coordinates with  $\vartheta_A \approx -15^\circ$ ), or, in polar coordinates,  $i_s = 6.4\text{A}$  and  $\vartheta_{i,OL} = 54^\circ$ .

In the zoomed plot, we can see that this current operating point is only intersecting with the discontinuous section of the respective curve near the  $d$ -axis. Since discontinuities are characterized by gradients of  $\partial\vartheta_A/\partial\vartheta_i = \pm\infty$ , we can directly see that the derivative condition acc. to (2.125), i.e.

$$\frac{\partial\vartheta_{A,CL}}{\partial\vartheta_{i,CL}} < 1, \quad (4.9)$$

is not met and thus the exemplary operating point is in fact instable.

In order to further discuss potentially stable CL points, we now select  $i_s = 7\text{A}$  and  $\vartheta_{i,OL} = 70^\circ$  as new current reference vector. Besides the intersection at the discontinuity, we can graphically identify further possible operating points at  $\vartheta_{i,CL} \approx 10^\circ$  and  $\vartheta_{i,CL} \approx 50^\circ$ , that meet condition

(2.124). For further analysis, we now need to evaluate the derivative condition (2.125), which is shown in Figure 4.12 (b).

Note that for determining the derivative  $\partial\vartheta_{A,CL}/\partial\vartheta_{i,CL}$ , two numerical differentiations of the initially measured flux linkage data are necessary. This results in an according amplification of measurement noise. In order to filter this noise in the curves of subfigure (b), the derivatives are calculated with current angle differences of  $\pm 5^\circ$ .

For reference, the absolute relation between anisotropy position and stator current operating point is shown in subfigure (a) of Figure 4.12. Here, we can see again the discontinuities along the  $d$ -axis (i.e. for current angles  $\vartheta_i = 0^\circ$ ) for current vectors of length 4A and more. In subfigure (b), we can see that around the discontinuities in the range of  $-40^\circ \leq \vartheta_i \leq 40^\circ$ , condition (2.125) is started being violated by large currents and in regions with smaller current angles also by currents of smaller amplitude. In order to not lose too much resolution, the respective derivative axis in (b) is limited to a range of  $-1.5$  to  $1.5$ .

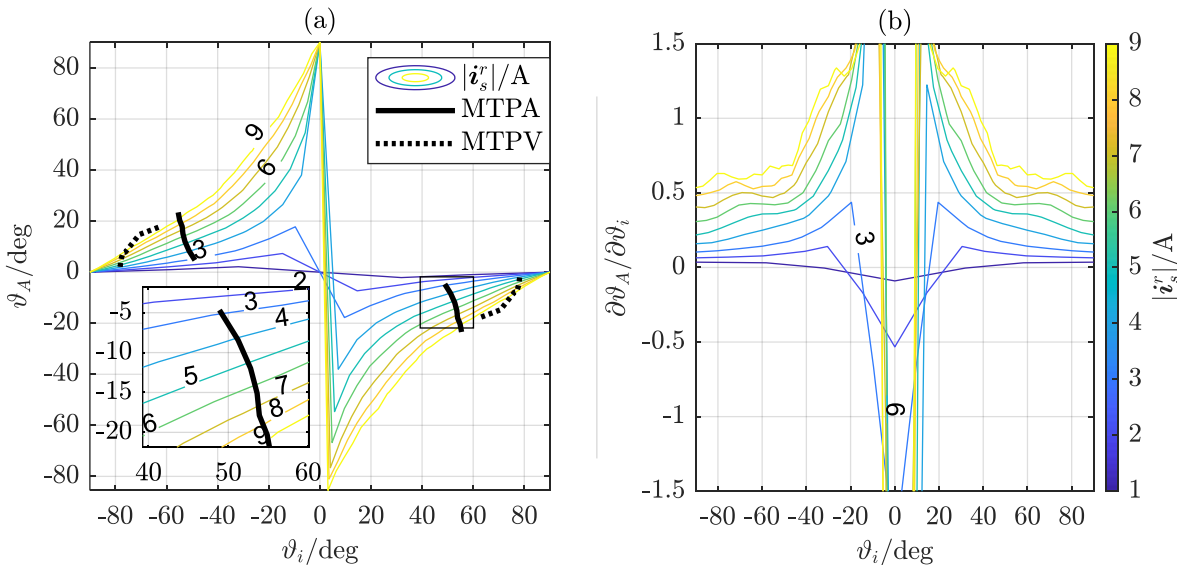


Figure 4.12: SynRM anisotropy angle (a) and its derivative (b) plotted over OL stator current angle in rotor oriented coordinate system; color bar is valid for (a) and (b)

When getting back to the last exemplary current operating point, we can see from subfigure (a) that it lies well within the practically relevant MTPA/MTPV region. Subfigure (b) reveals that from the two identified potentially stable CL operating points at  $10^\circ$  and  $50^\circ$ , only the latter satisfies the derivative condition (2.125). We can thus conclude, that a stable sensorless CL operation point exists, if a current vector of  $i_s = 7\text{A}$  and  $\vartheta_i = 70^\circ$  is given as reference. From the zoomed plot in subfigure (a), we can identify a misalignment of the resulting current vector of approximately  $-18^\circ$ , which means that the current vector in CL operation would be slightly outside the MTPA/MTPV region.

Note that the exemplary graphical identification of the stable point is not very precise. This can be seen on the identified angles,  $\vartheta_{i,OL} = 70^\circ$ ,  $\vartheta_{i,CL} \approx 50^\circ$  and  $\vartheta_A \approx -18^\circ$ , which obviously

do not exactly meet (2.124). For an overview of stable CL operating points, however, it is sufficient. For comparison, a simulative verification of the above graphical analysis gives us the exact angles of  $\vartheta_{i,OL} = 70^\circ$ ,  $\vartheta_{i,CL} = 52.9^\circ$  and  $\vartheta_A \approx -17.1^\circ$ .

Another aspect worth noting is, that this stability analysis only tells us, whether a stable operating point *exists*, when the machine is operated in sensorless closed-loop mode and the position estimator neglects magnetic cross-saturation. Whether this operating point can be reached in practice depends on the bandwidths of the position estimator and the current controllers. Only, if the current vector remains in stable regions around the stable CL operating point, we can expect the control scheme to be generally stable.

For the above-mentioned simulative stability analysis, a simple iterative adaption of the actual current vector was performed. A given OL current reference vector was rotated iteratively towards the respective anisotropy angle, until the changes of the resulting current vectors became sufficiently small. The instant rotation of the current vector in between two simulation steps corresponds to the case of unlimited bandwidths of position estimator and current controllers. If the termination criterion was not reached within a certain number of iterations, the corresponding OL reference vector was considered instable.

The results of these simulations for all current reference vectors within the measured area are shown in Figure 4.13. All subfigures show the angle differences between CL and OL current vectors, i.e. the anisotropy angle at the resulting CL current vector. Only stable CL operating points are shown.

Subfigures (a) and (b) show the resulting stable CL operating errors, when the current grid points as shown in (a) are given as OL reference. We can see that only reference vectors with  $|i_d| < 3\text{A}$  result in stable CL operation. Before becoming instable, CL errors of up to  $\pm 25^\circ$  occur. When comparing the resulting MTPA and MTPV trajectories, as shown in subfigure (b), the black OL references lead to the grey CL trajectories, which show significant derivations from the desired behavior. Along the MTPA trajectory, the SynRM can only be operated in CL-operation up to approximately  $i_d = \pm 4.5\text{A}$  and  $i_q = \pm 2.7\text{A}$ , which corresponds to around  $M = \pm 6.1\text{Nm}$  (see Figure 4.6 (a) ), or 64% of the rated torque. Along the MTPV trajectory, stable operation is possible up to approximately  $[i_d \ i_q]^T = [\pm 4.9\text{A} \ \pm 7.6\text{A}]^T$ , which allows torques of about  $M = \pm 17.3\text{Nm}$  (182% rated torque).

Especially at higher loads, both CL trajectories are far from being optimal in terms of their initial purpose, i.e. maximum torque per ampere, or per volts. In order to improve the CL behavior of the machine, we get back to the above-mentioned idea of controlling the machine in an anisotropy reference frame (see Figure 4.10). When comparing Figure 4.10 and Figure 4.13 (c), we see that the overlapping regions are instable in CL operation. For that reason, the depicted stable CL errors resulting from reference vectors in anisotropy coordinates are bijective. In subfigure (d), we can see that we obtain the desired CL behavior. When applying the black trajectories to the CL current controllers, the resulting grey trajectories are identical with the real MTPA and MTPV trajectories (see Figure 4.9 (f), for instance), i.e. the machine is operated along the optimal trajectories.

It is worth noting, that by controlling the SynRM in anisotropy coordinates, the valid CL operating area can be effectively extended. Although we see that the trajectories at maximal load are identified as unstable by the simulations, this is simply a result of the increasing noise in the measured flux linkage planes at high currents. The reasons for that noise were already explained in section 4.1.2, where the inductance maps in Figure 4.7 are discussed and in the above discussions of the results shown in Figure 4.12 (b).

It can thus be stated that the simulations might falsely identify operating points in the border regions of the measured area as unstable. From Figure 4.12, we can see that the stability conditions for CL control are met along both, MTPA and MTPV trajectories. It is thus possible

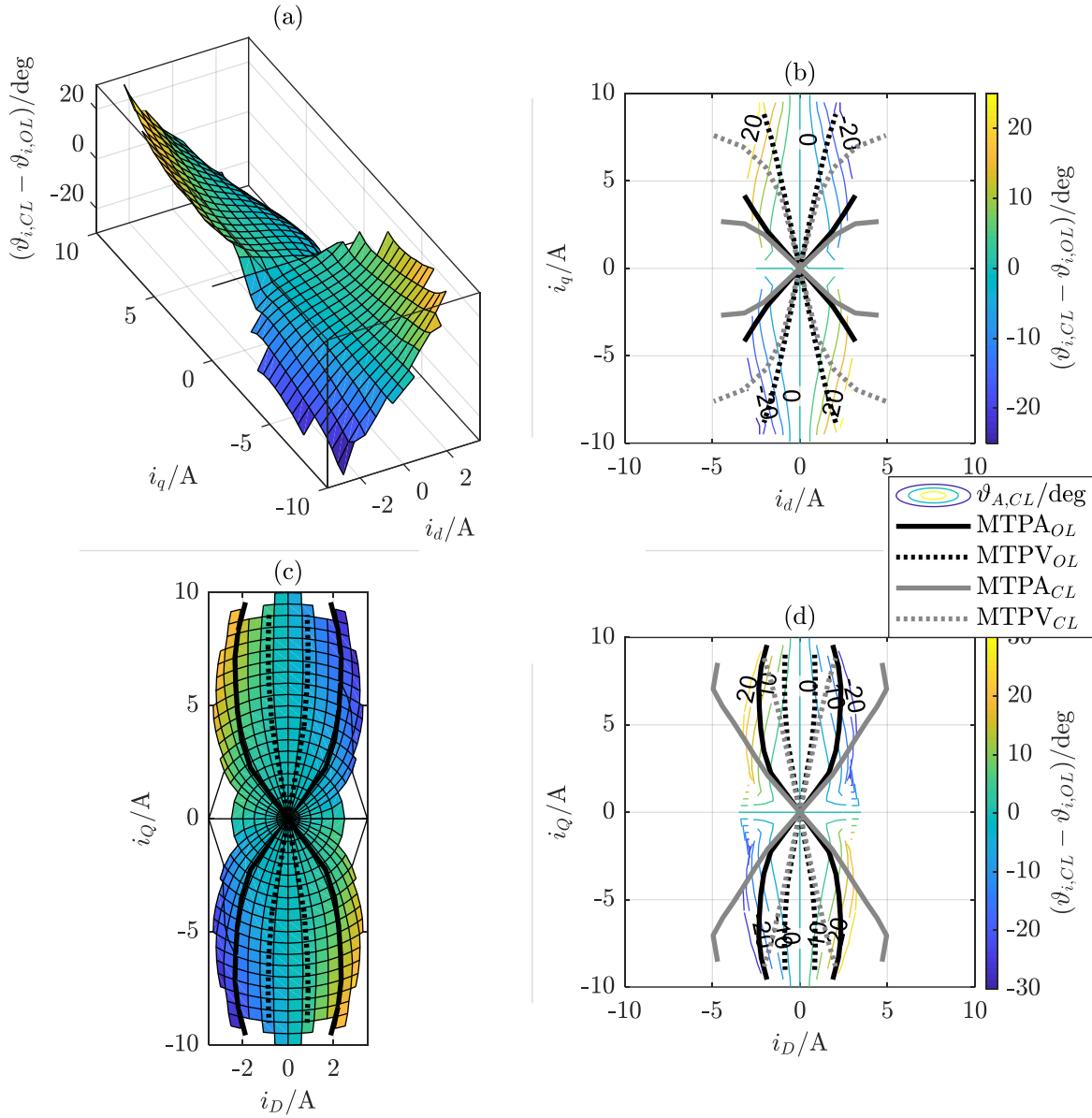


Figure 4.13: SynRM closed-loop control error plotted over stator current in dq plane with closed-loop (grey) and open-loop (black) MTPA and MTPV trajectories for reference

to control the analyzed SynRM in closed-loop mode in the complete measured region along both trajectories, if they are transformed into anisotropy coordinates, before applying them as references to the CL sensorless current controllers. In contrast to more sophisticated sensorless control schemes that take magnetic cross-saturation into account, no additional parameters are needed online in this approach<sup>10</sup>.

## 4.2 The Interior Permanent Magnet Synchronous Machine

### 4.2.1 The Relation between Magnetic Energy, Flux Linkage and Stator Current

Before starting the discussion of the IPMSM measurement results, we are addressing the general similarities and differences between this PM machine type and the formerly discussed PM free reluctance machines. Figure 4.14 exemplarily shows a comparison of the flux linkage maps of the SynRM from section 4.1 and a virtual IPMSM that has exactly the same design and material properties but additionally permanent magnets in the flux barriers.

The first point to note is that compared to the SynRM flux linkage maps presented in Figures 4.4 and 4.5, the maps here are rotated by 90°. This is necessary in order to account for the different definitions of  $d$ - and  $q$ -axis for PM and PM-free machines (cf. Figure 2.13 on page 26). The second point is that the origin of both flux linkage maps is shifted along the  $d$ -axis to the virtual magnetic origin of the machine, which was discussed in section 2.2.3.1.

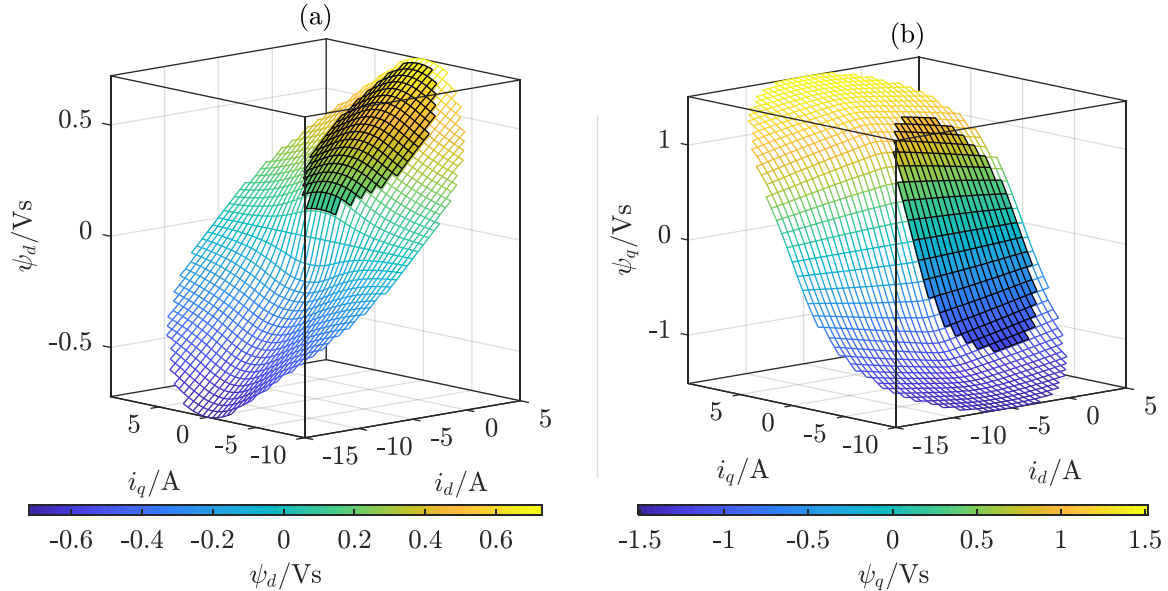


Figure 4.14: Hypothetical flux linkages plotted over stator currents in  $dq$  plane for imaginary machine based on SynRM (white filling) but with permanent magnets in the flux barriers; colored fillings show the feasible operating areas; (a):  $d$  axis flux linkage; (b):  $q$  axis flux linkage

<sup>10</sup> When assuming, that the trajectories are stored as lookup-tables for optimal current control in any case

Apart from those two modifications, i.e. a rotation and a parallel shift, the maps with white fillings are the same SynRM maps, as presented in the former section. In the given example,  $i_{PM}$  is chosen to 5A, which leads to a permanent magnetic flux linkage of  $\psi_{PM} = 0.469Vs$  at the point of zero stator currents.

When we now select an exemplary current limit of 4.9A, such that the given maps do not need to be extrapolated, we obtain the flux linkage maps of our virtual IPMSM. They are represented by the regions with colored fillings in Figure 4.14.

We see that the permanent magnet shifts the feasible operating area along the  $d$ -axis. The magnetic origin is not in the center of the maps anymore, and, as in this example, can even be outside of the feasible operating area. We can thus not expect IPMSM flux linkage maps to be point symmetric anymore. They should, however, still be symmetric to the  $d$ -axis.

With this hypothetical flux linkage maps in mind, we can now inspect the measured flux linkage maps from the real IPMSM, which was introduced in Table 3. Figure 4.15 shows the flux linkage map of the  $d$ -axis and Figure 4.16 that of the  $q$ -axis. In the 3D overviews in subfigures (a), we can generally find the forms that we expected from above hypothetical considerations.

Compared to the flux linkage curves of the SynRM, we can note only moderate magnetic saturation in both axes. The  $d$ -axis flux linkage is already beginning to saturate due to the permanent magnetic field without any stator currents. Along the  $q$ -axis, where  $i_d = 0$ , there is a noticeable cross-saturation effect on the  $d$ -axis flux linkage. This supports the statement from section 2.2.3.1, that PMSMs cannot be adequately modelled, when assuming constant  $\psi_{PM}$  and neglecting mutual absolute inductances (as done, for instance, in [75]).

In Figure 4.16 (b), we can see that the permanent magnet also causes noticeable cross saturation effects on the  $q$ -axis flux linkage. All curves of non-zero, constant  $q$ -currents show at least slightly reduced  $q$ -axis flux linkages at  $i_d = 0$ .

In Figure 4.15 (b), we see that the magnetic origin is outside the measured area. As shown by the black, dotted line, we extrapolated the  $d$ -axis flux linkage curve without cross-saturation (i.e. where  $i_q = 0$ ) to the virtual magnetic origin, i.e. to the point, where  $\psi_d = 0$ . This polynomial extrapolation leads to a PM equivalent current of  $i_{PM} = 15.8A$ , which is approximately 1.6 times the rated motor current.

The main qualitative difference between the measured maps and those from the hypothetical IPMSM that was derived from the SynRM measurements can be noted in the field-weakening region for  $d$ -axis currents smaller than  $-6A$ . In Figure 4.15 (b), for instance, the curves for non-zero  $q$ -currents lie above the zero-current curve. This means, that the  $d$ -axis flux linkage increases with increasing  $q$ -currents, which is thus corresponding to *magnetic cross-desaturation*, i.e. the opposite of what we would expect when reminding the explanation of cross-saturation in section 2.2.3.1 (see Figure 2.17 on page 35). The cross-desaturation is also observable in subfigure (c), when following the curves of constant  $d$ -currents  $< -6A$ , that lead to increasing flux linkage with increasing  $q$ -current. Figure 4.16 (b) does also show cross-desaturation, when, for constant  $q$ -currents, the  $q$ -axis flux linkage begins to slightly decrease with negative, decreasing  $d$ -currents.

The reason for that behavior can be found in the superposition of PM field and electromagnetic field. As it was already discussed in section 2.2.3.1, the magnetic field of negative  $d$ -currents interacts with the permanent magnetic field such that its field lines close within the rotor. For mechanical reasons, the flux barriers in the rotor are supported by bridges. Those bridges are typically highly saturated due to the permanent magnetic field. If an additional electromagnetic field is imposed to the rotor, the bridges can be partly desaturated. Of course, this local desaturation can occur at other highly saturated rotor regions, as well.

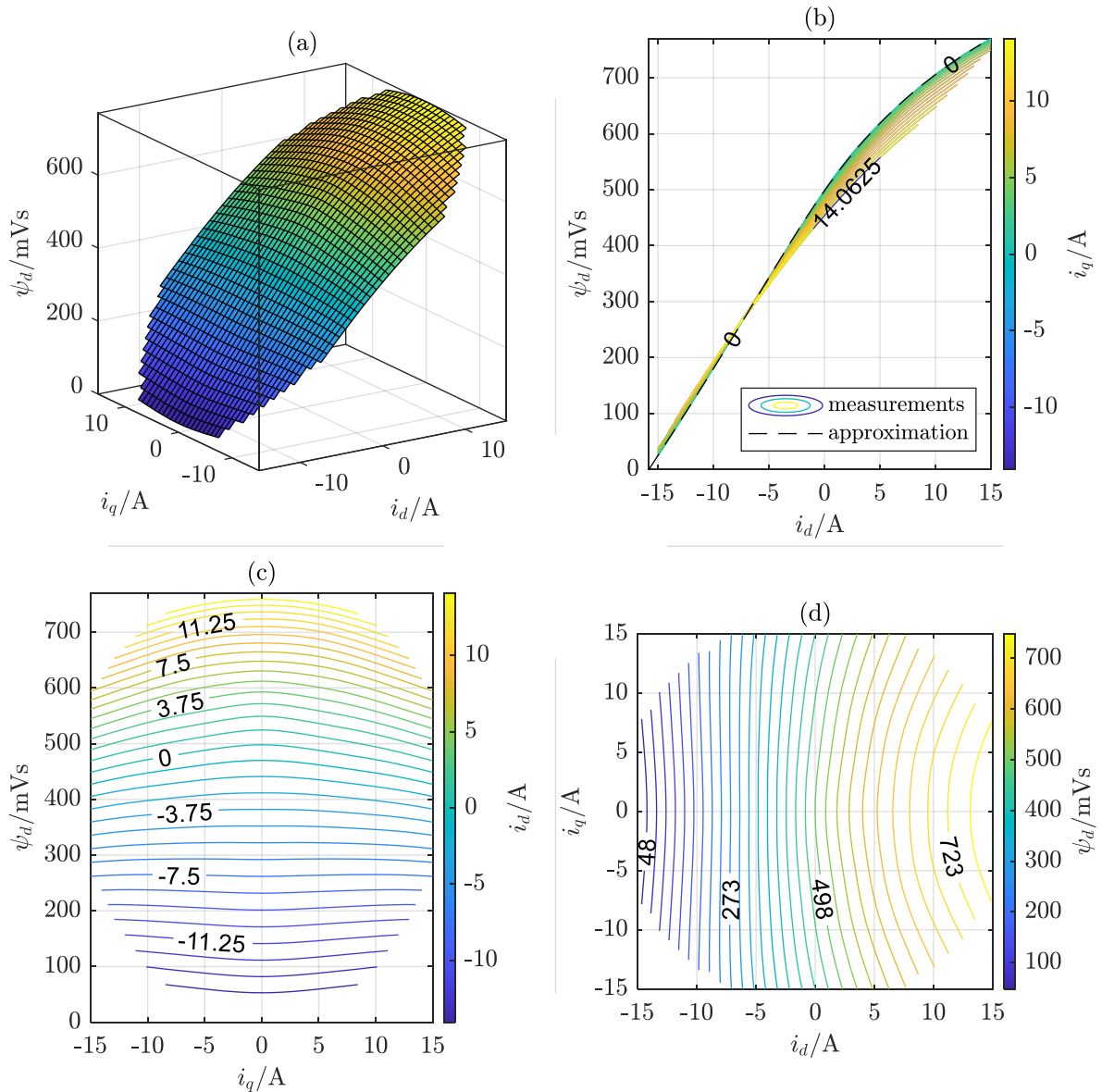


Figure 4.15: IPMSM  $d$ -axis flux linkage plotted over stator currents in  $dq$  plane; (a): 3D view of flux linkage surface, color represents flux linkage value, see color bar from (d); (b): corresponding  $xz$  contour plot; (c): corresponding  $yz$  contour plot; (d): corresponding  $xy$  contour plot

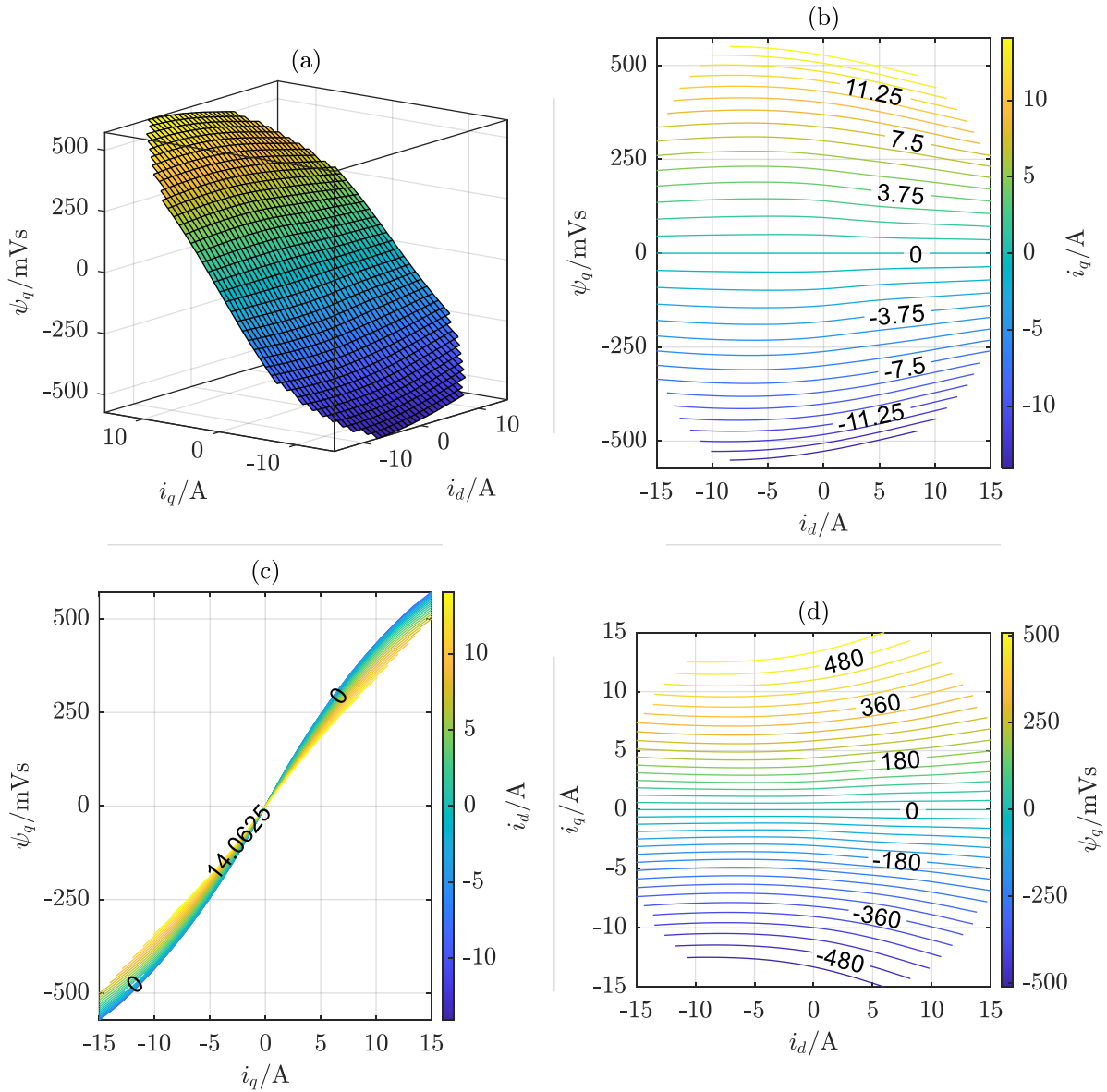


Figure 4.16: IPMSM  $q$ -axis flux linkage plotted over stator currents in  $dq$  plane; (a): 3D view of flux linkage surface, color represents flux linkage value, see color bar from (d); (b): corresponding  $xz$  contour plot; (c): corresponding  $yz$  contour plot; (d): corresponding  $xy$  contour plot

Without precise knowledge of the rotor geometry and material properties of the given IPMSM, it is difficult to further analyze the observed desaturation effects. A *finite element analysis* (FEA) would also extend the scope of this work. However, in [98], for instance, it is shown that the observed cross-demagnetization can also be analytically obtained for IPMSMs.

The magnetic co-energy scalar field together with the above flux linkages as vector field is shown in Figure 4.17. The co-energy is computed acc. to (2.88) (see page 41), i.e. in the definition with virtual magnetic origin, where the PM is represented by the above-mentioned equivalent current of  $i_{PM} = 15.8$ A. Although not within the measured area, we see that the

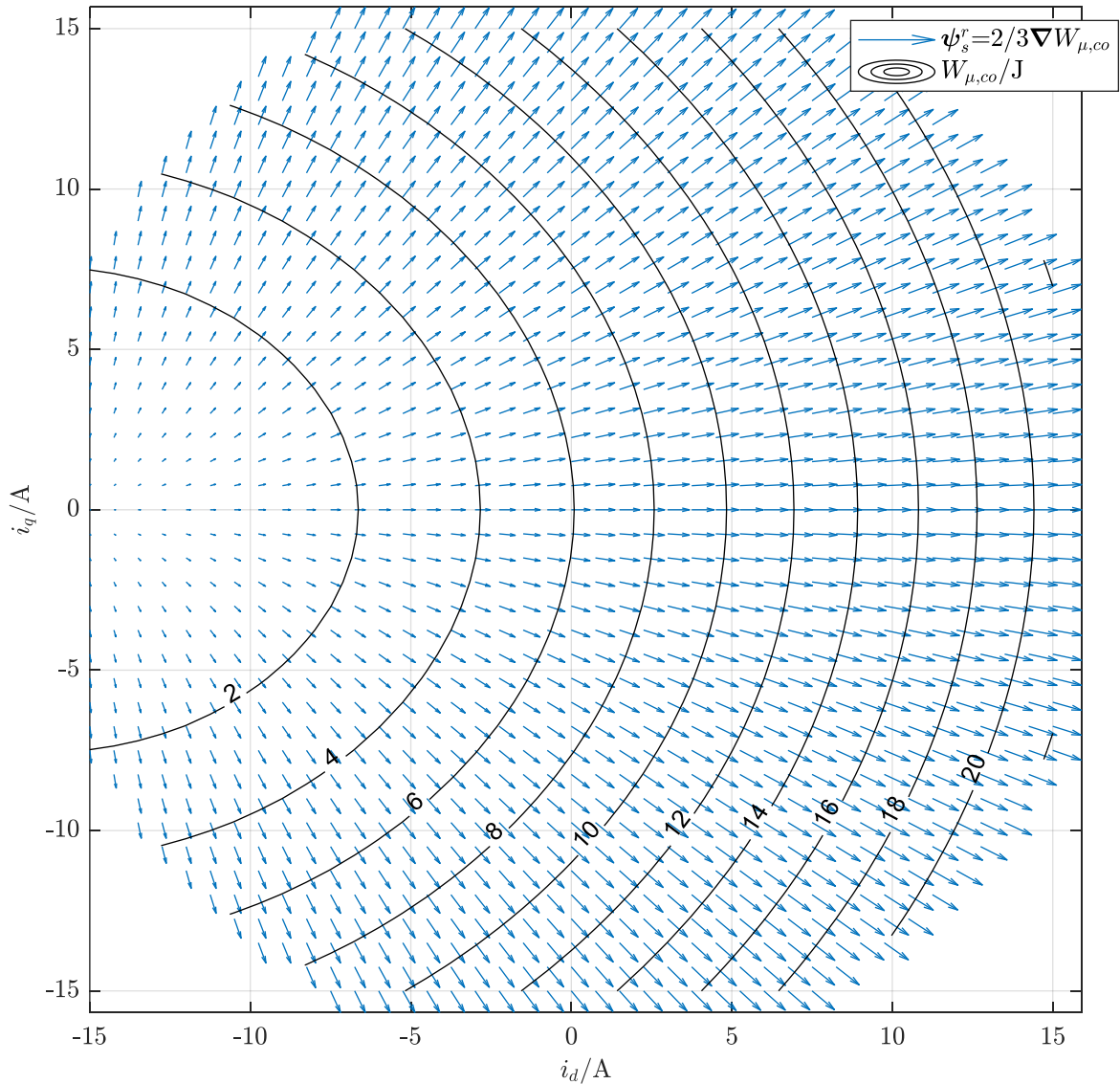


Figure 4.17: IPMSM flux linkage space vector field and the corresponding magnetic co-energy scalar field in the  $dq$  current plane

flux linkage vectors tend to zero towards the magnetic origin. We do also see the axial symmetry around the  $d$ -axis.

As discussed in section 2.2.3.2, the concept of virtual magnetic origin leads to overall non-negative co-energy fields. We can identify the co-energy associated with the permanent magnet to be approximately  $W_{\mu,co,PM} = 6\text{J}$ , since the corresponding curve passes through the point of zero current.

In the given form with virtual magnetic origin, we can ideally compare the IPMSM co-energy fields with those of the SynRM as presented in Figure 4.2. We can observe that the loci of constant co-energy of the IPMSM are less elliptic than those of the SynRM. This indicates less

magnetic anisotropy. Also, the major and minor axes are exchanged, which is a consequence of the different definitions of the  $d$ -axes for PM and PM-free synchronous machines.

### 4.2.2 Torque Generation, MTPA and MTPV

The torque produced by the IPMSM at different operating points can be calculated from the above flux linkage maps. The results are shown in Figure 4.18.

In contrast to the trajectories of the SynRM, the MTPA and MTPV trajectories of the IPMSM do not intersect at the point of zero torque. This would only be the case, if the MTPA strategy included the PM equivalent current into its optimization process. Then, both trajectories would intersect at the point of virtual magnetic origin. However, since the PM equivalent current is not associated with Ohmic losses, only the real stator currents are considered in the MTPA strategy. The corresponding trajectory thus has its origin at the point of zero stator current.

We see that the MTPA strategy requires increasing field weakening currents with increasing absolute torque values. This is a consequence of the combination of permanent magnetic and reluctance effects together with magnetic saturation.

In contrast to the PM equivalent current, the PM flux linkage can cause losses, namely iron losses in the stator yoke. The MTPV strategy thus aims at minimizing the overall flux linkage. Since the virtual magnetic origin is outside the measured area, the MTPV trajectory lies at the border of the measured area, where the flux linkages are minimal.

Under the aspect of energy efficiency and field-weakening at high rotor speeds, the relevant operating area of the IPMSM's stator currents and flux linkages lies between both trajectories.

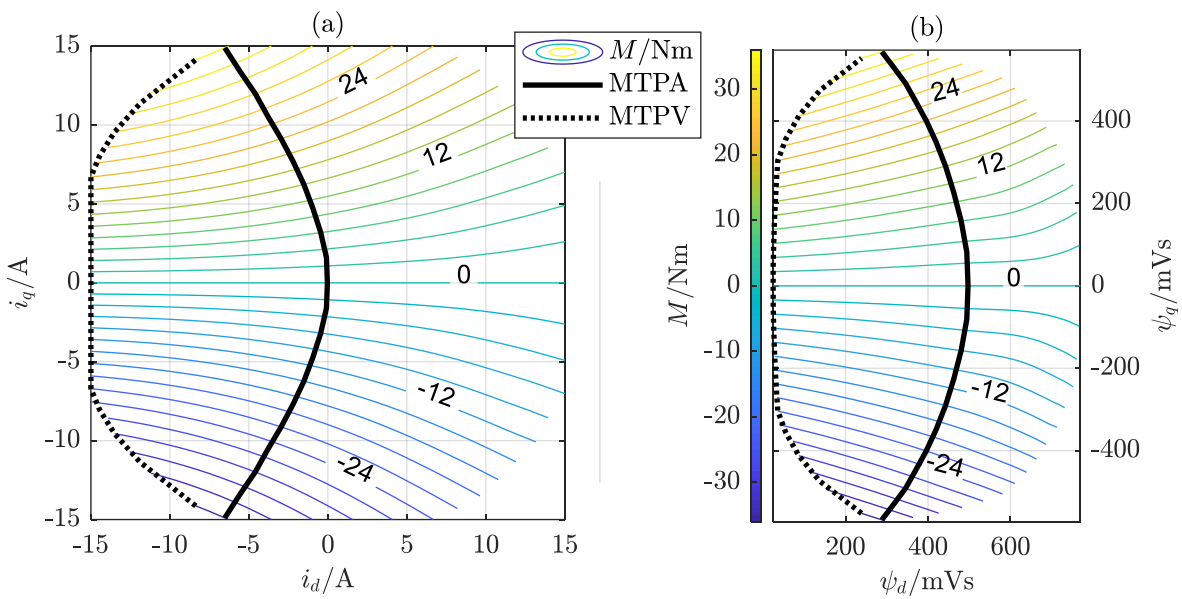


Figure 4.18: IPMSM torque contour lines plotted over stator currents (a) and flux linkage (b) in  $dq$  plane; legend and color bar are valid for both subfigures

### 4.2.3 Affine Model Parameters

In the exact same way as described in section 4.1.3 for the SynRM, the IPMSM inductances are determined from the flux linkage maps and presented in Figure 4.19. When starting from the origin of the stator currents, we can observe, that the main axes inductances,  $L_{dd}$  and  $L_{qq}$ , are desaturating with negative  $d$ -currents. This process can be explained by the active field weakening of the PM field. It does, however, not proceed towards the virtual magnetic origin, as we would expect it from the simplified model, where the PM field and stator field perfectly cancel each other out. Instead, we see that the  $d$ -axis begins to saturate again for  $d$ -currents smaller than  $-8\text{A}$ . In the  $q$ -axis, this effect sets in with  $i_d \leq -3.5\text{A}$ .

Again, identifying the exact reasons for that early saturation would require detailed finite element analysis and is thus out of scope of this work. It is, however, a clear indication that the superposition of permanent magnetic and electromagnetic fields leads to additional saturation in certain rotor regions and that this local saturation has a stronger influence on the overall flux linkage than the desaturation of other regions that were saturated from the PM field.

Another indication of the complex superposition of PM and opposed electromagnetic field is observable in the mutual inductance map. As expected, it is zero everywhere on the  $d$ -axis. In  $q$ -direction, however, the zero-locus progresses from approximately  $-3.75\text{A}$  on the  $d$ -axis towards  $\mathbf{i}_s^r = [-9\text{A} \quad \pm 12.75\text{A}]^T$ . Note again, that this curve should theoretically be parallel to the  $q$ -axis and intersect the  $d$ -axis at  $-i_{PM} = -15.8\text{A}$ . A more detailed analysis of this effect including FEA can be found in [99]. The region left from that locus is characterized by the magnetic cross-desaturation that was discussed in section 4.2.1.

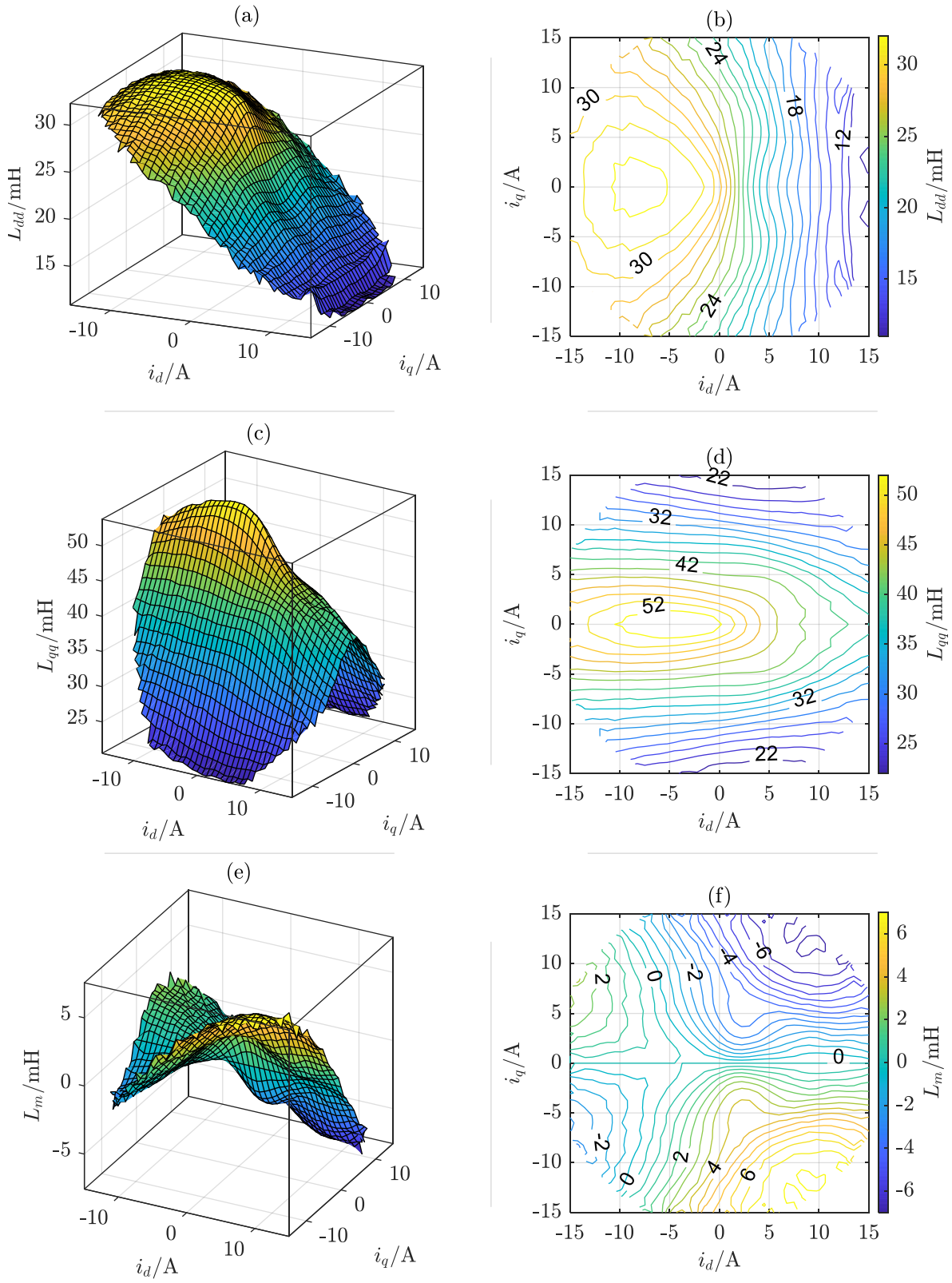


Figure 4.19: IPMSM inductances plotted over stator currents in  $dq$  plane; (a)&(b):  $d$  axis inductance; (c)&(d):  $q$  axis inductance (e)&(f): mutual inductance

Figure 4.20 shows the large-signal flux linkages depending on their stator current operating points for the affine machine model. They are computed acc. to (4.7) from the flux linkage maps and the inductance maps already presented above. Since those maps were already discussed in detail, we cannot reveal any new information about the magnetic characteristics of the IPMSM. The only thing worth noting here is the non-monotonic form of both maps, which highlights the non-linearity of the measured flux linkage maps.

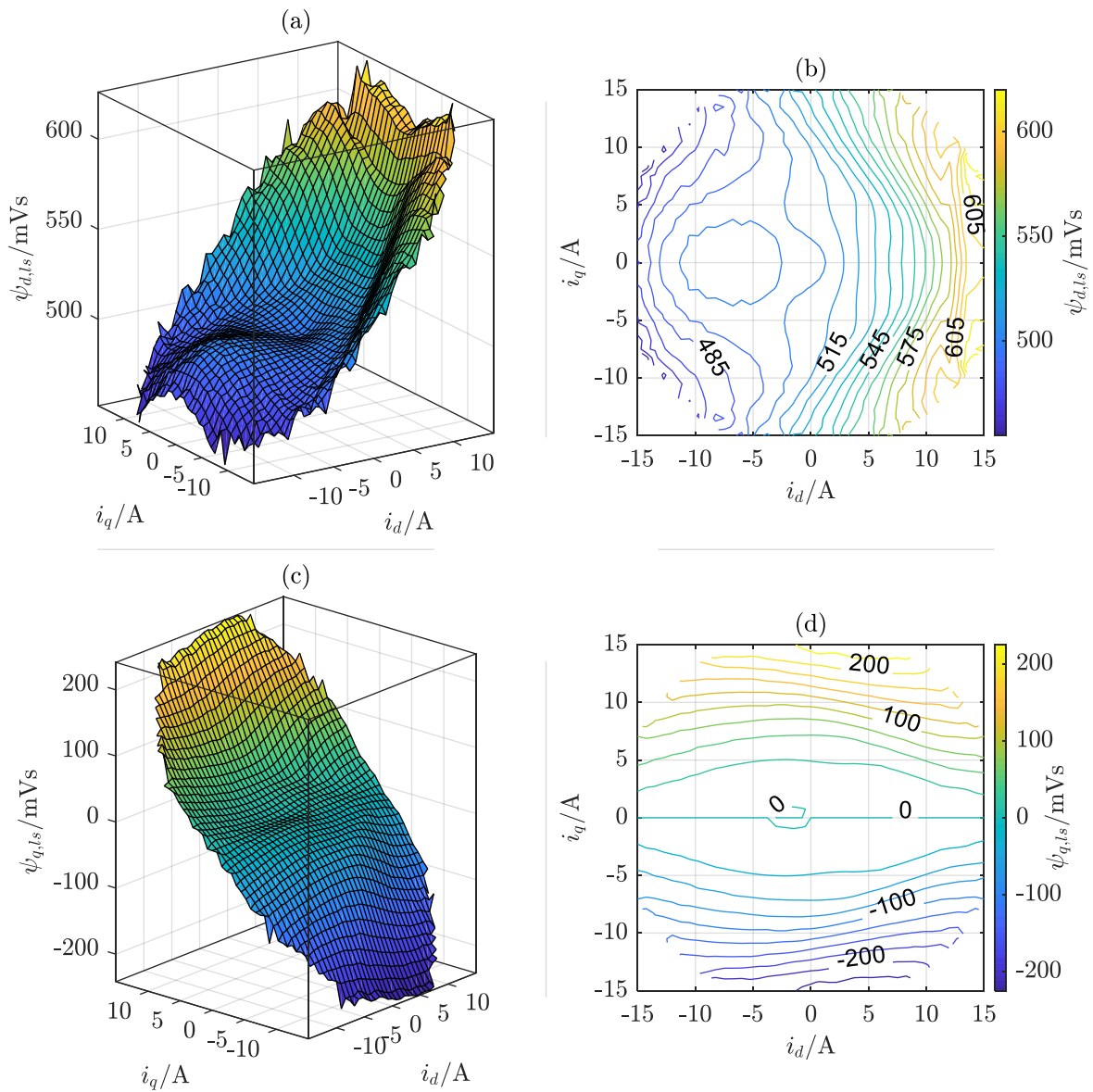


Figure 4.20: IPMSM large-signal flux linkages for linearized models plotted over stator currents in  $dq$  plane; (a)&(b):  $d$  axis flux linkage; (c)&(d):  $q$  axis flux linkage

#### 4.2.4 Characteristics for Sensorless Control

The important characteristics for anisotropy based sensorless control of the IPMSM are shown in Figure 4.21. We can observe that, in contrast to the SynRM results, the saliency ratio in subfigures (a) and (b) is always negative. This is a consequence of the different main axis definition between both machine types and is in accordance with the mathematical definitions in (2.119) (see page 47).

In wide regions, the absolute values of the saliency ratio are above 10%, which is generally sufficient for anisotropy based sensorless control. However, we can also identify two regions around  $\mathbf{i}_s^r = [-9A \quad \pm 12.75A]^T$ , where the saliency ratio approaches zero, i.e. points of magnetic isotropy. Since these regions are located in the relevant operating area between the MTPA and MTPV trajectories, we can predict problems in conventional sensorless control operation.

We already know these two points from the discussions of the inductance maps in the former section, where we identified the mutual inductances to be zero. We further know that the anisotropic inductance parameter,  $L_{A,\Delta}$ , will only be zero, if both,  $L_\Delta$  and  $L_m$ , are zero. Consequently, we see two zero-loci passing the above-mentioned points in subfigure (d). Similar to the SynRM results, the anisotropy position on those loci lies exactly between the  $d$ - and the  $q$ -axes, i.e. at  $\pm 45^\circ$ . This can be seen in subfigure (f).

The above-mentioned points, where the zero-loci of  $L_\Delta$  and  $L_m$  are intersecting, are thus characterized by no magnetic anisotropy and, in consequence, by an undefined anisotropy position. This is expressed by the discontinuities in  $\vartheta_A$ , where the values jump between  $\pm 90^\circ$ . Depending on the sign of  $L_m$  right next to the intersection on the zero- $L_\Delta$ -loci, a conventional anisotropy based position estimator would track the positive or negative  $q$ -axis instead of the actual positive  $d$ -axis.

Except for the discontinuity points, the zero-loci of  $L_m$  are identical with the zero-loci of  $\vartheta_A$ . Along a corresponding trajectory, a parameter-free anisotropy-based position observer would thus identify the correct rotor position. Since this trajectory lies within the relevant operating area between MTPA and MTPV trajectories, we can expect a comparably good sensorless control performance of the IPMSM as long as the absolute values of  $L_{A,\Delta}$  are sufficiently large to be reliably measured with the given current measurement system.

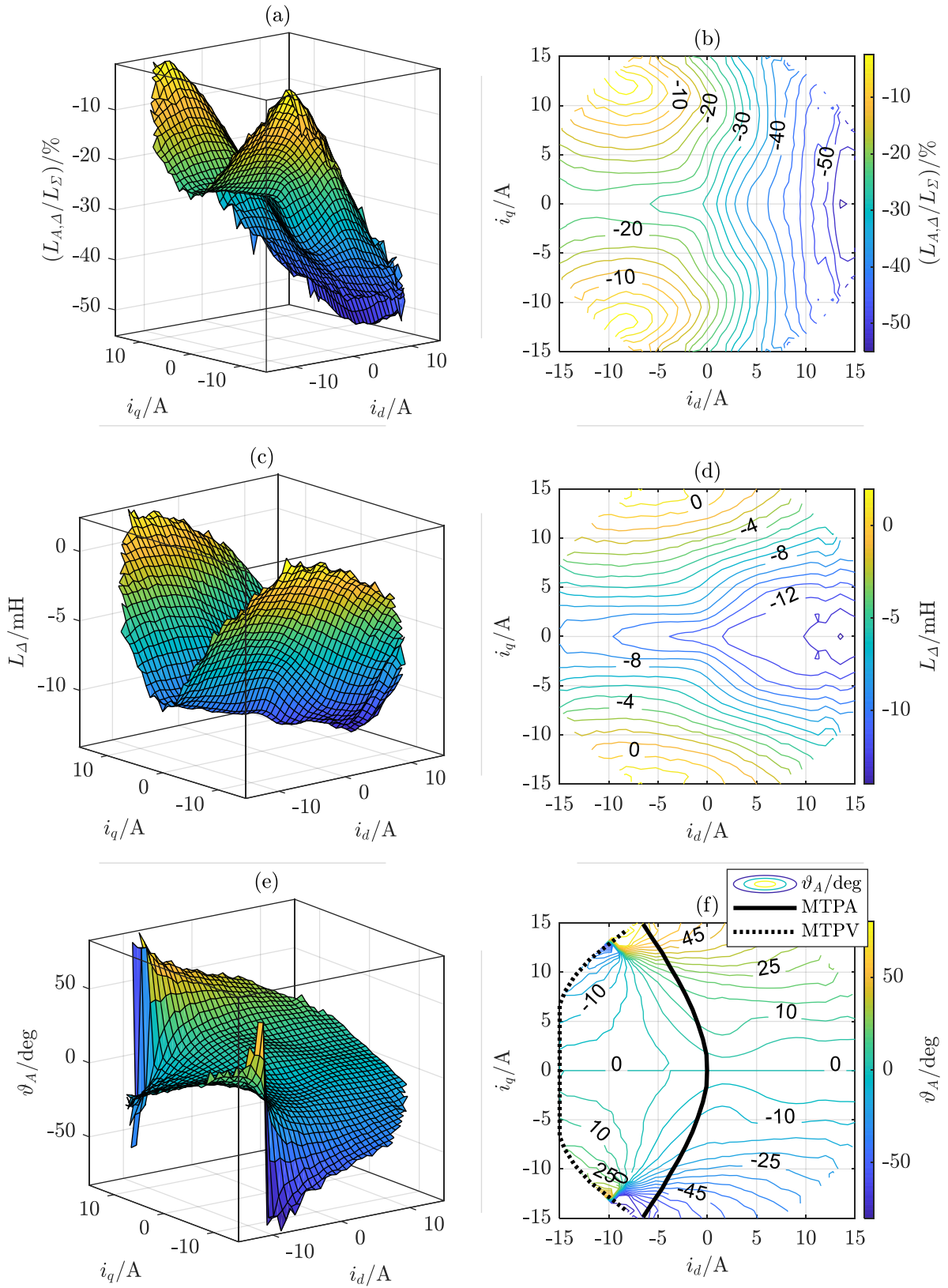


Figure 4.21: IPMSM anisotropy characteristics plotted over stator currents in  $dq$  plane; (a)&(b): saliency ratio; (c)&(d): half difference between  $d$  and  $q$  axis inductances; (e)&(f): angle difference between  $D$  and  $d$  axis, MTPA and MTPV trajectories for reference

The corresponding graphical stability analysis of the IPMSM in closed-loop sensorless control operation is shown in Figures 4.22 – 4.24. In Figure 4.22, we see that with increasing current amplitudes, the differences between open-loop reference current angle and the corresponding closed-loop current angle grow. The above-mentioned discontinuities in the anisotropy position are observable at current angles around  $\pm 125^\circ$ . Except for those discontinuities, we can find bijective assignments between OL and CL current angles, which fulfill the first condition for stable closed-loop operation acc. to (2.124) or (4.8).

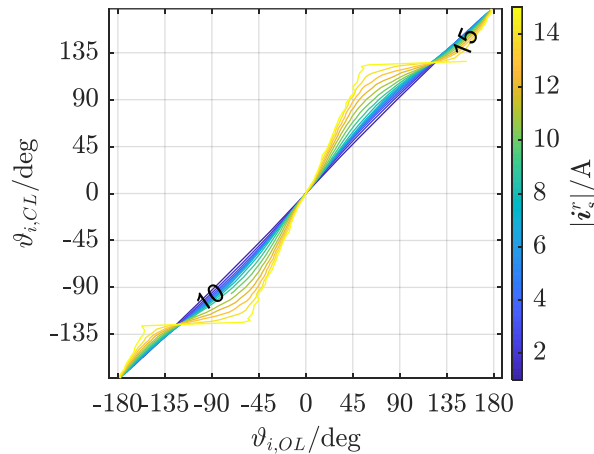


Figure 4.22: IPMSM potentially stable CL operating points plotted over OL stator current angle reference in rotor oriented coordinate system

The second stability condition acc. to (2.125) or (4.9) is analyzed in Figure 4.23 (b), again computed with a current angle difference of  $\pm 5^\circ$  in order to reduce the noise influence on the numerical differentiations. We can clearly see the discontinuities at  $\pm 125^\circ$ , which cause large negative values. In order to maintain a sufficient resolution in the continuous regions, the ordinate axis is limited to  $|\partial\vartheta_A/\partial\vartheta_i| \leq 1.25$ .

We can see that the angle derivate values are below one at all operating points. We have, however, to keep in mind that the discontinuities are characterized by  $\partial\vartheta_A/\partial\vartheta_i = \pm\infty$ . Furthermore, close to the discontinuity points, we do hardly have any anisotropy to detect (cf. Figure 4.21 (b)). We can thus conclude that the IPMSM is generally stable in sensorless closed-loop operation, except for the small regions around  $\mathbf{i}_s^r = [-9\text{A} \quad \pm 12.75\text{A}]^T$ , where the magnetic anisotropy becomes too small to be reliably detected.

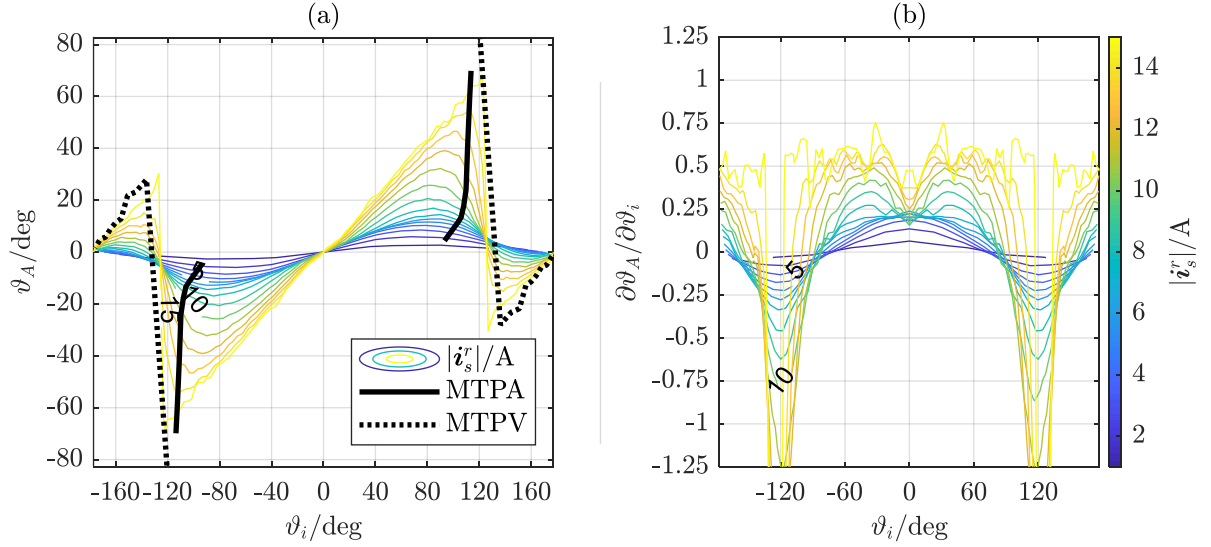


Figure 4.23: IPMSM anisotropy angle (a) and its derivative (b) plotted over stator current angle in rotor oriented coordinate system; color bar is valid for (a) and (b)

This statement is confirmed by iterative simulations, whose results are shown in Figure 4.24. Analogously to the CL analysis of the SynRM, the stable operating areas of the IPMSM in closed-loop sensorless operation are shown. In the above subfigures, we see the misalignment angles of the stator currents for the respective  $dq$  current references defined by the grid points.

It can be observed that wide regions of the measured area allow stable sensorless operation with errors of up to  $\pm 60^\circ$ . In the relevant regions on the left side of the MTPA trajectory, the errors remain between  $-15^\circ$  to  $+10^\circ$ . Along the black MTPA trajectory, the machine can be operated up to a reference current of approximately  $\mathbf{i}_{s,OL}^r = [-3.8 \quad \pm 10.5]^\top$ . The resulting real current trajectory in closed-loop operation is drawn in grey and arrives at approximately  $\mathbf{i}_{s,CL}^r = [-5.7 \quad \pm 9.7]^\top$ . From the computed torque data as shown in Figure 4.18, we can determine an effective torque reduction of 2.3% at these points.

The absolute torque that can be obtained with the “open-loop ( $dq$ ) reference strategy” lies within  $\pm 24.6\text{Nm}$ , or  $\pm 122\%$  of the rated torque. When the current references are transformed into anisotropy coordinates, the stable operating range can be extended to  $\pm 32.4\text{Nm}$ , which corresponds to  $\pm 160\%$  of the rated torque. This is indicated in Figure 4.24 (d) by the grey MTPA trajectory. In comparison to the black trajectory in (b), we can see that we obtain the desired MTPA behavior of the machine in closed-loop sensorless operation.

When considering the MTPA reference trajectory in anisotropy coordinates in (d), we see, how it is inflected towards the positive D-current plane. It thus remains right within the stable operating area, which leads to the observable extension of the stable closed-loop operation.

As it was done before with the SynRM, the transformed currents in subfigure (c) are shown in a polar grid in order to avoid overlapping of neighboring grid points and thus improve the clarity of presentation. It is worth noting, that the resulting reduction of resolution in the

border regions lead to the incorrect impression, that stable operating areas are smaller in (d) than in (b).

Note also, that the MTPV trajectory is not extended, when changing from the  $dq$  to the  $DQ$  reference strategy. This is due to the fact that the transformed  $DQ$  reference trajectory is inflected out of the measured area and we did not extrapolate it in the simulations. In practice, we can expect that the MTPV strategy in anisotropy coordinates is stable up to the regions with undetectably small magnetic anisotropy.

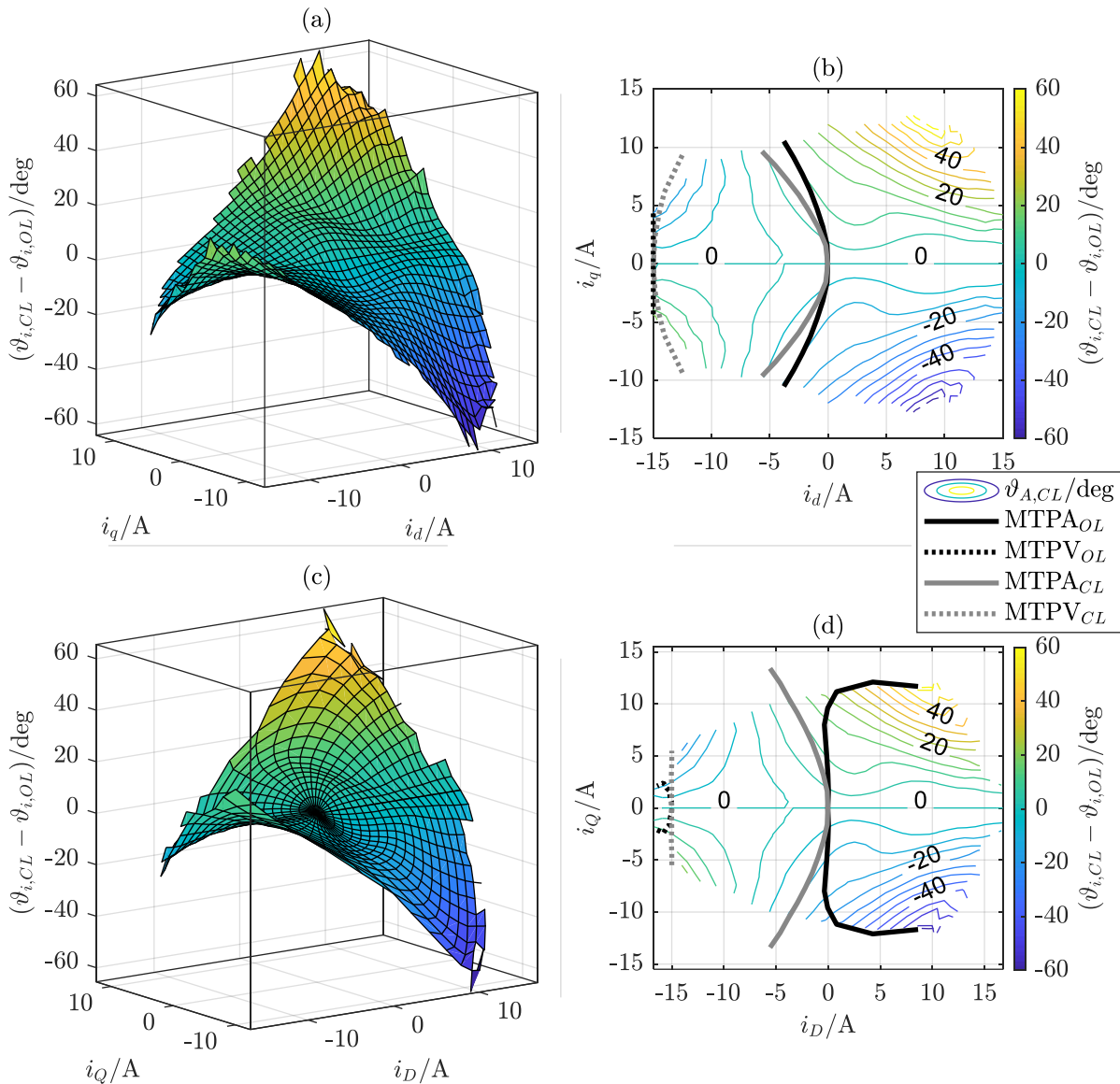


Figure 4.24: IPMSM closed-loop control error plotted over stator current in  $dq$  plane with MTPA and MTPV trajectories in contour plot (b)

### 4.3 The Surface Permanent Magnet Synchronous Machine

#### 4.3.1 The Relation between Magnetic Energy, Flux Linkage and Stator Current

Unlike IPMSMs, machines with surface permanent magnets usually do not have salient rotor geometries. As it was discussed in section 2.2.1, the permanent magnets have approximately the same permeability as air and do thus not lead to shape anisotropy. The only mechanism, that can cause magnetic anisotropy in the measurements, that are presented in this section, is magnetic pre-saturation caused by the permanent magnets in the  $d$ -axis field path.

This is visualized in Figure 4.25, where we averaged the SynRM flux linkage maps in both axes to eliminate any shape anisotropy. The maps with white fillings are the result. The colored fillings indicate the valid operational regions of that hypothetical SPMSM, when we assume again a PM equivalent current of  $i_{PM} = 5\text{A}$  and a current limit of  $4.9\text{A}$ .

We see that the resulting flux linkage maps are in their form qualitatively comparable to those of an IPMSM. We can expect stronger self-saturation in the  $d$ -axis and stronger cross-saturation in the  $q$ -axis for positive  $d$ -currents. The different levels of saturation in both axes will lead to the magnetic anisotropy, that will be observable in the measurements.

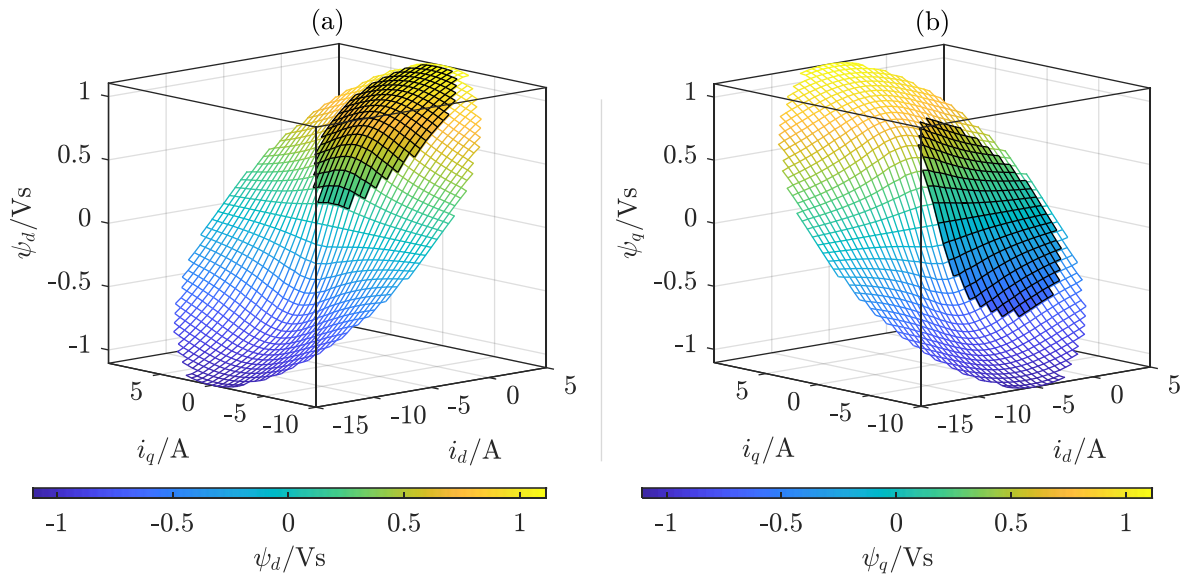


Figure 4.25: Hypothetical flux linkages plotted over stator currents in  $dq$  plane for imaginary machine based on averaged SynRM characteristics (white filling) but with surface mounted permanent magnets; colored fillings show the feasible operating areas; (a):  $d$  axis flux linkage; (b):  $q$  axis flux linkage

The actually measured flux linkage maps of the SPMSM, which is described in Table 3, are shown in Figures 4.26 and 4.27. Again, we can find the qualitative form of the measured maps in good accordance with the expectations from above considerations. In the measured region, the SPMSM is the least saturating of all three machines, which are evaluated in this work.

In Figure 4.26 (b), it is observable that the virtual magnetic origin is well outside the measured area. By means of polynomial extrapolation, we obtain a PM equivalent current of  $i_{PM} = 24.2\text{A}$ . The corresponding PM flux linkage at zero currents is  $\psi_{PM} = 235\text{mVs}$ , which is  $\sim 4\%$  higher than the value of  $226.3\text{mVs}$ , which was obtained from the manufacturer specifications. The most likely explanation for that deviation is, that the machine was measured at a lower PM temperature than the manufacturer specifications are valid for.

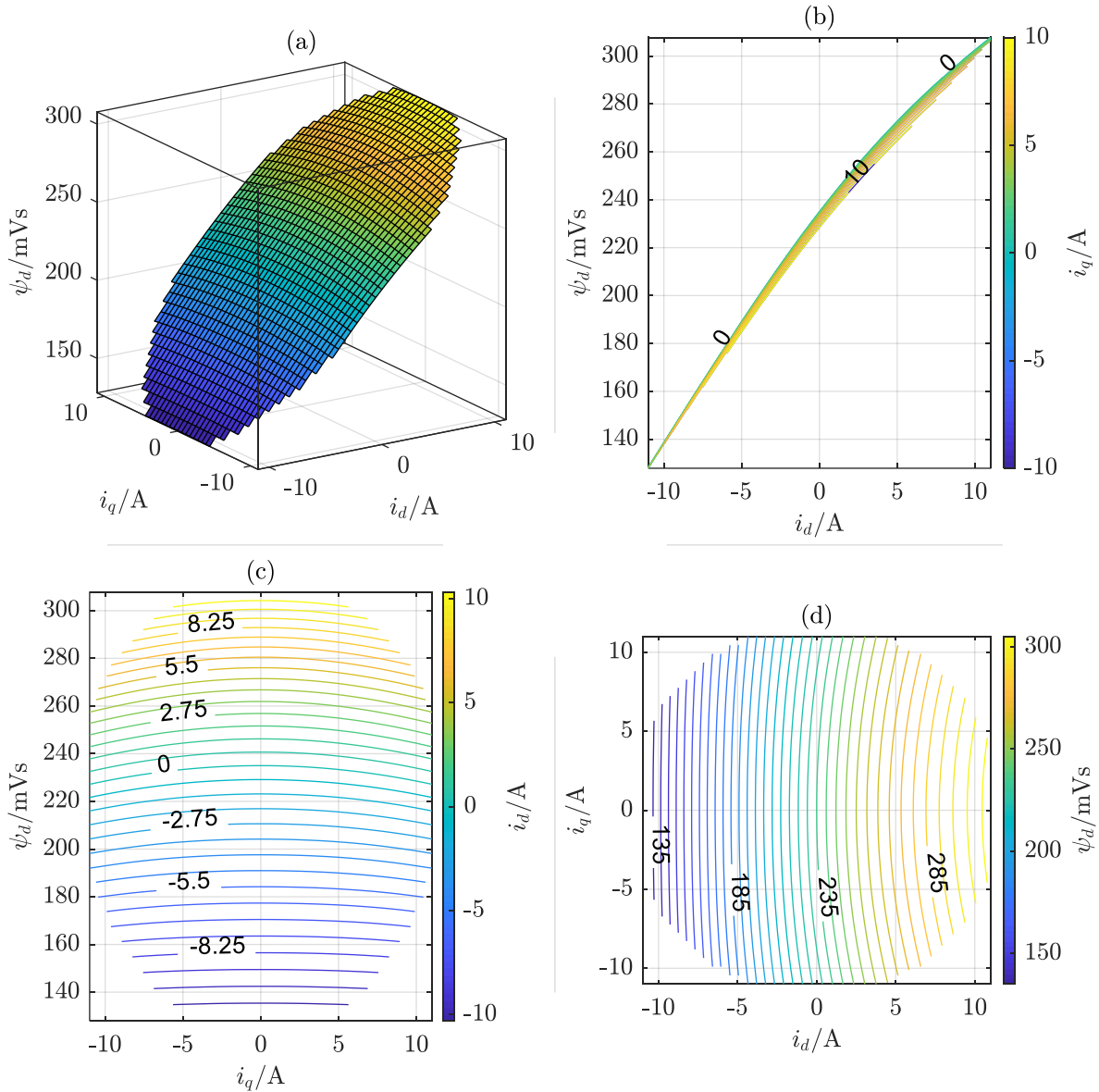


Figure 4.26: SPMSM  $d$ -axis flux linkage plotted over stator currents in  $dq$  plane; (a): 3D view of flux linkage surface, color represents flux linkage value, see color bar from (d); (b): corresponding  $xz$  contour plot; (c): corresponding  $yz$  contour plot; (d): corresponding  $xy$  contour plot

In contrast to the IPMSM flux linkage maps, we do not see any cross-demagnetization effects for negative  $d$ -currents. This indicates a more homogeneous saturation in the rotor iron, which is expectable due to the absence of flux barriers and associated bridges. We cannot state, however, that SPMSMs do not show demagnetization effects at all, since the presented measurements are not reaching as close to the magnetic origin as the IPMSM measurements do.

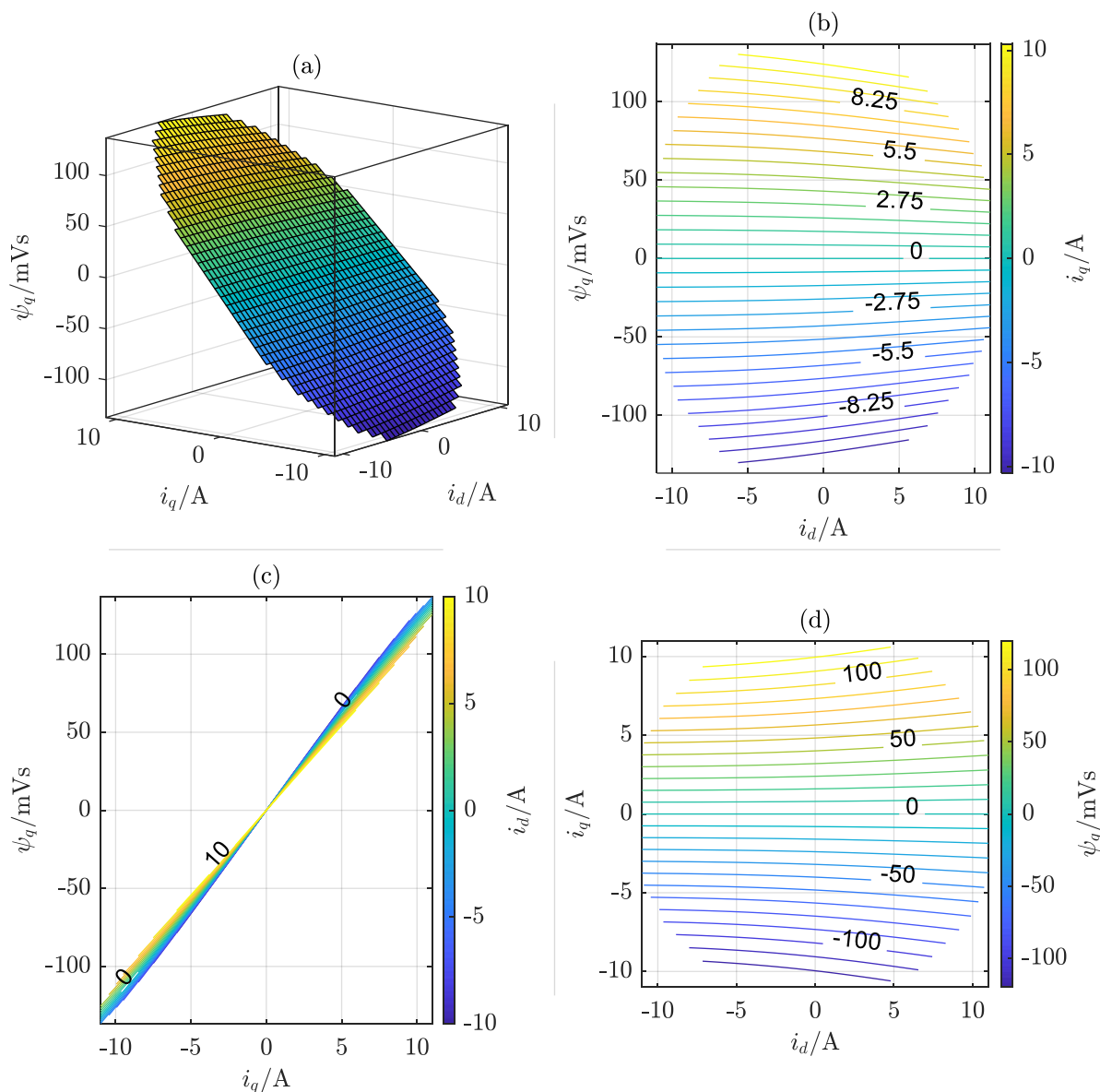


Figure 4.27: SPMSM  $q$ -axis flux linkage plotted over stator currents in  $dq$  plane; (a): 3D view of flux linkage surface, color represents flux linkage value, see color bar from (d); (b): corresponding  $xz$  contour plot; (c): corresponding  $yz$  contour plot; (d): corresponding  $xy$  contour plot

Figure 4.28 shows the magnetic co-energy of the SPMSM together with the flux linkages as vector field. Again, we only have positive co-energy values. The permanent magnet influence can be identified as approximately  $W_{\mu,co,PM} = 4.3\text{J}$ . As expected, the loci of constant co-energy are nearly circular.

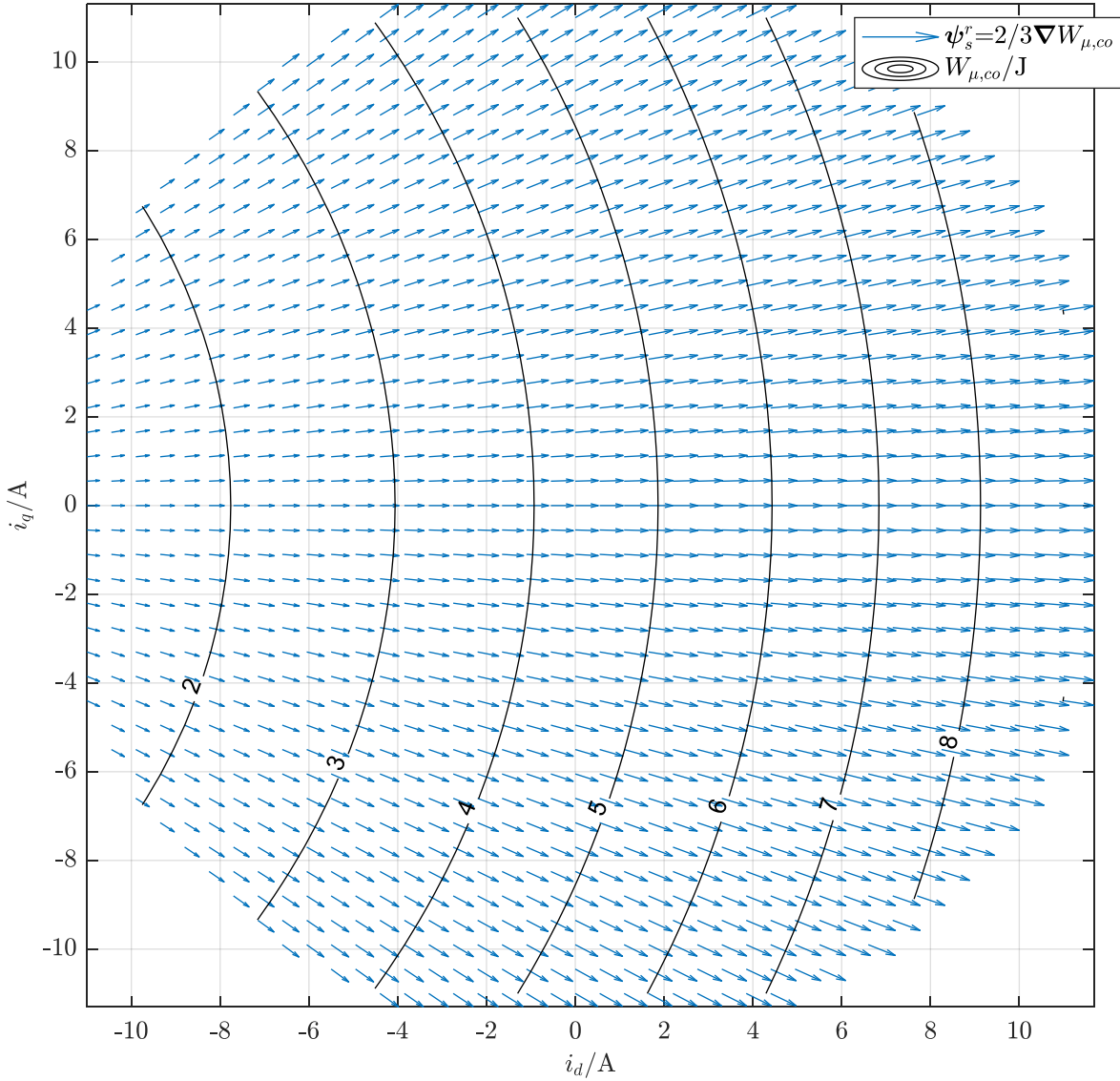


Figure 4.28: SPMSM flux linkage space vector field and the corresponding magnetic co-energy scalar field in the  $dq$  current plane

### 4.3.1 Torque Generation, MTPA and MTPV

The torque of the given SPMSM at different stator current and flux linkage operating points is shown in Figure 4.29. As expected, it qualitatively looks similar to the results from the IPMSM. The valid operating area in energy efficient control strategies is enclosed by the MTPA and MTPV trajectories.

The latter is located on the border of the measured area, where the flux linkages are minimal. Compared to the IPMSM, the MTPA strategy requires less field weakening, which results from the absence of shape anisotropy and the corresponding reluctance torque. Nevertheless, there is a reluctance torque component, which must be a consequence of the magnetic saturation caused by the permanent magnet. It is worth noting, that, in non-saturating machines, the MTPA would lie on the  $q$ -axis of the stator currents.

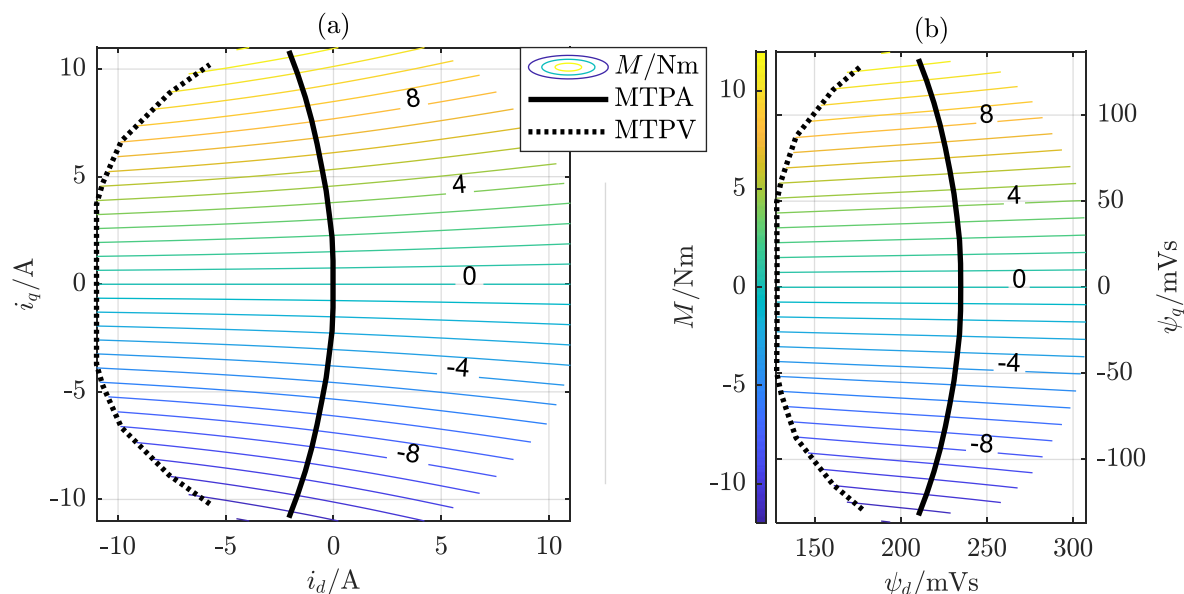


Figure 4.29: SPMSM torque contour lines plotted over stator currents (a) and flux linkage in  $dq$  plane; legend and color bar are valid for both subfigures

#### 4.3.2 Affine Model Parameters

The differential inductances obtained from above flux linkage maps of the SPMSM are shown in Figure 4.31. We can observe curve forms that are qualitatively comparable to those of the IPMSM. The most striking difference is that the desaturation process is not reversed within the field weakening area. Additionally, the mutual inductances in subfigure (f) do not show a vertical zero-locus, which corroborates the impression from the flux linkage maps, that no cross-demagnetization is present.

The fact that the inductance maps are slightly noisy results from the overall smaller flux linkage values in combination with the numerical differentiation.

We see that the superposition of PM field and positive  $d$ -axis stator current field causes the strongest saturation in the machine, since  $L_{dd}$  approximately halves its value compared to its maximum in the field-weakening region.

For  $L_{qq}$ , such a strong saturation is not observable. It is worth noting, that the minimal value of  $L_{qq}$  is larger than the maximum of  $L_{dd}$ , which is a consequence of the strong PM influence compared to the electromagnetic fields from the stator windings in the feasible operating area (note, that  $i_{PM}$  is around 2.7 times the rated current of the machine).

Figure 4.30 shows the large-signal flux linkages of the SPMSM. Compared to the IPMSM, we can note a large region for negative  $d$ -axis currents, where  $\psi_{q,ls} \approx 0$ . This indicates that the machine is nearly linear, here – at least in the  $q$ -axis.

Overall, we can expect this machine to be the least demanding in terms of sensorless control strategies. This statement is confirmed in the following section.

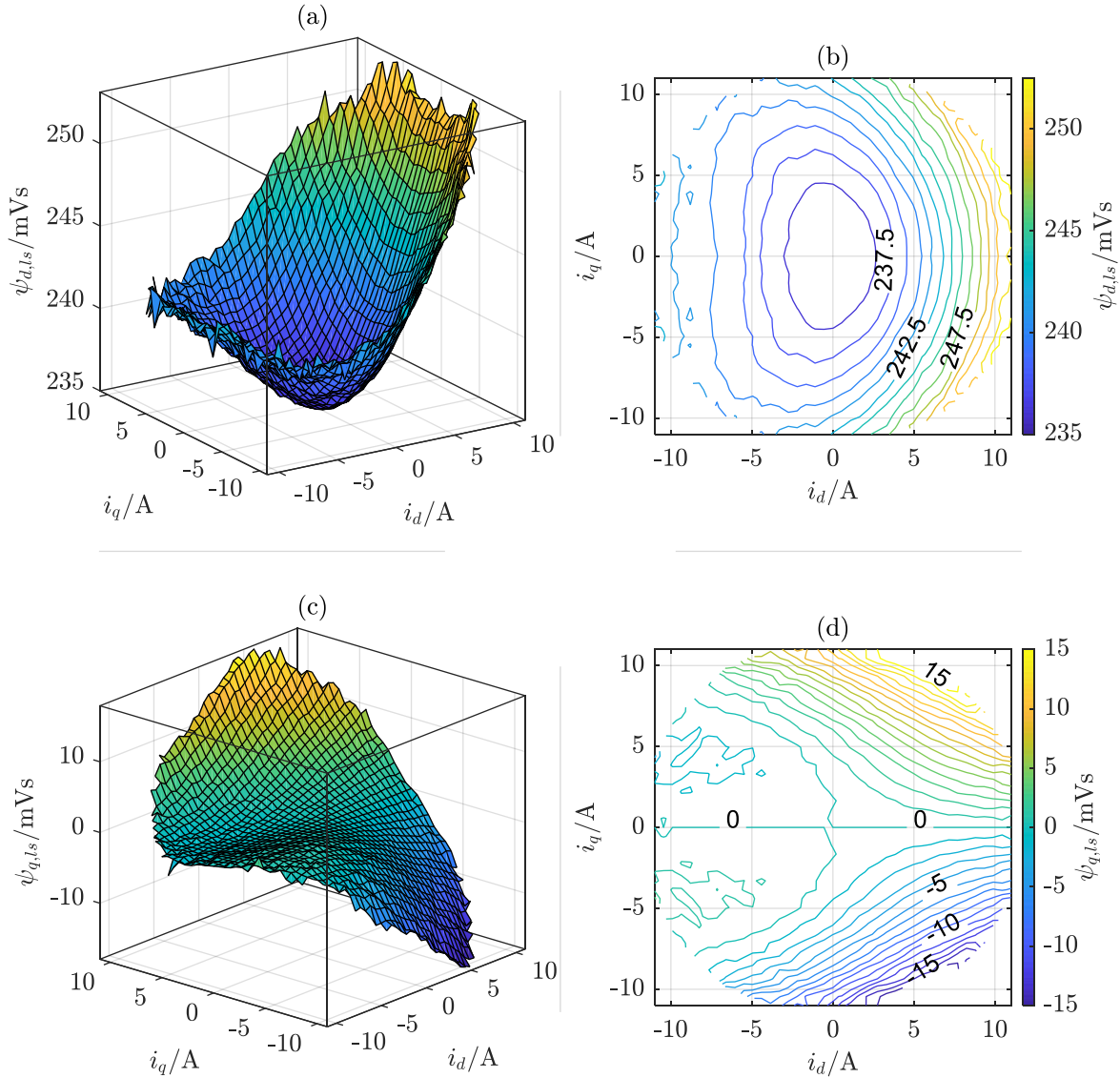


Figure 4.30: SPMSM large-signal flux linkages for linearized models plotted over stator currents in  $dq$  plane; (a)&(b):  $d$  axis flux linkage; (c)&(d):  $q$  axis flux linkage

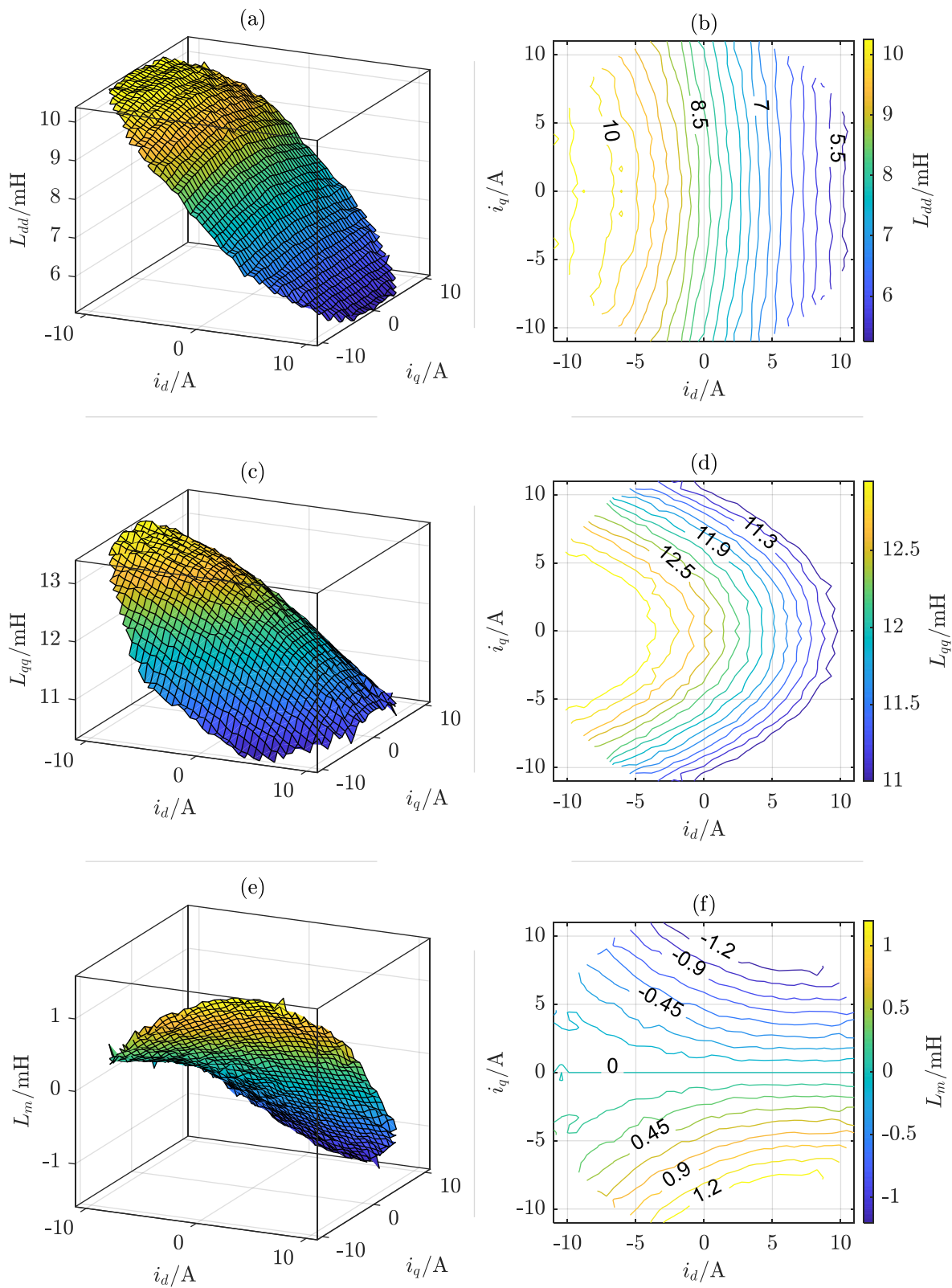


Figure 4.31: SPMSM inductances plotted over stator currents in  $dq$  plane; (a)&(b):  $d$  axis inductance; (c)&(d):  $q$  axis inductance (e)&(f): mutual inductance

### 4.3.3 Characteristics for Sensorless Control

The abovementioned fact that the  $q$ -axis inductance is larger than the  $d$ -axis inductance at any operating point can be observed in the anisotropy maps shown in Figure 4.33 (a) – (d). We can see that  $L_{\Delta}$  as well as the saliency ratio  $L_{\Delta,A}/L_{\Sigma}$  are always negative. In the measured region, there is no point, where the  $q$ -axis is more saturated than the  $d$ -axis. For that reason, we do not have the problem of insignificant anisotropy and, accordingly, do not have discontinuities in the anisotropy position as shown in subfigures (e) and (f).

We can generally say that with absolute values of the saliency ratio of more than 12% and anisotropy angles between  $\pm 20^\circ$ , the SPMSM does not show any challenges for anisotropy-based sensorless control.

Figure 4.32 confirms, that the machine is not demanding in closed-loop sensorless control operation. We see that the relation between open-loop and closed-loop current angles is nearly linear and always bijective. Condition one for stable CL control acc. to (4.8) is thus always fulfilled.

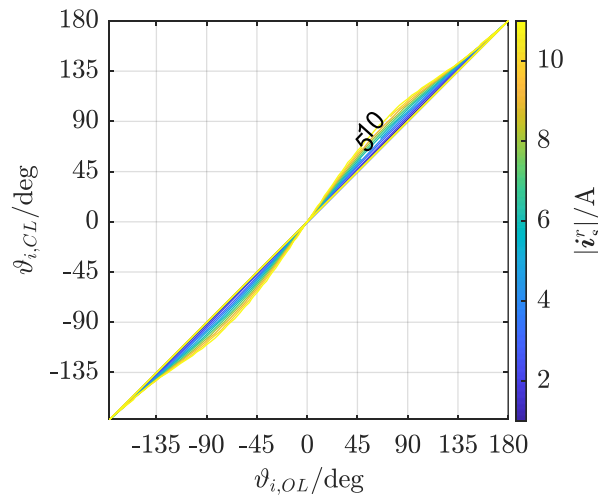


Figure 4.32: SPMSM potentially stable CL operating points plotted over OL stator current angle reference in rotor oriented coordinate system

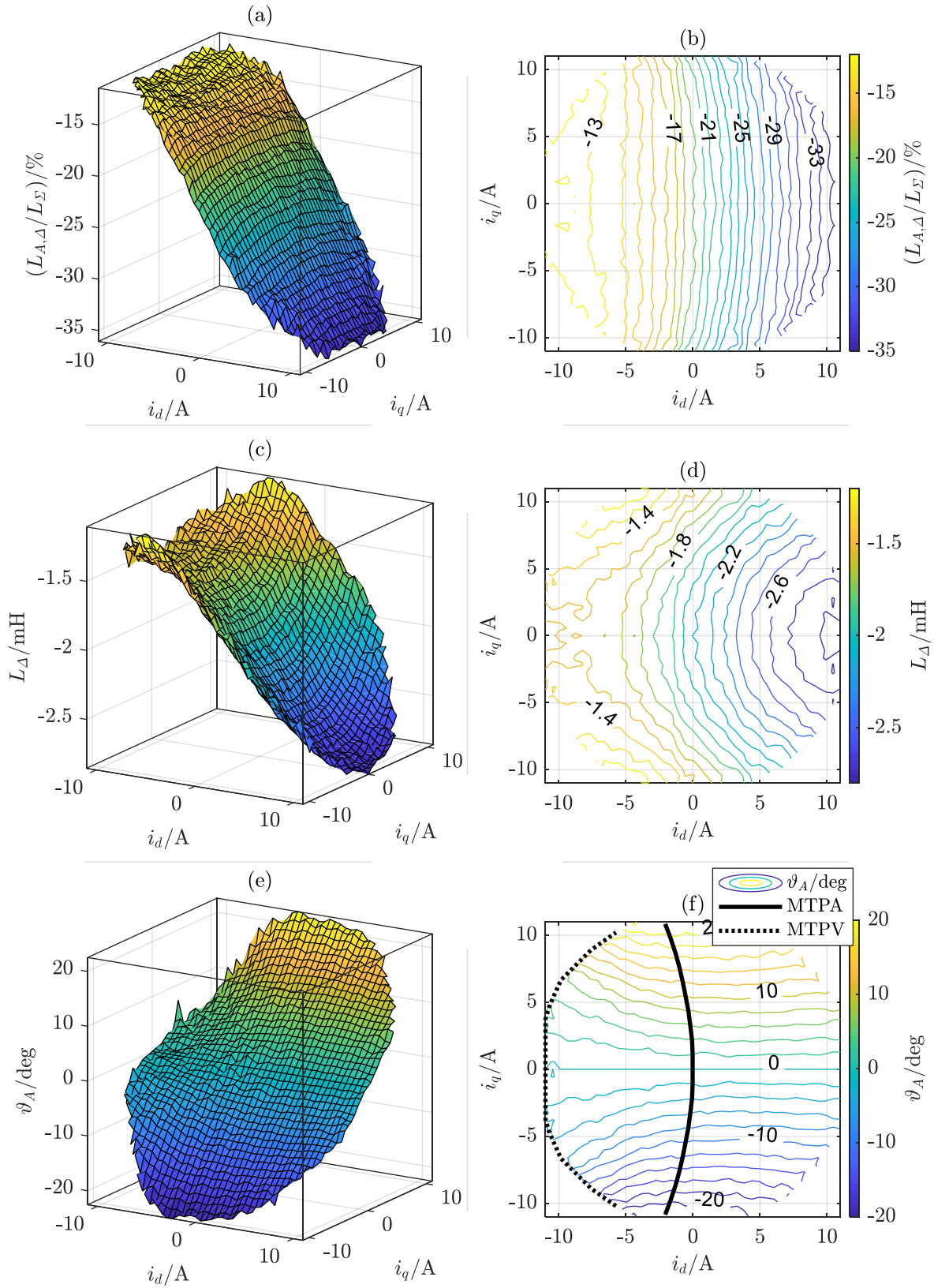


Figure 4.33: SPMSM anisotropy characteristics plotted over stator currents in  $dq$  plane; (a)&(b): saliency ratio; (c)&(d): half difference between  $d$  and  $q$  axis inductances; (e)&(f): angle difference between  $D$  and  $d$  axis, MTPA and MTPV trajectories for reference

Condition two acc. to (4.9) is analyzed in Figure 4.34. Except for the already discussed noise in the signals, we can observe comparably smooth curve forms in (a), leading to angle derivate values between  $-0.5$  and  $0.4$ .

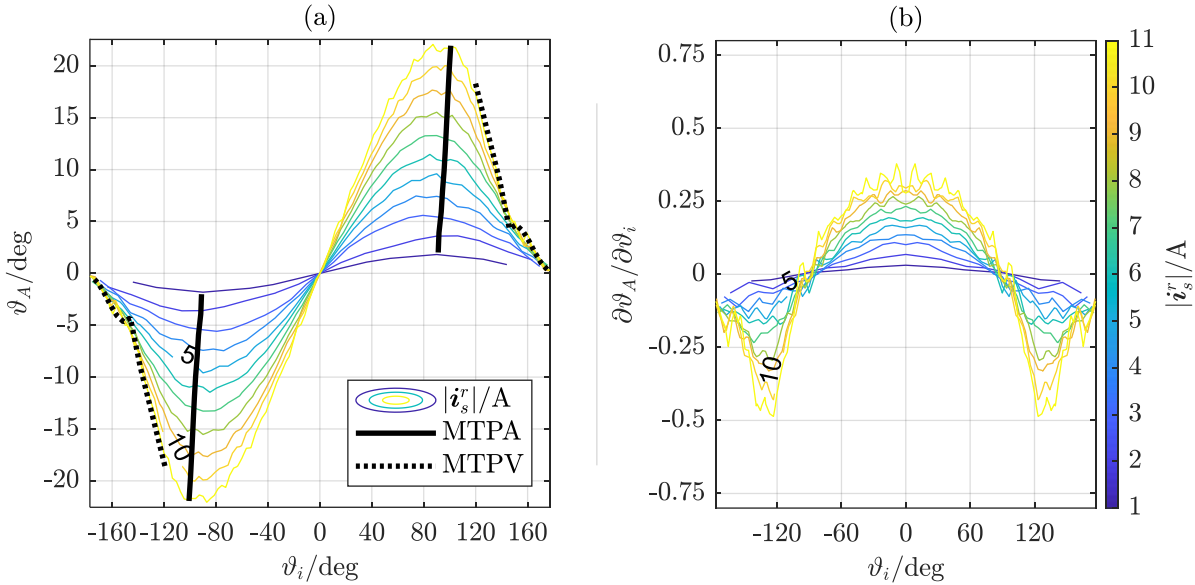


Figure 4.34: SPMSM anisotropy angle (a) and its derivative (b) plotted over stator current angle in rotor oriented coordinate system; color bar is valid for (a) and (b)

Overall, the SPMSM fulfills all conditions for stable closed-loop control in anisotropy-based sensorless control schemes. This is confirmed by simulations, whose results are presented in Figure 4.35. We can observe that all operating points in the measured region are stable. It is worth noting again, that the noise in the border regions leads to bad extrapolation results and thus causes some operating points to be falsely identified as instable.

The main difference between the  $dq$  and the  $DQ$  reference strategies can be observed in the MTPA trajectories in CL operation. As discussed before, the black reference trajectory in open-loop rotor coordinates leads to a non-optimal CL trajectory (grey) in subfigure (b).

Within the measured area, torques of up to  $\pm 11.5 \text{ Nm}$  are possible in MTPA control, which corresponds to approximately 131% of the rated machine torque of  $8.8 \text{ Nm}$ . The suboptimal CL trajectory in subfigure (b) results in maximal torques of around  $\pm 10.9 \text{ Nm}$ , or an effective torque reduction of 5.3%. This efficiency reduction can be avoided, when transforming the reference trajectories in anisotropy coordinates. As shown in subfigure (d), the resulting CL trajectories are identical to the original MTPA and MTPV trajectories (cf. the black trajectories in (b)).

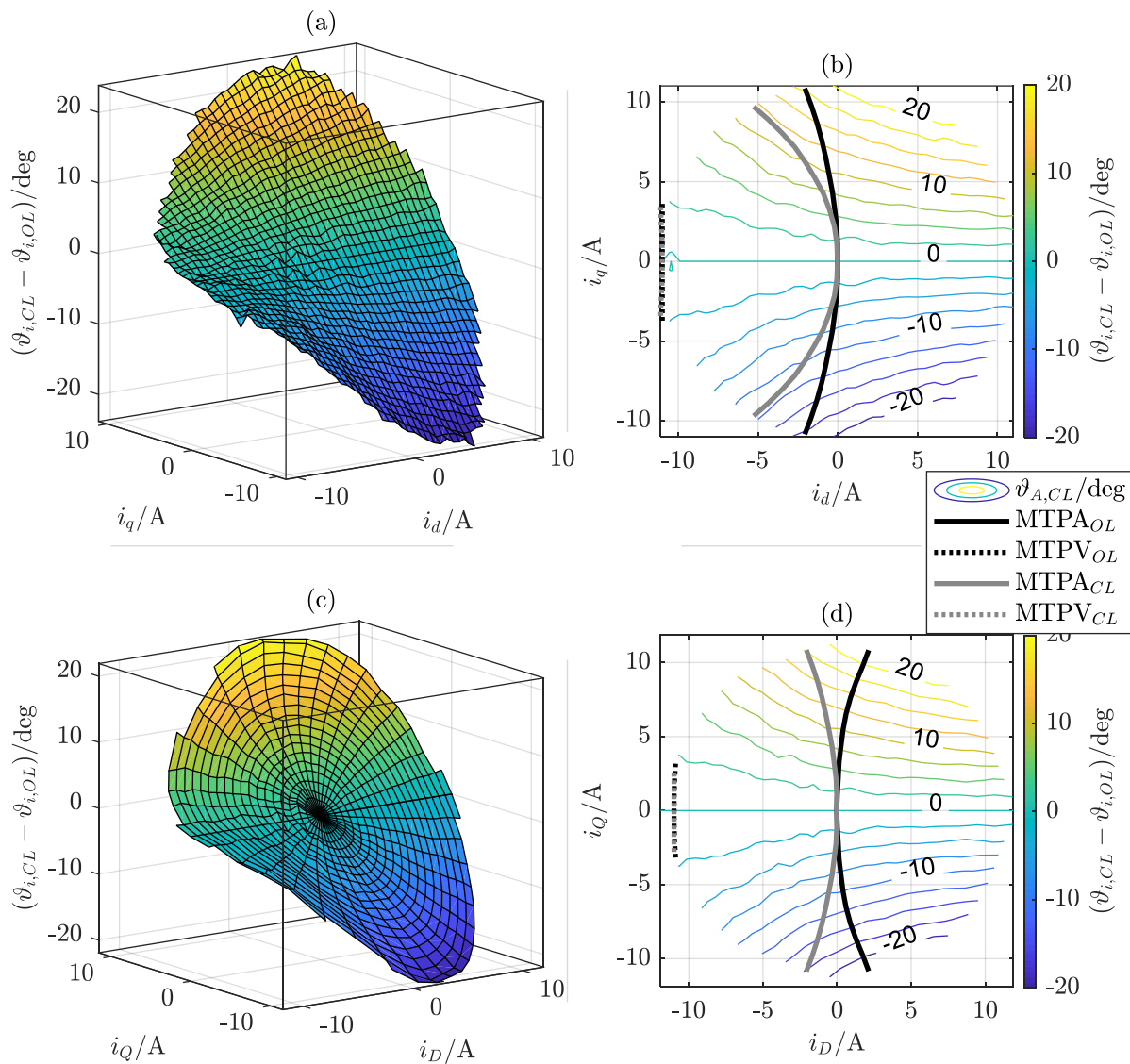


Figure 4.35: SPMSM closed-loop control error plotted over stator current in dq plane with MTPA and MTPV trajectories in contour plot (b)



# CHAPTER 5

---

## Optimizing Measured Inductance Maps

---

Before in the following chapter measurement schemes for inductance and flux linkage maps are presented, discussed and results are shown, this chapter addresses a possibility to refine the measurement results. The outcomes of these refinement processes are already shown and discussed in Chapter 4. Also, in Chapter 6 the measurement results are compared to the refined results in order to analyze different sources of error in the proposed measurement schemes. This chapter is therefore limited to describing the theory of proposed optimization processes.

### 5.1 Motivation

---

When measuring the magnetic characteristics of synchronous machines, we have to deal with errors. We can generally distinguish between two types of errors – random errors and systematic errors. While random errors can typically be averaged out for a sufficiently large number of repeated measurements at a given operating point, systematic errors are more difficult to eliminate. In Chapter 6, it is pointed out that different measurement techniques are prone to different types of systematic errors, such as voltage errors, harmonic distortions or iron effects, for instance. The basic idea of this chapter is to develop a generic methodology to minimize systematic errors as good as possible without having to deal with the individual sources of errors.

We make use of two basic principles that allow to identify systematic errors: *symmetry considerations* and *physical laws*. Both lead to hard constraints on inductance, flux linkage and magnetic co-energy maps. The following section discusses the concrete mathematical expressions of these constraints and in section 5.3, an algorithm is proposed, that enforces these constraints on the measured maps and by that way allows to eliminate systematic errors violating these constraints.

## 5.2 Symmetry and Physical Constraints

---

### 5.2.1 Symmetry Considerations

As it was discussed in the introduction of synchronous machines in section 2.2.1, they are constructed rotationally symmetric. This symmetry must be observable in the magnetic characteristics, as well.

In section 2.2.3, we defined the point of magnetic origin, where no magnetic energy and co-energy is observable from the stator windings. It was given by

$$\boldsymbol{\psi}_{s,0}^r = \begin{bmatrix} 0 \\ 0 \end{bmatrix}, \quad (5.1)$$

$$\boldsymbol{i}_{s,0}^r = \begin{bmatrix} -i_{PM} \\ 0 \end{bmatrix} \quad (5.2)$$

and

$$W_{\mu} |_{\boldsymbol{\psi}_{s,0}^r} = W_{\mu,co} |_{\boldsymbol{i}_{s,0}^r} = 0. \quad (5.3)$$

In Chapter 4, where the measurement results of a SynRM, an IPMSM and an SPMSM were presented, it was discussed already, that the magnetic energy and co-energy fields are symmetrical to that point<sup>11</sup>.

With respect to this symmetry point as defined by (5.1) to (5.3), we can now determine a set of symmetry constraints for the magnetic characteristics of SMs.

As discussed in Chapter 4, we can express the magnetic characteristics of synchronous machines in various ways. When starting from an energetic point of view, it is useful to describe the magnetic energy as a scalar field in the flux linkage space vector plane, and to consider the magnetic co-energy in a stator current space vector plane, respectively.

As done before, we focus on the magnetic co-energy in a current plane, since the latter are directly measured. Note, however, that the following considerations are valid analogously for the magnetic energy in the flux linkage plane.

Since the stator can be assumed to be magnetically isotropic, we describe all quantities in rotor reference frames. In this case, the point symmetry towards the magnetic origin leads to two perpendicular symmetry axes. They are parallel to the  $d$ - and  $q$ - axes of the rotor reference frame and intersect at the point of magnetic origin.

Mathematically, we can express the energetic symmetry as

$$W_{\mu,co} |_{[i_d \ i_q]^T} = W_{\mu,co} |_{[i_d \ -i_q]^T}, \quad (a) \quad (5.4)$$

$$W_{\mu,co} |_{[i_d+i_{PM} \ i_q]^T} = W_{\mu,co} |_{[-i_d-i_{PM} \ i_q]^T}, \quad (b)$$

---

<sup>11</sup> When neglecting local desaturation processes in PMSMs. For the purposes of this thesis, where the PMSMs are not weakened to negative  $d$ -axis flux linkages within the measured current regions, this simplification is valid.

With the given relations between magnetic co-energy, stator current and flux linkage acc. to the gradient equation (2.91), we can directly derive the symmetry constraints for the stator current and flux linkage vector fields from (5.4) as

$$\begin{aligned}
 \psi_d|_{[i_d \ i_q]^T} &= \psi_d|_{[i_d \ -i_q]^T}, & (a) \\
 \psi_d|_{[i_d+i_{PM} \ i_q]^T} &= -\psi_d|_{[-i_d-i_{PM} \ i_q]^T}, & (b) \\
 \psi_q|_{[i_d \ i_q]^T} &= -\psi_q|_{[i_d \ -i_q]^T}, & (c) \\
 \psi_q|_{[i_d+i_{PM} \ i_q]^T} &= \psi_q|_{[-i_d-i_{PM} \ i_q]^T}. & (d)
 \end{aligned} \tag{5.5}$$

In the same manner, we can find the symmetry constraints for the inductances by determining the partial derivatives of (5.5) acc. to (2.66). We then obtain

$$\begin{aligned}
 L_{dd}|_{[i_d \ i_q]^T} &= L_{dd}|_{[i_d \ -i_q]^T}, & (a) \\
 L_{dd}|_{[i_d+i_{PM} \ i_q]^T} &= L_{dd}|_{[-i_d-i_{PM} \ i_q]^T}, & (b) \\
 L_{qq}|_{[i_d \ i_q]^T} &= L_{qq}|_{[i_d \ -i_q]^T}, & (c) \\
 L_{qq}|_{[i_d+i_{PM} \ i_q]^T} &= L_{qq}|_{[-i_d-i_{PM} \ i_q]^T}, & (d) \\
 L_m|_{[i_d \ i_q]^T} &= -L_m|_{[i_d \ -i_q]^T}, & (e) \\
 L_m|_{[i_d+i_{PM} \ i_q]^T} &= -L_m|_{[-i_d-i_{PM} \ i_q]^T}. & (f)
 \end{aligned} \tag{5.6}$$

In order to finalize the set of symmetry constraints, we can define the constraints on the symmetry axes as

$$\begin{aligned}
 \psi_d|_{[-i_{PM} \ i_q]^T} &= 0, & (a) \\
 \psi_q|_{[i_d \ 0]^T} &= 0, & (b) \\
 L_m|_{[i_d \ 0]^T} &= 0, & (c) \\
 L_m|_{[-i_{PM} \ i_q]^T} &= 0. & (d)
 \end{aligned} \tag{5.7}$$

With (5.4) - (5.7), we now have a set of equations defining the symmetry constraints for all types of synchronous machines.

### 5.2.2 Physical Considerations

The symmetry constraints, as defined in the former section, can be considered best, if the measured inductance maps are gridded and arranged symmetrically along the symmetry axes in the stator current plane. For this section, it is further necessary that the distances between the grid points are sufficiently small, such that the inductances – expressed by the differential relation between flux linkage and current – can be approximated by a difference quotient, as it was discussed in section 2.1.2 (cf. Figure 2.9 at page 22). In accordance with the definition of the inductance matrix in (2.66), we can then write the approximate inductances as

$$L_{dd} = \frac{\Delta\psi_d}{\Delta i_d}, \tag{a} \tag{5.8}$$

$$L_{qq} = \frac{\Delta\psi_d}{\Delta i_d}, \quad (b)$$

$$L_m = \frac{\Delta\psi_d}{\Delta i_q} = \frac{\Delta\psi_q}{\Delta i_d}, \quad (c)$$

where (5.8)(c) is already the first physical constraint. Its non-approximative definition was given in (2.67) and the equations (2.92) and (2.93) demonstrated, how the law of energy conservation and the fact that the physical origin of inductances are conservative magnetic co-energy scalar fields directly leads to this constraint.

Since this work focusses on the relation of inductances, flux linkages and co-energy, we interpret the differential constraints in their integral form. The above statement can then be reinterpreted in a way that integrating the inductance maps along different paths must lead to unique flux linkage maps. Furthermore, integrating the resulting flux linkage maps must lead to unambiguous co-energy maps.

Figure 5.1 illustrates this statement exemplarily for  $\psi_d$  in the simple case of four  $dq$  current grid points. When starting from the point 00, we can determine the flux linkage at point 11 in two different ways, applying the approximative integral equations

$$\psi_{d,11} = \psi_{d,00} + \frac{1}{2}(L_{dd,00} + L_{dd,01})\Delta i_d + \frac{1}{2}(L_{m,01} + L_{m,11})\Delta i_q, \quad (a)$$

$$\psi_{d,11} = \psi_{d,00} + \frac{1}{2}(L_{m,00} + L_{m,10})\Delta i_q + \frac{1}{2}(L_{dd,10} + L_{dd,11})\Delta i_d, \quad (b)$$

where the integration from one grid point to its neighbor applies the mean inductance values of both points.

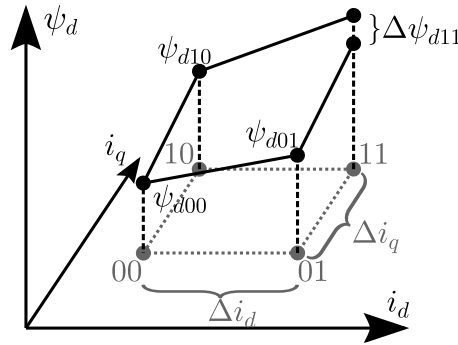


Figure 5.1: Example of two different integration paths in the  $dq$  current plane that lead to different results for the  $d$ -axis flux linkage

As indicated, the two integration paths can pass either through point 01 or 10. In any case, however, we must obtain the same result for  $\psi_{d,11}$ . This means that  $\Delta\psi_{d,11}$  must be zero and thus (5.9) directly leads to another equality constraint, relating the inductances of the four points with each other. We get

$$(L_{m,00} + L_{m,10} - L_{m,01} - L_{m,11})\Delta i_q = (L_{dd,00} + L_{dd,01} - L_{dd,10} - L_{dd,11})\Delta i_d. \quad (5.10)$$

For the  $q$ -axis flux linkage, we obtain analogously

$$(L_{m,00} + L_{m,01} - L_{m,10} - L_{m,11})\Delta i_d = (L_{qq,00} + L_{qq,10} - L_{qq,01} - L_{qq,11})\Delta i_q . \quad (5.11)$$

The same procedure for the magnetic co-energy with corresponding integration along the flux linkages leads to

$$\begin{aligned} (L_{dd,00} + L_{dd,01} - L_{dd,10} - L_{dd,11})(\Delta i_d)^2 + 2L_{m,11}\Delta i_q\Delta i_d \\ = (L_{qq,01} + L_{qq,11} - L_{qq,00} - L_{qq,10})(\Delta i_q)^2 + 2L_{m,00}\Delta i_d\Delta i_q . \end{aligned} \quad (5.12)$$

When substituting (5.10) into (5.12), we get

$$L_{m,00} + L_{m,11} = L_{m,11} + L_{m,00} \quad (5.13)$$

and for the combination of (5.11) and (5.12), we end up with

$$L_{m,01} + L_{m,10} = L_{m,10} + L_{m,01} . \quad (5.14)$$

It becomes clear that (5.10) – (5.12) are linearly dependent and for that reason the constraint (5.8)(c) for each measured grid point in combination with (5.10) and (5.11) for each quadruple of neighboring grid points are sufficient to ensure the physical validness of the inductance maps. In consequence, we are able to derive unambiguous flux linkage and co-energy maps, independently from the chosen integration paths by applying the following set of equality constraints:

$$L_m|_{[i_d \ i_q]^T} = L_{dq}|_{[i_d \ i_q]^T} = L_{qd}|_{[i_d \ i_q]^T} , \quad (a)$$

$$\begin{aligned} (L_m|_{[i_d \ i_q]^T} + L_m|_{[i_d \ i_q+\Delta i_q]^T} - L_m|_{[i_d+\Delta i_d \ i_q]^T} - L_m|_{[i_d+\Delta i_d \ i_q+\Delta i_q]^T})\Delta i_q \\ = \end{aligned} \quad (b)$$

$$(L_{dd}|_{[i_d \ i_q]^T} + L_{dd}|_{[i_d+\Delta i_d \ i_q]^T} - L_{dd}|_{[i_d \ i_q+\Delta i_q]^T} - L_{dd}|_{[i_d+\Delta i_d \ i_q+\Delta i_q]^T})\Delta i_d , \quad (5.15)$$

$$\begin{aligned} (L_m|_{[i_d \ i_q]^T} + L_m|_{[i_d+\Delta i_d \ i_q]^T} - L_m|_{[i_d \ i_q+\Delta i_q]^T} - L_m|_{[i_d+\Delta i_d \ i_q+\Delta i_q]^T})\Delta i_d \\ = \end{aligned} \quad (c)$$

$$(L_{qq}|_{[i_d \ i_q]^T} + L_{qq}|_{[i_d \ i_q+\Delta i_q]^T} - L_{qq}|_{[i_d+\Delta i_d \ i_q]^T} - L_{qq}|_{[i_d+\Delta i_d \ i_q+\Delta i_q]^T})\Delta i_q .$$

Note that constraints for inverse inductances can be obtained analogously, when considering currents and magnetic energy in a flux linkage plane. For conciseness, these constraints are not discussed here.

In comparison to the symmetry constraints from the former sub section, it should be noted that the constraints of this section are physically reasonable in any case. Enforcing symmetry on the measurements, however, can also introduce errors, because real machines are typically not perfectly symmetric for mechanical reasons or due to tolerances in the production processes. On the other hand, there are asymmetric effects (e.g. iron effects or inverter distortions) that can be effectively canceled out by the symmetry constraints. Depending on the application, it might thus be useful to apply only the physical constraints, or a combination of both, physical and symmetry constraints. This issue is further discussed in the context of measurement results in Chapter 6.

### 5.3 The Optimization Problem

Symmetry of measured inductance or flux linkage maps can be enforced comparably simple by averaging the measurement results along the respective symmetry axis. However, enforcing the

physical constraints, or both, symmetry and physical constraints, simultaneously, requires a more sophisticated strategy.

We obviously have to modify the measurement results in order to enforce the constraints. A natural approach is to restrict these modifications to the absolute minimum. This can be interpreted as a classical constrained optimization problem. Especially in the linear case, there are several effective algorithms and software solutions that can be applied [100].

We thus define correction variables for each inductance value at each grid point, i.e.

$$L_{dd}|_{[i_d \ i_q]^T} = \check{L}_{dd}|_{[i_d \ i_q]^T} + \check{\check{L}}_{dd}|_{[i_d \ i_q]^T} , \quad (\text{a})$$

$$L_{dq}|_{[i_d \ i_q]^T} = \check{L}_{dq}|_{[i_d \ i_q]^T} + \check{\check{L}}_{dq}|_{[i_d \ i_q]^T} , \quad (\text{b})$$

$$L_{qd}|_{[i_d \ i_q]^T} = \check{L}_{qd}|_{[i_d \ i_q]^T} + \check{\check{L}}_{qd}|_{[i_d \ i_q]^T} , \quad (\text{c})$$

$$L_{qq}|_{[i_d \ i_q]^T} = \check{L}_{qq}|_{[i_d \ i_q]^T} + \check{\check{L}}_{qq}|_{[i_d \ i_q]^T} , \quad (\text{d})$$

where the correction variables are denoted by a ‘ $\check{\check{\cdot}}$ ’. Adding them to the measured inductance parameters ( $\check{\cdot}$ ) gives us the corrected inductance values that comply with the given constraints.

The sets of correction variables for all grid points can be collected in a vector,  $\check{\check{\mathbf{L}}}$ , and we can then compute them by solving the linear optimization problem

$$\check{\check{\mathbf{L}}} = \underset{\text{subj. to (5.6), (5.15)}}{\arg \min} \quad (\|\check{\check{\mathbf{L}}}\|_{\ell}) , \quad (5.17)$$

where the norm  $\ell$  defines, whether the sum of the absolute values of all correction variables ( $\ell = 1$ ) or the sum of squares of all correction variables ( $\ell = 2$ ) is minimal, or whether the maximal absolute value of each single correction variable is minimal ( $\ell = \infty$ ).

All optimized results presented and discussed in this thesis are obtained by minimizing the sum of squares, i.e. with  $\ell = 2$ . The respective solution of the optimization problem (5.17) is substituted into (5.16) in order to obtain symmetric and physically reasonable inductance maps. These optimized maps can be integrated along arbitrary paths to determine unambiguous flux linkage and (co-) energy maps.

It shall be emphasized at this point, that the results of the direct flux linkage measurements (see section 6.3) are converted into inductance maps acc. to (5.8), before optimizing them. Afterwards, they are converted back into flux linkage maps by means of (5.9), where the integration constant is chosen in accordance with (2.80), i.e.

$$\mathbf{f}^r(\mathbf{i}_s^r = \mathbf{0}) = \begin{bmatrix} \psi_{PM} \\ 0 \end{bmatrix}. \quad (5.18)$$

Of course, it would be possible to formulate an optimization problem for symmetric and unambiguous (co-) energy maps directly from flux linkage measurements. However, in order to obtain best comparability between inductance and flux linkage measurement schemes, this work generally applies the above-mentioned inductance optimization algorithm.

# CHAPTER 6

---

## Measuring Flux Linkage in Synchronous Machines

---

### 6.1 State of the Art Measurement Techniques

---

#### 6.1.1 Preliminaries: Distinguishing Between EMF, BEMF and HF Based Methods

When we talk about measuring the flux linkage in synchronous machines, we are basically interested in the relation between the flux linkage and stator current space vectors as it was stated in section 2.2.3. The mathematical translation of this statement was defined in (2.55) as

$$\boldsymbol{\psi}_s^r = \boldsymbol{f}^r(\boldsymbol{i}_s^r), \quad (6.1)$$

where  $\boldsymbol{f}^r$  is a bijection that maps each current space vector with a flux linkage vector. In order to find  $\boldsymbol{f}^r$ , we thus need to measure both, the current and the flux linkage, at steady operating points within the region of interest. The latter is naturally defined by the maximal admissible currents that do neither harm the motor nor the inverter due to thermal overload.

How both, current and flux linkage, can be simultaneously measured, becomes apparent when reminding the electric model of synchronous machines in stator coordinates. It was defined also in section 2.2.3 as

$$\boldsymbol{u}_s^s = R_s \boldsymbol{i}_s^s + \underbrace{\frac{d}{dt} \boldsymbol{\psi}_s^s}_{EMF}. \quad (6.2)$$

We can see that the flux linkage information is contained in the second term on the RHS of (6.2). In the following, we will refer to this term as electromotive force (EMF). All flux linkage measurement methods that base on current and voltage signals extract the information from the EMF. There are, however, methods that need a sufficiently high rotor speed and those that work at standstill but depend on test signal injection. The reason for that can be seen, when the electric model in rotor coordinates is reminded as

$$\mathbf{u}_s^r = R_s \mathbf{i}_s^r + \underbrace{\omega_r \mathbf{J} \psi_s^r}_{\text{BEMF}} + \underbrace{\frac{d}{dt} \psi_s^r}_{\text{HF}}. \quad (6.3)$$

The coordinate transformation splits the EMF into two terms. The second term on the RHS of (6.3) will be referred to as *back electromotive force* (BEMF) from now on. The BEMF can be seen as the motional part of the EMF. It contains the direct flux linkage space vector, which can thus be evaluated without any mathematical integration. It is, however, proportional to the electric rotor speed,  $\omega_r$ , and hence zero at standstill.

The third term on the RHS is a voltage proportional to the time rate of change of the flux linkage space vector. It is therefore the dynamically induced part of the EMF and as such, it is consequentially zero at steady state operation. For extraction of the flux linkage information, the change of the flux linkage must be enforced by appropriate applied voltages. This is typically done by imposing *high frequency* (HF) currents or voltages to the motor under test, whereat “high” refers to the fact that the frequency of the injected signal is well above the BEMF frequency, i.e.  $\omega_r/2\pi$ . In this way, it is possible to separate the HF signal from the BEMF signal by filtering techniques. We consequently refer to the third term on the RHS as HF term in the following. As it does not depend on the rotor speed, it can be evaluated also at standstill.

### 6.1.2 EMF Based Techniques

Solving the motor model in stator coordinates, (6.2), for the EMF term and subsequently integrating it gives us

$$\psi_s^s = \int (\mathbf{u}_s^s - R_s \mathbf{i}_s^s) dt + \psi_{s,c}^s, \quad (6.4)$$

where  $\psi_{s,c}^s$  is the flux linkage space vector at the beginning of the integration process. Eq. (6.4) is a standard open-loop flux estimator, as it is usually employed in sensorless control schemes [66 pp. 125–128].

An EMF based measurement scheme relies only on one parameter, namely  $R_s$ , and the typically available current and voltage signals. Furthermore, the rotor position is necessary in order to transform the corresponding current and flux linkage space vectors into rotor coordinates as requested by (6.1).

The challenge of this method is the integration process, which requires knowledge of the initial flux linkage and a drift compensation. As it is typical for open-loop integrators, the quality of its output suffers from integration drifts. They occur due to various reasons, as, for instance, offsets in the measurements, parameter errors, or inaccurate integration techniques. A drift compensation is thus necessary in order to obtain accurate flux linkage results. A typical approach in literature is to replace the integrator with a first order *low-pass filter* (LPF) [66 p. 128, 101]. At high frequencies, it acts like an integrator, but it suppresses low frequencies and thus constant errors.

The EMF flux linkage estimator is an effective method to determine the desired magnetic characteristics of the motor under test. Independent from whether the rotor is spinning or not, we only need to track voltages and currents, and map them with the estimated flux linkages.

The drift and initialization problems, however, make it usually necessary to separate the BEMF and HF components that are both contained in the EMF. Additionally, the iron loss phenomena have different effects on both signals, which makes it for the sake of reproducibility more convenient to separate both. For that reason, no methods are known in literature that extract the flux linkage information from both terms simultaneously. All methods can thus be assigned to the group of either BEMF based or HF based techniques.

### 6.1.3 BEMF Based Techniques

The most obvious approach to obtain the flux linkage information from the BEMF term is to solve the motor model in rotor coordinates, (6.3), for the flux linkage space vector. Hence,

$$\boldsymbol{\psi}_s^r = -\frac{1}{\omega_r} \mathbf{J} \left( \mathbf{u}_s^r - R_s \mathbf{i}_s^r - \frac{d}{dt} \boldsymbol{\psi}_s^r \right). \quad (6.5)$$

As we can see, Eq. (6.5) still contains the HF term, namely  $d\boldsymbol{\psi}_s^r/dt$ . In order to extract the BEMF flux linkage information from (6.5), we thus need to eliminate the HF component. A common approach in literature is to apply a constant current vector,  $\mathbf{i}_s^{r*}$ , to the motor under test [75–77, 102–105]. Since  $\mathbf{f}^r$  is bijective, we can conclude that if

$$\frac{d}{dt} \mathbf{i}_s^r = 0, \quad (6.6)$$

then also

$$\frac{d}{dt} \mathbf{f}^r(\mathbf{i}_s^r) = 0 \quad (6.7)$$

and thus

$$\frac{d}{dt} \boldsymbol{\psi}_s^r = 0. \quad (6.8)$$

Provided that we have a constant current vector, the flux linkage from the BEMF term can hence be evaluated from

$$\boldsymbol{\psi}_s^r = -\frac{1}{\omega_r} \mathbf{J}(\mathbf{u}_s^r - R_s \mathbf{i}_s^r). \quad (6.9)$$

In practice, however, the conditions (6.6)–(6.8) cannot be completely achieved because of harmonic distortions due to slotting, non-sinusoidal winding schemes, etc. (see section 2.2.3). This fact can be considered by appropriate filter techniques, as it is done for instance in [105] with a *fast Fourier transform* (FFT). Another possibility is to measure currents and voltages over a period that contains complete rotor turns. This technique was already used in prior publications [106, 107] and will consequently be applied within this work, as well. Simultaneously, it was proposed in [102].

The idea behind this technique is that all distortions caused by the motor itself must be periodic to a complete rotor turn and are thus harmonics of the fundamental frequency of the motor. The latter is the frequency at which the rotor turns, i.e. it correlates with the mechanic speed by

$$f_m = \frac{\omega_m}{2\pi} = \frac{1}{2\pi} \frac{d\vartheta_m}{dt}. \quad (6.10)$$

Provided that the fundamental current as well as the temperature distribution remain the same during one complete turn, the flux linkage at the beginning of the measurement period must be exactly the same as at the end. In mathematical terms, this means that the overall change in the flux linkage over the measurement interval,  $T_{meas}$ , is zero, i.e.

$$\int_{(T_{meas})} \left( \frac{d}{dt} \psi_s^r \right) dt = 0. \quad (6.11)$$

Due to that fact, averaging the measured signals over the measurement period will not only reduce the influence of noise, it will also effectively eliminate the harmonic components in current and flux linkage and the unknown HF term.

When the rotor velocity is held constant, e.g. by a coupled load motor, we get

$$\frac{1}{T_{meas}} \int_0^{T_{meas}} \left( \frac{d}{dt} \psi_s^r \frac{1}{\omega_r} \right) dt = 0 \quad (6.12)$$

and hence

$$\bar{\psi}_s^r = -\frac{1}{T_{meas}} \int_0^{T_{meas}} \left( \frac{1}{\omega_r} \mathbf{J}(\mathbf{u}_s^r - R_s \mathbf{i}_s^r) \right) dt. \quad (6.13)$$

Note that most of the BEMF based methods in literature neglect harmonics and will hence require sufficiently large measurement intervals to reduce their influence (see leakage effect in section 2.4.2).

As mentioned before, a sufficiently large rotor velocity is inevitable for all BEMF based methods. The speed, however, does not have to be constant. In [103], for instance, (6.9) is evaluated during periods of constant acceleration and deceleration. This has the advantage that no load motor is necessary, however, at the expense of harmonic distortions and the fact that only current vectors can be evaluated that accelerate or decelerate the rotor sufficiently fast.

Many parameter identification methods in literature can also be seen as flux linkage measurement techniques. They base on linearized models at given operating points as described in section 2.2.3. Although they identify absolute inductances rather than flux linkages, both quantities can be directly converted into each other and hence deriving the flux linkage would only require an additional straightforward computation step.

Parameter identification for linear models is a general, well examined area [74 pp. 357–456]. A wide variety of methods exist. In the context of electric drives, least squares based methods are predominant, as proposed for instance in [77, 104] to name but a few. It should be noted, however, that often the linearized models are incorrect, as they do not properly distinguish between differential and absolute inductances as in [77]. This means that the expectable results will be inaccurate in saturated regions. Additionally, the simplified models do not allow to properly assign the methods to either of the HF or BEMF groups in many cases.

### 6.1.4 HF Based Techniques

The HF term as defined in (6.3), namely  $d\psi_s^r/dt$ , does only contain differential flux linkage information. This means that in order to obtain the absolute flux linkages, a mathematical integration procedure is necessary. This integration can be done in time domain, resulting in the flux linkage estimator from section 6.1.2. Note that at standstill, the BEMF term is zero and therefore (6.4) can be rewritten in rotor coordinates as

$$\psi_s^r = \int (\mathbf{u}_s^r - R_s \mathbf{i}_s^r) dt + \psi_{s,c}^r. \quad (6.14)$$

The same problems related with the open-loop integration as described in section 6.1.2 must hence be taken into account.

In [108] a rectangular voltage and in [55] a sinusoidal voltage is applied in order to excite current responses. The corresponding voltage and current signals together with a simple resistance estimate are directly applied to (6.14). Due to the short measurement times, the integrator drift is neglected. The initialization of the integrator, however, is very important here, as an error in  $\psi_{s,c}^r$  leads to corresponding offsets in the resulting flux linkage maps. This can be seen in [108], where the  $d$ -axis flux linkage map shows an offset of exactly the PM flux linkage value, which was neglected in the initialization of  $\psi_{s,c}^r$ .

In contrast to the BEMF based methods, no constant current and flux linkage values are available in the methods proposed in [55, 108]. For that reason, the mapping of flux linkage and current signals happens on basis of their transient states. In order to excite currents covering the complete region of interest, *large-signal HF injection* is necessary.

Other known large-signal methods determine absolute [78] or absolute and differential inductances [79]. The method described in [78] is comparably complex, as it determines the inductance values from the parameters of PI type current controllers. The parameters have to be tuned iteratively in such a way that their step response is critically damped. In [79], a current decay test starting from a high current is performed in order to obtain the inductance values. The calculation algorithm is obtained straightforward from the linearized model. The measurements, however, cannot be directly performed with a VSI, as the method requires a special test arrangement.

In contrast to the above HF methods, most techniques in literature determine only differential inductances, or, more precisely, their small-signal approximations [109–114]. In order to obtain good approximations, the excitation signal has to be as small as possible, but large enough for a sufficient *signal-to-noise ratio* (SNR). These techniques can thus be classified as *small-signal HF based methods*.

Unlike the large-signal techniques, a constant operating point within the region of interest is enforced. To this fundamental component the HF signal is superimposed. Only the HF current and voltage signals are then evaluated to obtain the differential inductance matrix,  $\mathbf{L}_s^r$ , which was defined in section 2.2.3 as the Jacobian matrix of  $\mathbf{f}^r$ . The resulting inductance values are mapped with the fundamental current components.

Although none of the above small-signal methods evaluate the flux linkage information contained in these inductance surfaces, we count them as flux linkage measurement methods, since it is principally possible to extract that information. As indicated above, an integration process is necessary, again. The time domain integrator, however, has to be replaced by an integration of the inductance maps in a  $dq$  current plane, as already discussed in Chapter 5.

Typical small-signal HF schemes apply sinusoidal signal injection. Since decoupling of  $d$ - and  $q$ -axis simplifies the inductance evaluation, the signal is often injected in either  $d$ - or  $q$ -direction. After evaluating the corresponding inductance, the procedure can be repeated for the other axis [55, 107, 109–112]. The separation of fundamental and HF components can be done either by appropriate filtering techniques [55, 109, 110, 114] or by applying special HF current controllers [111, 112]. Also more sophisticated injection schemes are published. In [114] a rotating voltage injection is applied, whereas in [113] a VSI modulation technique for multi-sine signals is proposed in order to evaluate the inductances at different frequencies simultaneously.

The frequency dependence of the resulting inductances is explicitly addressed in [55, 111–113]. While [113] only shows the dependency without further analysis, [55] presents results that indicate a major influence of magnetic hysteresis on the small-signal inductances. In [111, 112], the frequency dependency is explained generally by iron losses and an HF resistance matrix is introduced and experimentally identified in order to account for those losses.

By far most small-signal HF techniques are performed at standstill with a fixed rotor. This is an effective method to eliminate the BEMF term. From the above publications, only [114] allows a spinning rotor. This is, however, only possible due to simplifications, which reduce the accuracy of the parameter identification. As a matter of fairness, it should be mentioned, though, that [114] is primary an online identification technique aiming at improved torque control and not necessarily at obtaining accurate flux linkage maps.

A problem that arises from measurements at standstill is that spatial harmonics in the air gap field make the results dependent on the rotor position. In order to obtain a complete model, many sets of measurements at different rotor positions are thus necessary. As will be discussed in the following section, this work will avoid that problem by performing the HF measurements at a spinning rotor.

## **6.2 Ensuring a Comparable Measurement Environment**

---

In recent publications, especially in view of anisotropy based sensorless control, it is stated that the differential inductances differ from those derived from the flux linkage maps [21, 55, 110–112]. This work will address this phenomenon by comparing the results of a BEMF based and a small-signal HF based measurement scheme. Both schemes presented below are developed in the frame of this thesis, whereat the focus was put on *comparability and reproducibility*. They aim at achieving highest possible accuracy with the given hardware setup. In this way, the results can be optimally compared in order to evaluate the iron loss phenomenon that is generally seen as reason for differences between the theoretical differential and the so-called HF (differential) inductances.

For the sake of comparability and reproducibility, the presented methods rely on evaluation algorithms that can be processed offline. During a measurement period, all raw data of the phase currents, the DC link voltage, the torque, the rotor position and the calculated duty cycles are logged. By this way, all algorithms can be applied to the same data.

As mentioned before, the temperature of the complete motor, the power cables and the power electronics is an important issue. It influences the resistance of cable and stator windings and the susceptibility of rotor and stator yokes and the PM material (see section 2.1.2). Additionally, it influences the switching times and the forward voltage drops of the semiconductors in the inverter (see section 3.2.3). It is thus crucial, to ensure constant temperature distributions during the measurements.

Another important aspect is the chosen rotor velocity. For the sake of comparability, it should be the same during both, BEMF and HF measurements. Furthermore, it should be constant in order to allow proper separation of BEMF and HF components during the measurements. Even when we assume steady state operation in rotor coordinates, the associated rotating magnetic field causes iron losses in the stator, whereat the rotational speed determines the height of the losses. As direct consequence, magnetic hysteresis occurs, which is difficult handle mathematically (see section 2.1.2). It is thus desirable to perform the measurements at low speed. On the other hand, low speed means low BEMF and thus bad SNR for BEMF based measurements.

Besides iron losses and SNR, also the problem of harmonic distortions plays a role in choosing the rotor speed. As already mentioned, the BEMF and for the same reason also the HF based measurements require measurement periods that cover integer numbers of rotor turns in order to avoid negative effects of the harmonics on the measurements. For that reason, the rotor speed has to be chosen fast enough to allow measurement times that result in an acceptable effort for data acquisition, buffering, transmission and processing.

In conclusion, a tradeoff between iron losses, SNR and measurement effort is necessary. Unless otherwise stated, we thus choose a measurement speed of 1/3 of the nominal motor speed within this work.

In order to appropriately account for all of the above issues, the flux linkage measurements are embedded into a similar procedure as the measurements of the inverter voltage distortions, namely:

1. Initialization:
  - a. The load motor is operated in speed control mode at the desired constant rotor speed.
  - b. The motor under test is operated in field oriented current control. A constant current space vector is applied to the motor in order to heat up inverter, cable and motor. The vector is aligned with the  $d$ -axis and its absolute value is around 80 % of the nominal current.
  - c. When the surface temperature of the motor arrives at a steady state (between 42°C to 45°C for all tested motors), both, current and speed control, are turned

off and the exact motor cable and stator windings resistance,  $R_{cal}$ , is measured with an Ohmmeter. Additionally, current measurement offsets are determined and compensated for in the following.

- d. Constant speed control of the load motor and current control of the motor under test are activated again. The current reference is set to nominal current on the  $d$ -axis. For a period of 100 electrical rotor turns, the  $d$ -axis current and voltage are measured and averaged. From these values, the approximate resistance is calculated by  $R_a = u_{d,avg}/i_{d,avg}$ . As inverter distortion voltages and iron loss effects are not compensated for, the value differs from  $R_{cal}$ . It is, however, a good measure for temperature changes.
2. Measurements:
    - a. The resistance estimation from step 1.d is repeated. If the obtained value is below 99.5% of  $R_a$ , the resistance estimation is repeated until the desired temperature is reached again. As the resistance estimation is performed at rated current, it can sufficiently heat up motor, cable and inverter. If the estimated resistance value is above 100.5% of  $R_a$ , a zero current reference is applied for an appropriate time interval. Afterwards, the resistance estimation is repeated.
    - b. A pre-defined current reference vector is applied. After the  $dq$  currents arrive at steady state, the BEMF or HF based measurements are performed as described in the following sections. For a time period corresponding to 15 complete rotor turns, all current and DC link voltage measurements as well as the corresponding inverter duty cycles are buffered in the real time system. Afterwards, the buffered data is transmitted to and saved at the PC for post-processing.
    - c. When further designated current references are defined for measurements, the whole process is repeated from step 2.a.
  3. Post-processing:

The flux linkage information contained in the logged raw data is extracted by the evaluation techniques described in the following sections.

## 6.3 BEMF Based Measurement Method

---

### 6.3.1 Measurement Scheme and Algorithm

In an attempt to be as precise as possible, the BEMF based methods from literature are modified within this work. The main problem of the conventional methods is their dependency on the rotor velocity signal. As described in section 3.3.3, the speed signal obtained from an incremental encoder suffers from the discretization of the position signal and its differentiation. This is a known problem in drive systems and a common remedy is to filter the speed signal [2 pp. 294–296]. This, on the other hand, introduces a delay in the speed signal, which again is problematic, particularly with regard to dynamic measurement schemes as in [103].

Another problem related with the velocity in known BEMF methods is the difficulty to eliminate harmonic distortions. Both techniques described in section 6.1.3 are restricted to constant rotor speeds. The FFT filtering technique from [105] can only work at a constant

fundamental frequency to be filtered out. The complete rotor turn evaluation from [102] bases on the assumption (6.12), which cannot be guaranteed, when  $\omega_r$  is a time-dependent variable instead of a constant parameter. Although we will also perform the measurements at constant velocities, the fact that this restriction is omitted in the following method can make it interesting also for other schemes, as for example [103].

In order to eliminate the rotor velocity signal from the BEMF based flux linkage determination, we evaluate the measurement signals in stator coordinates. Our approach is hence to evaluate the EMF term as described in section 6.1.2. The drift and initialization problems associated with the open-loop integrator are approached in the sense of the discussed LPFs. However, since the LPF method depends on the chosen filter time constants, we follow a more systematic approach.

When we assume a constant voltage offset,  $\mathbf{u}_{offset}^s$ , perturbing the measurements, we get

$$\frac{d}{dt}\psi_s^s + \frac{d}{dt}\psi_{s,err}^s = \mathbf{u}_s^s - R_s \mathbf{i}_s^s + \mathbf{u}_{offset}^s, \quad (6.15)$$

where  $d\psi_{s,err}^s/dt$  is the corresponding error in the flux linkage derivative, when the RHS of (6.15) serves as input for the flux linkage evaluation.

In the same manner as in section 6.1.3, we assume steady currents and hence the same starting and end points of the flux linkage independently from the rotor speed or harmonic distortions, as long as the measurement period,  $T_{meas}$ , covers an exact rotor turn or an integer multiple thereof. Equation (6.11) is thus still valid and when determining the arithmetic average of (6.15), we obtain

$$\frac{1}{T_{meas}} \int_0^{T_{meas}} \left( \frac{d}{dt} \psi_{s,err}^s \right) dt = \mathbf{u}_{offset}^s. \quad (6.16)$$

We can therefore eliminate the offset voltage causing the integrator drifts by subtracting the arithmetic average from the measurements. The result can then be used as input for an open-loop integrator.

Note that determining the arithmetic average of a signal is a special form of a *low-pass filter* (LPF) [92 pp. 318–320] and subtracting a low-pass filtered signal from the original signal gives us a *high-pass filtered* (HPF) signal.

The remaining problem of selecting the correct initialization value,  $\psi_{s,c}^s$ , for the integrator can be solved in exactly the same way. We know that the flux linkage vector is rotating synchronously with the electrical rotor position and after each complete turn arrives at the same position. We can thus conclude that the mean value of all flux linkage values during one rotor turn must be zero. Therefore, we can initialize the integrator with a random value, e.g.  $\psi_{s,c}^s = \mathbf{0}$ , and eliminate the resulting initialization error by subtracting the arithmetic average from the calculated flux linkages.

Note that this operation requires a BEMF signal in order to work properly. If only an HF component would be present, removing its average value would mean to remove the information about the steady state flux linkage at the actual operating point we are actually interested in.



we thus generally consider absolute values. Only in cases, where a relative view is useful to simplify the analysis, it is applied.

In Figures 6.2 and 6.3, we see the results of BEMF based  $d$ - and  $q$ -axis flux linkage measurements for the IPMSM at one third, minus one third and two thirds of the rated speed. The results are presented as surfaces in the left subfigures (a), (c) and (e) and shall give a qualitative overview. Additionally, the corresponding current contour lines are projected to the bottom of the respective figure's plot box. That same contour lines are shown in the right subfigures (b), (d) and (f) by fully colored surfaces.

All results are obtained from the procedure described in section 6.3.1, however, without compensating the inverter effects on the applied voltages as described in section 3.2.3. We can see that the results at different speeds are comparable on average but that the maps are slightly unsymmetrical. This can be seen best in comparison to the white contour lines on the right subfigures, which represent the corrected flux linkage maps as a result of the optimization process described in Chapter 5.

In both,  $d$ - and  $q$ -axis flux linkage maps, the asymmetry is obviously depending on the rotor speed. At one third of the rated motor speed in clockwise and counter-clockwise direction, the distortions change their directions as well, leading to similar results mirrored horizontally at the  $d$ -axis. At two thirds of the rated motor speed, the asymmetry is strongly reduced. This indicates that the asymmetric distortions in the measurements are inverse proportional to the rotor speed.

Additionally, the complete measured  $d$ -axis flux map at  $2/3 \omega_N$  is lower-valued than the physically reasonable results. This difference is increasing with increasing  $d$ -axis currents. At the same time, the  $q$ -axis flux linkage is very similar to the optimized results at the region with maximal  $d$ -currents. Instead, we can observe increasing deviations between both results with negative  $d$ -axis currents.

Especially the differences in the  $d$ -axis flux linkage maps indicate, that a simple symmetrization of the measured flux linkage maps along the  $d$ -axis does not automatically lead to physically reasonable results.

We know already that the results should be distorted by the inverter effects described in Chapter 3. They lead to errors in the applied voltages, that are only depending on the stator currents. Over a complete rotor turn, the respective voltage perturbations change depending on the actual current space vector in stator coordinates. The form and especially the amplitudes of the inverter distortion voltages, however, are independent from the rotor speed. At the same time, the BEMF voltage signal is proportional to the rotor speed, thus leading a decreasing influence of the inverter distortions with increasing speed.

This can be seen in Figures 6.4 and 6.5, where the flux linkage maps obtained from the same measurement data are shown, when the inverter effects are compensated by subtracting the voltage distortions as shown in Figure 3.3 from the FOC reference stator voltage vectors in stator coordinates.

We see that the results at  $\pm$  one third of the rated speed are now more symmetrical and generally closer to the physically reasonable optimum. It is also interesting to note, that the measured results are now very similar to those measured at two thirds of the rated speed without compensation of the inverter distortions (cf. subfigures (f) in Figures 6.2 – 6.3 and (b) in Figures 6.4 – 6.5). With compensated inverter effects at  $2/3 \omega_N$ , however, we can observe a slight asymmetry.

This indicates that another speed-dependent effect perturbs the measurements. At  $1/3 \omega_N$ , it seems to act comparably symmetric and mainly reduces the measured  $d$ -axis flux linkage values. At  $2/3 \omega_N$ , it causes asymmetries in the same order of magnitude than the inverter effects but mirrored at the  $d$ -axis (thus leading to comparably symmetric results, when the inverter effects are not compensated).

Since all other sources of error are eliminated as good as possible, these remaining differences to the physically reasonable optimum should be caused by iron effects, i.e. eddy currents and magnetic hysteresis. While determining explicit eddy currents and hysteretic states of the machine would go beyond the scope of this work, we will analyze their effects on the magnetic characteristics of the machine and how these effects act on control strategies like MTPA or on anisotropy based sensorless control. These issues are addressed further in section 6.5. For now, we can conclude that BEMF based measurement schemes are sensitive to voltage errors due to inverter switching effects, especially at low rotor speeds.

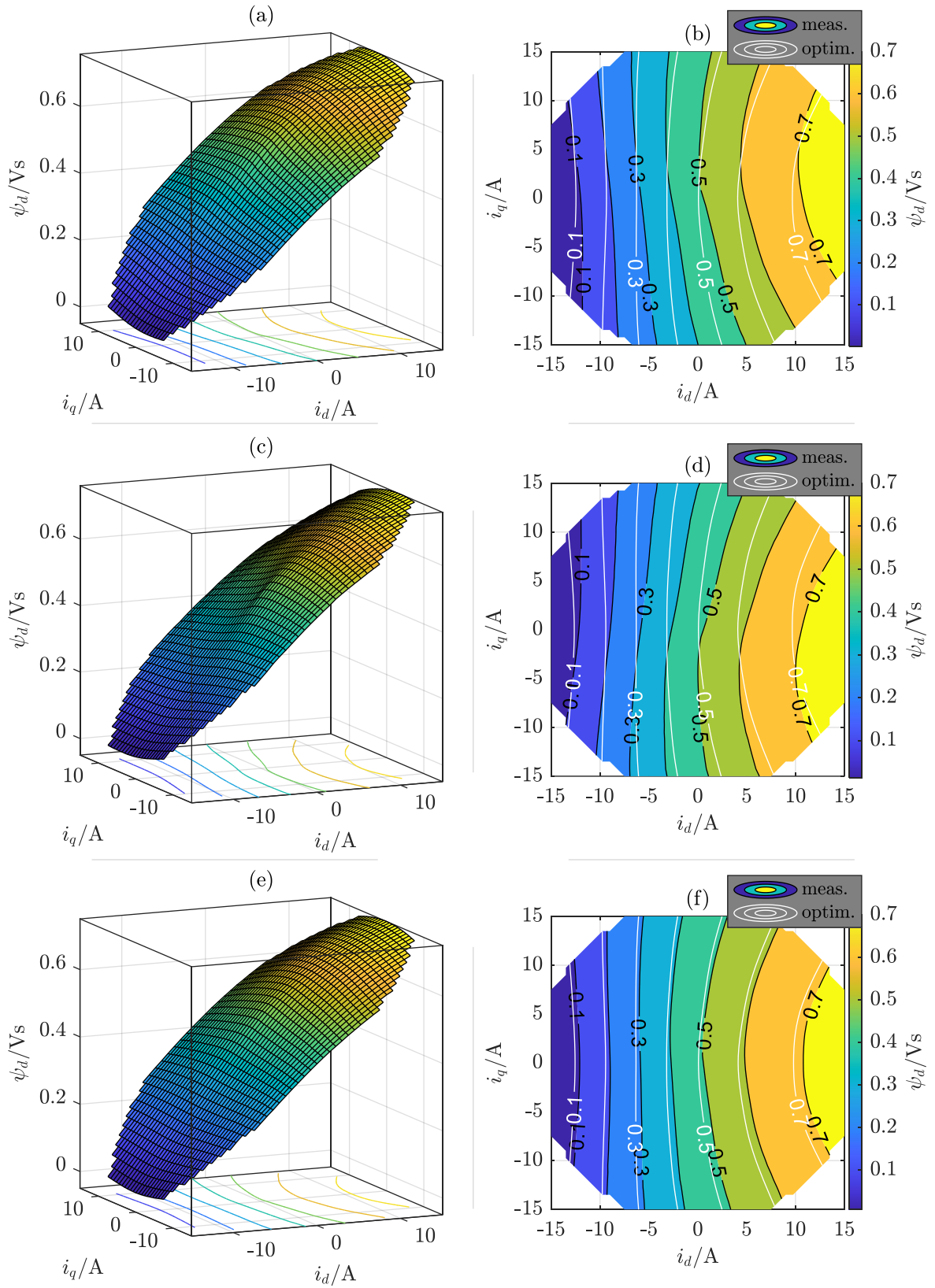


Figure 6.2:  $d$ -axis flux linkage measurement results for the IPMSM at  $1/3\omega_N$  (a, b), at  $-1/3\omega_N$  (c, d) and at  $2/3\omega_N$  (e, f) without compensation of inverter effects

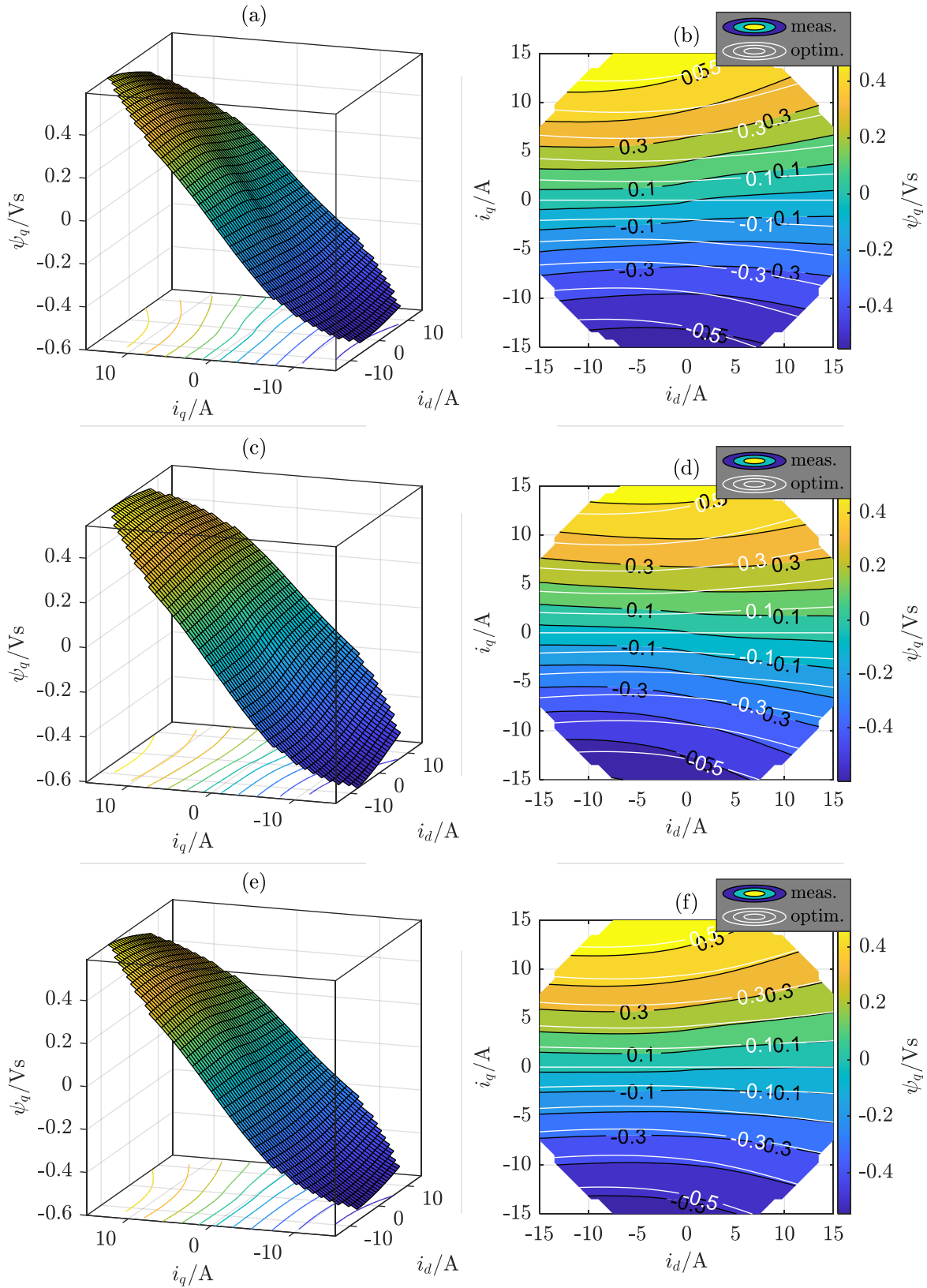


Figure 6.3:  $q$ -axis flux linkage measurement results for the IPMSM at  $1/3\omega_N$  (a, b), at  $-1/3\omega_N$  (c, d) and at  $2/3\omega_N$  (e, f) without compensation of inverter effects

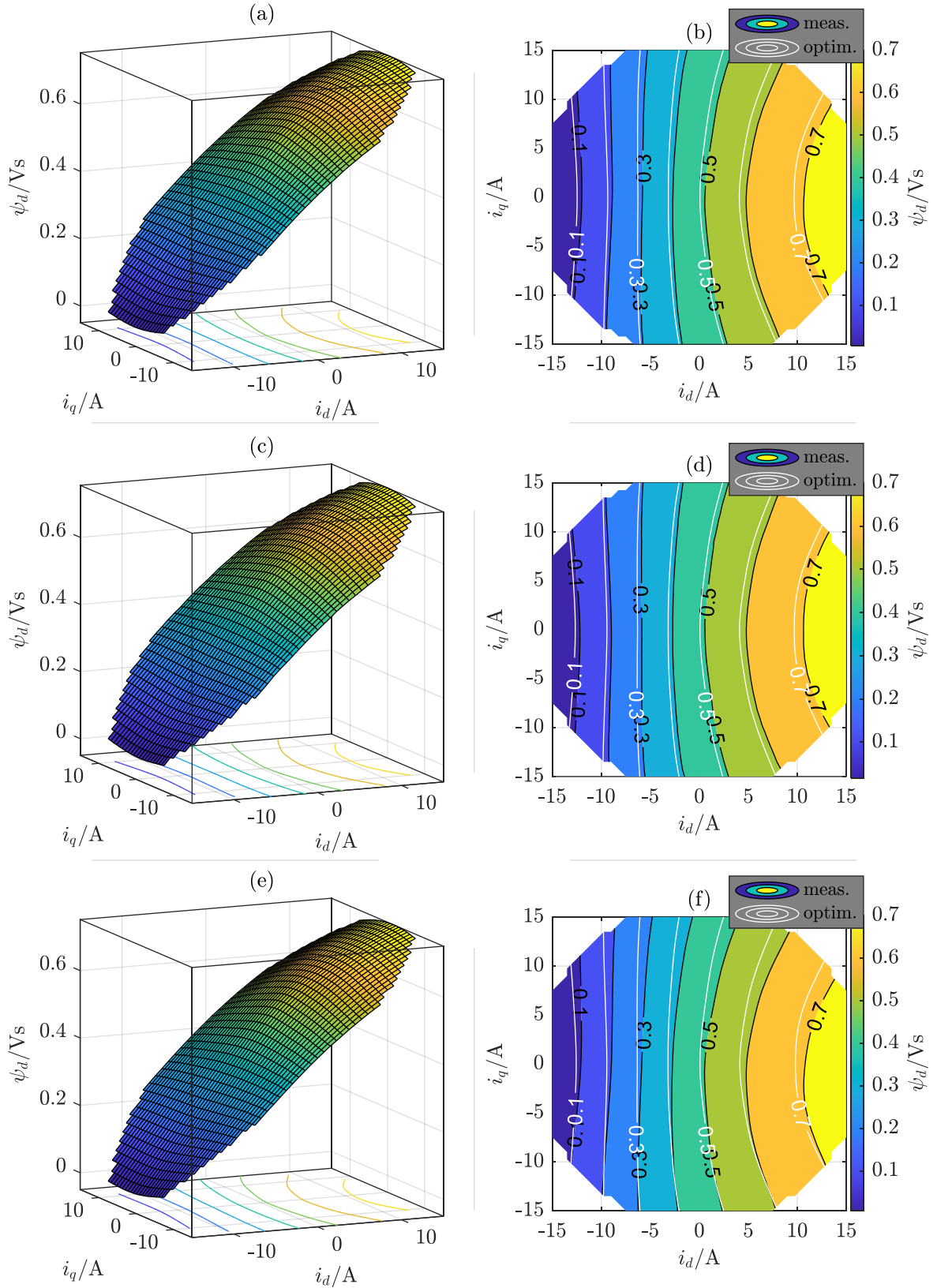


Figure 6.4:  $d$ -axis flux linkage measurement results for the IPMSM at  $1/3\omega_N$  (a, b), at  $-1/3\omega_N$  (c, d) and at  $2/3\omega_N$  (e, f) with compensation of inverter effects

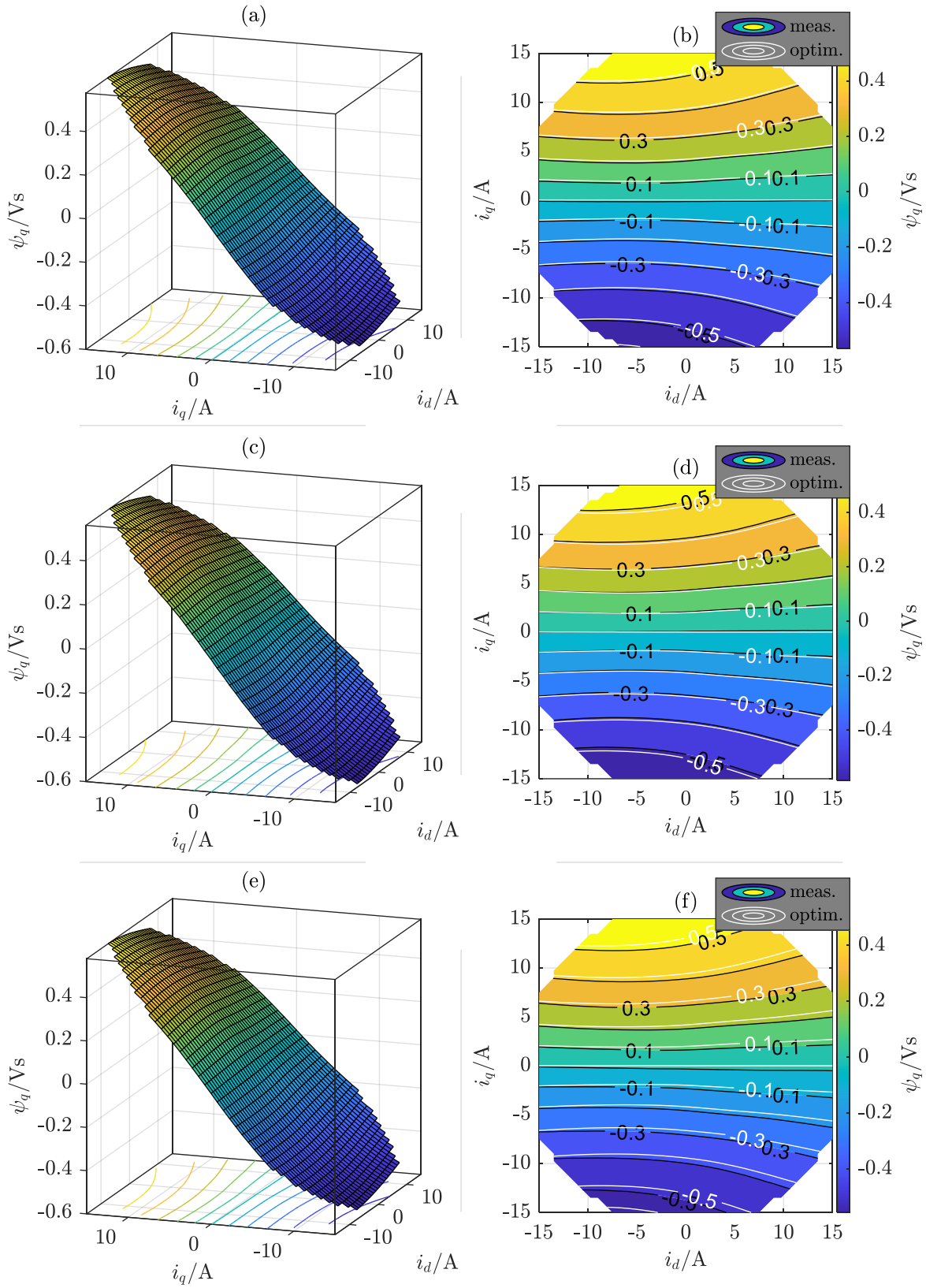


Figure 6.5:  $q$ -axis flux linkage measurement results for the IPMSM at  $1/3\omega_N$  (a, b), at  $-1/3\omega_N$  (c, d) and at  $2/3\omega_N$  (e, f) with compensation of inverter effects

When comparing the optimized results (white contour lines), we can note that – independent from the measurement speed and whether or not the inverter distortions are compensated – they are almost identical. In order to quantitatively compare the optimized results, Table 4 shows the sums of all absolute differences (i.e. the  $\ell_1$  norm) between the respective  $d$ - and  $q$ -axis flux linkage maps in relation to the  $\ell_1$  norm of the reference flux linkage map. For the latter, the optimized results of the measurements at one third rated speed and with compensated inverter effects are selected (these exact results were already shown and discussed in Chapter 4.2).

Since in comparison to itself, there is no difference, the respective entries in the table are zero. Compared to the measured (i.e. non-optimized) results, we see a relative  $\ell_1$  difference of 3.18% in the  $d$ -axis and 2.33% in the  $q$ -axis. Without inverter error compensation, the differences to the measurements are 4.79% and 8.03%, respectively. In comparison to the optimized results, however, we have only 0.02% and 0.03% differences, which allows to conclude that the optimization process as described in Chapter 5 can effectively eliminate the influence of the inverter voltage errors.

The maximal differences to the non-optimized flux linkage maps are 5.13% in the  $d$ -axis and 8.03% in the  $q$ -axis. When the inverter distortions are compensated, we still see differences of up to 3.28% and 5.63% in the  $d$  and  $q$  axes, respectively. As already mentioned, these deviations can be explained best by iron effects.

The largest differences between the optimized results occur in the  $d$ -axis at reversed speed and in the  $q$ -axis at double speed. The differences, however, remain below 0.5% in any case. This indicates that also the influence of iron effects on the flux linkage measurements can be strongly reduced by the optimization process.

Table 4: Comparison of the differences between the measured and corrected IPMSM flux linkage maps, where the corrected flux linkage map with compensated inverter effects measured at 1/3 of the rated speed is the reference

$\ell_1$ norm of differences in %	$d$ -axis, optim.	$q$ -axis, optim.	$d$ -axis, meas.	$q$ -axis, meas.
@ $1/3 \omega_N$ , inv. comp.	0.00	0.00	3.18	2.33
@ $-1/3 \omega_N$ , inv. comp.	0.32	0.18	2.66	2.12
@ $2/3 \omega_N$ , inv. comp.	0.29	0.47	3.28	5.63
@ $1/3 \omega_N$ , no inv. comp.	0.02	0.03	4.79	8.03
@ $-1/3 \omega_N$ , no inv. comp.	0.30	0.23	5.13	7.72
@ $2/3 \omega_N$ , no inv. comp.	0.26	0.43	3.22	5.64

The above conclusions concerning the inverter effects are supported by the BEMF based flux linkage measurements of the SPMSM and the SynRM. Figures 6.6 and 6.7 show the measured and optimized  $d$ - and  $q$ -axis flux linkage maps of the SynRM at one third rated speed without (subfigures on top) and with (bottom subfigures) compensation of inverter effects. Again, the optimized results are presented as white contour lines in the right subfigures.

Since the SynRM has noticeably larger inductances than the IPMSM, we get larger absolute flux linkage vectors and thus a stronger BEMF voltage signal. As the voltage perturbations caused by the inverter remain constant for the respective current operating points, the flux linkage maps without compensated inverter effects are only slightly distorted. When the inverter distortions are eliminated, the obtained flux linkage maps are very similar to the optimized results, which is confirmed quantitatively by Table 5.

Here, we see that the optimized results are practically identical and only corrections of less than 1.4% are necessary to obtain physically feasible results, if the inverter effects are compensated. If not, the necessary corrections of up to 9% are comparable to the results from the IPMSM.

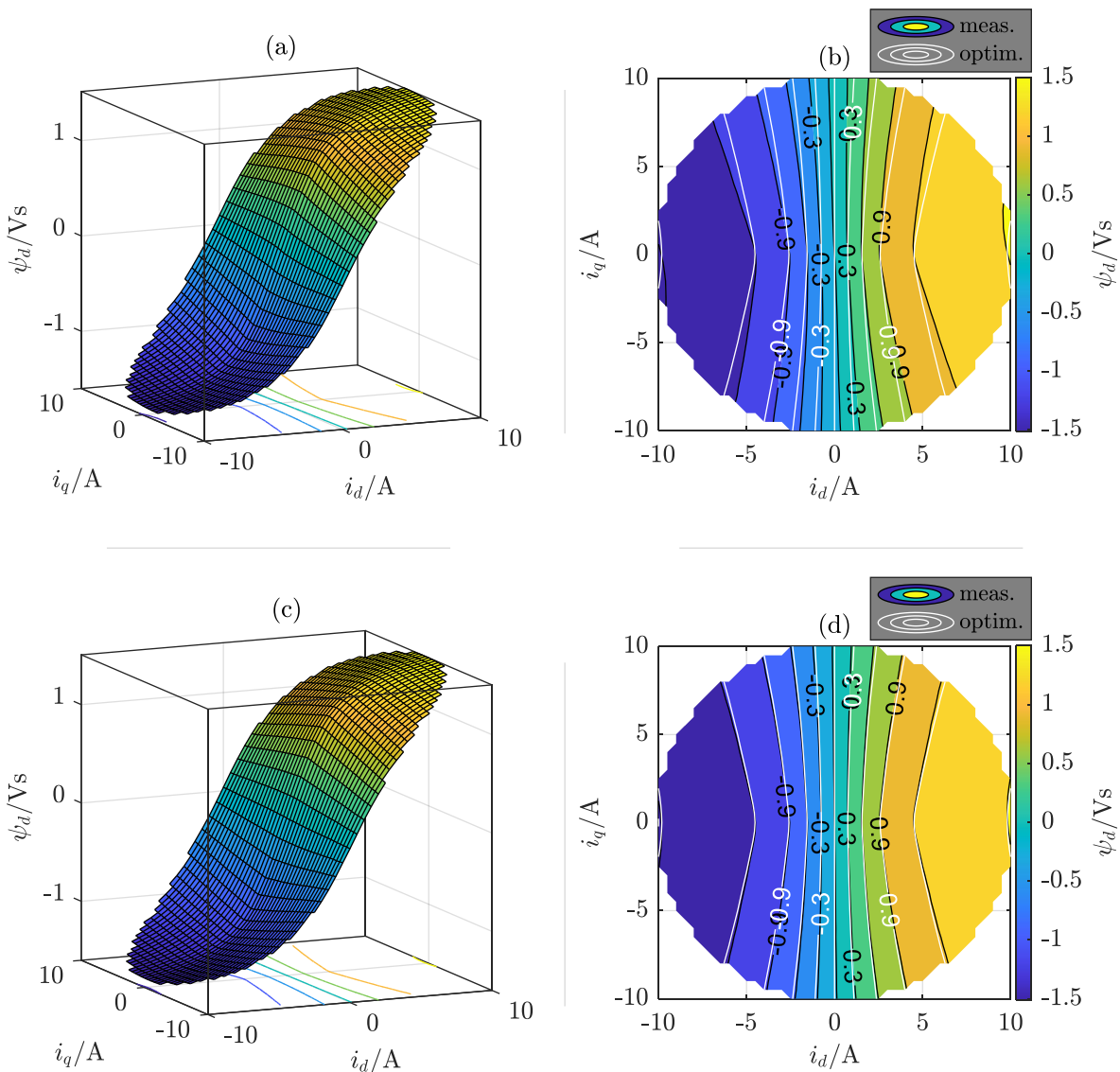


Figure 6.6:  $d$ -axis flux linkage measurement results for the SynRM at  $1/3\omega_N$ , without (a, b) and with (c, d) compensation of inverter effects

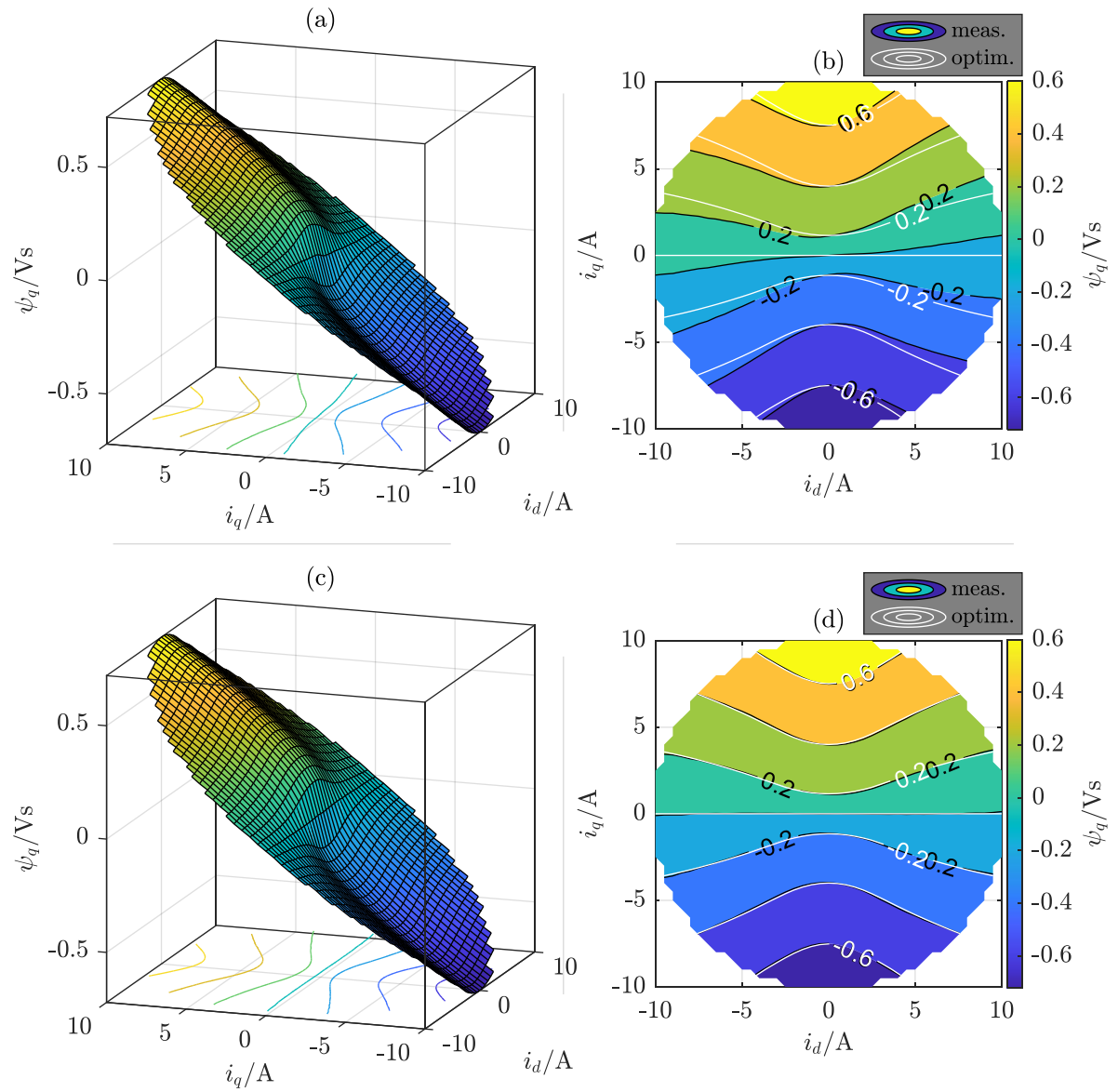


Figure 6.7:  $q$ -axis flux linkage measurement results for the SynRM at  $1/3\omega_N$ , without (a, b) and with (c, d) compensation of inverter effects

Table 5: Comparison of the differences between the measured and corrected SynRM flux linkage maps, where the corrected flux linkage map with compensated inverter effects measured at  $1/3$  of the rated speed is the reference

$\ell_1$ norm of differences in %	$d$ -axis, optim.	$q$ -axis, optim.	$d$ -axis, meas.	$q$ -axis, meas.
@ $1/3\omega_N$ , inv. comp.	0.00	0.00	1.34	0.97
@ $1/3\omega_N$ , no inv. comp.	0.00	0.01	4.60	8.99

From the discussion of the final results in Chapter 4, we know that the SPMSM has the least magnetic energy and thus the smallest flux linkage values of all three machines. It is thus the most demanding machine in terms of SNR and we can expect the biggest influence of the inverter distortions on the results. This is confirmed in Figures 6.8 and 6.9, where the same analysis is shown for the SPMSM as before for the IPMSM and the SynRM. Additionally, as a worst-case analysis, the influence of parameter errors in the identified stator resistance is shown in the top subfigures. The middle subfigures show the results for correctly identified stator resistance but still without compensation of the inverter effects. The bottom subfigures show the results for both, correct resistance and compensated inverter effects.

As expected, the inverter error voltages lead to noticeably stronger asymmetric distortions in the flux linkage maps of both axes, than it is observed at the other machines. When completely neglecting the stator resistance, the maps are even further distorted. We can see, however, that the optimization of the measurements can also effectively compensate this error. This is observable by comparing the white contour lines as well as in the quantitative analysis in Table 6.

Due to the permanent magnet in the  $d$ -axis, the absolute flux linkage values in the  $q$ -axis are smaller and thus the relative errors are larger, here. With more than 17%, the differences in the  $q$ -axis without inverter error compensation are much bigger than it was observed at the IPMSM.

It is worth noting, that even with correct resistance and compensated inverter errors, the  $q$ -axis flux linkages have to be corrected by in total 11 % in order to obtain physically feasible results. When inspecting Figure 6.9 (f), we see that the differences increase with increasing  $d$ -axis currents and with increasing absolute values of the  $q$ -axis currents. The largest differences occur in regions with large positive  $d$ -currents and large positive or negative  $q$ -currents, i.e. in regions with the highest magnetic saturation. This was also observable at the IPMSM, as well, but here, it is better to see.

The most likely reasons for this behavior are iron effects, or eddy currents in particular. At high currents, and when a positive  $d$ -axis current supports the PM flux linkage, large flux linkages vectors rotate at electrical rotor speed in the machine. As discussed in section 2.1.2, changing flux linkages cause eddy currents in conducting material, i.e. in the stator yoke in this case. Since the SPMSM has almost twice the rated speed of the IPMSM at the same number of pole pairs, the time rate of change of the flux linkage in the stator yoke is much higher, which – in combination with the generally worse SNR in the SPMSM – explains the bigger differences between measured and optimized flux maps.

Note that magnetic hysteresis seems to be of marginal relevance in this case. In section 2.1.2, it was discussed that with increasing saturation, coherent rotation begins to dominate the magnetization process. Since this effect is reversible, we can expect a decreasing influence of hysteresis with increasing flux linkage vectors, which contradicts the observed behavior.

The worst case of erroneous measurement results consists of a combination of inverter voltage errors and a 100% resistance parameter error. The graphical analysis in (a) and (b) of Figures 6.8 and 6.9 shows, how asymmetric the measured maps are and how big the differences between measurements and optimized results are. As reported in Table 6, physically reasonable results require corrections of almost 12% in the  $d$ - and nearly 43% in the  $q$ -axis. The resulting optimized maps, however, differ less than 0.2% and 0.7% from the optimized  $dq$  reference maps which were derived from measurements with correct resistance value and compensated inverter errors. We can thus state that the proposed optimization algorithm does also effectively reduce resistance parameter errors.

Table 6: Comparison of the differences between the measured and corrected SPMSM flux linkage maps, with and without resistance parameter error, where the corrected flux linkage map with compensated inverter effects measured at  $1/3$  of the rated speed is the reference

$\ell_1$ norm of differences in %	$d$ -axis, optim.	$q$ -axis, optim.	$d$ -axis, meas.	$q$ -axis, meas.
@ $1/3 \omega_N$ , inv. comp., correct $R$	0.00	0.00	1.10	10.99
@ $1/3 \omega_N$ , no comp., correct $R$	0.05	0.20	4.71	17.57
@ $1/3 \omega_N$ , no comp., no $R$	0.16	0.61	11.71	42.68

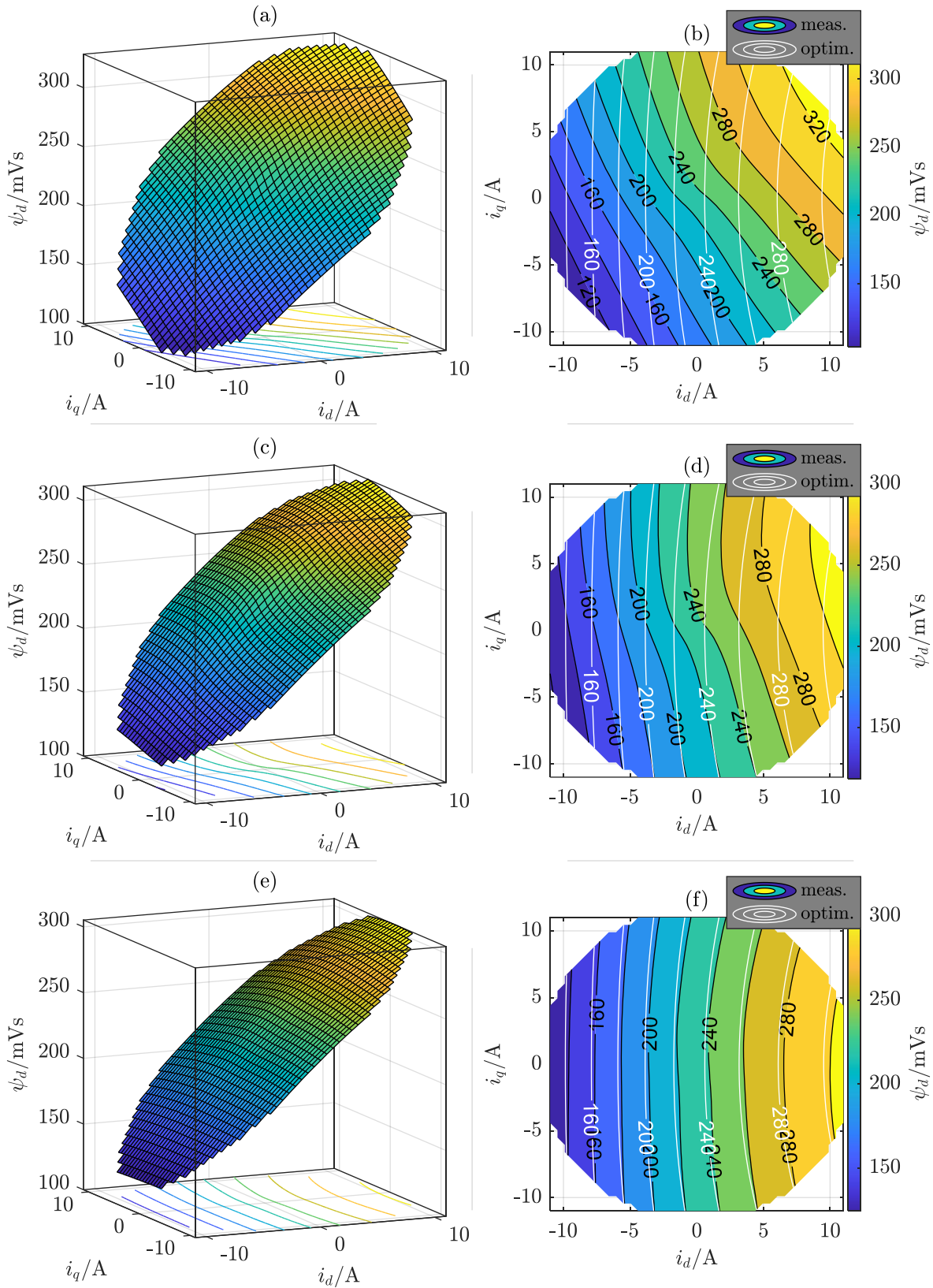


Figure 6.8:  $d$ -axis flux linkage measurement results for the SPMSM at  $1/3\omega_N$ ; (a, b): neglected stator resistance and no compensation of inverter effects; (c, d): correct resistance and no compensation of inverter effects; (e, f): correct resistance and compensation of inverter effects

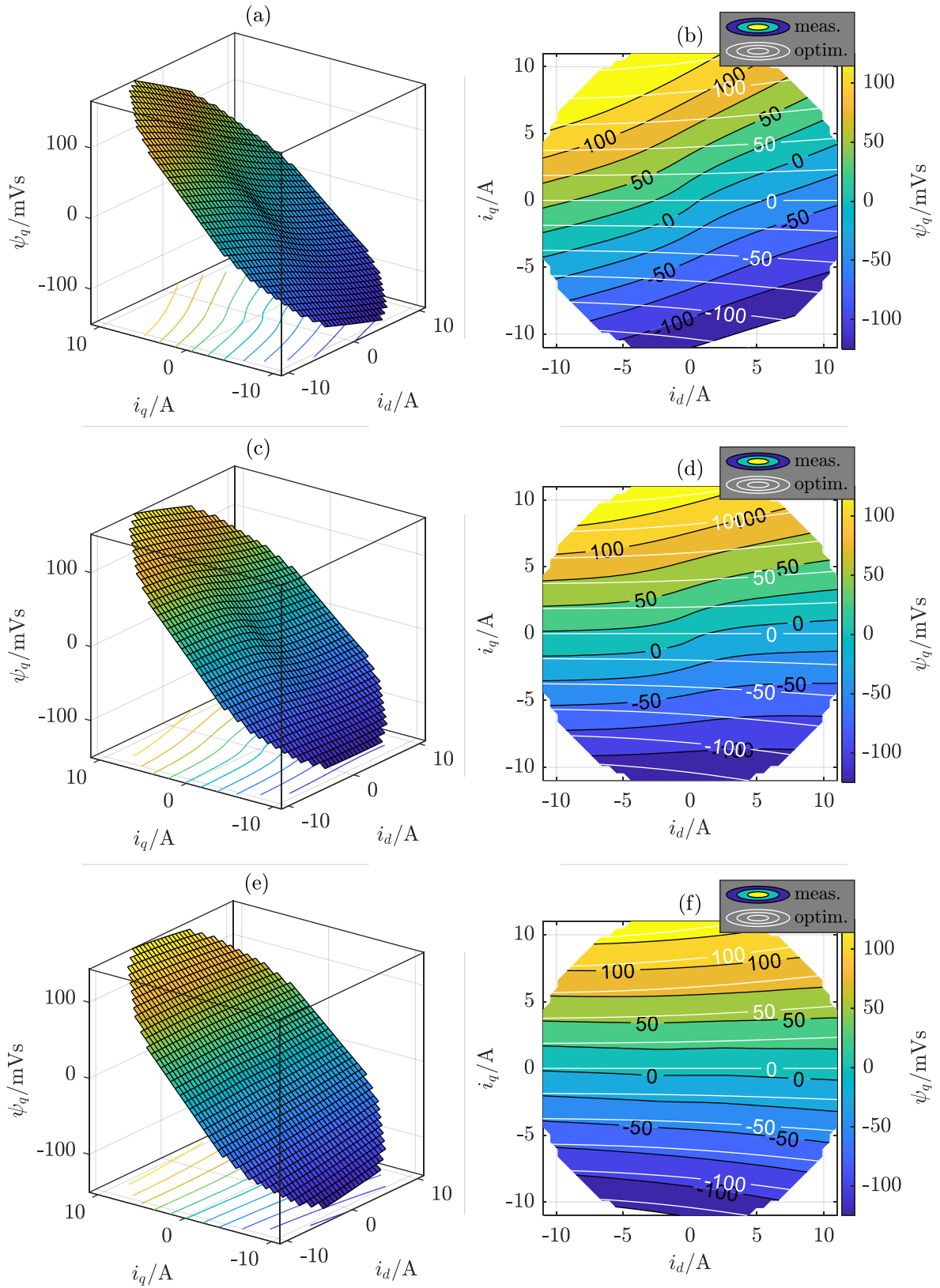


Figure 6.9:  $q$ -axis flux linkage measurement results for the SPMSM at  $1/3\omega_N$ ; (a, b): neglected stator resistance and no compensation of inverter effects; (c, d): correct resistance and no compensation of inverter effects; (e, f): correct resistance and compensation of inverter effects

## 6.4 Small-Signal HF Based Measurement Method

---

### 6.4.1 Measurement Scheme and Algorithm

In terms of hardware requirements and test preparation effort, HF based measurement schemes are usually advantageous over BEMF based techniques (except for those with free motor shafts, e.g. [103]). When carried out at standstill, only a brake is necessary and we do thus not have to care about the load machine, its control setup and how to dissipate the brake energy.

Within this work, the focus lies on comparing BEMF and HF based measurement schemes. Therefore, an HF based method is proposed that can be carried out simultaneously to the BEMF method from section 6.3. Both methods must not interfere with each other, which results in the following requirements:

- The HF method should not be restricted to standstill operation
  - Filter techniques will be necessary to separate the HF signals from the fundamental components
- The HF method should be compatible with steady current operating points and injected HF signals should not disturb the fundamental FOC current controllers
  - Small signal injection is necessary
  - Open-loop voltage injection is easier to handle than closed-loop HF current controllers, that might interfere with the FOC controllers or natural machine harmonics
- The arithmetic mean of the injection signals should be zero for periods of complete rotor turns
  - This avoids interference of both BEMF and HF signals due to the leakage effect
- Both, the  $d$  and  $q$  axes should be magnetized simultaneously in order to avoid the need for separate measurement periods
  - This disqualifies uniaxial injection schemes
- Ideally, the HF scheme should be processible completely offline to allow comparing the influence of different effects on the exact same set of data
  - This leads again to open-loop voltage injection rather than HF current control that would rely on online processing of measurements that might be distorted by different effects – analyzing these effects would be more difficult since the influence of the online processes must be considered

In order to comply with all requirements, a rotating small signal voltage injection scheme is proposed. The online part of the scheme is kept simple, as only a voltage vector rotating at constant speed and amplitude is computed and added to the fundamental field oriented current controller output. During the measurement periods of 15 rotor turns, the FOC dynamics are strongly reduced to avoid interference of the current controllers with the HF signals. No further changes are necessary to integrate the HF measurement scheme into the existing BEMF scheme.

The offline process of determining the flux linkage information from the measured currents consists of three separate tasks:

1. Separating the HF current signal from all other harmonic components
2. Determining the differential inductances as accurate as possible
3. Computing the flux linkages from those inductance maps

The third step is already described in Chapter 5. The steps one and two are discussed in the following subsections. Since the optimal way of extracting the HF current signal from the measurements depends on the typical small signal current response to rotating voltages for linearized SM models, this issue is addressed first.

#### 6.4.1.1 Small Signal HF Current Response to Rotating Voltage Injection

The basis for analyzing the current response to rotating voltage excitation is the linearized small signal model as described in section 2.2.3. When rewriting (2.70) in state space representation, we obtain

$$\frac{d}{dt} \mathbf{i}_{s,\Delta}^r = \mathbf{A}^r \mathbf{i}_{s,\Delta}^r + \mathbf{B}^r \mathbf{u}_{s,\Delta}^r, \quad (6.17)$$

where the system matrix  $\mathbf{A}^r$  and the input matrix  $\mathbf{B}^r$  for SM models in rotor coordinates are given by

$$\mathbf{A}^r = -\mathbf{L}_{s,op}^r{}^{-1} (R_s \mathbf{I} + \omega_{r,op} \mathbf{J} \mathbf{L}_{s,op}^r), \quad (6.18)$$

$$\mathbf{B}^r = \mathbf{L}_{s,op}^r{}^{-1}, \quad (6.19)$$

and the  $\Delta$ -operands indicating the approximative small-signal character of the model are moved to the indices for conciseness.

It is worth noting that (6.17) is accurately describing the small signal current progression as long as the absolute current,  $\mathbf{i}_s^r = \mathbf{i}_{s,op}^r + \mathbf{i}_{s,\Delta}^r$ , remains sufficiently close to the operating point for which the parameters  $\omega_{r,op}$  and  $\mathbf{L}_{s,op}^r$  are valid. Besides this prerequisite, no further simplifications are necessary. The actual rotor speed as well as the ohmic voltage at the stator resistance are considered.

Note also, that the large signal model (2.72) is negligible without further error, when proper filter techniques are applied to separate the HF signal components from the rest of the measurements since in this case the constant operating point offsets are filtered out.

When, during the measurement periods, the operating point is constant and the HF signal remains sufficiently small, equation (6.17) is a *linear, time-invariant* (LTI) system. The general solution of this *inhomogeneous differential equation* is the sum of the *homogenous solution* and the *particular solution* [74 pp. 706-707]. The homogenous solution describes the transient current progression as a result of its initial value at the time  $t_0$  without any input signal. The particular solution describes the system response to any given input signal. Both solutions are found by means of the matrix exponential of the system matrix. It is defined analogously to the Taylor series expansion of the scalar exponential function as

$$\exp(\mathbf{A}t) = \sum_{n=0}^{\infty} \mathbf{A}^n \frac{t^n}{n!}. \quad (6.20)$$

The solution of (6.17) is now given by

$$\mathbf{i}_{s,\Delta}^r(t) = \exp(\mathbf{A}^r(t-t_0)) \mathbf{i}_{s,\Delta}^r(t_0) + \int_{t_0}^t \exp(\mathbf{A}^r(t-\tau)) \mathbf{B}^r \mathbf{u}_{s,\Delta}^r(\tau) d\tau, \quad (6.21)$$

where the first term on the RHS is the homogeneous solution and the second term is the particular solution.

Analogously to the Fourier series of space vectors in section 2.4.1, we now assume a rotating voltage input vector,  $\mathbf{u}_{s,k}^r$ , with constant amplitude,  $u_{s,k}$ , constant rotational frequency,  $\omega_k$ , and an initial phase,  $\phi_{u,k}$ , such that

$$\mathbf{u}_{s,k}^r(t) = u_{s,k} \mathbf{T}(\omega_k t + \phi_{u,k}) \mathbf{e}_1. \quad (6.22)$$

In Appendix B.6 it is shown that for this special case of rotating input vectors, the integral in the particular solution acc. to (6.21) can be solved analytically. The sum of homogeneous and particular solution results in

$$\mathbf{i}_{s,HF}^r(t) = \exp(\mathbf{A}^r(t-t_0)) (\mathbf{i}_{s,HF}^r(t_0) - \mathbf{K}_p^r \mathbf{u}_{s,k}^r(t_0)) + \mathbf{K}_p^r \mathbf{u}_{s,k}^r(t), \quad (6.23)$$

where  $\mathbf{K}_p^r$  is a matrix describing the particular solution of (6.17). It can be calculated from the system and input matrices by

$$\mathbf{K}_p^r = -(\mathbf{A}^r + \omega_k^2 \mathbf{I})^{-1} (\mathbf{A}^r \mathbf{B}^r + \omega_k \mathbf{B}^r \mathbf{J}). \quad (6.24)$$

It is worth noting that, for a given operating point,  $\mathbf{K}_p^r$  is a constant matrix, which translates a rotating small signal voltage vector at any time into a corresponding current vector at that same time.

We can see from (6.23), that the overall system response consists of two components – one describing the exponentially decaying<sup>12</sup> response to the initial current and voltage vectors and the other describing the steady state current response. This basically opens up two possibilities for parameter identification techniques. Either the steady state current response or the transient current response to given initial current and voltage vectors can be analyzed. We will choose the first possibility within this work, since we know from section 2.4 that Fourier analysis allows to accurately separate the relevant rotating voltage and current space vectors from all the fundamental and harmonic components that might impair our results. Additionally, the transient processes can be easily eliminated by waiting a sufficient amount of time<sup>13</sup> after activating the voltage injection at a given operating point, before starting the measurement.

We do thus only have to focus on  $\mathbf{K}_p^r$  to find a way to determine the inductance matrix  $\mathbf{L}_{s,op}^r$ , which is contained in both, the system and the input matrices. When substituting the latter acc. to (6.18) and (6.19) into (6.24), we obtain (see Appendix B.7 for details)

---

<sup>12</sup> Given that the real components of all eigenvalues of  $\mathbf{A}^r$  are negative, see also Section 6.4.1.3

<sup>13</sup> For all eigenvalues of  $\mathbf{A}^r$ ,  $\Re\{\lambda_n\}(t-t_0) \leq -5$  must be ensured, see also Section 6.4.1.3

$$\mathbf{K}_p^r = (R_s^2 \mathbf{I} + 2\omega_{r,op} R_s L_\Sigma \mathbf{J} + (\omega_k^2 - \omega_{r,op}^2) \mathbf{L}_{s,op}^r)^{-1} (R_s \mathbf{I} - (\omega_k - \omega_{r,op}) \mathbf{L}_{s,op}^r \mathbf{J}). \quad (6.25)$$

We can see that  $\mathbf{K}_p^r$  is a nonlinear function of  $\mathbf{L}_{s,op}^r$  and the presence of the latter in the inverse expression as well as in the numerator makes it difficult to solve (6.25) for  $\mathbf{L}_{s,op}^r$ . We can also note that  $\mathbf{K}_p^r$  contains the mean inductance,  $L_\Sigma$ , as it was defined in the theory section about sensorless control (see section 2.2.3 from pages 42 to 49). This is the key to obtain the desired results. When splitting up  $\mathbf{L}_{s,op}^r$  into its mean and anisotropic components, we get

$$\mathbf{L}_{s,op}^r = L_\Sigma \mathbf{I} + L_{A,\Delta} \mathbf{S}(\vartheta_A). \quad (6.26)$$

By substituting (6.26) into (6.25) and performing several simplifications, that are described in Appendix B.7, we can find

$$\mathbf{K}_p^r = \frac{N_{I+} \mathbf{I} + N_{J+} \mathbf{J} + (N_{I-} \mathbf{I} + N_{J-} \mathbf{J}) \mathbf{S}(\vartheta_A)}{D} \quad (6.27)$$

where the numerator terms are

$$N_{I+} = R_s \left( R_s^2 + (\omega_k - \omega_{r,op}) \left( L_\Sigma^2 (\omega_k - \omega_{r,op}) + L_{A,\Delta}^2 (\omega_k + \omega_{r,op}) \right) \right), \quad (a)$$

$$N_{J+} = - \left( (\omega_k + \omega_{r,op}) L_\Sigma \left( R_s^2 + (\omega_k - \omega_{r,op})^2 (L_\Sigma^2 - L_{A,\Delta}^2) \right) \right), \quad (b) \quad (6.28)$$

$$N_{I-} = -2R_s L_\Sigma L_{A,\Delta} \omega_k (\omega_k - \omega_{r,op}), \quad (c)$$

$$N_{J-} = (\omega_k - \omega_{r,op}) L_{A,\Delta} \left( R_s^2 - (\omega_k^2 - \omega_{r,op}^2) (L_\Sigma^2 - L_{A,\Delta}^2) \right) \quad (d)$$

and the denominator is

$$D = R_s^2 \left( R_s^2 + 2 \left( (\omega_k^2 + \omega_{r,op}^2) L_\Sigma^2 + (\omega_k^2 - \omega_{r,op}^2) L_{A,\Delta}^2 \right) \right) + (\omega_k^2 - \omega_{r,op}^2)^2 (L_\Sigma^2 - L_{A,\Delta}^2)^2. \quad (6.29)$$

When analyzing the structure of  $\mathbf{K}_p^r$  acc. to (6.27), we see that all machine parameters are contained in scalar expressions that either scale the unit matrix,  $\mathbf{I}$ , or the 90° rotational matrix,  $\mathbf{J}$ . Additionally, there is an expression that is multiplied with the double-angle rotational matrix,  $\mathbf{S}(\vartheta_A)$ , which was found already in (2.107) to be

$$\mathbf{S}(\vartheta) = \mathbf{T}(2\vartheta) \mathbf{X}. \quad (6.30)$$

It is important to remind that the matrix  $\mathbf{X}$  is the analogon to the conjugate complex operator, which flips a vector along the axis of abscissae. For the product of  $\mathbf{T}(\vartheta)$  and  $\mathbf{X}$ , we can find the relation

$$\mathbf{T}(\vartheta) \mathbf{X} = \mathbf{X} \mathbf{T}(-\vartheta). \quad (6.31)$$

We can now find that the product of  $\mathbf{S}(\vartheta_A)$  and the rotating voltage vector acc. to (6.22) results in

$$\mathbf{S}(\vartheta_A) \mathbf{u}_{s,k}^r(t) = u_{s,k} \mathbf{T}(2\vartheta_A) \mathbf{X} \mathbf{T}(\phi_{u,k}) \mathbf{T}(\omega_k t) \mathbf{e}_1. \quad (6.32)$$

By applying (6.31), we can eliminate  $\mathbf{X}$  by moving it to the right, where it cancels out when multiplied with the unit vector  $\mathbf{e}_1$ . We then finally see that the product of  $\mathbf{S}(\vartheta_A)$  and  $\mathbf{u}_{s,k}^r(t)$  gives us a vector rotating in reverse direction of  $\mathbf{u}_{s,k}^r(t)$ .

$$\mathbf{S}(\vartheta_A)\mathbf{u}_{s,k}^r(t) = u_{s,k} \mathbf{T}(2\vartheta_A)\mathbf{T}(-\phi_{u,k})\mathbf{T}(-\omega_k t) \underbrace{\mathbf{X}\mathbf{e}_1}_{\mathbf{e}_1}. \quad (6.33)$$

Since only one term in (6.27) contains  $\mathbf{S}(\vartheta_A)$ , we can state that  $\mathbf{K}_p^r$  splits up the steady state current response to a rotating voltage vector into two current vectors – one rotating in same and one rotating in opposite direction. This is why the numerator terms in (6.28) are denoted with the indices + (same direction) and – (reverse direction).

The graphical interpretation of this statement is shown in Figure 6.10. It reveals that the current response of synchronous machines to a rotating voltage vector is generally elliptic. When we split up  $\mathbf{K}_p^r$  into its + and – parts and remind the fact known from section 2.4.1 that  $\omega_k = -\omega_{-k}$ , we obtain the respective pos. and neg. rotating current vectors,

$$i_{s,k}\mathbf{T}(\phi_{i,k})\mathbf{T}(\omega_k t)\mathbf{e}_1 = \frac{N_{I+}\mathbf{I} + N_{J+}\mathbf{J}}{D} u_{s,k}\mathbf{T}(\phi_{u,k})\mathbf{T}(\omega_k t)\mathbf{e}_1, \quad (a)$$

$$i_{s,-k}\mathbf{T}(\phi_{i,-k})\mathbf{T}(\omega_{-k} t)\mathbf{e}_1 = \frac{N_{I-}\mathbf{I} + N_{J-}\mathbf{J}}{D} u_{s,k}\mathbf{T}(2\vartheta_A)\mathbf{T}(-\phi_{u,k})\mathbf{T}(-\omega_k t)\mathbf{e}_1. \quad (b)$$

When expressing the matrices  $\mathbf{I}$  and  $\mathbf{J}$  in terms of the rotation matrix, we get

$$\mathbf{I} = \mathbf{T}(0), \quad (a)$$

$$\mathbf{J} = \mathbf{T}(\pi/2) \quad (b)$$

and can state that only rotation matrices occur in (6.34). Since those matrices are commutative, i.e.

$$\mathbf{T}(\vartheta_1)\mathbf{T}(\vartheta_2) = \mathbf{T}(\vartheta_2)\mathbf{T}(\vartheta_1), \quad (6.36)$$

we can simplify and rewrite (6.34) as

$$i_{s,k}\mathbf{T}(\phi_{i,k})\mathbf{e}_1 = u_{s,k}\mathbf{T}(\phi_{u,k})\frac{N_{I+}\mathbf{I} + N_{J+}\mathbf{J}}{D}\mathbf{e}_1, \quad (a)$$

$$i_{s,-k}\mathbf{T}(\phi_{i,-k})\mathbf{e}_1 = u_{s,k}\mathbf{T}(2\vartheta_A)\mathbf{T}(-\phi_{u,k})\frac{N_{I-}\mathbf{I} + N_{J-}\mathbf{J}}{D}\mathbf{e}_1. \quad (b)$$

When analyzing the last terms on the RHS of (6.37), we see a vector sum of the unit vector  $\mathbf{e}_1$  scaled by  $N_{I\pm}/D$  and the unit vector  $\mathbf{e}_2 = \mathbf{J}\mathbf{e}_1$  scaled by  $N_{J\pm}/D$ , as indicated in Figure 6.11. We can now easily see that the last terms rotate the unit vector  $\mathbf{e}_1$  by  $\text{atan2}(N_{J\pm}, N_{I\pm})$  and scale it by  $\sqrt{N_{I\pm}^2 + N_{J\pm}^2}/D$ . We thus rewrite (6.37) as

$$i_{s,k}\mathbf{T}(\phi_{i,k})\mathbf{e}_1 = u_{s,k}\frac{\sqrt{N_{I+}^2 + N_{J+}^2}}{D}\mathbf{T}(\phi_{u,k})\mathbf{T}(\text{atan2}(N_{J+}, N_{I+}))\mathbf{e}_1, \quad (a)$$

$$i_{s,-k}\mathbf{T}(\phi_{i,-k})\mathbf{e}_1 = u_{s,k}\frac{\sqrt{N_{I-}^2 + N_{J-}^2}}{D}\mathbf{T}(2\vartheta_A)\mathbf{T}(-\phi_{u,k})\mathbf{T}(\text{atan2}(N_{J-}, N_{I-}))\mathbf{e}_1. \quad (b)$$

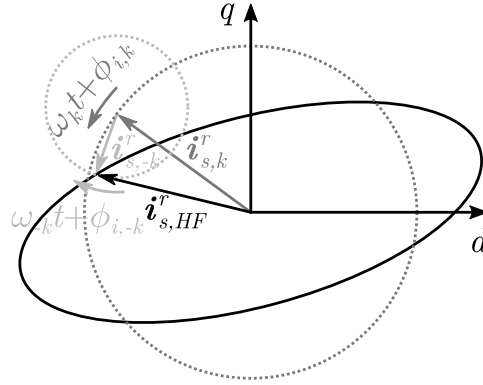


Figure 6.10: Elliptic HF current trajectory as sum of two vectors rotating in mathematically positive and negative direction each with constant amplitude and frequency

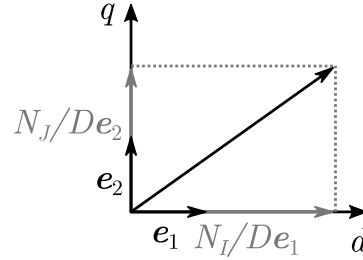


Figure 6.11: Graphical interpretation of the last terms on the RHS of (6.37)

By comparing the amplitudes and phases of the vectorial equations (6.38), we find the current amplitudes

$$i_{s,k} = u_{s,k} \frac{\sqrt{N_{I+}^2 + N_{J+}^2}}{D}, \quad (\text{a}) \quad (6.39)$$

$$i_{s,-k} = u_{s,k} \frac{\sqrt{N_{I-}^2 + N_{J-}^2}}{D} \quad (\text{b})$$

and the phases

$$\phi_{i,k} = \phi_{u,k} + \text{atan2}(N_{J+}, N_{I+}), \quad (\text{a}) \quad (6.40)$$

$$\phi_{i,-k} = 2\vartheta_A - \phi_{u,k} + \text{atan2}(N_{J-}, N_{I-}). \quad (\text{b})$$

From (6.28), (6.39) and (6.40), we can draw the following conclusions:

- The current amplitudes are proportional to the voltage amplitude
- Since both,  $N_{I-}$  and  $N_{J-}$  are proportional to  $L_{A,\Delta}$ , there is no reversely rotating current in magnetically isotropic machines
- The current amplitudes do not depend on the voltage phase
- The current phases do not depend on the voltage amplitude

- Only the phase of the reversely rotating current vector contains information about the magnetic anisotropy angle,  $\vartheta_A$

Another important aspect to note is that (6.39) and (6.40) describe the steady state current response to a voltage vector rotating circularly with  $\omega_k$ . If the applied voltage is elliptic (or, in its most extreme form, alternating), there is also a negatively rotating voltage component, which itself produces two current vectors in same and reverse rotating directions. The respective current vectors rotating in the same direction superimpose, such that we get the much more complicated expressions

$$i_{s,k} = \sqrt{u_k^2 F_k^2 + u_{-k}^2 F_{-k}^2 + 2u_k u_{-k} F_k F_{-k} \cos(\phi_{u,k} + \phi_{u,-k} + \Phi_k - \Phi_{-k} - 2\vartheta_A)}, \quad (a)$$

$$i_{s,-k} = \sqrt{u_{-k}^2 F_k^2 + u_k^2 F_{-k}^2 + 2u_k u_{-k} F_k F_{-k} \cos(\phi_{u,k} + \phi_{u,-k} + \Phi_k - \Phi_{-k} - 2\vartheta_A)} \quad (b)$$

and

$$\phi_{i,k} = \text{atan2}(u_k F_k \sin(\phi_{u,k} + \Phi_k) + u_{-k} F_{-k} \sin(-\phi_{u,-k} + 2\vartheta_A + \Phi_{-k}), \\ u_k F_k \cos(\phi_{u,k} + \Phi_k) + u_{-k} F_{-k} \cos(-\phi_{u,-k} + 2\vartheta_A + \Phi_{-k})), \quad (a)$$

$$\phi_{i,-k} = \text{atan2}(u_{-k} F_k \sin(\phi_{u,-k} + \Phi_k) + u_k F_{-k} \sin(-\phi_{u,k} + 2\vartheta_A + \Phi_{-k}), \\ u_{-k} F_k \cos(\phi_{u,-k} + \Phi_k) + u_k F_{-k} \cos(-\phi_{u,k} + 2\vartheta_A + \Phi_{-k})), \quad (b)$$

where

$$F_k = \frac{\sqrt{N_{I+}^2 + N_{J+}^2}}{D}, \quad (a)$$

$$F_{-k} = \frac{\sqrt{N_{I-}^2 + N_{J-}^2}}{D}, \quad (b) \quad (6.43)$$

$$\Phi_k = \text{atan2}(N_{J+}, N_{I+}), \quad (c)$$

$$\Phi_{-k} = \text{atan2}(N_{J-}, N_{I-}). \quad (d)$$

#### 6.4.1.2 Determining the Differential Inductances

The former subsection has excessively discussed the current responses of synchronous machines to rotating voltage vectors. When both, the applied voltages and the resulting currents are known, these results allow us to determine the inductance matrix. According to (6.26), we need to identify the three parameters  $L_\Sigma$ ,  $L_{A,\Delta}$  and  $\vartheta_A$  to reconstruct  $\mathbf{L}_{s,op}^r$ . The best way to obtain this for circularly rotating voltages, as in the given case, is to split up the problem into two steps. We have two equations acc. to (6.39) which can be solved for the two unknowns  $L_\Sigma$  and  $L_{A,\Delta}$  and in a second step we can directly determine  $\vartheta_A$  from (6.40).

Manually solving (6.39) for  $L_\Sigma$  and  $L_{A,\Delta}$ , however, is not an easy task, since we have to calculate the squares of the numerator and denominator expressions (6.28) and (6.29). This leads to fractions with fourth degree polynomials of  $L_\Sigma$  and  $L_{A,\Delta}$  in both, numerator and

denominator. By means of the *symbolic math toolbox for MATLAB* [115], however, it was possible to find the solutions

$$L_{\Sigma} = \frac{\sqrt{\left(i_k u_k (\omega_k - \omega_{r,op})\right)^2 - \left(R_s \left((i_k^2 + i_{-k}^2) \omega_k - (i_k^2 - i_{-k}^2) \omega_{r,op}\right)\right)^2}}{(i_k^2 - i_{-k}^2)(\omega_k^2 - \omega_{r,op}^2)}, \quad (a)$$

$$L_{A,\Delta} = \pm \frac{i_{-k} \sqrt{u_k^2 (\omega_k - \omega_{r,op})^2 - 4R_s^2 (i_{-k}^2 \omega_k^2 - (i_k^2 - i_{-k}^2) \omega_k \omega_{r,op})}}{(i_k^2 - i_{-k}^2)(\omega_k^2 - \omega_{r,op}^2)}, \quad (b)$$

where  $L_{A,\Delta}$  acc. to (6.44)(b) is negative for PMSMs and positive for SynRMs in accordance with its definition in section 2.2.3.

After determining  $L_{\Sigma}$  and  $L_{A,\Delta}$ , we can calculate  $\vartheta_A$  from (6.40). It is convenient to eliminate the phase of the voltage vector by computing the sum of (6.40)(a) and(b). Solving the result for  $\vartheta_A$  gives us

$$\vartheta_A = \frac{1}{2} (\phi_{i,k} + \phi_{i,-k} - \text{atan2}(N_{J+}, N_{I+}) - \text{atan2}(N_{J-}, N_{I-})). \quad (6.45)$$

It is well worth noting that the anisotropy position is a nonlinear function of the resistance,  $R_s$ , as well as of the rotor speed,  $\omega_{r,op}$ . To the authors knowledge, all anisotropy based sensorless algorithms neglect one or both of these parameters. By means of (6.45), it is possible to predict the resulting estimation errors. This issue is taken up again in the discussion of the results in section 6.5.

#### 6.4.1.3 Obtaining Accurate Current and Voltage Measurements

The equations (6.44) show us that the inductance parameters of synchronous machines are nonlinear functions of the rotating HF voltage and current space vector amplitudes. We do thus have to determine these amplitudes of the fundamental HF voltage and current vectors as precisely as possible. As mentioned before, this is done by Fourier analysis and there are some points to be taken into account. These points are addressed in this subsection.

The theoretic foundations of the Fourier analysis for space vectors were set in section 2.4. It was shown that two effects, that always occur in sampled signals, should be considered, when Fourier analysis is applied to reconstruct the underlying continuous signal: the leakage effect and the aliasing effect.

The leakage effect does only occur, when spectral components are present that are nonperiodic to the measurement time range. However, if this cannot be avoided completely, it was shown that by increasing the measurement times, the leakage effect can be reduced as much as needed.

The aliasing effect is more difficult to handle with the given rapid prototyping system as described in section 3.1. For the given PWM at a sampling frequency of  $f_S = 10\text{kHz}$ , it cannot be guaranteed that the measured current signal is limited in bandwidth to remain within the Nyquist band of  $\pm f_S/2$ . How eventually occurring alias frequencies can be effectively eliminated, is analyzed in the following.

In section 2.3, it was shown how voltage source inverters apply modulation techniques to reconstruct continuous reference voltages. In consequence, the voltages applied to the machine are sequences of discrete voltage space vectors. The progression of the voltages in time can thus be mathematically expressed as *piecewise constant* (PWC) vector function.

When we consider such a PWC function with  $m$  sections, where during each section from time  $t_i$  to  $t_{i+1}$  the voltage space vector in stator coordinates,  $\mathbf{u}_i^s$ , is constant, we can determine its Fourier coefficients by (see Appendix B.8 for details)

$$\mathbf{u}_0^s = \frac{1}{T_1} \sum_{i=1}^m ((t_{i+1} - t_i) \mathbf{u}_i^s), \quad (\text{a})$$

$$\mathbf{u}_k^s = \frac{1}{k\pi} \sum_{i=1}^m \left( \sin \left( \frac{k\pi}{T_1} (t_i - t_{i-1}) \right) \mathbf{T} \left( -\frac{k\pi}{T_1} (t_i + t_{i-1}) \right) \mathbf{u}_i^s \right), \quad \forall k \in \mathbb{Z}, k \neq 0. \quad (\text{b})$$

Equation (6.46) allows us to analyze the harmonic spectrum of a rotating HF voltage vector, which is modulated by the VSI at a constant sampling frequency,  $F_S$ . When assuming an HF rotating voltage reference,

$$\mathbf{u}_{HF}^s = u_{HF} \mathbf{T}(\omega_{HF} t_i + \phi_{u, HF}) \mathbf{e}_1, \quad (\text{6.47})$$

and determining the resulting modulated PWC voltages,

$$\mathbf{u}_i^s = \text{SVM}(\mathbf{u}_{HF}^s), \quad (\text{6.48})$$

as well as the switching times as described in section 2.3.2, we can see that the space vector modulation influences the fundamental component of that HF signal and also introduces harmonic components that are far above the Nyquist frequency. This is exemplarily illustrated in Figure 6.12 for an HF signal with  $\phi_{u, HF} = 0$  rotating at a frequency of  $f_S/3$ , thus leading to a triangular signal after the SVM. From top to bottom, the results for reference vectors of length  $2/3 u_{DC}$ ,  $1/\sqrt{3} u_{DC}$  and  $0.1/\sqrt{3} u_{DC}$  are shown.

The first case describes the maximum possible triangle the VSI can supply. As the triangle is aligned with the  $u, v, w$  axes, no modulation is necessary – the respective voltage vectors are applied for complete PWM cycles, as shown in (b). Subfigure (a) shows the corresponding harmonic spectrum normalized to the reference amplitude corrected by the mean saturation factor,  $\bar{k}_{sat}$ , of the SVM. We can see that the fundamental component of the HF signal is approximately  $0.83 u_{HF} \bar{k}_{sat}$ . We thus inject at a lower amplitude than desired. Additionally, harmonic components occur, even if they decrease relatively fast at higher frequencies.

While the first case describes a simple discretization by a *zero-order hold* (ZOH), the second and third cases demonstrate the effect of the SVM for large (second case) and small (third case) HF amplitudes. The modulation introduces new discontinuities, which result in higher harmonic components. With decreasing active voltage vector period lengths, the harmonic spectrum widens up and the fundamental component slightly increases. For the third case at small signal injection, we can observe a wide spectrum of harmonics converging to two nested sinc functions. The amplitude of the fundamental HF voltage is approximately  $0.87 u_{HF} \bar{k}_{sat}$ .

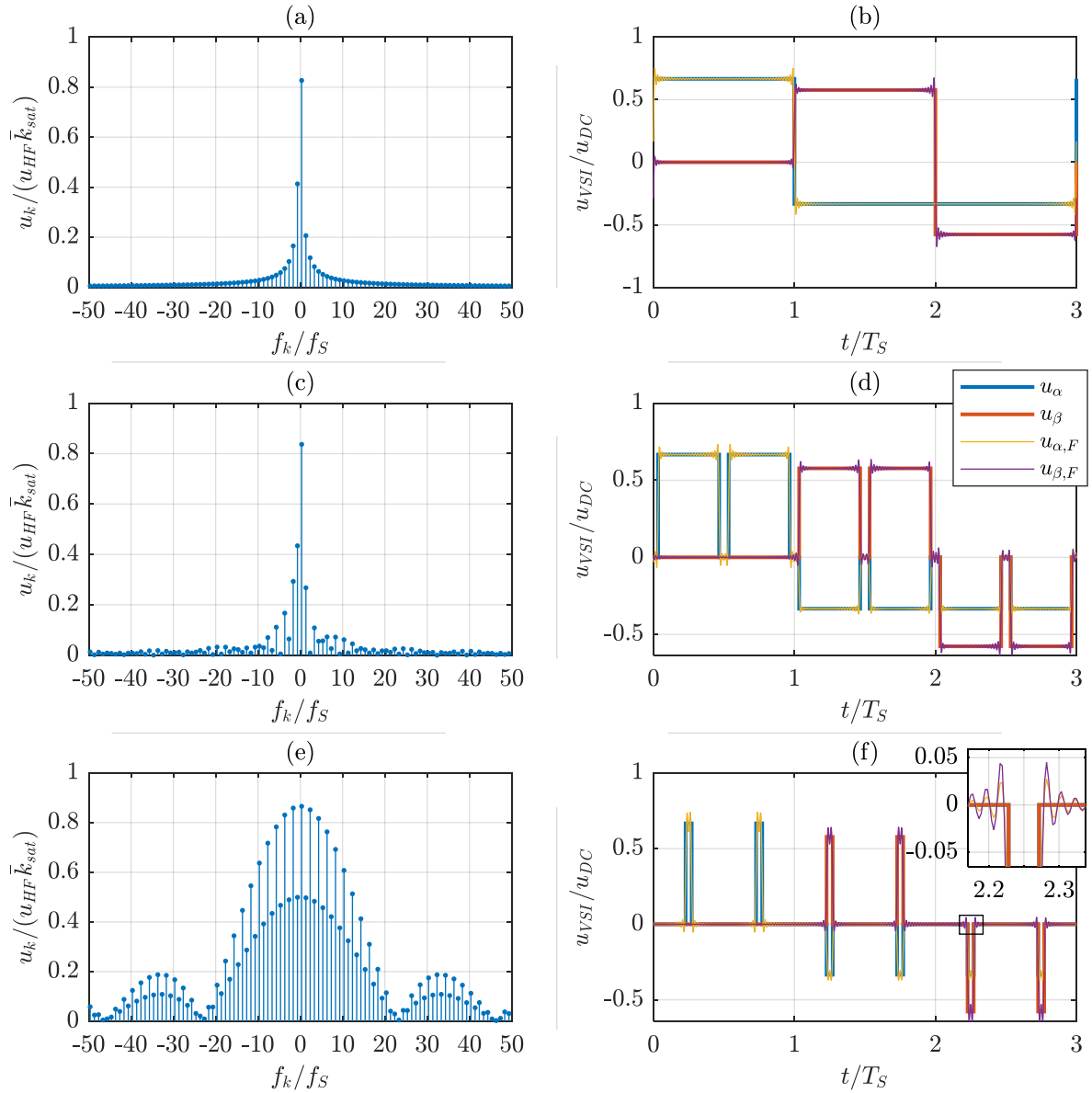


Figure 6.12: Fourier analysis of PWC voltage space vectors resulting from the SVM of reference vectors rotating with  $f_s/3$  and with amplitudes of  $2/3 u_{DC}$  (top),  $1/\sqrt{3} u_{DC}$  (middle) and  $0.1/\sqrt{3} u_{DC}$  (bottom); the left subfigures show the normalized amplitudes of the spectral components of the corresponding VSI output voltages in time domain shown on the right (thick lines); for comparison, also the respective Fourier series are plotted (thin lines)

Note that the problem worsens when the HF injection is superimposed by a FOC voltage component. This is shown in Figure 6.13 for the same injection voltages but with a FOC voltage that corresponds to the ohmic voltage at the stator resistance, when the IPMSM is loaded at rated torque at standstill.

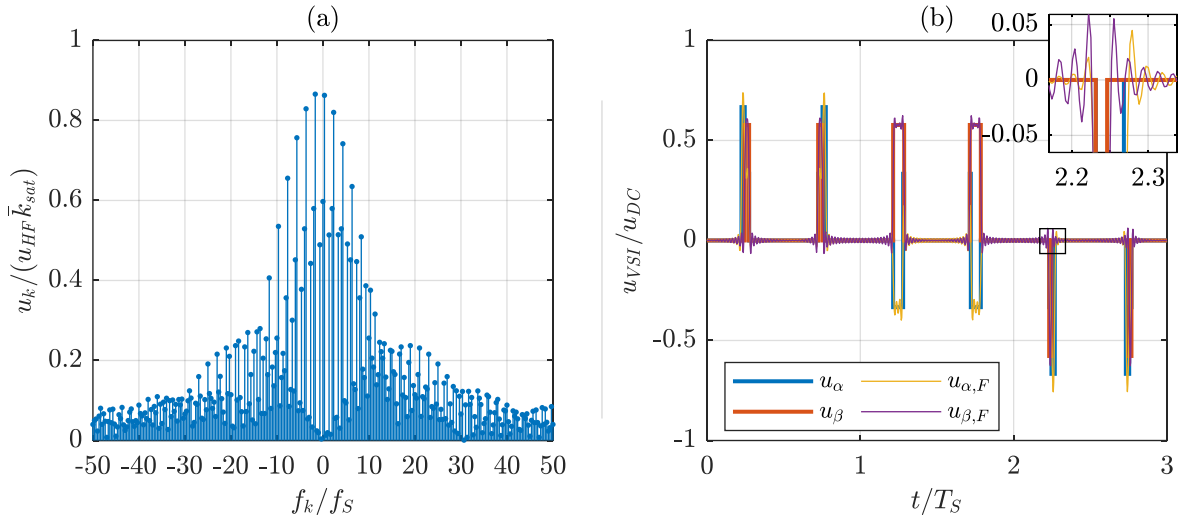


Figure 6.13: Fourier analysis of a PWC voltage space vector resulting from the SVM of the sum of the reference vector from Figure 6.12 (e) and (f) and a constant voltage vector corresponding to the ohmic voltage at the phase resistances of the IPMSM at rated load at standstill; the left subfigure shows the normalized amplitudes of the spectral components of the corresponding VSI output voltages in time domain shown on the right (thick lines); for comparison, also the respective Fourier series are plotted (thin lines)

We see that the FOC voltage causes unsymmetrical voltage curves and thus introduces additional harmonic components. While the influence on the fundamental HF components is not noticeable here, we see in the following that there can be differences in other cases.

We can conclude for now that the SVM causes two problems:

1. the amplitude of the injected signal is smaller than the reference signal; for triangular injection, for instance, it ranges from approximately 83% to 87%, depending on the modulation level
2. instead of injecting a single voltage vector rotating at one specific frequency, we inject several vectors with different amplitudes rotating at harmonic frequencies well outside the Nyquist band; when measuring the resulting current responses at a sampling rate of  $F_S$ , we can expect the occurrence of harmonic components at alias frequencies, leading to measurement errors

The first problem is further analyzed in Figure 6.14 for the given system with a sampling rate of  $f_S = 10\text{kHz}$  and positive injection frequencies within the Nyquist band from 0 to 5kHz. The amplitudes of the resulting fundamental HF components as shown in Figure 6.14 (a) are normalized to the eventually saturated reference amplitude. In addition to the modulated curves, the fundamental component of the reference signal discretized with a ZOH is plotted.

We can see that the fundamental amplitudes decrease with increasing frequencies and with increasing reference amplitudes. While the ZOH curve is continuous, we can find discontinuities

in the modulated curves, as exemplarily highlighted by the three zoomed plots. The discontinuities typically occur at frequencies that lead to injection patterns that are at least partly aligned with the phase axes and thus have time periods, where only one active space vector is applied.

Please note that the discontinuities in the middle, zoomed window around 3.33kHz correspond to the first two cases of triangular injection from Figure 6.12. As already mentioned, the special case of triangular injection aligned with the phase axes at maximum modulation level corresponds to ZOH discretization. In contrast, with reduced reference amplitude, zero vectors occur, and the resulting additional switching operations introduce higher harmonics but also increase the fundamental amplitude.

In Figure 6.14(b), we see that the SVM causes a phase shift of the injected voltage vector that decreases linearly with increasing frequency. The phase shift does not depend on the modulation level and is the same as for ZOH discretization.

As discussed in section 2.3.2, the SVM requires to identify the actual sector of the reference vector, which makes it difficult to express the SVM algorithm in a closed mathematical form without case discriminations. It is thus difficult to further analytically describe the harmonic distortions caused by the SVM.

The ZOH, however, is well known in literature [92 pp. 222–224] and its influence on the fundamental component of the discretized signal is given by

$$\begin{aligned} u_{1,HF} &= u_{HF} \operatorname{sinc}\left(\frac{f_{HF}}{f_S}\right), & (a) \\ \phi_{u,1,HF} &= \phi_{u,HF} - \pi \frac{f_{HF}}{f_S}. & (b) \end{aligned} \quad (6.49)$$

With the above analysis, we are able to calculate the series of rotating voltage space vectors that are applied to the synchronous machine. The next step is to correctly determine the relevant HF current response.

With equation (6.23), we found the current vector response to rotating voltages. Note that the solution does also include the case of constant voltage inputs, since we can set  $\omega_k = 0$ . When we rewrite (6.23) accordingly as

$$\mathbf{i}_{s,HF}^r(t) = \exp(\mathbf{A}^r(t - t_0)) (\mathbf{i}_{s,HF}^r(t_0) - \mathbf{K}_p^r \mathbf{u}_{s,0}^r) + \mathbf{K}_p^r \mathbf{u}_{s,0}^r, \quad (6.50)$$

we see that the current response consists of a constant current vector,  $\mathbf{K}_p^r \mathbf{u}_{s,0}^r$ , and a transient term that describes the current progression from an initial state to that offset.

Analogously to the machine model in section 2.2.3.1 we can linearize (6.50) at a given operating time,  $t_{op}$ , by means of Taylor series expansion up to the first term of the Taylor polynomial and obtain

$$\mathbf{i}_{s,HF}^r(t) \approx \mathbf{i}_{s,HF}^r(t_{op}) + \left. \frac{d\mathbf{i}_{s,HF}^r(t)}{dt} \right|_{t_{op}} \Delta t, \quad (6.51)$$

where the time rate of change of the HF current vector is given by

$$\frac{d}{dt} \mathbf{i}_{s, HF}^r(t) = \mathbf{A}^r \exp(\mathbf{A}^r(t - t_0)) (\mathbf{i}_{s, HF}^r(t_0) - \mathbf{K}_p^r \mathbf{u}_{s,0}^r). \quad (6.52)$$

After substituting (6.52), (6.51) can be rewritten as

$$\mathbf{i}_{s, HF}^r(t) \approx (\mathbf{I} + \mathbf{A}^r \Delta t) \exp(\mathbf{A}^r(t_{op} - t_0)) (\mathbf{i}_{s, HF}^r(t_0) - \mathbf{K}_p^r \mathbf{u}_{s,0}^r) + \mathbf{K}_p^r \mathbf{u}_{s,0}^r. \quad (6.53)$$

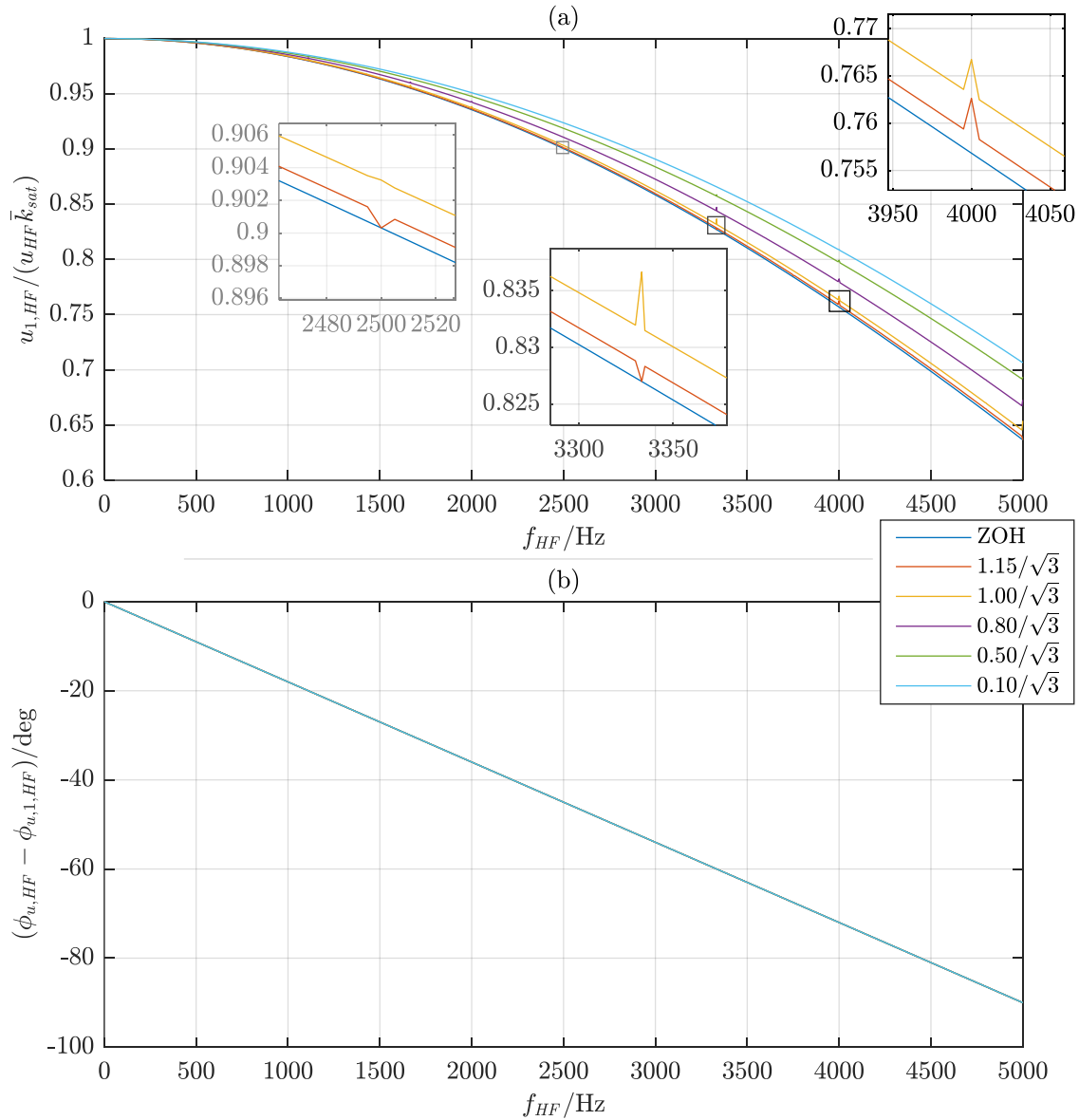


Figure 6.14: Analysis of the influence of the SVM on the fundamental component (amplitude in (a) and phase shift in (b)) of the HF reference signal at different amplitudes and frequencies

When subtracting (6.50) and (6.53), we obtain the linearization error,

$$\mathbf{e}_{lin} = \left( (\mathbf{I} + \mathbf{A}^r \Delta t) \exp(\mathbf{A}^r(t_{op} - t_0)) - \exp(\mathbf{A}^r(t - t_0)) \right) (\mathbf{i}_{s,HF}^r(t_0) - \mathbf{K}_p^r \mathbf{u}_{s,0}^r). \quad (6.54)$$

By means of eigendecomposition, we can diagonalize  $\mathbf{A}^r$  by

$$\mathbf{A}^r = \mathbf{V}^r \mathbf{D}^r \mathbf{V}^{r-1}, \quad (6.55)$$

where  $\mathbf{D}^r$  is the diagonal matrix of the eigenvalues  $\lambda_1$  and  $\lambda_2$  of  $\mathbf{A}^r$  [65 p. 113] and  $\mathbf{V}^r$  is a constant matrix containing the eigenvectors of  $\mathbf{A}^r$ .

The matrix exponential can likewise be decomposed to [65 pp. 108–109]

$$\exp(\mathbf{A}^r(t - t_0)) = \mathbf{V} \exp(\mathbf{D}^r(t - t_0)) \mathbf{V}^{-1}, \quad (6.56)$$

where

$$\exp(\mathbf{D}^r(t - t_0)) = \begin{bmatrix} \exp(\lambda_1(t - t_0)) & 0 \\ 0 & \exp(\lambda_2(t - t_0)) \end{bmatrix}. \quad (6.57)$$

With (6.55) to (6.57), the linearization error can be rewritten as

$$\mathbf{e}_{lin} = \mathbf{V} \left( (\mathbf{I} + \mathbf{D}^r \Delta t) \exp(\mathbf{D}^r(t_{op} - t_0)) - \exp(\mathbf{D}^r(t - t_0)) \right) \mathbf{V}^{-1} (\mathbf{i}_{s,HF}^r(t_0) - \mathbf{K}_p^r \mathbf{u}_{s,0}^r). \quad (6.58)$$

It thus only depends on the differences between the scalar exponential functions and their linear approximations, i.e.

$$\mathbf{e}_{lin} = \mathbf{f}(1 + \lambda_i \Delta t - \exp(\lambda_i(t - t_0))). \quad (6.59)$$

We can also see from (6.55) to (6.57) that both eigenvalues of  $\mathbf{A}^r$  must have negative real parts in order to obtain a stable transient towards the constant offset term acc. to (6.50). These real parts determine the time constants,

$$\tau_i = -\frac{1}{\Re(\lambda_i)}. \quad (6.60)$$

In VSI supplied drive systems, the PWM cycle times,  $T_S$ , are typically significantly smaller than the time constants of the synchronous machine. For the given machines, the minimum and maximum time constants within the feasible operating areas are reported in Table 7.

Table 7: Minimum and maximum time constants of the tested machines within feasible operating ranges

$\tau_i$ in ms	$\min(\boldsymbol{\tau}_1)$	$\min(\boldsymbol{\tau}_2)$	$\max(\boldsymbol{\tau}_1)$	$\max(\boldsymbol{\tau}_2)$
SynRM	5.19	7.96	60.26	75.24
IPMSM	4.34	6.63	18.67	25.02
SPMSM	5.04	6.84	11.68	13.40

It is striking out that the largest differences between the machines occur in the maximum values of the time constants, which range from 11.7ms at the SPMSM to more than 75.2ms for the SynRM. The minimum time constants, however, are comparably similar with values from 4.3ms up to 8ms.

For the given test rig with  $T_S = 100 \mu\text{s}$ , we can note that the smallest occurring time constant of all three machines is more than 43 times larger than the PWM cycle time. For the model linearized at  $t_{op} = t_0$  and when only considering the real parts of the eigenvalues, we can determine a maximal relative difference between the exponential function and its approximation acc. to (6.59) of  $\pm 0.03\%$  after a time of  $\Delta t = T_S$  (i.e. at  $t = t_0 + T_S$ ). During that time, the transient current progressions in response to a constant voltage vector can thus be assumed to be linear in good approximation.

Consequently, we can assume that a PWC voltage sequence applied to a synchronous machine leads to *piecewise affine* (PWA) current responses.

Since we are interested in the harmonic components of the PWA current response, we have to apply Fourier analysis here, as well. In literature [92 pp. 224–225], discretizing a harmonic signal by a PWA function is denoted as *first-order hold* (FOH). Its influence on the fundamental component of the discretized current signal is given by

$$i_{1,HF} = i_{HF} \text{sinc}^2 \left( \frac{f_{HF}}{f_S} \right), \quad (\text{a}) \quad (6.61)$$

$$\phi_{i,1,HF} = \phi_{i,HF}. \quad (\text{b})$$

From (6.61)(b), we see that the fundamental component of the HF current signal is not phase shifted. Since we actually do not know the ‘real’ current amplitude,  $i_{HF}$ , when measuring the currents, (6.61)(a) is only useful in so far as we can see that the scaling factor between the ‘real’ or reference signal and its fundamental component at PWA signals is the square of that same scaling factor at PWC signals acc. to (6.49).

When denoting the respective scaling factors with  $c_1$  and the phase shifts with  $\Delta\phi_1$ , we can thus write

$$c_{1,PWC} = \text{sinc} \left( \frac{f_{HF}}{f_S} \right), \quad (\text{a})$$

$$c_{1,PWA} = \text{sinc}^2 \left( \frac{f_{HF}}{f_S} \right) = c_{1,PWC}^2, \quad (\text{b}) \quad (6.62)$$

$$\Delta\phi_{1,PWC} = -\pi \frac{f_{HF}}{f_S}, \quad (\text{c})$$

$$\Delta\phi_{1,PWA} = 0. \quad (\text{d})$$

The graphical interpretation of (6.62) is shown in Figure 6.15.

In order to understand, how the two SVM problems mentioned above deteriorate our current and voltage measurements, we exemplarily calculate the small signal current response of the IPMSM at standstill and rated torque to an HF voltage vector rotating at  $F_S/3$  with an amplitude of  $0.1/\sqrt{3} u_{DC}$ . The applied motor model bases on the parameters that are obtained from the corrected BEMF measurements as shown in section 4.2. The results are shown in Figure 6.16.

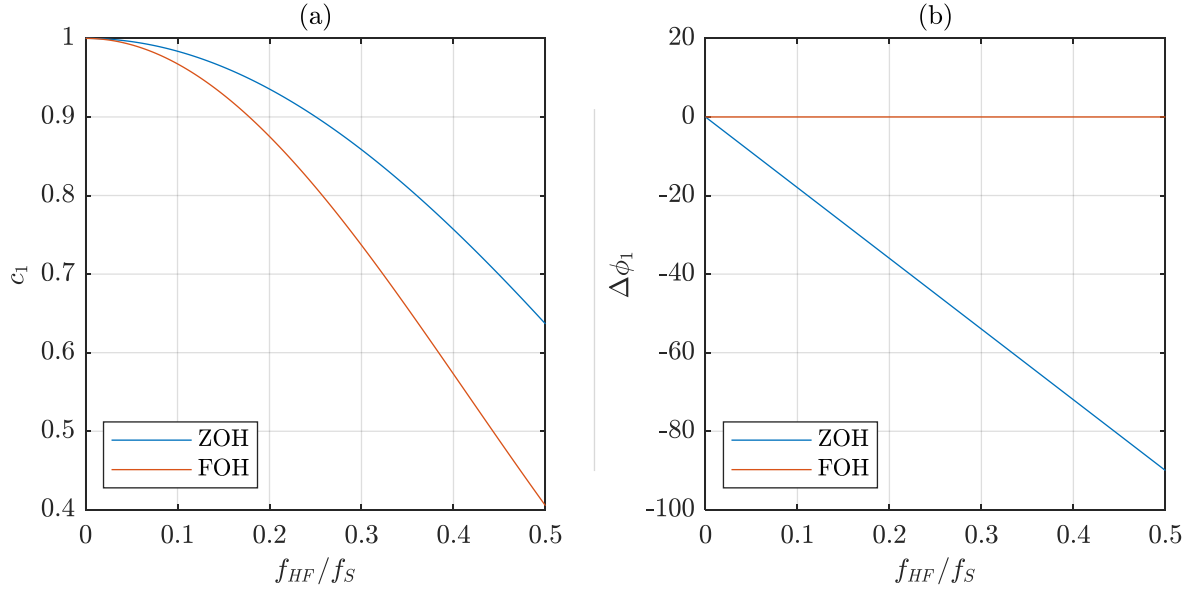


Figure 6.15: Comparison of the scaling (a) and phase shift (b) of a harmonic HF reference signal, which is discretized by means of ZOH or FOH

The modulated voltage vector and (a small section of) its spectrum are shown in (a) and (b). They are known already from Figure 6.13. The resulting current spectrum is calculated from the generic, particular steady state solution for elliptic input voltages acc. to Eqs. (6.41) and (6.42). It is shown in (d) and its corresponding Fourier series in time domain are the blue curves in (c) and (e) for the  $\alpha$  and  $\beta$  axes, respectively. As expected, we see approximately PWA current progressions with time derivative values depending on the actual constant voltage vectors.

In the description of the test rig, it was mentioned that the measured currents are analogously filtered. The filtered current signals are plotted in orange in subfigures (c), (d) and (e). In time domain, we can see that it has no relevant influence on the current at the sampling times (see purple signals). In frequency domain, this can also be observed, additionally to the fact that the filter is obviously not designed as anti-aliasing filter. The filtered current signal has relevant spectral components outside the Nyquist band from  $-F_S/2$  to  $+F_S/2$ . As we can see in (f), these components are alias frequencies. When Fourier analyzing the sampled data, we get the repeated spectrum of (f) with the superposition of all corresponding alias components.

When only considering that part of the spectrum of (f) within the Nyquist band, we get the yellow reconstructed signal in time domain as shown in subfigures (c) and (e). We can see that the Fourier series accurately predicts the currents at the sampling times. Since it neglects the PWA current progressions in between the sampling times, however, the apparent fundamental HF current components we are interested in, are obviously distorted by the aliasing effect, which can be seen by comparing the amplitudes in (d) and (f).

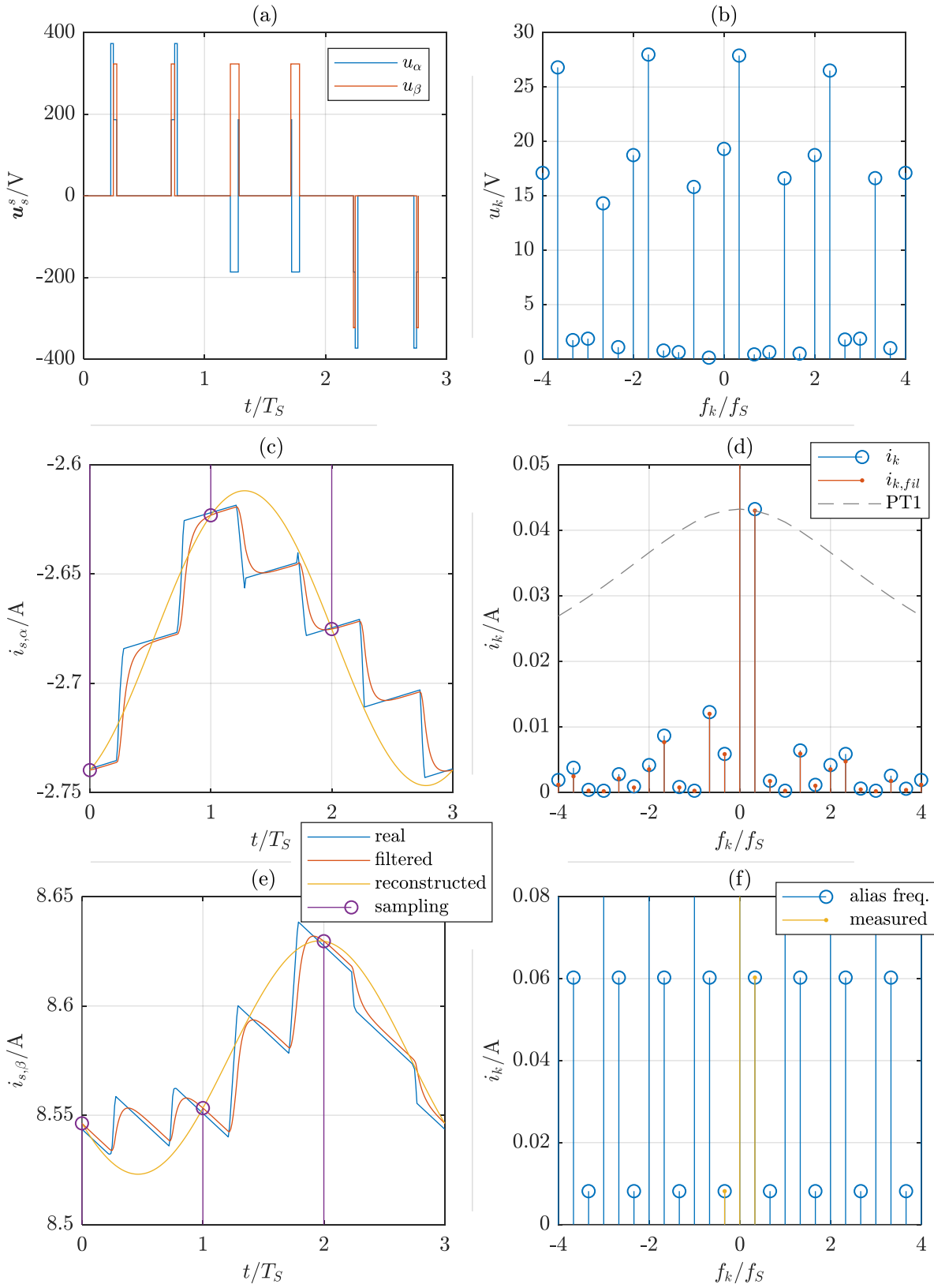
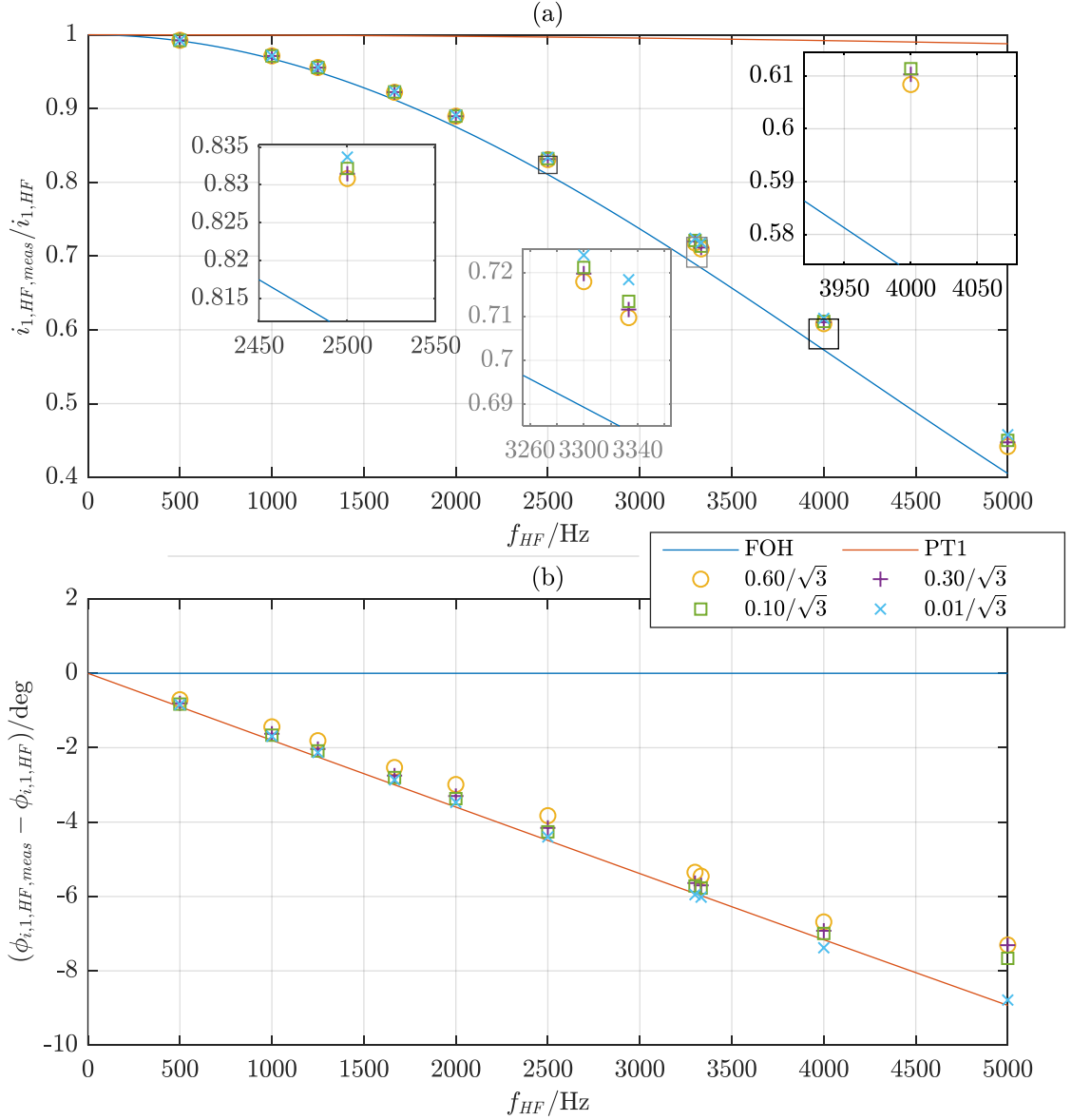


Figure 6.16: Calculated current response in  $\alpha$  (c) and  $\beta$  (e) axes to a triangular voltage injection (see (a) for modulated voltage signal in time domain and (b) for its respective spectrum); (d) shows the spectrum of the calculated current; (f) shows the apparent spectrum of the sampled current due to the aliasing effect

When we now only consider the fundamental HF current components and repeat the computations from Figure 6.16 for different injection frequencies and amplitudes, we obtain the results as shown in Figure 6.17.



We can see that the reductions of the measured fundamental current amplitudes are close to the influence of FOH discretization of harmonic signals. Moreover, when comparing the ZOH and FOH scaling factors with and without the influence of the SVM, we find the approximation

$$\frac{c_{1,PWC}}{c_{1,PWC,SVM}} \approx \frac{c_{1,PWA}}{c_{1,PWA,SVM}}. \quad (6.63)$$

By means of (6.62), we can solve (6.63) for the PWA scaling factor considering the SVM and get

$$c_{1,PWA,SVM} \approx \text{sinc} \left( \frac{f_{HF}}{F_S} \right) c_{1,PWC,SVM}. \quad (6.64)$$

With (6.64), we are now able to determine the fundamental component of the HF current response from the sampled current measurements. Although we do not know the exact current progressions in between the sampling points, the knowledge about the qualitative (namely PWA) current progressions allows us to estimate the actual fundamental current response to the applied fundamental HF voltage. In other words, we can eliminate the aliasing effect caused by the SVM by this approach.

Since we do not have a generic analytic solution for the PWC scaling factor considering the SVM,  $c_{1,PWC,SVM}$ , it must be calculated individually for each measurement series by Fourier analysis of the actual inverter duty cycles. We can then determine all scaling factors and correct the fundamental HF current and voltage components by

$$u_{1,HF} = u_{HF} c_{1,PWC,SVM}, \quad (a)$$

$$\phi_{u,1,HF} = \phi_{u,HF} - \pi \frac{f_{HF}}{F_S}, \quad (b) \quad (6.65)$$

$$i_{1,HF} = i_{1,HF,meas} c_{1,PWA,SVM}. \quad (c)$$

Note, however, that determining  $c_{1,PWC,SVM}$  requires lots of computational effort. For that reason, we substitute (6.65) into the inductance solutions (6.44) and can discover that  $c_{1,PWC,SVM}$  cancels out. We obtain

$$L_{\Sigma} = \frac{\sqrt{\left( i_{1,HF,meas} u_{HF} (\omega_{HF} - \omega_{r,op}) \right)^2 - c_{PWA} \left( R_s \left( \begin{array}{l} (i_{1,HF,meas}^2 + i_{-1,HF,meas}^2) \omega_{HF} \\ -(i_{1,HF,meas}^2 - i_{-1,HF,meas}^2) \omega_{r,op} \end{array} \right) \right)^2}}{c_{PWC} (i_{1,HF,meas}^2 - i_{-1,HF,meas}^2) (\omega_{HF}^2 - \omega_{r,op}^2)}, \quad (a) \quad (6.66)$$

$$L_{A,\Delta} = \pm \frac{i_{-1,HF,meas} \sqrt{u_{HF}^2 (\omega_{HF} - \omega_{r,op})^2 - 4R_s^2 c_{PWA} \left( \begin{array}{l} i_{-1,HF,meas}^2 \omega_{HF}^2 - \\ (i_{1,HF,meas}^2 - i_{-1,HF,meas}^2) \omega_{HF} \omega_{r,op} \end{array} \right)}}{c_{PWC} (i_{1,HF,meas}^2 - i_{-1,HF,meas}^2) (\omega_{HF}^2 - \omega_{r,op}^2)}, \quad (b)$$

and can thus determine the HF inductance parameters without computing  $c_{1,PWC,SVM}$ .

Another important point that needs to be considered for accurate results is the proper selection of HF injection frequencies. From section 2.2.3, we know that there are several sources of harmonic distortions caused by synchronous machines, such as, for instance, discrete winding distributions or magnetic saturation. Without detailed analysis, qualitative considerations lead

to the conclusions that there are harmonic space vectors rotating at integer multiples of the rotor speed.

With a maximal electrical rotor speed of 58.3Hz during the measurements within this work, we can assume that no relevant motor harmonics occur above the Nyquist frequency. We do thus not have to expect additional errors from the aliasing effect due to motor harmonics.

We should, however, avoid interference of these harmonics with the HF signal. The injection frequencies should thus be chosen such that they are non-integer multiples of the rotor speed,  $f_m$ . On the other hand, they should allow practicable measurement time periods, that contain complete rotor turns as well as complete periods of the injected signal, while considering the fixed sampling frequency  $f_S$ . This means that  $f_{HF}$  should be selected such that there are reasonable long common period lengths for the combination of  $f_m$ ,  $f_{HF}$  and  $f_S$ .

One last topic to address in the context of current measurements is the influence of the PT1 filter. In Figures 6.16 and 6.17, we already saw that its influence on the measured fundamental current amplitude is marginal, whereas the occurring phase shifts are almost completely caused by the filter. When discussing the resulting errors in the identified inductance values and the anisotropy position, we need to take into account that the filter acts directly on the stator currents. This means that its influence is symmetric to a current frequency of zero Hertz, as it is shown within the relevant frequency range of  $\pm F_S/2$  in Figure 6.18. The negatively and positively rotating HF current components acc. to (6.41) – (6.43), however, are determined for a model in a rotor reference frame. For machines not at standstill, the filter is thus unevenly influencing the corresponding currents.

Of all three machines evaluated within this work, the SPMSM is operated at the highest electrical rotor frequency of  $f_r = 150\text{Hz}$  at rated speed. Although not measured at this speed, this case is exemplarily considered in Figure 6.18 with an injection frequency of  $f_{HF} = 1\text{kHz}$ . The negatively rotating current frequency is thus  $f_{-1, HF} = 2f_r - f_{HF} = -700\text{Hz}$ . The asymmetric filter influence on the measured currents is observable in both subfigures. The amplitude reductions acc. to subfigure (a) are below 1.3% even at worst case. It can thus be generally neglected when determining the inductances acc. to (6.44). The asymmetric filter influence is negligible as well.

When determining the anisotropy position, we need to remind that (6.45) contains the sum of negatively and positively rotating current phases. At standstill, the filter influence thus completely cancels out. At higher rotor speeds, however, the resulting filter asymmetry causes a position error. As demonstrated in subfigure (b) by the green line, this error is nearly constant at approximately  $-0.8^\circ$  for all feasible injection frequencies at the worst case of maximum electrical rotor speed. Although the filter causes a phase delay of up to  $\pm 9^\circ$ , its influence on the anisotropy position can thus be neglected as well.

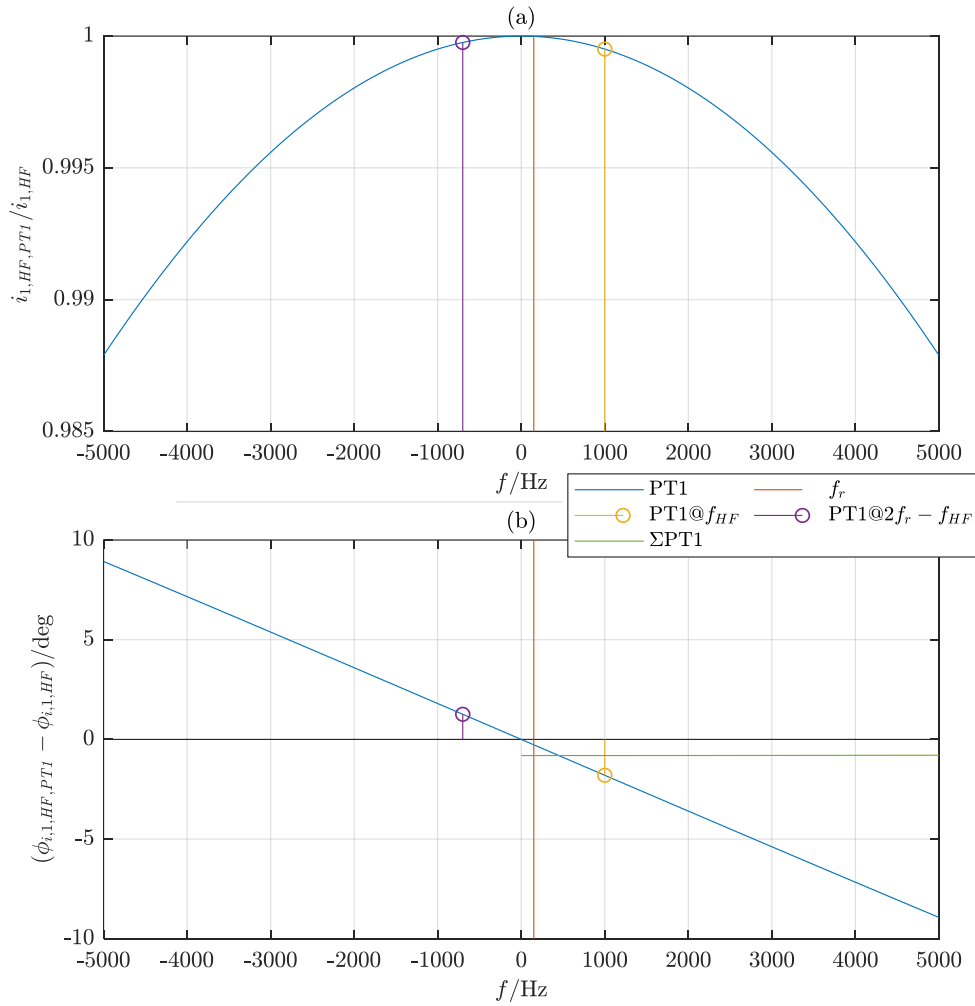


Figure 6.18: Influence of the PT1 filter on the measured current amplitudes (a) and phases (b); exemplary positively and negatively rotating current values for the SPMSM at rated speed with an HF injection frequency of 1kHz

## 6.4.2 Measurement Results

The measurement results presented in this section are split up into two categories. In the first set of measurements, we analyze the influence of the frequency of the rotating HF voltage vectors applied to the different types of synchronous machines. In the second part, we generate flux linkage maps from the measured inductance parameters as discussed in Chapter 5. They are analyzed and compared to the corrected flux linkage maps as shown in Chapter 4.

For the same reason as in the BEMF results in section 6.3.2, the discussion of measurement results focusses on the IPMSM.

### 6.4.2.1 Results for Variable HF Frequencies

For the measurements presented here, we have selected injection frequencies from 5kHz downwards to at least 2 times the electrical rotor speed in steps of size  $1000/18 \text{ Hz} = 55.5 \bar{5} \text{ Hz}$ . Before we present the measured inductance parameters, we verify that the injection frequencies

do not interfere with the motor harmonics. This is demonstrated in Figure 6.19, where the relevant current spectra at different operating points without HF signal injection (blue lines) are compared against the fundamental HF current responses (orange and yellow) to rotating voltage vectors.

We see in subfigure (b) that even at a rotor speed of  $2/3 \omega_{m,N}$  the harmonics of relevant magnitude are in the range between  $\pm 400\text{Hz}$ . When we compare the respective zoomed plots, we see relevant changes in the spectra at the three operating conditions. Only a strong minus fifth harmonic with respect to the electrical rotor speed appears constant. In all three cases, however, we can note that the injection frequencies indeed do not overlap with the motor harmonics, or with other non-injection related harmonics, respectively. The latter can result, for instance, from the IGBT related inverter distortions as discussed in section 3.2.3 and shall not be further analyzed here, since they are not relevant for the HF measurements.

Another aspect worth noting is that at rated load in (c), we see the leakage effect around the fundamental FOC current component at rotor frequency. It is resulting from the fact that the rotor speed is not perfectly constant or not exactly at the expected value (i.e.  $1/3 \omega_{m,N}$ ) during the measurements, causing small deviations between the expected and real period times. Due to the long measurement periods that cover 14 mechanical, or 42 electrical rotor turns, the frequency leakage is limited to a small range of approximately 100Hz around the electrical rotor frequency. With an amplitude of almost 10A, however, the FOC current is more than 850 times larger than the negatively rotating HF current responses in that region. For that reason, even the very limited leakage effect can distort the measurements at very low injection frequencies (see the first two negatively rotating current magnitudes in the zoomed plot in (c)).

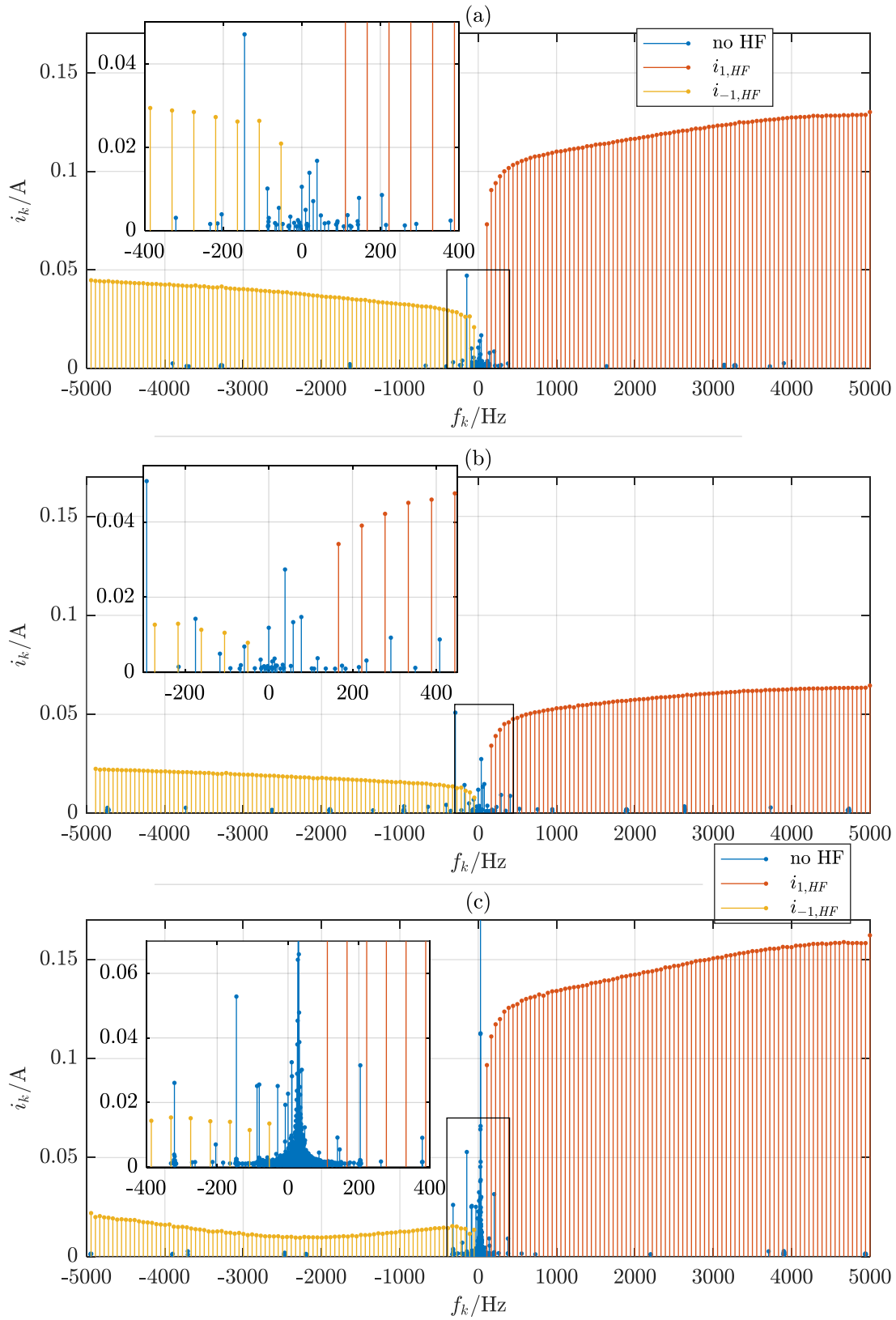


Figure 6.19: Comparison of the measured current spectra without HF injection with the current responses to HF injection at the selected frequencies at  $1/3 \omega_{m,N}$  and no load (a), at  $2/3 \omega_{m,N}$  and no load (b) and at  $1/3 \omega_{m,N}$  and rated load

Figure 6.20 shows the current responses of the IPMSM at  $1/3 \omega_{m,N}$  and no load to rotating HF voltage injection. As shown in (a), the voltage amplitude is increasing with the injection frequency. This shall ensure a constant magnitude of the current response.

We know from section 6.4.1, that the particular solution,  $\mathbf{K}_p^r$ , for linear systems stimulated with rotating input signals involves a denominator term with  $\omega_k^2$  and a numerator term with  $\omega_k$  (see Eq. (6.24) on page 146). With increasing frequencies, the offset terms in both, numerator and denominator, thus become more and more insignificant and we can expect the current amplitude to be proportional to  $u_{HF}/\omega_{HF}$ . For that reason, we can define a factor,  $K_{HF}$ , that scales the voltage amplitude with the injection frequency and allows us to obtain approximately constant current magnitudes. It is important to note, though, that the particular solution is valid for a model in rotor reference frame. We thus must translate the effectively injected frequencies by means of the electrical rotor frequency,  $f_r$ .

In conclusion, and when considering the fact that the fundamental component of the injected voltage is impaired by ZOH discretization, we let the HF reference voltage amplitude increase with the injection frequency by

$$u_{HF} = \frac{K_{HF}}{\text{sinc}\left(\frac{f_{HF}}{f_S}\right)} (f_{HF} - f_r). \quad (6.67)$$

Figure 6.20 (a) shows the respective voltage magnitudes. For conciseness, the positively (denoted with ‘+’ in the legend) and negatively (‘-’) rotating voltages are plotted over the same positive injection frequency.

We can see that the measured positively rotating voltage curve is increasing nonlinearly with the frequency resulting in a nearly linear actual fundamental HF voltage applied to the machine. The measured curves are obtained from the sampled duty cycles, which are converted by means of (2.135) to reference voltages and subsequently transformed into its Fourier coefficients acc. to (2.143). We can see that no noticeable negatively rotating (‘-’) voltages are measured as it is desired.

In subfigures (b) and (c), we see the magnitudes and phases of the Fourier coefficients of the HF current responses. The expected signals are plotted as reference. They are obtained from the corrected voltages from (a) and the parameters of the IPMSM reference model presented in section 4.2. Although we do not have relevant negatively rotating HF voltage components, we apply Equations. (6.41) and (6.42) for elliptic input signals. Additionally, in order to be as precise as possible, the PT1 current filter is considered. As intended, the current magnitudes are nearly constant at high frequencies. At low frequencies, however, they decrease due to the constant factors in the numerator and denominator terms of  $\mathbf{K}_p^r$ .

We can see that the measured current amplitudes and phases differ significantly from the expected ones. The biggest part of these differences can be explained by the SVM, leading to PWA currents with significantly reduced fundamental HF current components. After correcting the measurements by means of (6.65), we obtain results much closer to the expected ones.

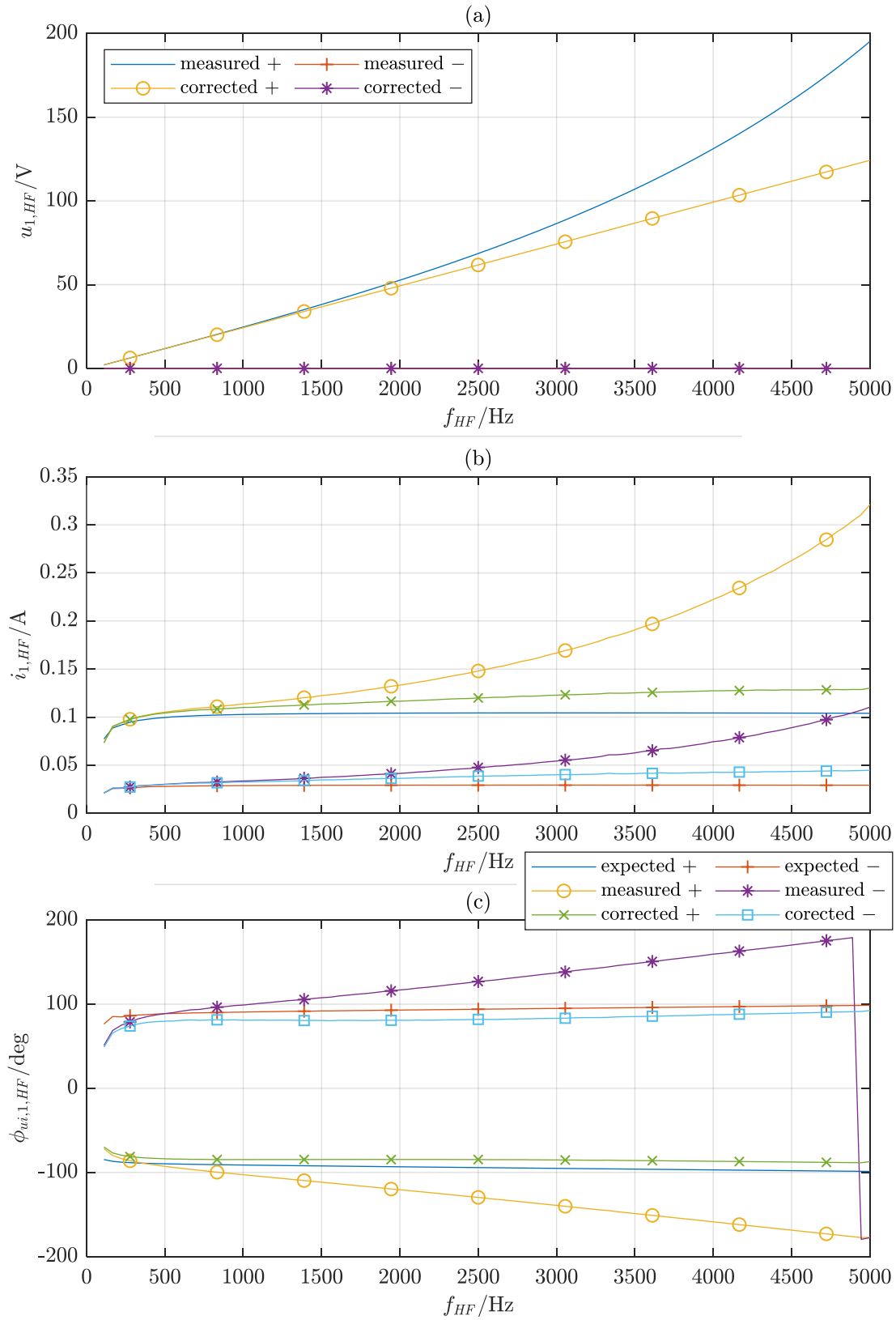


Figure 6.20: Theoretical and measured magnitudes (b) and phases (c) of the fundamental current responses to rotating HF voltage injection (a) for the IPMSM at  $1/3 \omega_{m,N}$ , no load and  $K_{HF} = 0.025Vs$

Please note that the current phases in (c) are plotted in relation to the respective voltage phases, i.e.

$$\phi_{ui,1,HF} = \phi_{i,\pm 1,HF} \mp \phi_{u,1,HF}. \quad (6.68)$$

We know that the influence of the PT1 current filter causes phase errors below  $\pm 9^\circ$ . Additionally, Eq. (6.62) states that the SVM causes no phase delays in the PWA current responses. The differences between measured and expected phases are thus mainly caused by the SVM influence on the measured voltage phases, that go up to  $-90^\circ$ , as shown in Figure 6.15.

It is also important to note that the negatively rotating current amplitudes are approximately four times smaller than the respective positive ones. They are therefore more affected by measurement noise.

Except for iron effects, all potential sources of errors are compensated as good as possible in the corrected signals. The remaining differences to the expected signals should thus be mainly caused by iron effects. In [81], it is pointed out that eddy currents lead to increasing stator current responses to voltage steps. In our case that means bigger amplitudes in the measured currents. Since eddy currents correlate with the excitation frequency, we consequently see increasing current amplitudes with increasing injection frequencies. It is worth noting that the increase in amplitude is larger than the expected decrease due to the current filter.

In subfigure (c), we can note phase shifts smaller than  $\pm 10^\circ$  that remain nearly constant for all frequencies. This independence from the injection frequency indicates that eddy currents do not have a relevant influence on the measured current phases. Instead, magnetic hysteresis effects are the most likely explanation for the observed phase shifts. From the simplified considerations in section 2.2.3.4, we already know that hysteresis can cause harmonic distortions. Although not explicitly shown in Figure 2.24 (see p. 52), we can also observe phase shifts in the fundamental signal component. In the depicted example, a phase delay of approximately  $30^\circ$  occurs. Phase differences of  $\pm 10^\circ$  are thus well within the range of possible hysteresis effects.

In Figure 6.21, we see the inductance parameters obtained from the voltage and current signals from Figure 6.20, calculated by means of (6.44), (6.45) and (6.66). The term ‘measured’ in the legends now refers to the parameters obtained from the measurements with all error compensations, that were discussed so far.

We see the influence of the iron effects on the measured inductance parameters. At low injection frequencies between 200 and 500 Hz, the measured inductance parameters correspond well with the expected values from the corrected BEMF measurements. Below 200 Hz, the anisotropy position shows its largest deviations of more than  $-5^\circ$ . As already discussed, the latter is expected to be a result of magnetic hysteresis, while eddy currents mainly distort the inductance parameters at higher injection frequencies.

It is worth reminding the statement from section 2.1.2.5 that the reversible susceptibility will always be smaller than the anhysteretic susceptibility. This is exactly what we see here in the

context of the mean inductances in subfigure (a). The only exception occurs at the lowest injection frequency. The reason for this deviation from the expectation will be discussed below.

For now, we can state that we generally obtain smaller mean inductance values than expected. With increasing injection frequencies, the HF inductances become smaller, which correlates with the above-mentioned increasing current amplitudes. At an injection frequency of 5kHz, the largest errors of more than  $-15\%$  occur. The differences between measured and expected anisotropic inductances as shown in (b) indicate that the eddy currents do not have the same influence on both axes. This could be expected, since it is known from former publications that eddy currents are stronger in the unlaminated permanent magnets than in the rest of the laminated stator and rotor iron [116]. As we can see,  $L_{A,\Delta}$  is up to approximately 5% more negative than the expected values at frequencies close to 5 kHz. The eddy currents thus let  $L_D$  decrease stronger than  $L_Q$ .

Besides the comparison of measured and expected parameter curves, Figure 6.21 also analyzes the influence of the different sources of error that were discussed above. We can see that if we do not eliminate the discretizing effects of the SVM (yellow curves), we get large errors in the obtained inductances at high injection frequencies. The identified anisotropy position is not affected, since the current phases are not influenced by the SVM and the voltage phases cancel out in (6.45).

Most publications dealing with HF injection at synchronous machines neglect the influence of the stator resistance,  $R_s$ , on the relation between currents and voltages (e.g. [10, 25]). Some also neglect the BEMF, which can be interpreted as neglecting the rotor speed<sup>14</sup>,  $\omega_r$ . In order to analyze the errors due to these simplifications, the green and purple curves are plotted. They demonstrate that neglecting the rotor speed causes relevant errors in the inductance values at low injection frequencies. In the anisotropy position, the errors are comparably small.

Neglecting the resistance has no relevant influence on the inductance values. It is, however, distorting the anisotropy position identification at low injection frequencies. This indicates that it might be worth to consider the resistance in anisotropy based sensorless control schemes with very low injection frequencies. This is further discussed in section 6.5.1.

Although not shown in Figure 6.21, it shall be mentioned that no relevant differences are observed with or without compensation of the inverter voltage errors due to the IGBT effects. Since the latter should only cause distortions at integer multiples of the rotor speed, it can generally be expected that HF injection techniques are insensitive to these types of voltage errors, as long as the injection frequency does not interfere with that specific rotor harmonics.

---

<sup>14</sup> This means that in Equations (6.44) and (6.45),  $\omega_{r,op}$  is set to zero. Since these equations base on a model in rotor coordinates, the rotor speed nevertheless has to be considered, when determining the injection frequency as seen by the rotor, i.e.  $\omega_k = \omega_{HF} - \omega_{r,op}$

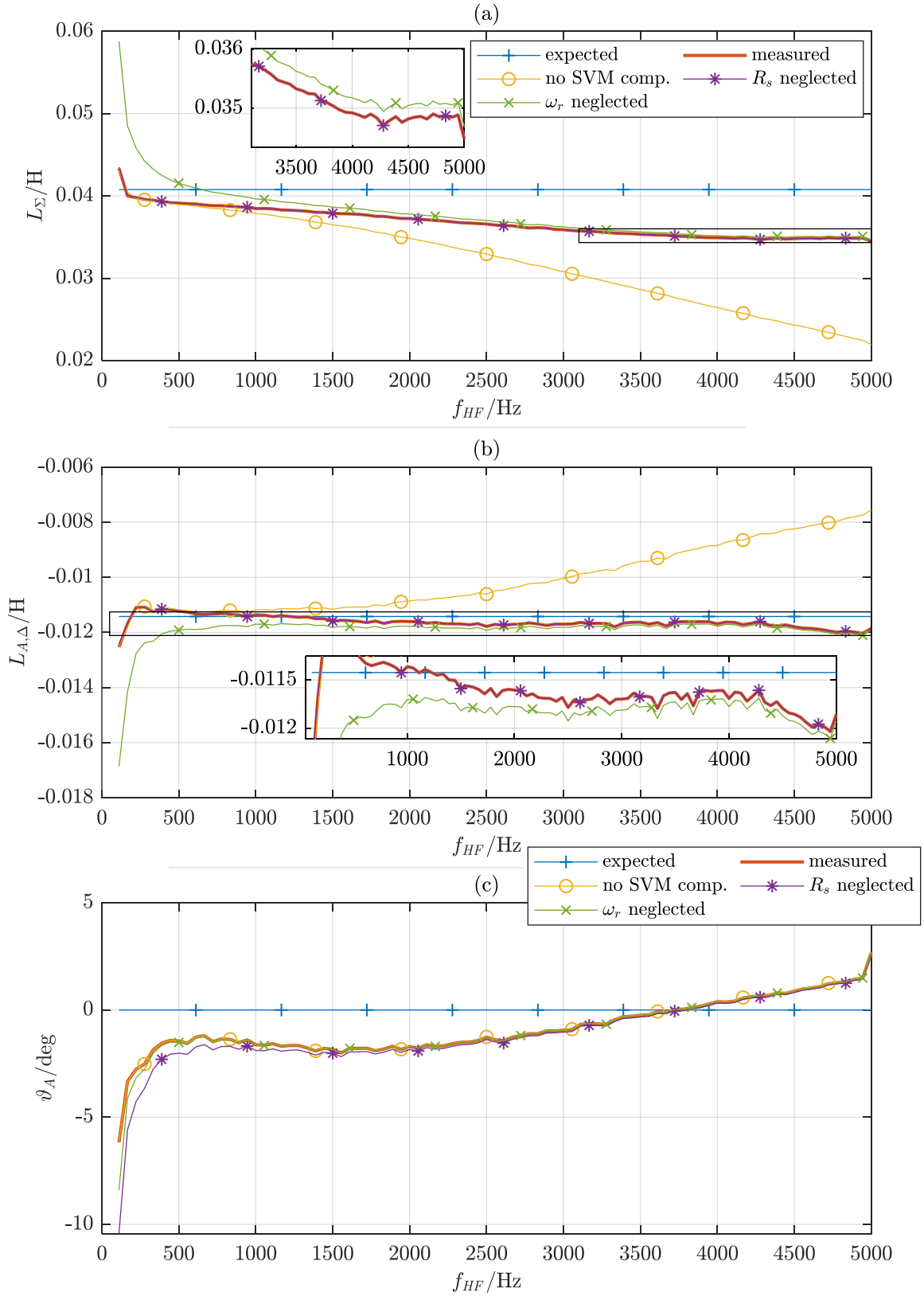


Figure 6.21: Comparison of the effects of different inductance parameter identification methods on  $L_\Sigma$  (a),  $L_{A,\Delta}$  (b) and  $\vartheta_A$  (c) for the IPMSM at  $1/3 \omega_{m,N}$ , no load and  $K_{HF} = 0.025Vs$

An overview of the identified HF inductance parameters in comparison to the expected reference parameters for different operating and measurement configurations is shown in Figures 6.22 and 6.23. We can observe only small differences in the identified parameters when the rotor speed or the injection amplitude are changed.

At very low injection frequencies, we can observe rapid changes and partially large errors in all identified parameters in both figures. We already identified three effects that can cause this behavior:

1. The current amplitudes decrease due to the constant factors in the numerator and denominator terms of  $\mathbf{K}_p^r$ , thus worsening the SNR
2. The frequency leakage effect from the FOC fundamental current can distort the low frequent current measurements
3. Although not visible in Figure 6.20 (a), at certain frequencies we get negatively rotating voltage components and thus an elliptic injection, whereas the identification algorithm assumes circular injection patterns

Points one and two can be compensated by increasing the injection amplitude at low frequencies and increasing the measurement period at large FOC current amplitudes. The third point addresses a systematic problem in the proposed identification algorithm, as it relies on perfectly circular injection patterns. The latter, however, cannot always be guaranteed, as it is shown in Figure 6.24.

In order to analyze the influence of elliptic injections, the ratio of negatively and positively rotating voltages is plotted for all measurement configurations shown in Figures 6.22 and 6.23. We can see that all voltages are nearly circular, as the reversely rotating voltage components are well below 1% of the injected voltages. At rated load, we can note at average a slightly higher level than in the unloaded case.

It stands out that, although still small, at the lowest frequencies the injection pattern grows more elliptic, partially with abrupt increases. The reason for that is not yet definitively clarified. Since at low frequencies the injection amplitude is very small, it would be understandable, if constant perturbations lead to continuously increasing relative errors. It is also possible that the FOC reacts to speed oscillations resulting from the HF injection near the fundamental speed. The rapid increase of negatively rotating voltages, however, points more into the direction of harmonic distortions, although this was not observed in the analysis of current harmonics in Figure 6.19.

Without further analyzing the reason for the elliptic voltages, we focus on determining their influence on the expected inductance parameters. For that reason, we apply the BEMF reference model to calculate the expected current responses to the measured elliptic voltages and substitute the results into the inductance equations for circular injection. When exemplarily taking the voltage data from Figure 6.24 (a) and (d) for the loaded and unloaded cases, we get the red curves denoted with ‘BEMF, proposed algorithm’, in Figures 6.22 and 6.23.

At the loaded case according to Figure 6.24 (d) the negatively rotating voltage components are well below 0.2% of the positively rotating voltage vectors. In consequence, the red curves in Figure 6.23 are close to the expected BEMF references at any injection frequency. When considering the unloaded case from Figure 6.24 (a), we note a single frequency of 166.67Hz, where the ratio of negatively and positively rotating voltages is almost 1%. At that frequency, we see larger differences in Figure 6.22 (b) and (c) between the BEMF reference and the estimated parameters determined by the proposed algorithm for circular voltages. Although the elliptic injection patterns do not completely explain the observed parameter errors at the lowest injection frequencies, we can state that even small elliptic HF voltages of less than 1% can lead to noticeable errors in the determined inductance parameters. We can thus conclude that all three points discussed above have their relevance in the observed errors at low injection frequencies.

At no load, the anisotropic inductance in Figure 6.22 (b) is identified with a relative error of less than 10%. At rated load, however, the error is up to approximately 50% at frequencies around 2kHz to 2.5kHz (cf. Figure 6.23 (b) ). It should be noted though, that the IPMSM is in a saturated state at rated load, where the anisotropic inductance is less than one third of the unloaded case.

It should also be kept in mind that  $L_{A,\Delta}$  is not a real inductance in a strict physical sense. It is rather describing the difference between two valid physical inductances, i.e.  $L_D$  and  $L_Q$ . While the latter cannot become zero (or negligibly small) in MQS systems,  $L_{A,\Delta}=0$  is a valid state, as it describes the common case of magnetic isotropy. Considering relative errors is thus only of limited relevance here.

Except for low injection frequencies below 500Hz, the identified anisotropy positions as shown in Figure 6.22 (c) show comparably small errors of at average below  $\pm 2.5^\circ$ , when the motor is unloaded. In the loaded case shown in Figure 6.23 (c), however, we see positive errors of about  $10^\circ$  around 1kHz and negative up to almost  $-19^\circ$  around 4kHz. It is interesting to note that the error is very small in the region at 2kHz, where the largest errors occur in the identified anisotropic inductance. The errors do apparently not correlate, although  $L_{A,\Delta}$  is the basis prerequisite in the definition of the anisotropy angle,  $\vartheta_A$ .

In the curves of the identified mean inductances in both subfigures (a), we can note increasing deviations from the reference with increasing frequencies. While at 500Hz, the errors are around  $-5\%$  at no load and  $-3.5\%$  at rated load, they increase to about  $-15\%$  and  $-18\%$ , respectively, at 5kHz. As already discussed, eddy currents are the most likely reason for this behavior. The observed effect is clearly influenced by the injection frequency, while the injection amplitude is only of minor relevance.

When reminding the generic definition of inductances as partial derivatives of flux linkages and currents, we can note that larger current amplitudes due to eddy currents result in smaller appearing mean inductances. Since the EMF of each eddy current loop scales linearly with the frequency, we can expect a linearly increasing error due to the resulting eddy currents. In good approximation, with a slight tendency to saturate at high frequencies, this can be observed in both subfigures (a) of Figures 6.22 and 6.23.

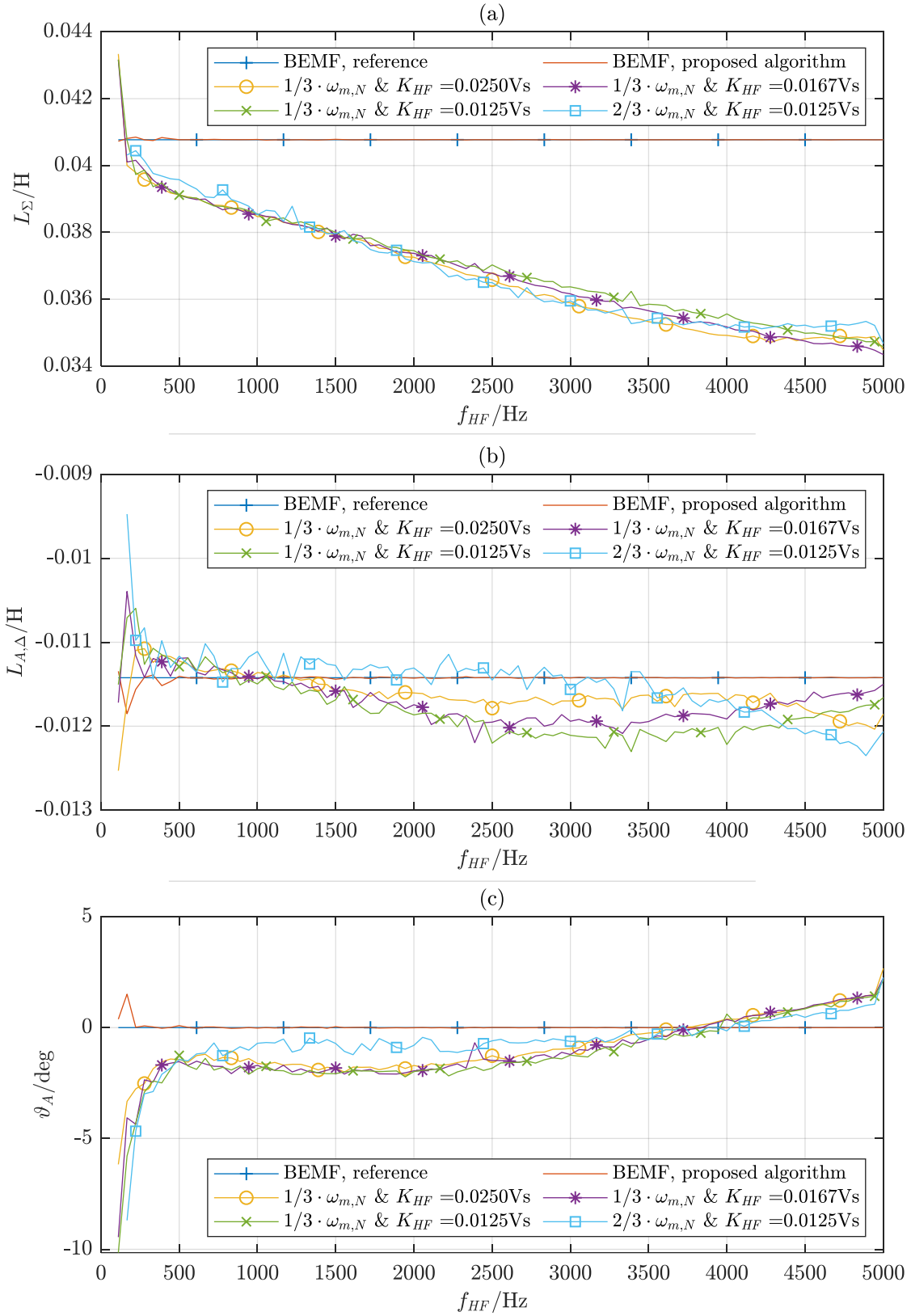


Figure 6.22: Comparison of the identified inductance parameters,  $L_{\Sigma}$  (a),  $L_{A,\Delta}$  (b) and  $\vartheta_A$  (c), for the unloaded IPMSM at different speeds and injection amplitudes

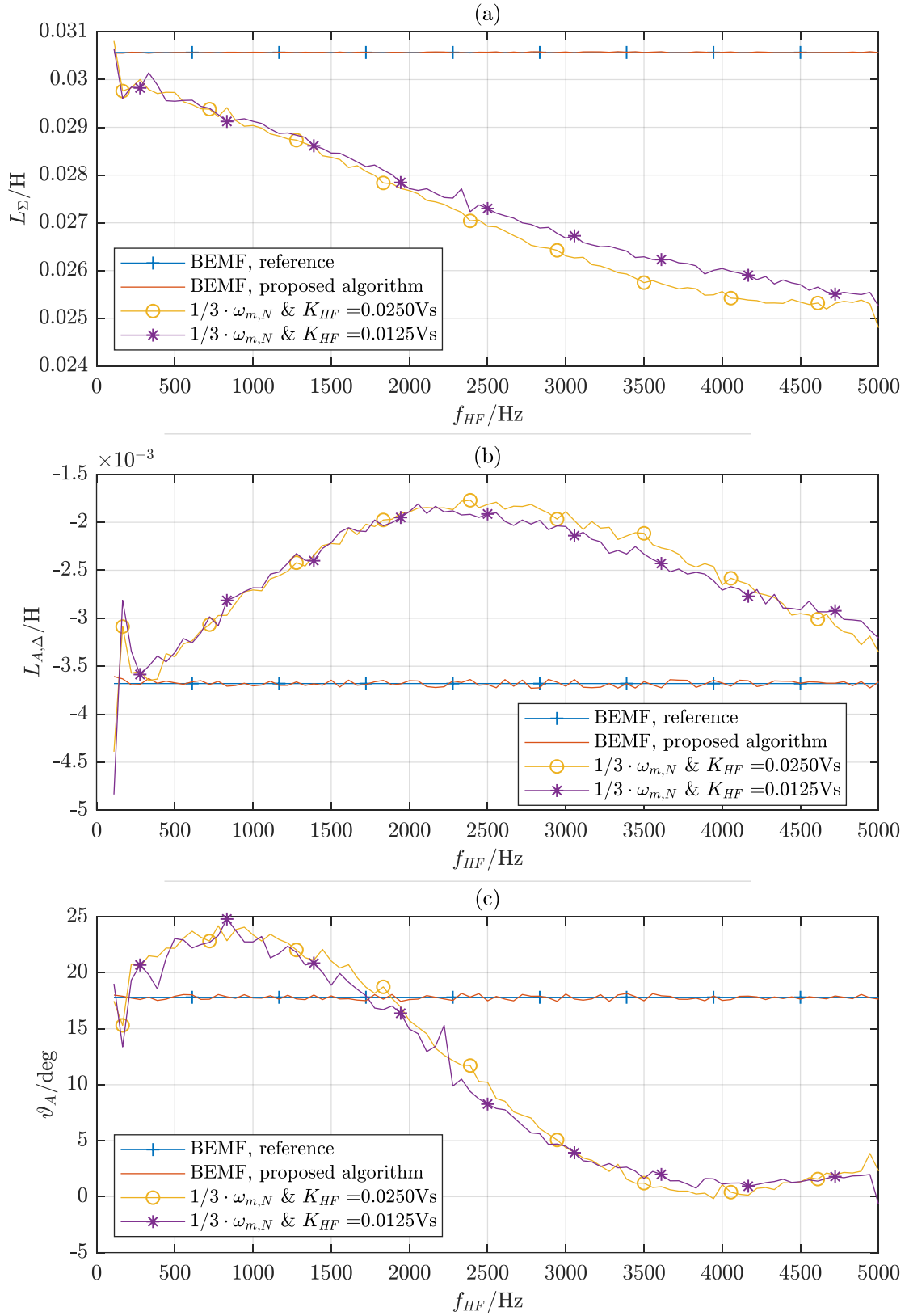


Figure 6.23: Comparison of the identified inductance parameters,  $L_{\Sigma}$  (a),  $L_{A,\Delta}$  (b) and  $\vartheta_A$  (c), for the IPMSM at rated load and different speeds and injection amplitudes

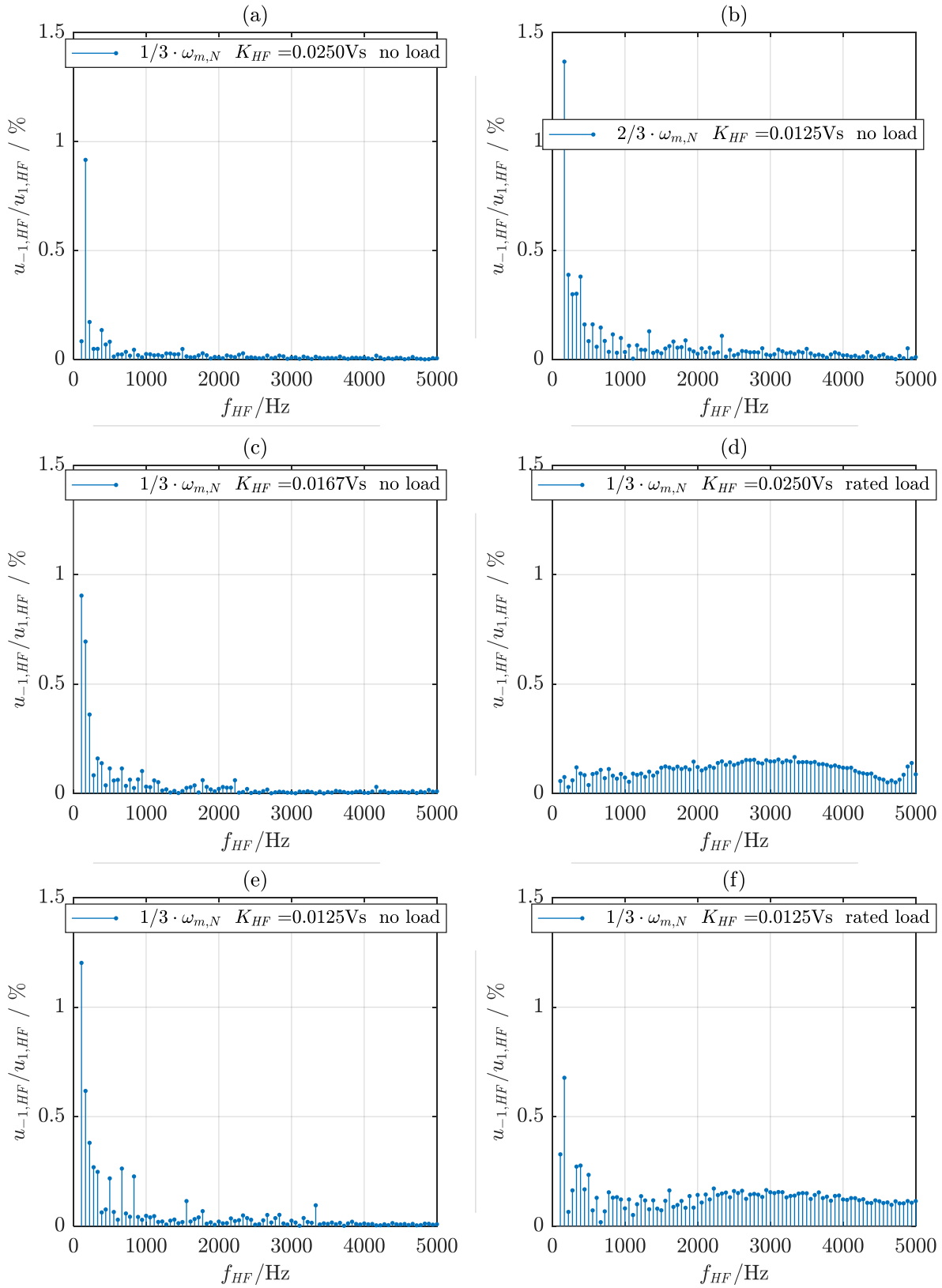


Figure 6.24: Ratio of negatively and positively rotating voltage amplitudes for HF measurements of the IPMSM at (a):  $1/3 \omega_{m, N}$ , no load,  $K_{HF} = 0.025 \text{Vs}$ ; (b):  $1/3 \omega_{m, N}$ , no load,  $K_{HF} = 0.0167 \text{Vs}$ ; (c):  $1/3 \omega_{m, N}$ , no load,  $K_{HF} = 0.0125 \text{Vs}$ ; (d):  $2/3 \omega_{m, N}$ , no load,  $K_{HF} = 0.0125 \text{Vs}$ ; (e):  $1/3 \omega_{m, N}$ , rated load,  $K_{HF} = 0.025 \text{Vs}$ ; (f):  $1/3 \omega_{m, N}$ , rated load,  $K_{HF} = 0.0125 \text{Vs}$

Analogously to the IPMSM results, Figure 6.25 shows the identified HF inductance parameters of the SPMSM in comparison to the expected reference parameters for different operating conditions. The subfigures on the left-hand side show the results in the unloaded case at 1/3 of the rated motor speed. On the right-hand side, we see the inductance parameters at rated load and 1/3 as well as 1/6 of the rated speed.

From the latter, we can state that the rotor speed does not have a relevant influence on the identified parameters. In the mean inductance curves acc. to subfigures (a) and (b), we see the influence of eddy currents, which lead to parameter errors of up to  $-25\%$  at the highest injection frequencies in both, loaded and unloaded cases.

In contrast to the IPMSM results, the mean inductance parameter errors show a cubic rather than a linear form with respect to the injection frequency. Additionally, when projecting the inductance curves downwards to the actual rotor frequency, we can note an offset to the expected reference value, indicating a stronger influence of magnetic hysteresis.

A hysteresis offset is also observable in the anisotropic inductance parameter in subfigure (c), while in a more saturated state at rated load, this effect is strongly reduced (see (d)). Nevertheless, eddy currents lead to frequency dependent parameter errors that go up to around 41% and 37% at maximum injection frequencies in both cases.

Another main difference to the IPMSM measurements is observable at the lowest injection frequencies. Especially in the anisotropic inductance and position curves, we have significant deviations between the BEMF reference and the parameters obtained from the proposed identification method assuming circular voltage injection. These deviations indicate that in fact negatively rotating injection components were present during the measurements.

This is confirmed by the analysis shown in Figure 6.26. In all three depicted combinations of loads and rotor speeds, we can find elliptic injection patterns of more than 1% for frequencies below 250Hz. Although finding even ratios of up to 36%, already these 1% deviations from perfectly circular injections cause relevant errors in the identified inductance parameters.

The example of the SPMSM thus underlines the necessity to ensure as circular injection patterns as possible to avoid additional parameter errors.

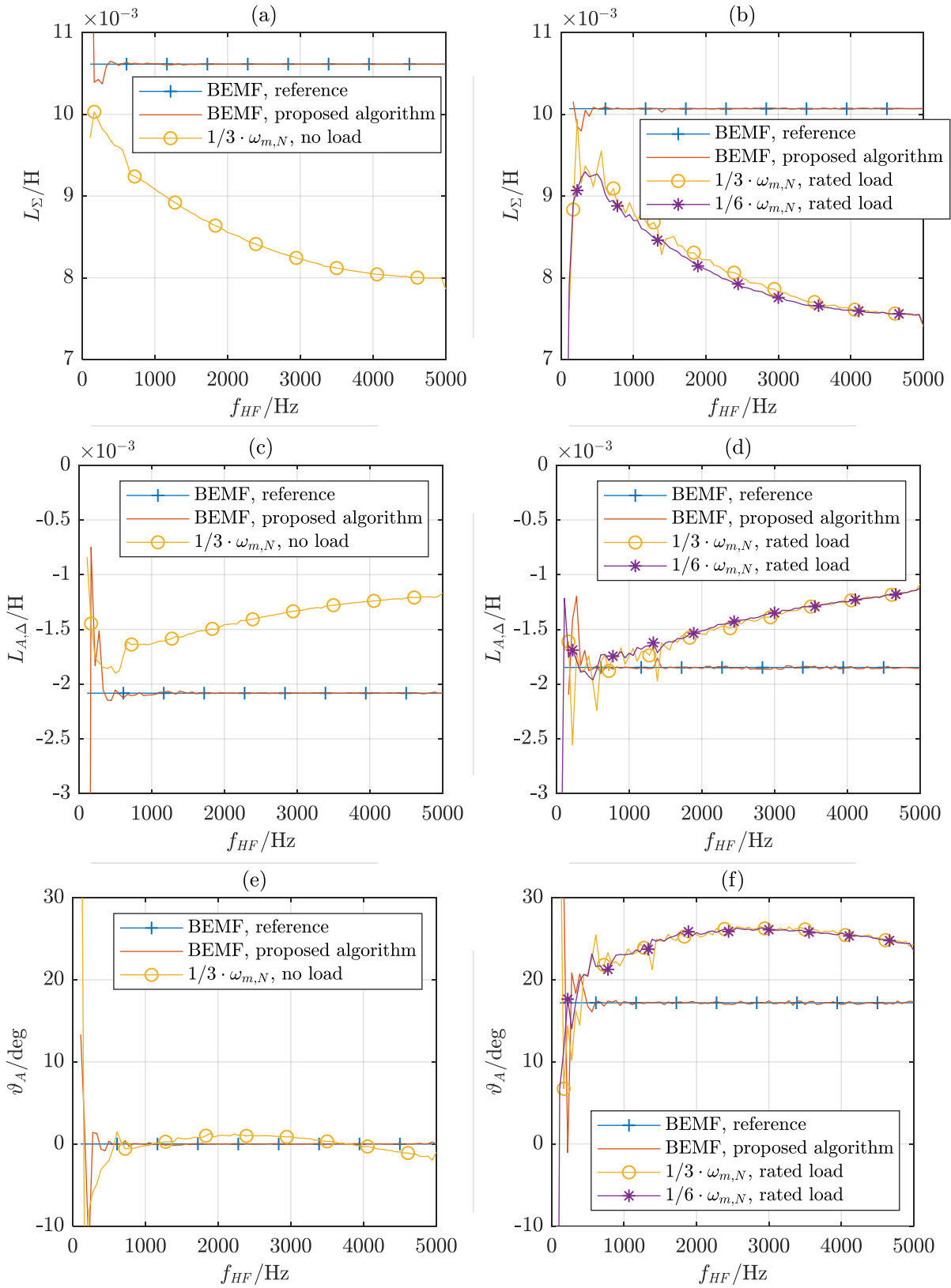


Figure 6.25: Comparison of the identified inductance parameters,  $L_{\Sigma}$  (a),  $L_{A,\Delta}$  (b) and  $\vartheta_A$  (c), for the SPMSM at  $K_{HF} = 0.025Vs$  and different speeds and loads

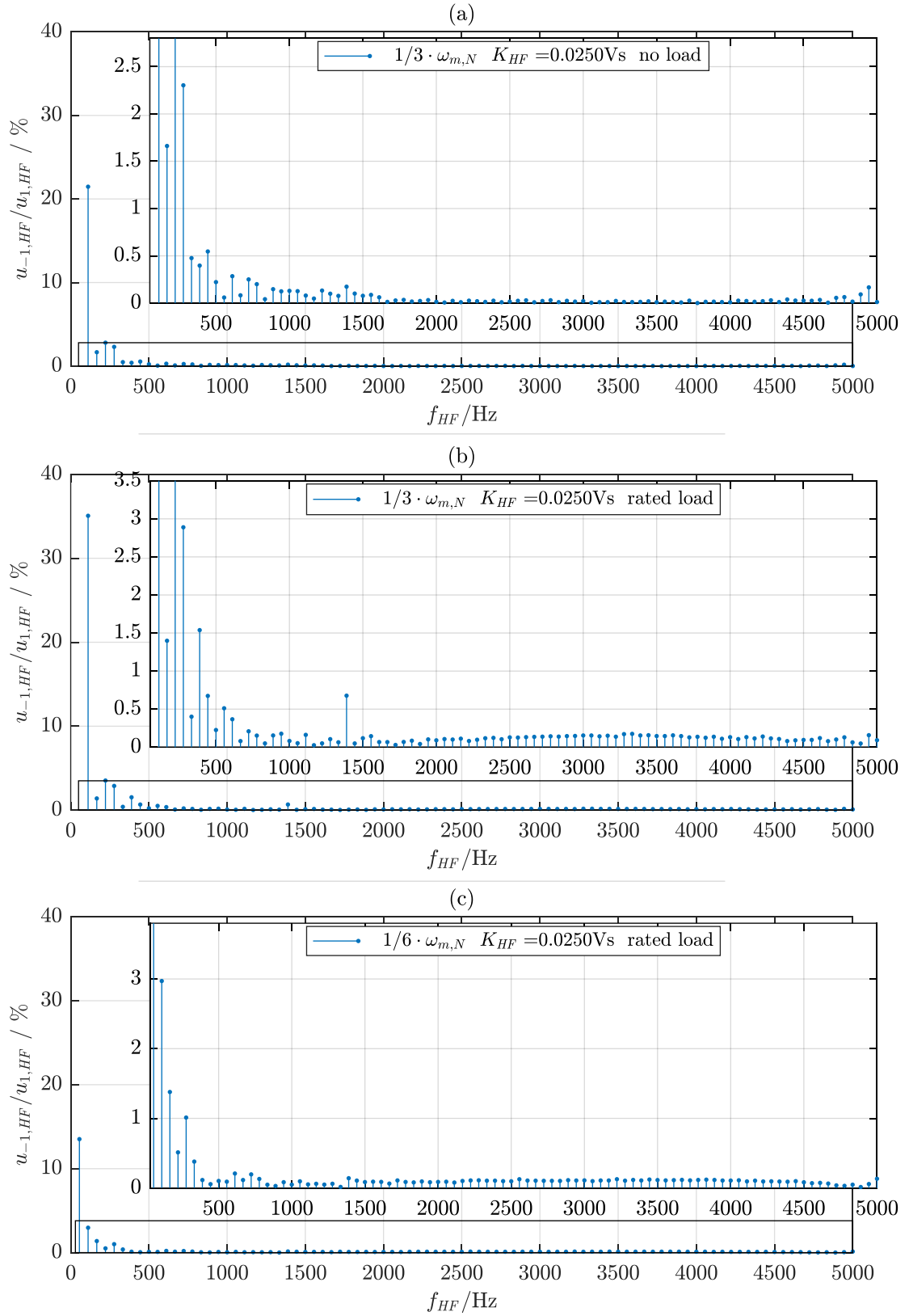


Figure 6.26: Ratio of negatively and positively rotating voltage amplitudes for HF measurements of the SPMSM at (a):  $1/3 \omega_{m,N}$ , no load,  $K_{HF} = 0.025Vs$ ; (b):  $1/3 \omega_{m,N}$ , rated load,  $K_{HF} = 0.025Vs$ ; (c):  $1/6 \omega_{m,N}$ , rated load,  $K_{HF} = 0.025Vs$

In order to conclude the analysis of frequency depending effects on the proposed parameter identification technique for different synchronous machine types, Figures 6.27 and 6.28 show the corresponding results for the SynRM.

In Figure 6.28, we can see again elliptic injection voltages at low frequencies. They are, however, only relevant at rated load and cause corresponding parameter errors in the anisotropic inductance and position curves acc. to subfigures (d) and (f) of Figure 6.27.

In both, loaded and unloaded case, we can see the hysteresis effect leading to offsets in the obtained inductance parameters. Especially when comparing the mean inductances curves in (a) and (b), we can see that the influence of hysteresis significantly reduces, when the machine is magnetically saturated.

As discussed in section 2.1.2.2, coherent rotation is predominant in saturated magnetic material. Since magnetic hysteresis mainly results from domain wall motions over pinning sites, it had to be expected, that hysteresis decreases with increasing saturation. Similar results have already been reported in [55].

In contrast to the permanent magnetic machines analyzed above, eddy currents lead to relatively linear inductance errors with increasing injection frequency. In subfigure (c), we do hardly see any frequency dependency in the anisotropic inductance curves. This means, that both axes are similarly influenced by eddy currents. In the loaded case in (d), however, we see that this symmetry breaks, when the machine is magnetically saturated.

Nevertheless, the anisotropy orientation is only slightly affected by both, magnetic hysteresis and eddy currents. We can see in (e) and (f), that the differences between expected and measured curves are much smaller than they are for the PM machines.

We can generally state that the influence of eddy currents is smaller in SynRMs than it is in PM machines. This does also indicate that the magnets are a relevant host for eddy currents.

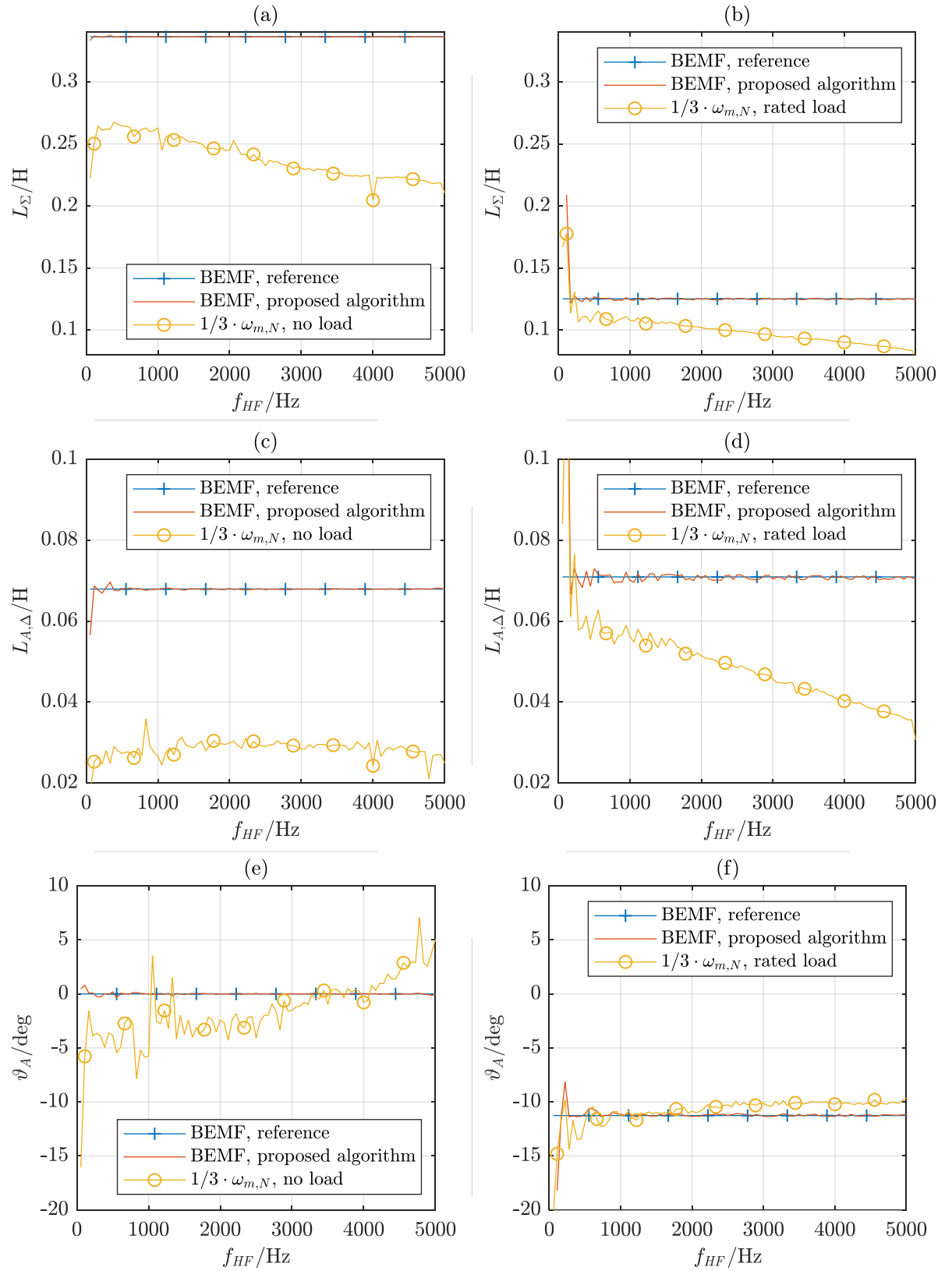


Figure 6.27: Comparison of the identified inductance parameters,  $L_{\Sigma}$  (a),  $L_{A,\Delta}$  (b) and  $\vartheta_A$  (c), for the SynRM at  $K_{HF} = 0.025\text{Vs}$  and different loads

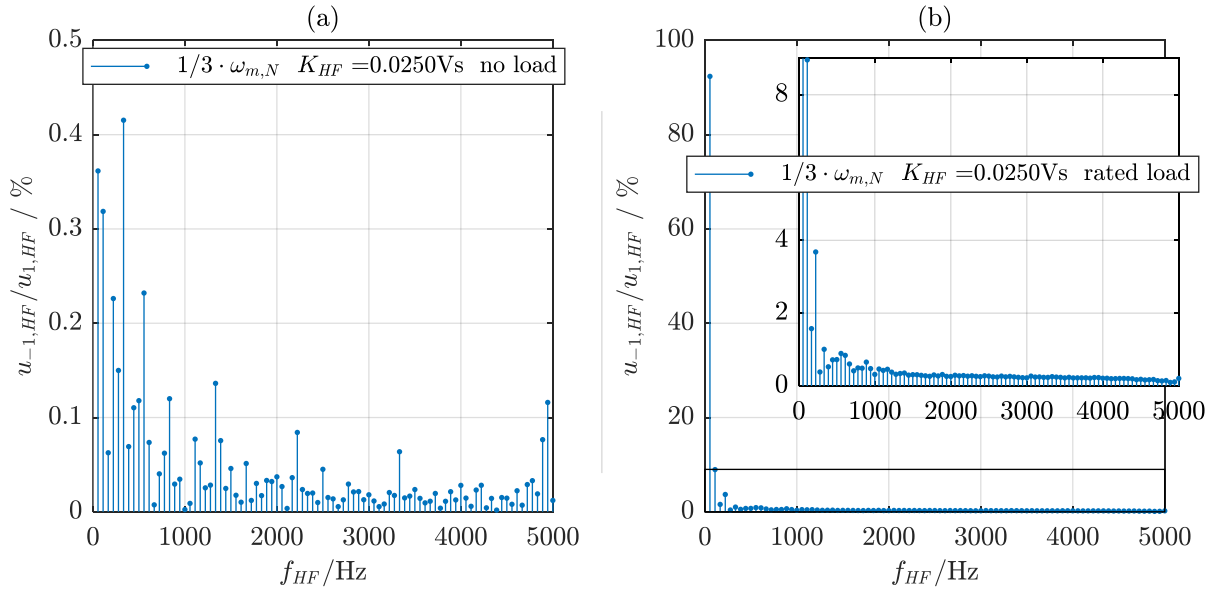


Figure 6.28: Ratio of negatively and positively rotating voltage amplitudes for HF measurements of the SynRM at (a):  $1/3 \omega_{m,N}$ , no load,  $K_{HF} = 0.025Vs$ ; (b):  $1/3 \omega_{m,N}$ , rated load,  $K_{HF} = 0.025Vs$

We can conclude that the proposed HF parameter identification method is insensitive to the injection amplitude, as long it guarantees sufficiently large current signals to obtain a good SNR. Although it can be expected that larger injection amplitudes cause additional eddy currents, the latter seem to have no additional effects on the proposed method. It can thus be advised to set the injection amplitude as large as possible with the available voltage margin of the VSI at the given operating point.

A weak point of the proposed method is the prerequisite that there must be no reversely rotating voltages. We have observed that already small amplitudes of less than 2% can lead to relevant parameter errors.

#### 6.4.2.2 Results for Variable Current Operating Points

In this section, we compare the BEMF reference maps to HF results at constant injection frequencies and different operating points. Since the HF results are obtained from the same sets of sampled data, we have the same measurement configurations as described before.

When setting the injection frequency to 875Hz, where the parameter errors in the IPMSM measurements were comparably small, we get the inductance maps presented in Figures 6.29 and 6.30.

In both figures, the upper subfigures (a) and (b) show the directly measured HF results, whereas the lower graphs (c) and (d) show the corrected maps after applying the optimization algorithm described in Chapter 5. In all contour graphs (b) and (d) on the RHS, the already discussed corrected maps obtained from BEMF measurements are represented by white contour lines for reference.

Compared to the inductance maps derived from the BEMF measurements (see Figure 4.21), we can note less noise. This indicates that the direct inductance measurement is advantageous over measuring and numerically differentiating flux linkage maps.

At all operating points in Figure 6.29, the mean HF inductance values are smaller than the respective BEMF references. This is in accordance with the results discussed in the former section, where we identified iron effects as the main reason for those deviations. We can note that the actual inductance reduction is not only depending on the HF frequency but also on the current operating point, as the differences are not constant.

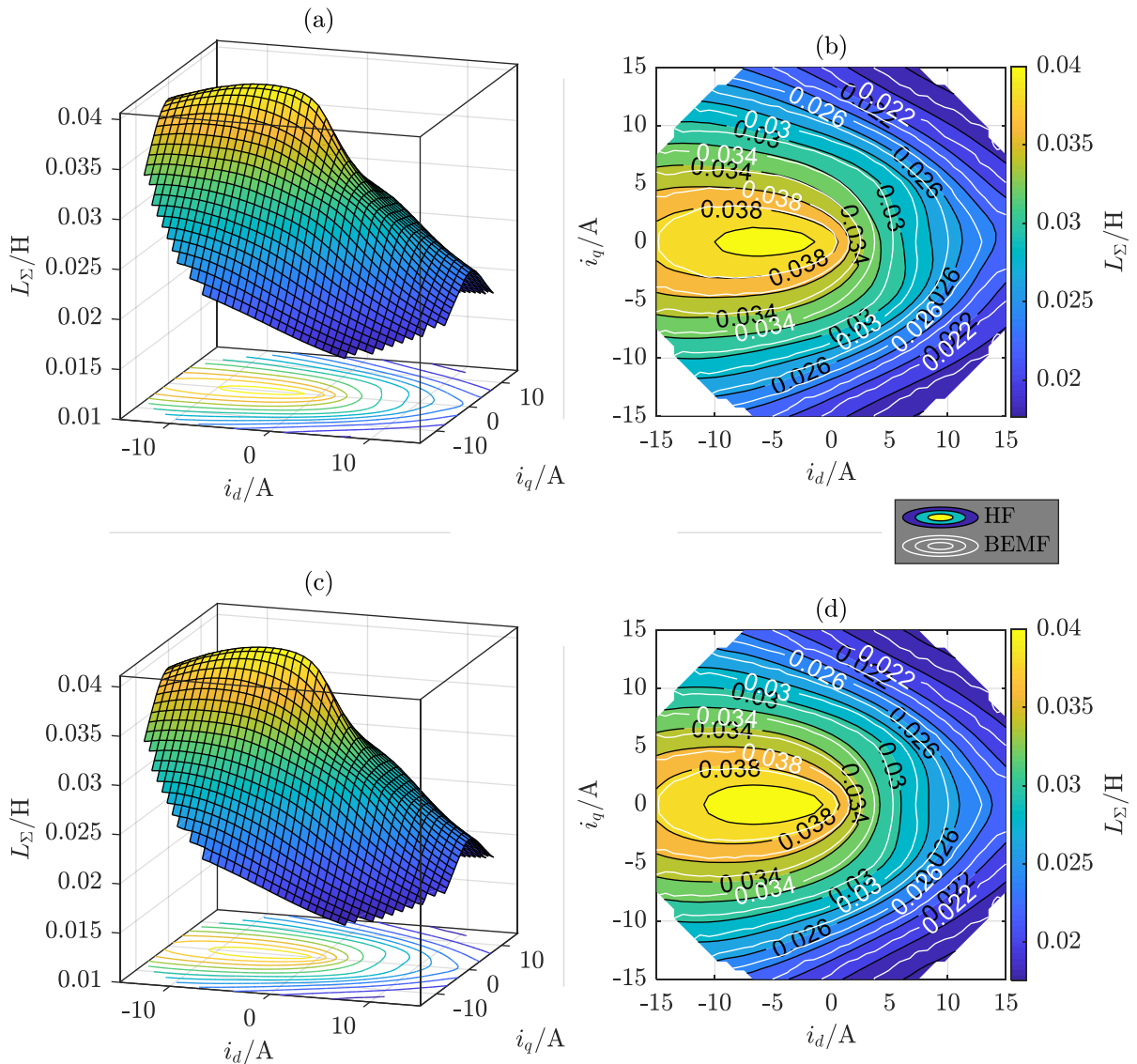


Figure 6.29: Comparison of directly measured ((a) and (b)) and corrected ((c) and (d)) IPMSM mean inductances obtained from HF measurements at  $1/3\omega_N$  and  $f_{HF} = 875\text{Hz}$ ; white contour lines in (b) and (d) are corrected BEMF based results for reference

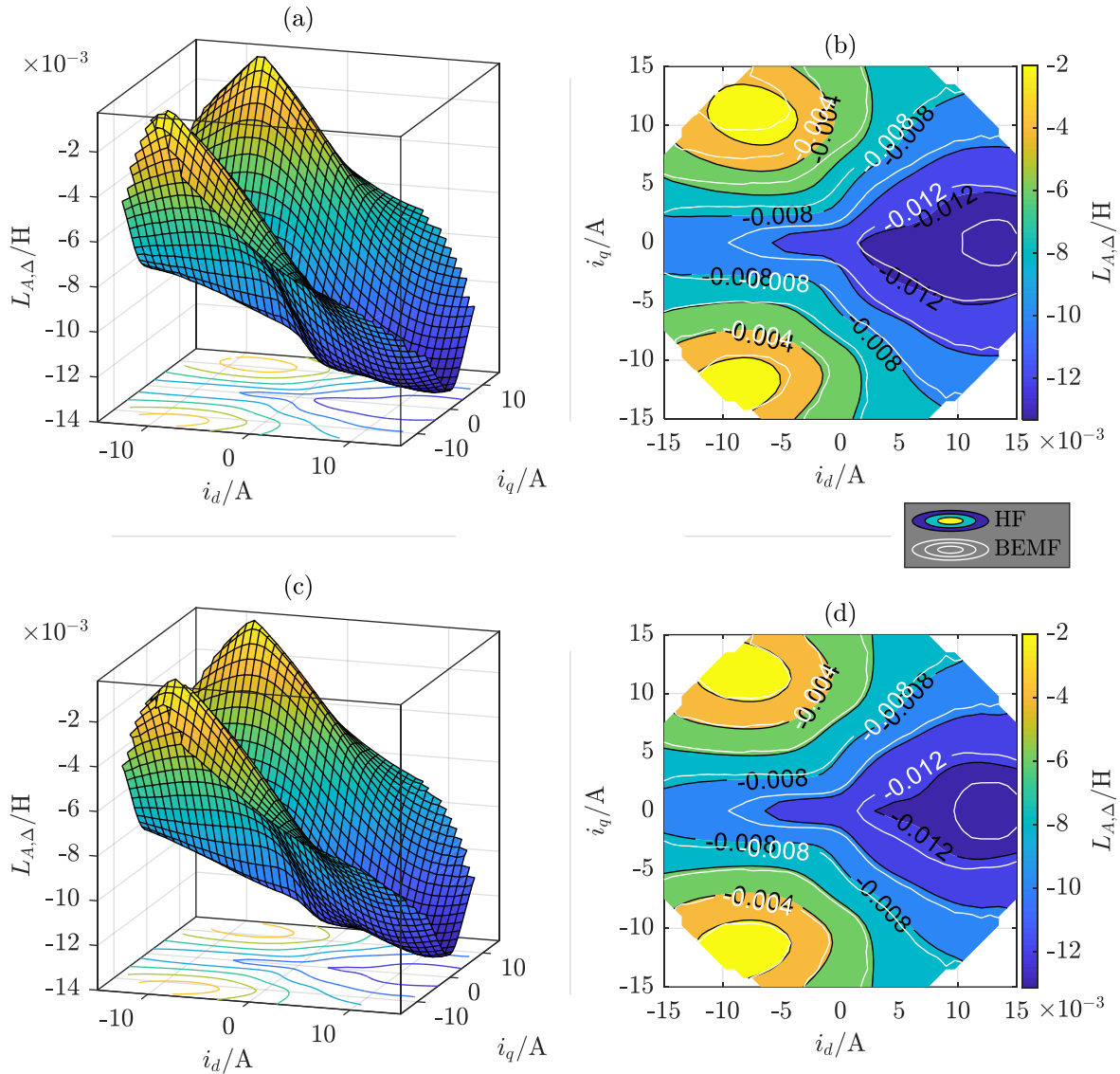


Figure 6.30: Comparison of directly measured ((a) and (b)) and corrected ((c) and (d)) IPMSM anisotropic inductances obtained from HF measurements at  $1/3\omega_N$  and  $f_{HF} = 875\text{Hz}$ ; white contour lines in (b) and (d) are corrected BEMF based results for reference

From the comparison of measured and corrected maps, we can see that the measured inductances are not perfectly symmetric. This is observable in both, isotropic and anisotropic inductance maps, whereas the asymmetry is stronger in the latter (c.f. Figure 6.30 (b)). For the same reasons as discussed before, these asymmetric differences are mainly resulting from iron effects. We can thus state that the repercussions of eddy currents and magnetic hysteresis on the HF current responses are different for motor and generator operation of the IPMSM.

When comparing the corrected BEMF and HF maps, we see smaller differences. Especially the anisotropy inductance maps now match comparably well. The optimization algorithm is thus

able to reduce the influence of iron effects to a certain extent. Especially in the typical operating ranges in the negative  $d$ -current plane, the measured inductance values are in good accordance.

At this point, we are focusing on the general parametric differences between HF and BEMF measurements. The conclusions from those differences in the context of sensorless control are drawn in section 6.5.1. For that reason, we are showing and analyzing the HF anisotropy angle measurements in that later section.

In order to conclude the comparison of BEMF and HF measurements, we present the flux linkage maps obtained from above corrected inductance maps. After transforming the

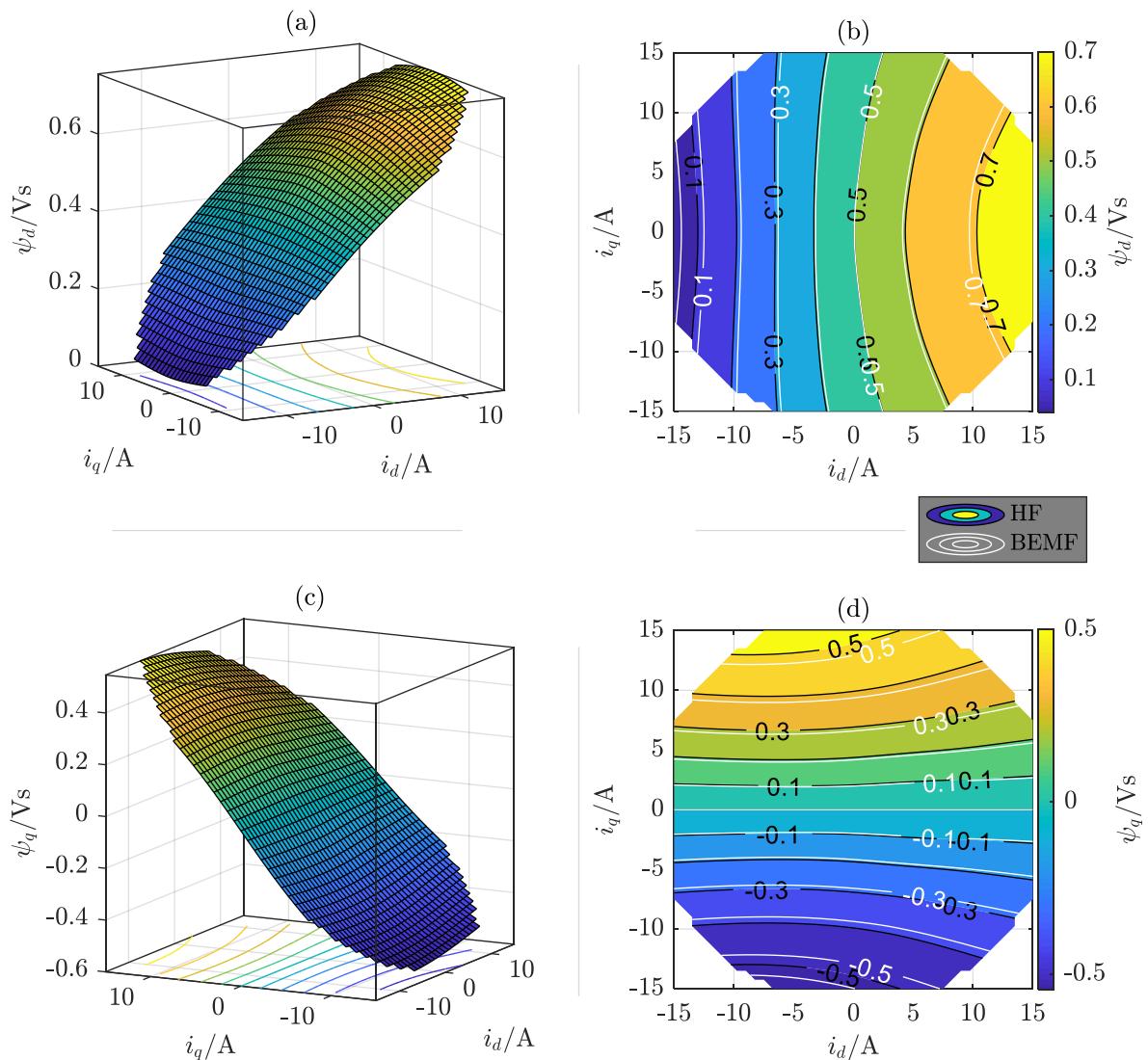


Figure 6.31: Comparison of and corrected  $d$ -axis ((a) and (b)) and  $q$ -axis ((c) and (d)) IPMSM flux linkage maps obtained from HF measurements at  $1/3\omega_N$  and  $f_{HF} = 875\text{Hz}$ ; white contour lines in (b) and (d) are corrected BEMF based results for reference

underlying data into  $d$ -,  $q$ - and  $m$ -inductances, we can apply (5.9) to integrate the respective inductance values along the  $d$ - and  $q$ -stator currents to obtain the flux linkage maps shown in Figure 6.31. Note again, that due to the correction algorithm, the integration paths can be arbitrarily chosen without influencing the resulting map.

The only additional information needed for valid flux linkage maps is their offset, or – in other words – an integration constant. We let this constant be the identified PM flux linkage, i.e. the flux linkage at zero stator currents. This means, for PMSMs we need at least one BEMF-based measurement at a feasible operating point, when deriving valid flux linkage maps from HF measurements.

We can observe that the HF and BEMF maps show only small differences. Around our selected fixed point, the maps are nearly identical. With increasing distance to that point, however, we can note the influence of iron effects in the HF measurements. Due to the integration process, the inductance errors sum up and, in consequence, the flux linkage maps slightly drift apart.

Depending on the application of those HF inductance maps, the drifts can have different impacts. In section 6.5.2, we exemplarily address the consequences for MTPA control strategies derived from HF measurements.

## 6.5 Discussions

---

### 6.5.1 Sensorless Control

In the former section, we already saw the isotropic and anisotropic inductance maps of the IPMSM. The third information needed to completely describe the inductance matrix in this case is the anisotropy orientation. It is shown in Figure 6.32.

As before, we can note unsymmetric differences between the measured angles and the BEMF references in subfigure (b). Especially in the negative  $d$ -current plane, where the MTPA and MTPV trajectories are located, we see that when directly evaluated from the HF signal injection method, we can expect deviations of more than  $\pm 10^\circ$  – especially around the points of magnetic isotropy. These errors can again be explained by iron effects, which make it necessary to distinguish between motor and generator operation.

As it was already observed in the former section at the inductance maps, the corrected HF and BEMF anisotropy position maps as shown in subfigure (d) show only small differences. Independently from the basic measurement scheme, we are thus able to obtain very similar results as long as we apply the correction algorithm.

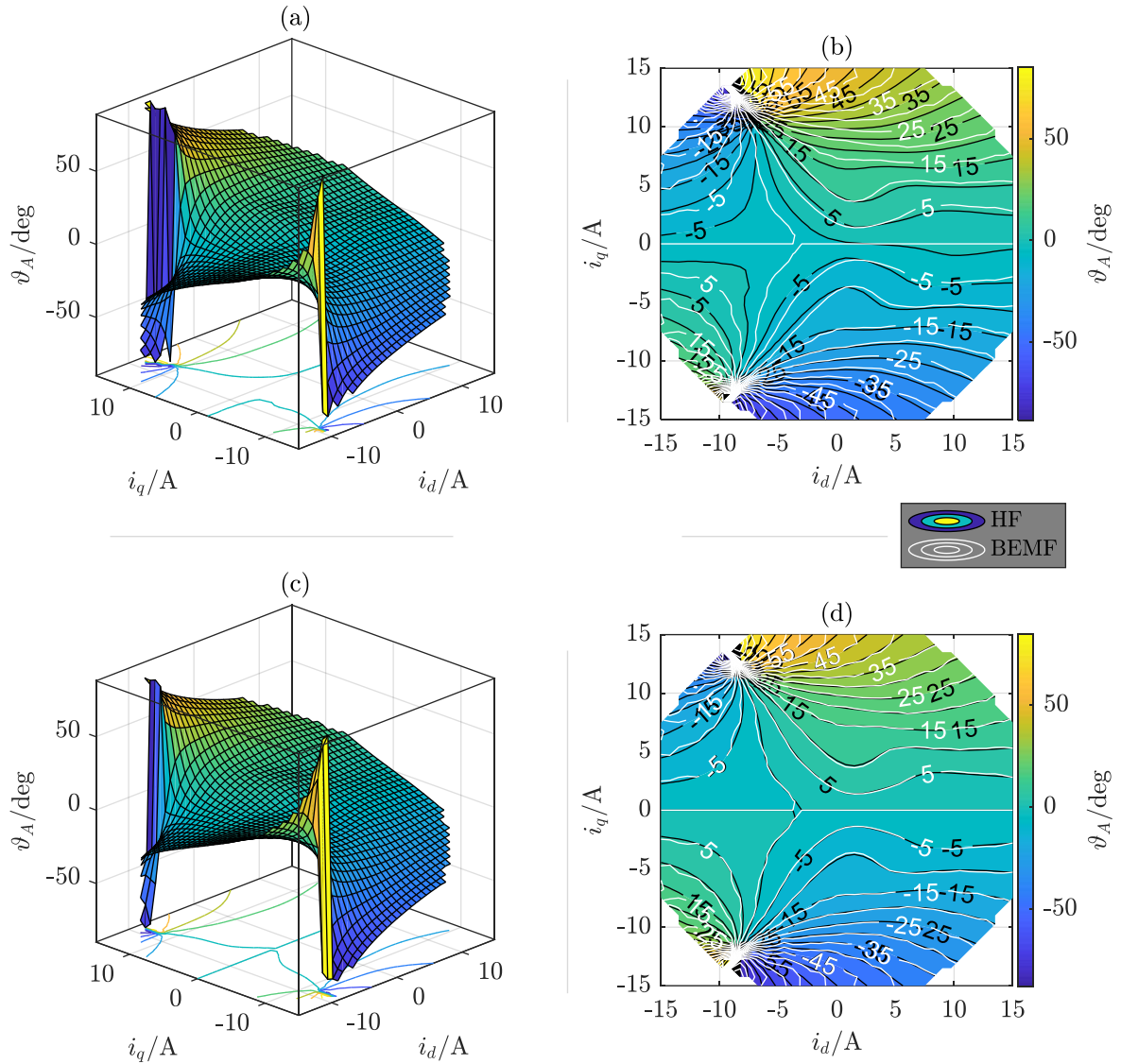


Figure 6.32: Comparison of directly measured ((a) and (b)) and corrected ((c) and (d)) IPMSM anisotropy orientation obtained from HF measurements at  $1/3\omega_N$  and  $f_{HF} = 875\text{Hz}$ ; white contour lines in (b) and (d) are corrected BEMF based results for reference

Another important information for sensorless control schemes is the saliency ratio, as it determines the position signal content in the system response to HF injection. It is shown in Figure 6.33. Again, we can note asymmetries in the direct measurements (see (b)), which are effectively eliminated by the correction algorithm (see (d)).

Note that although we saw certain differences between the corrected mean inductance maps (c.f. Figure 6.29 (d)), we can hardly find differences in the SR maps now, especially in the relevant negative  $d$ -current plane. The iron effects do seem to scale linearly with both isotropic

and anisotropic inductances and thus cancel out, when setting both inductance values in relation.

We can conclude that for the IPMSM we obtain very similar results independently from the measurement scheme. Since the optimization, however, is an offline algorithm, it is thus crucial for accurate sensorless operation to adequately consider iron effects.

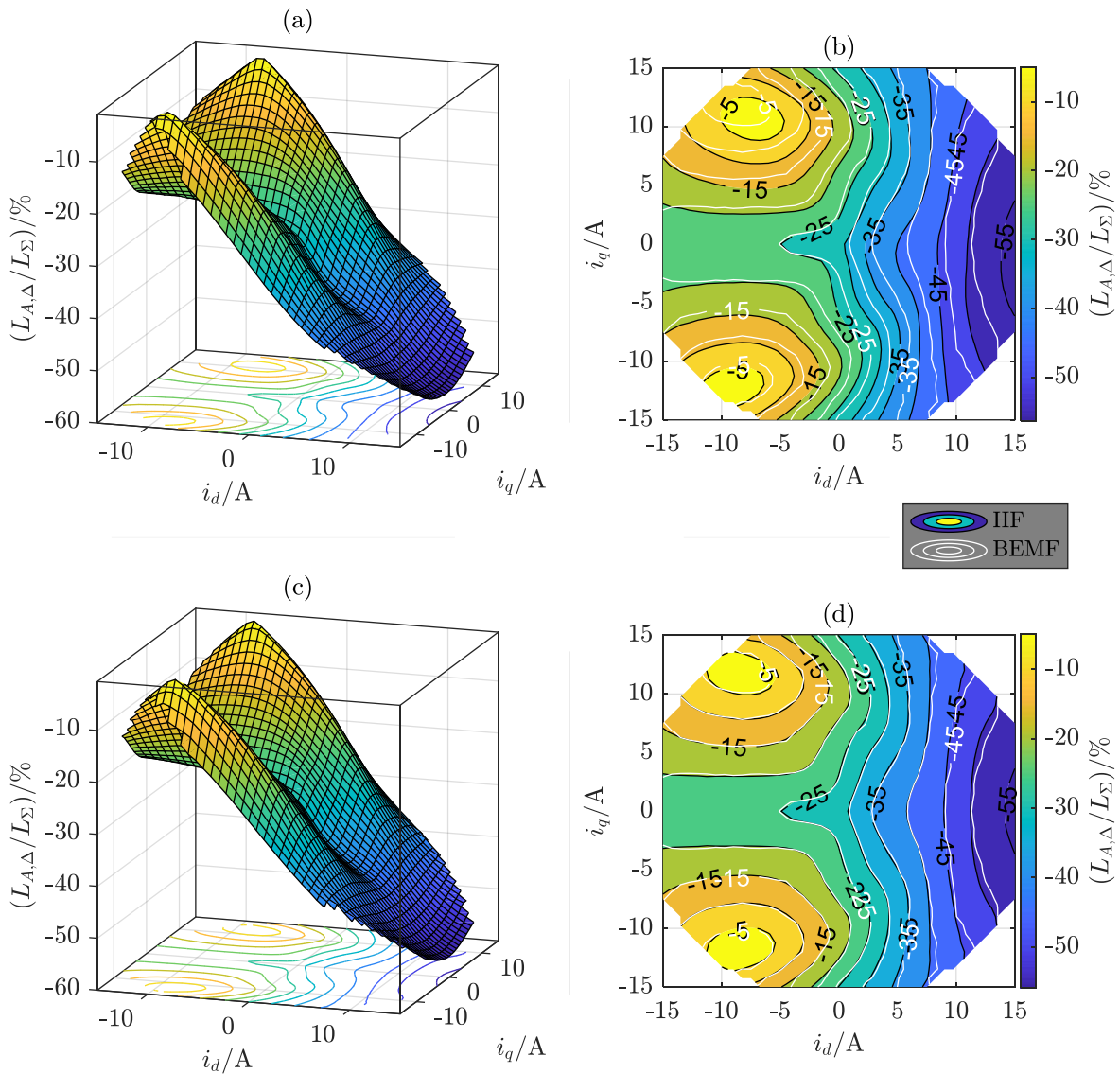


Figure 6.33: Comparison of directly measured ((a) and (b)) and corrected ((c) and (d)) IPMSM anisotropy ratio obtained from HF measurements at  $1/3\omega_N$  and  $f_{HF} = 875\text{Hz}$ ; white contour lines in (b) and (d) are corrected BEMF based results for reference

When repeating the above analysis for the SPMSM, we obtain the anisotropy position and SR maps as shown in Figures 6.34 and 6.35. We can again observe asymmetric differences between the measured HF maps and its BEMF counterparts. This time, however, the correction algorithm is only slightly reducing those differences.

In Figure 6.34 (d), we can find position errors of up to around  $\pm 9^\circ$  in the relevant negative  $d$ -current plane. Since the SR has its smallest values here because of magnetic desaturation, the occurrence of the largest position errors is explainable.

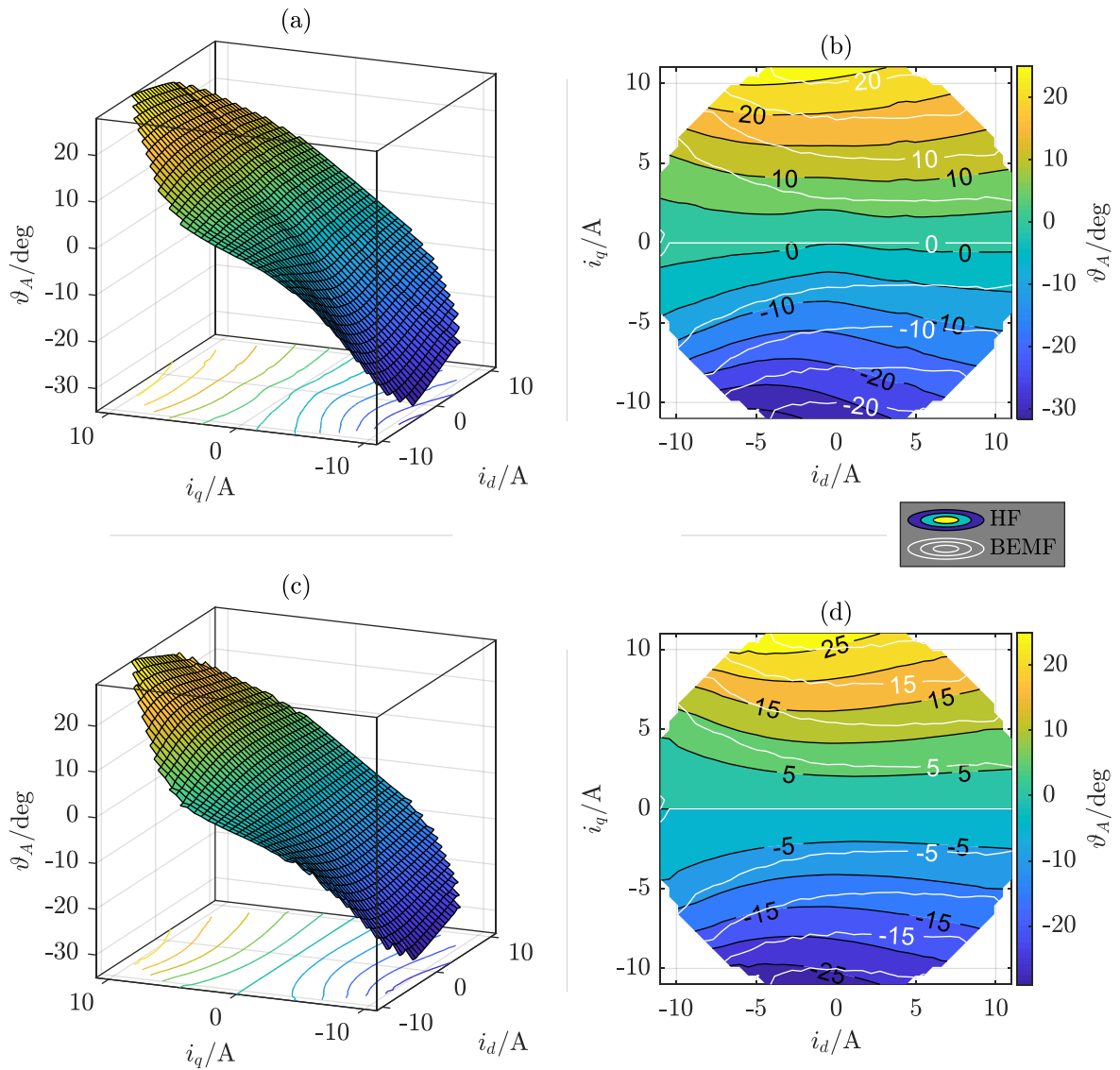


Figure 6.34: Comparison of directly measured ((a) and (b)) and corrected ((c) and (d)) SPMSM anisotropy orientation obtained from HF measurements at  $1/3\omega_N$  and  $f_{HF} = 1000\text{Hz}$ ; white contour lines in (b) and (d) are corrected BEMF based results for reference

We can conclude that the correction algorithm does not generally eliminate the different repercussions of iron effects on HF- or BEMF-based measurements. Especially machines like this SPMSM with comparably low inductances show relevant deviations and it seems advisable to take that into account, when deriving parameters for sensorless control schemes.

In comparison to the respective maps obtained from BEMF-based measurements (cf. Figure 4.33) note the significant better SNR in the HF evaluation.

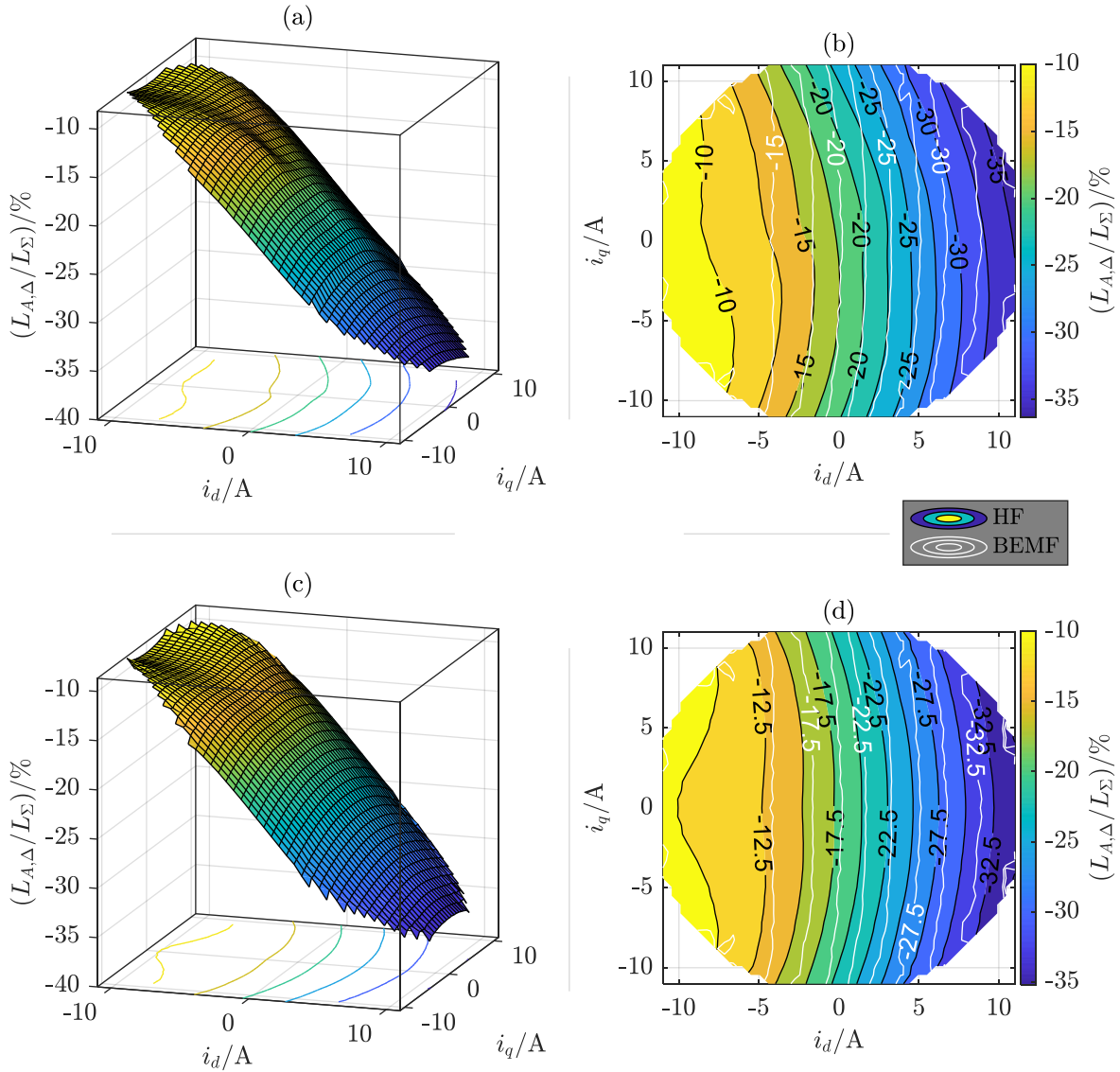


Figure 6.35: Comparison of directly measured ((a) and (b)) and corrected ((c) and (d)) SPMSM anisotropy ratio obtained from HF measurements at  $1/3\omega_N$  and  $f_{HF} = 1000\text{Hz}$ ; white contour lines in (b) and (d) are corrected BEMF based results for reference

In Figure 6.36, we see the anisotropy position maps of the SynRM and in Figure 6.37 the corresponding saliency ratios. The asymmetric differences between measured HF and corrected BEMF maps are less significant than they were at the PMSMs. This also indicates that eddy currents in the permanent magnets play a significant role in the deviations between HF and BEMF signals.

In the relevant control regions between MTPA and MTPV trajectories (compare Figure 4.9), the corrected HF and BEMF anisotropy positions show only small deviations. Along the  $\varphi$ -

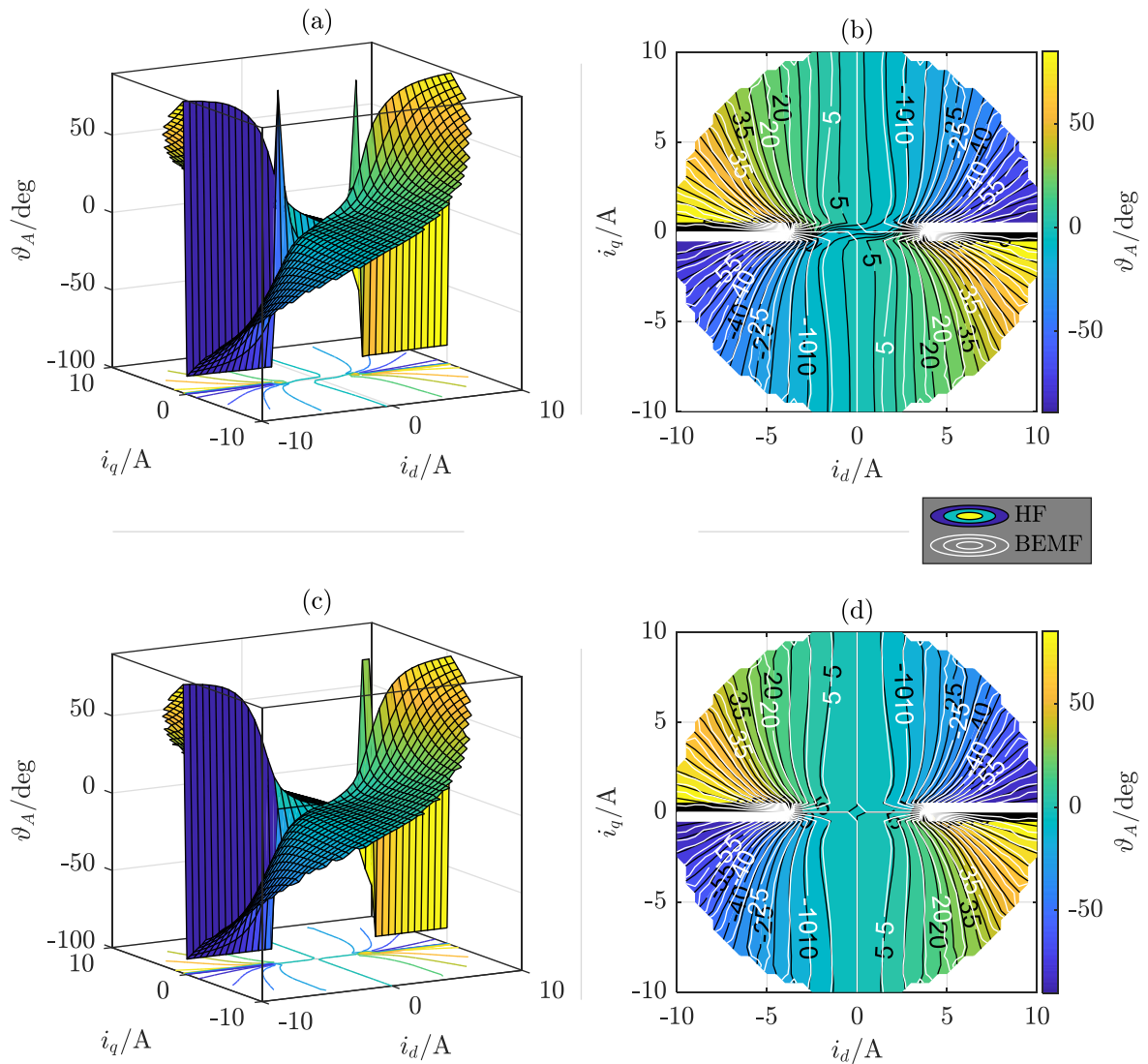


Figure 6.36: Comparison of directly measured ((a) and (b)) and corrected ((c) and (d)) SynRM anisotropy orientation obtained from HF measurements at  $1/3\omega_N$  and  $f_{HF} = 1000\text{Hz}$ ; white contour lines in (b) and (d) are corrected BEMF based results for reference

axis, we can note the biggest deviations, which can be explained by the small SR in combination with fast changing orientation angles in that region.

The SR maps of both, directly measured and corrected HF evaluation, show significant deviations to the BEMF references. We can thus state again that the correction algorithm does not completely eliminate the influence of iron effects. If the SR should be used in advanced sensorless control schemes, it is preferable to measure it directly with a corresponding HF injection scheme.

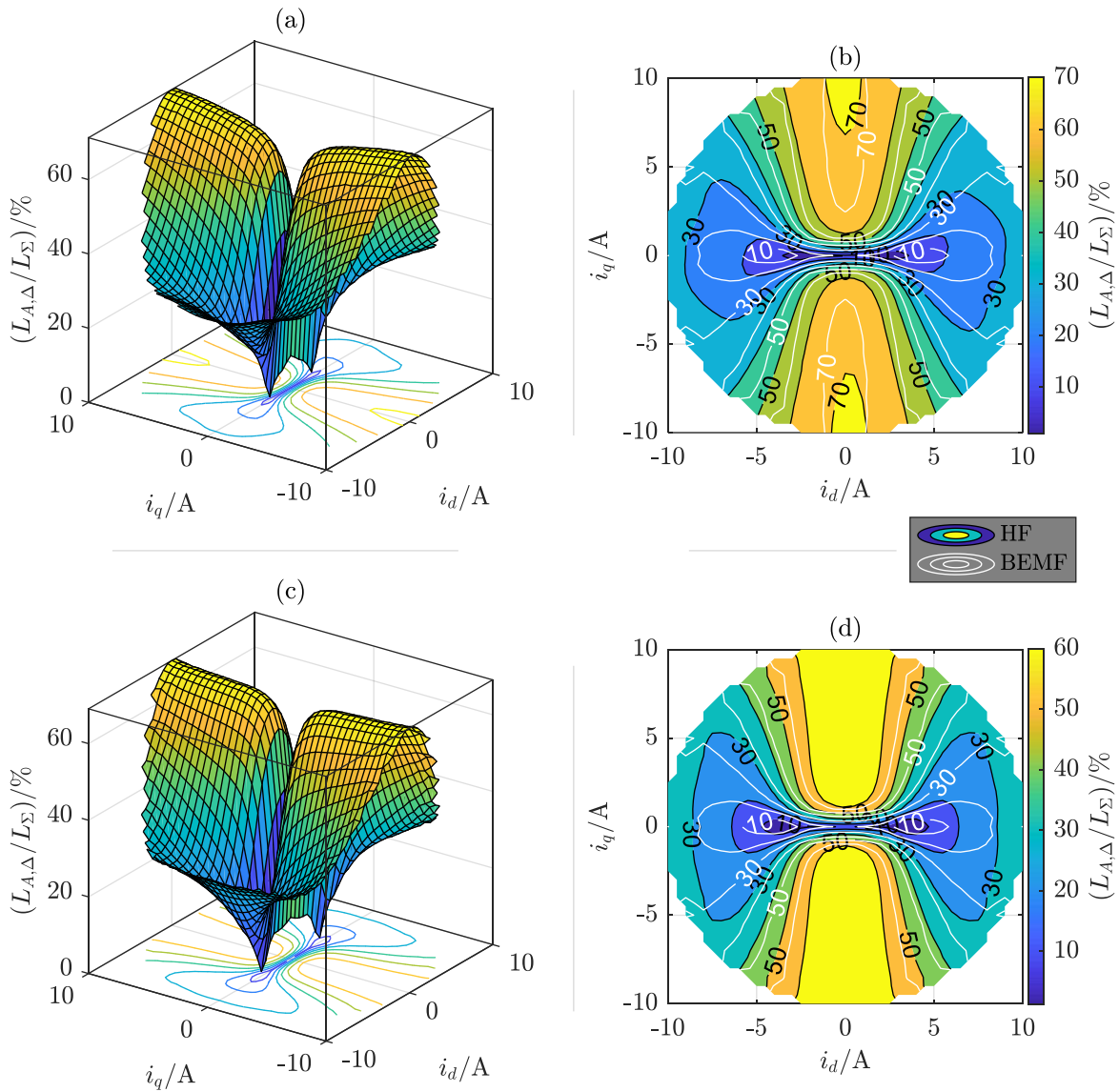


Figure 6.37: Comparison of directly measured ((a) and (b)) and corrected ((c) and (d)) SynRM anisotropy ratio obtained from HF measurements at  $1/3\omega_N$  and  $f_{HF} = 1000\text{Hz}$ ; white contour lines in (b) and (d) are corrected BEMF based results for reference

We can conclude for all three machines that the directly measured HF parameters are impaired by iron effects. Although in the case of the IPMSM the correction algorithm could eliminate most of the resulting deviations, the SPMSM and the SynRM maps show remaining differences to the BEMF reference maps. For that reason and since the correction cannot be performed online, for instance during sensorless operation, it is necessary to model the influence of eddy currents as well as of magnetic hysteresis.

A straightforward way of doing this is to approximate the parametric errors due to iron effects by polynomial functions of the injection frequency. In section 6.4.2.1, we saw that the anisotropy position error can have quite nonlinear forms that would require polynomials of high order to obtain accurate results. It is thus advantageous to model the parametric errors of the inductances in rotor coordinates. This is shown for the IPMSM in Figure 6.38. In the upper subfigures, we see the identified HF  $d$ -,  $q$ - and  $m$ -inductances for different injection frequencies in the unloaded (a) and loaded (b) case. Additionally, we see their 2<sup>nd</sup> order polynomial approximations and the expected non-frequency-dependent values from the BEMF measurements for reference.

Since we observed additional errors at the lowest injection frequency range due to, inter alia, negatively rotating voltage components, the polynomials are fitted to the measured data in the range above 800 Hz by least squares optimization. We can state that the quadratic polynomials do approximate the measured curve forms with sufficient accuracy. With this polynomial approach, we thus found a simple model for the iron effects that does require three parameters for each  $d$ -,  $q$ - and  $m$ -inductance curve at any relevant operating point.

When determining the anisotropy orientation acc. to (2.114) from those inductance polynomials, we obtain the curves presented in the lower subfigures – again for the unloaded case on the left (c) and at rated torque on the right (d). We can see that the nonlinear curve forms are reproduced well within the considered injection range. In sensorless control schemes, where the injection frequency changes during operation, we are thus able to identify the correct rotor position based on the identified anisotropy position.

It is worth noting that the obtained polynomial coefficients can be interpreted in the context of iron effects. Therefore, it is necessary to remind the differences between magnetic hysteresis and eddy currents. The fundamental magnetic hysteresis loop is characterized by injection frequencies that are tending to zero. Since injecting an “HF” signal with a frequency of zero is impossible, we can only extrapolate measurements at higher frequencies downwards zero. This extrapolated offset will then contain information about the influence of magnetic hysteresis, whereas all other values at non-zero injection frequencies describe the influence of eddy currents.

Another important aspect to note is that for non-zero rotor speeds, it is not possible to clearly separate hysteresis effects from eddy currents. If the extrapolated injection frequency in a rotor reference frame is zero, the stator at the same time sees an injection at rotor frequency. We do thus see a superposition of hysteresis effects in the rotor and a combination of hysteresis as well as eddy current effects in the stator. For simplicity, we neglect the latter and refer to hysteresis

effects only, when the extrapolated curves show an offset at injection frequencies that correspond to the rotor speed.

We can see that in the unloaded case, the approximated curves approach the BEMF references comparably well at rotor speed. The resulting angle difference is below two degrees, indicating only a small influence of magnetic hysteresis on the HF measurements. At rated load, we can note a stronger influence of magnetic hysteresis, leading to small offset errors of all  $d$ -,  $q$ - and  $m$ -inductances.

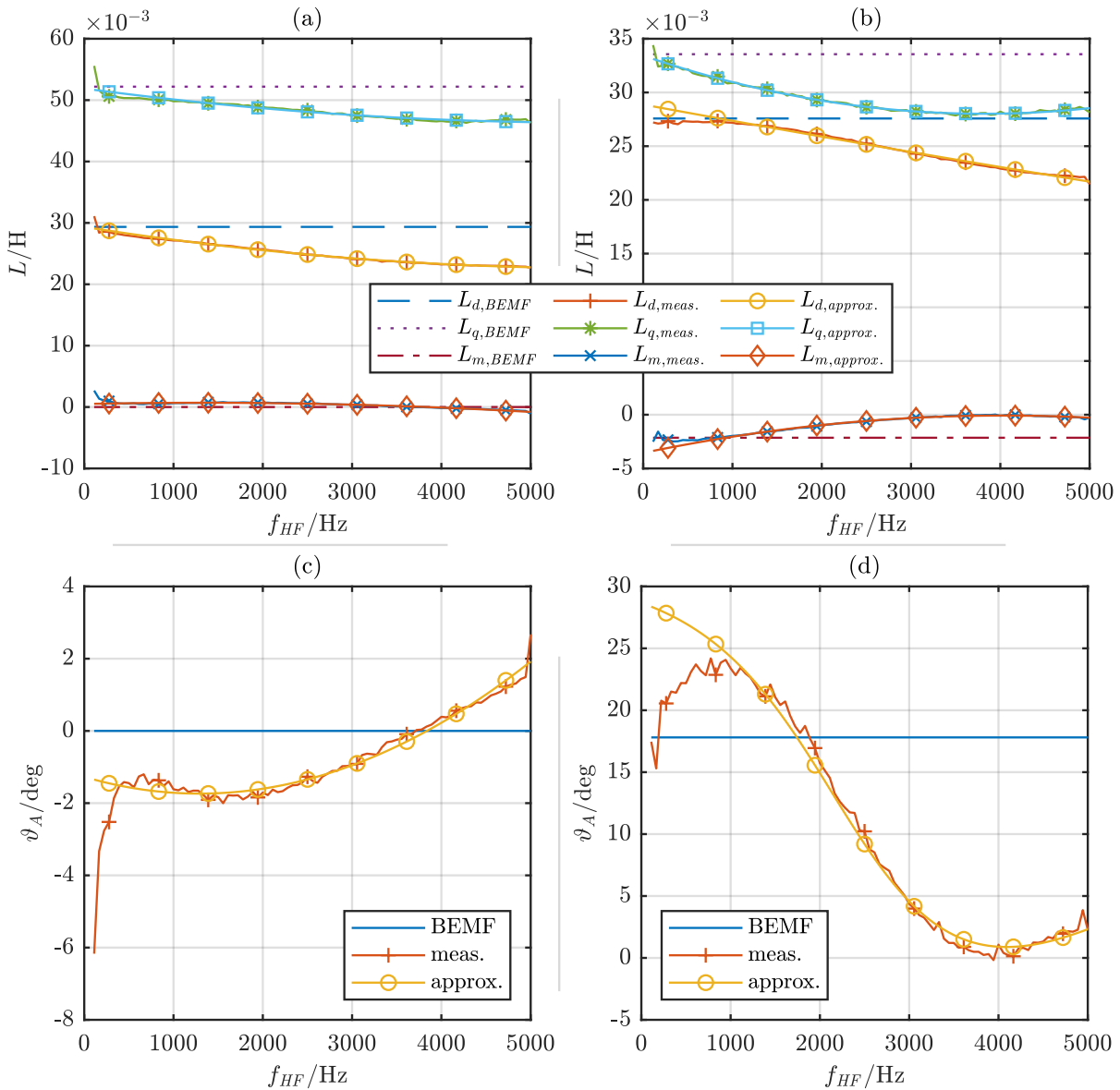


Figure 6.38: IPMSM inductance values and anisotropy orientation in the unloaded (left) and loaded (right) operating cases; comparison of BEMF reference inductance parameters with HF measurements and its polynomial approximations in subfigures (a) and (b); resulting anisotropy orientations in (c) and (d)

When applying the same polynomial iron effects model to the SPMSM measurements, we obtain the results presented in Figure 6.39. As before, we can determine the anisotropy position impaired by iron effects sufficiently well in the considered frequency range above 800 Hz.

We already discussed in section 6.4.2.1, that the SPMSM shows a stronger effect of magnetic hysteresis in the mean and anisotropic inductance curves (see Figure 6.25). This is also observable in both, loaded and unloaded cases, in the  $d$ -,  $q$ - and  $m$ -inductances.

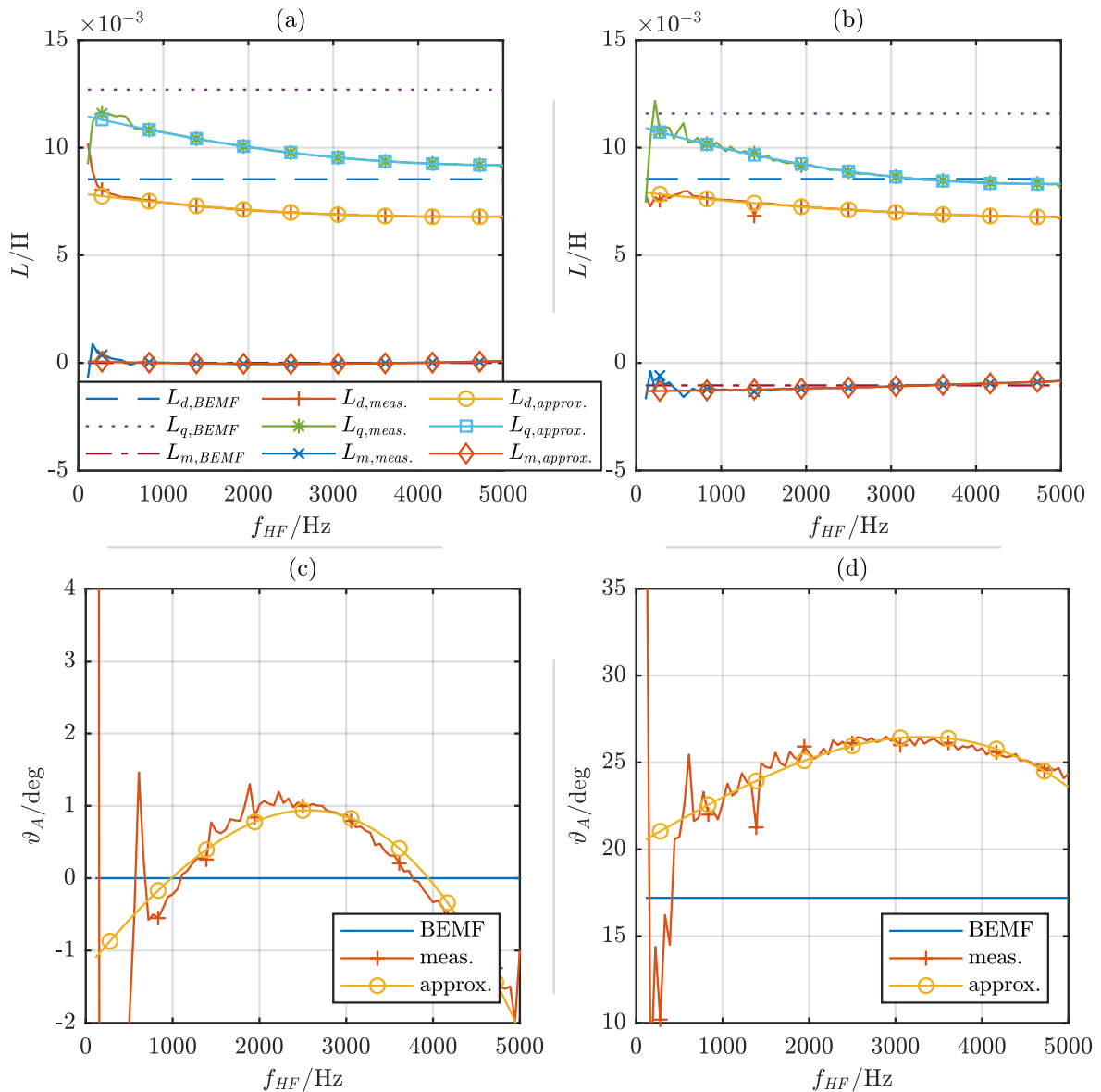


Figure 6.39: SPMSM inductance values and anisotropy orientation in the unloaded (left) and loaded (right) operating cases; comparison of BEMF reference inductance parameters with HF measurements and its polynomial approximations in subfigures (a) and (b); resulting anisotropy orientations in (c) and (d)

In order to verify the discussed polynomial model for the SynRM as well, we show the respective results in Figure 6.40. Again, we see that the approximated anisotropy positions match well with the measured curves. We can thus conclude that the polynomial approximations of the direct, quadrature and mutual inductance curves are a good way to eliminate the influence of iron effects in sensorless control schemes at arbitrary injection frequencies with a comparable low number of nine parameters needed for each relevant operating point.

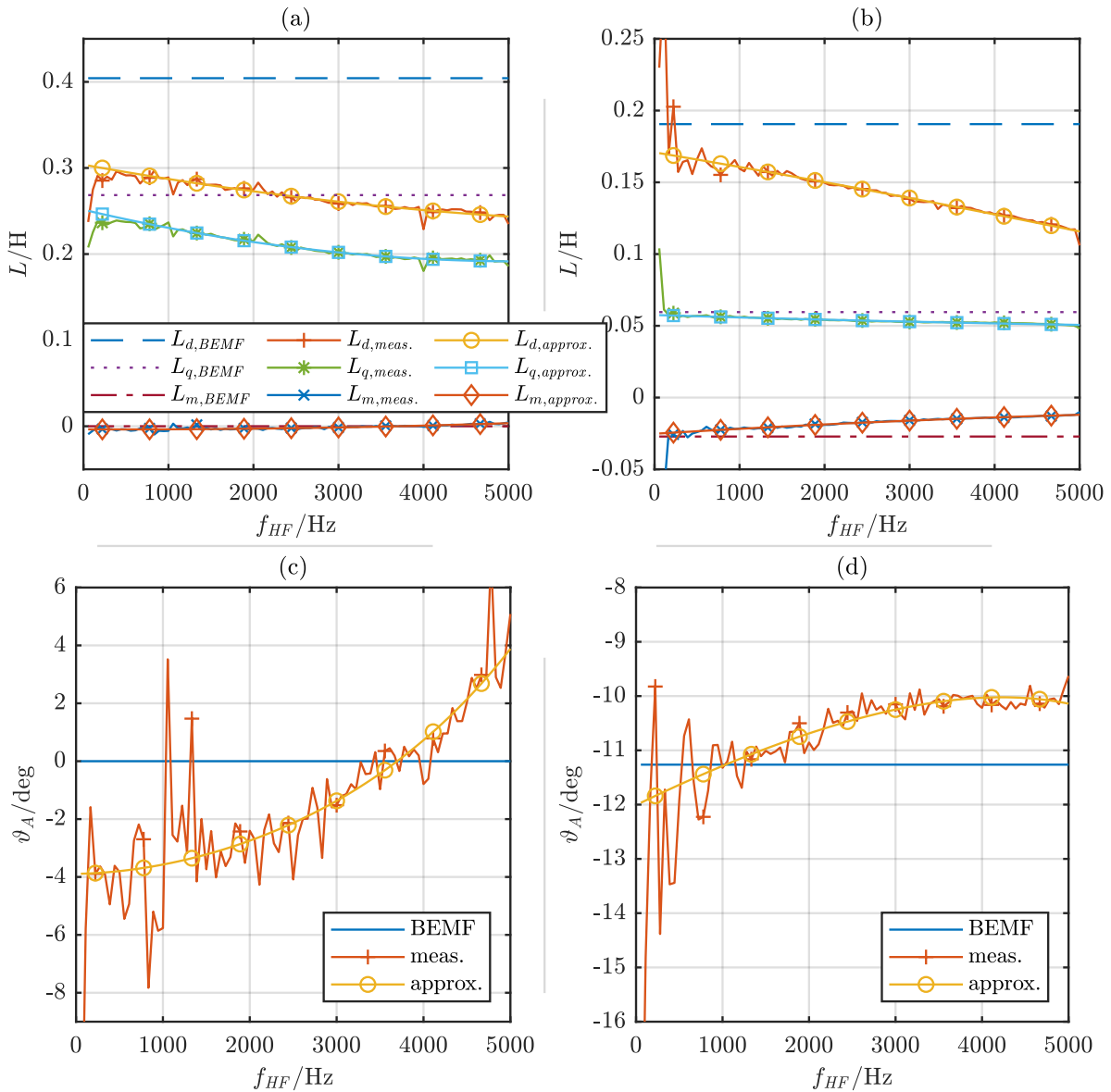


Figure 6.40: SynRM inductance values and anisotropy orientation in the unloaded (left) and loaded (right) operating cases; comparison of BEMF reference inductance parameters with HF measurements and its polynomial approximations in subfigures (a) and (b); resulting anisotropy orientations in (c) and (d)

So far, we separately discussed inductance maps at certain injection frequencies for variable operating points and inductance curves at certain operating points for variable injection frequencies. In order to allow comparing the results, the IPMSM maps are measured at three different injection frequencies. For the unloaded case and at rated load, we can then plot the results as shown in Figure 6.41.

We see again the anisotropy orientation angles from the BEMF measurements as reference. The curves denoted with ‘approx. 1’ correspond to the polynomial models we just discussed in Figure 6.38. When fitting the 2<sup>nd</sup> order polynomials to the inductance values from the measurements of the three maps, we obtain the curves denoted with ‘approx. 2’, where the measured points are separately marked by ‘x’.

The first polynomial curves approximate a high number of measurements in a least squares sense, whereas the second approximation curves exactly fit the three respective measurement points. The noise we observed in above measurements (see Figures 6.38 to 6.40) in consequence leads to noticeable differences between both approximations. With a higher number of measured maps, we would thus be able to reduce the differences between both curves.

The effect of the proposed optimization algorithm for measured maps is shown by the ‘o’ markers. In the unloaded case, the stator current of the motor is zero. In this case, we know that the mutual inductances must be zero as well. Since the optimization algorithm enforces this condition, the resulting anisotropy positions for all three measurements are zero and thus identical with the BEMF reference in subfigure (a).

At rated load in subfigure (b), we see that the optimization is not able to completely eliminate the influence of iron effects in the HF measurements. This has been observed before in the discussions of the anisotropy orientation maps, especially at the SPMSM and the SynRM (see

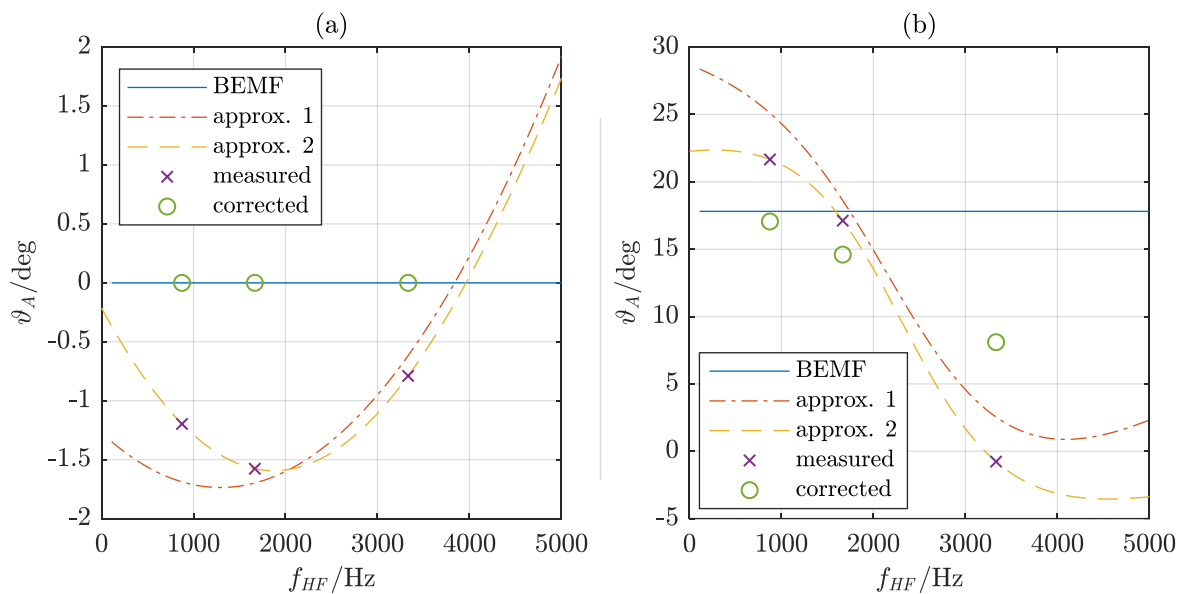


Figure 6.41: Comparison of the interpolated influence of iron effects on the identified anisotropy position for the IPMSM in an unloaded case (a) and at rated load (b)

Figures 6.34 and 6.36). While we found only minor differences between the corrected BEMF and HF maps in Figure 6.32, we can now see that at higher frequencies than 875 Hz, we will have larger differences as well.

We can thus conclude that the influence of iron effects on HF-based measurements is reduced on average but not completely eliminated. Best results for maps free of distortions from iron effects can be obtained from BEMF-based measurements in combination with the proposed correction algorithm.

As we preempted in section 6.4.2.1, this discussion on sensorless control is concluded with an analysis of the expectable position estimation errors in sensorless control schemes that evaluate the current response to rotating voltage injections, when the stator resistance is neglected (see for instance [10, 25]). We therefore evaluate the inductance parameters of all three machines along their MTPA trajectories. As before, we use the corrected BEMF measurement results as data source. We can thus map each torque value with a corresponding set of inductance parameters. When assuming the rotor to be at rest and defining a range of reasonable injection frequencies, we can determine the numerator terms acc. to (6.28) and substitute them into the anisotropy position equation (6.45). We perform this procedure one time with the correct stator resistance and the second time with  $R_s = 0$ . After subtracting both results from each other, we obtain the results presented in Figure 6.42, where

$$\vartheta_{A,err} = \vartheta_A|_{R_s=0} - \vartheta_A. \quad (6.69)$$

We can see that for all three machines we get negative position errors that depend on the torque as well as the injection frequency. It was already analyzed in section 6.4.2 that neglecting the stator resistance only leads to relevant anisotropy position errors, when the injection frequency is low. The results in Figure 6.42 confirm this for all three machines.

The largest occurring errors are around  $-7^\circ$  for the PM machines and  $-5^\circ$  for the SynRM. The load dependency of the errors seems to correlate with the level of rotor saliency. We thus do have nearly constant errors over different torques at the SPMSM in subfigure (b), while the SynRM in (c) shows the strongest torque dependency.

When comparing the position error maps of all three machines, we find that the SPMSM is the most critical machine, followed by the IPMSM and the SynRM shows the least sensitivity to stator resistance errors. In all three cases however, selecting injection frequencies above 500Hz allows us to neglect the stator resistance without relevant position estimation errors.

It is worth noting that the presented results are generic error predictions for rotating injection schemes. Depending on the actual algorithmic implementation and applied filtering techniques, the errors in specific sensorless control schemes might significantly differ. The figure shall just give an overview of the theoretical underlying signal content for all types of rotating injection schemes.

Please also note, that the error analysis for other injection schemes can be done analogously but requires the more complex elliptic solutions acc. to (6.41) – (6.43).

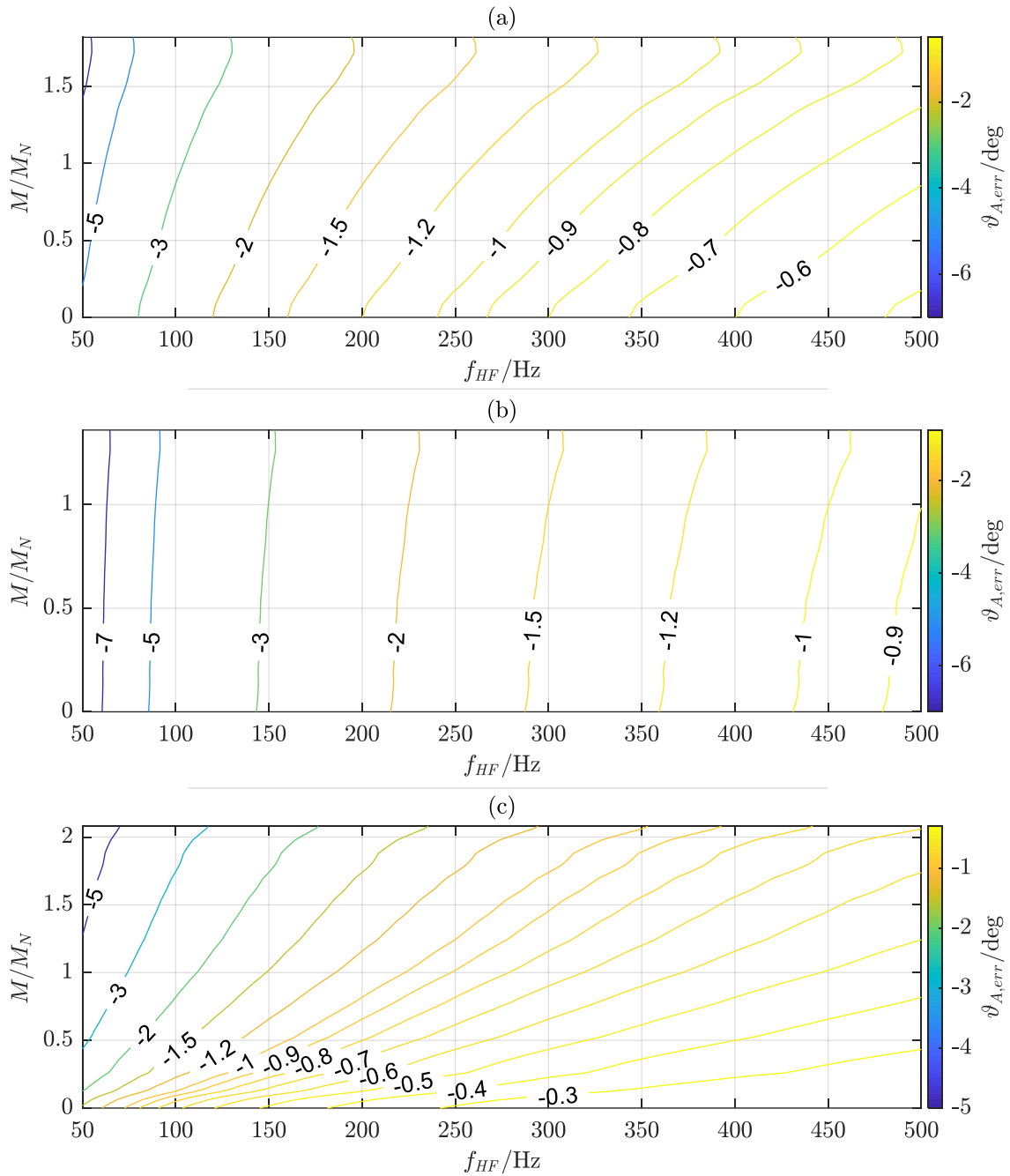


Figure 6.42: Comparison of the position estimation errors at standstill and variable loads along the MTPA trajectory for low injection frequencies for the IPMSM (a), the SPMSM (b) and the SynRM (c)

### 6.5.2 Differences in Torque

As already discussed, the motor torque is resulting from the cross product of stator current and flux linkage space vectors. A comparison of the IPMSM torque maps obtained from BEMF and HF measurements after applying the proposed optimization algorithm is shown in Figure 6.43.

While subfigure (a) gives us a three-dimensional impression of the motor torque obtained from HF measurements at different stator currents, subfigure (b) directly compares those torque values with the BEMF reference. We can note that both measurement schemes lead to very similar results. This is remarkable, since we observed clearly visible drift errors due to iron effects in the border regions of the HF flux linkage maps which are the basis for this torque map (cf. Figure 6.31).

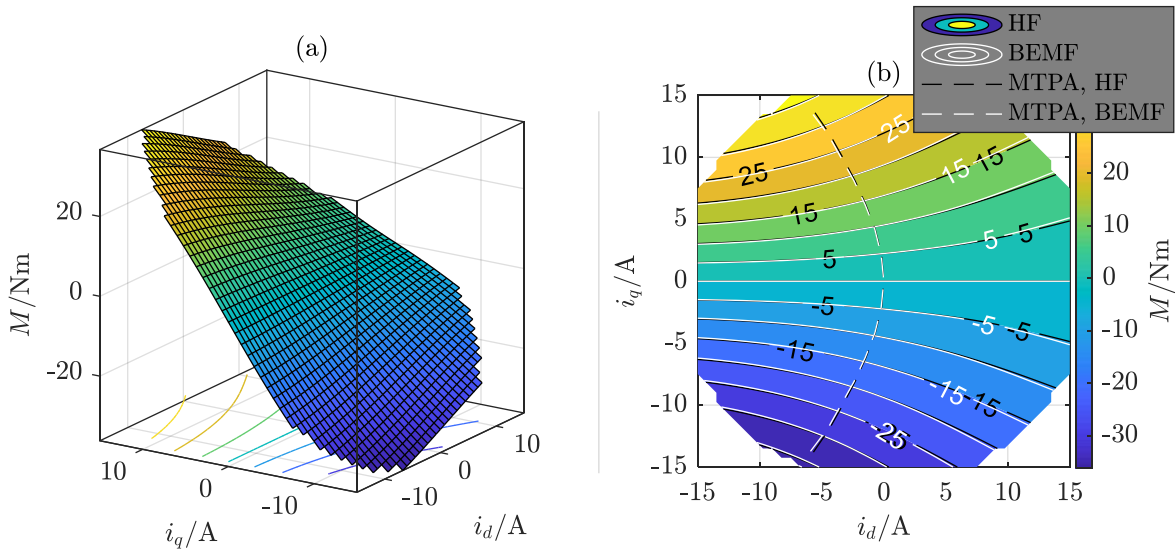


Figure 6.43: Comparison of IPMSM torque maps obtained from optimized HF (black and colored) and BEMF (white) measurements

When deriving the MTPA trajectories from both torque maps, we also get nearly identical results. Although we can expect the resulting torque differences to be negligible as well, we further analyze both trajectories in Figure 6.44. In subfigure (a), we can find the angular differences between both trajectories, plotted over the magnitudes of the respective stator current space vectors. We can see that the maximal displacement of the HF trajectory is below one degree. The influence of these displacements is analyzed in subfigure (b).

The angular displacement of the HF trajectory leads to relative torque errors, which are represented by the solid blue line. In this analysis, we apply the current vector values of the HF trajectory to the BEMF torque map. When we, instead apply it to the HF torque map, we get relative errors as shown by the dashed orange line. We can see that in both cases, the maximal errors are below 0.5% of the respective BEMF reference and should thus indeed be negligible in most applications.

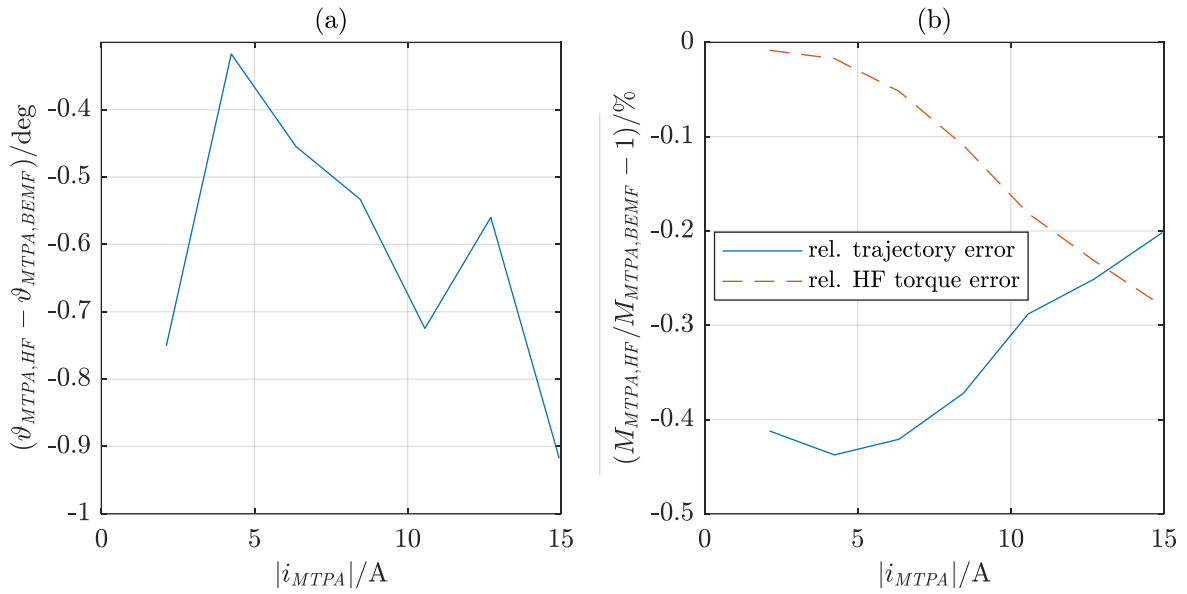


Figure 6.44: Angular differences between (a) and relative torque errors along (b) MTPA trajectories obtained from corrected IPMSM BEMF and HF measurements

The results of the same analysis for the SPMSM are shown in Figures 6.45 and 6.46. We see that both torque maps obtained from BEMF and HF measurements fit well, but not as good as for the IPMSM. The BEMF map and the resulting MTPA trajectory show a slightly higher level of curvature towards the negative  $d$ -axis current. Since the SPMSM has a non-salient rotor, this curvature can only be caused by magnetic saturation. We can thus state that the HF measurements lead to slightly lower saturated flux linkage maps. This was already observed at the IPMSM and iron effects are identified as reason for that.

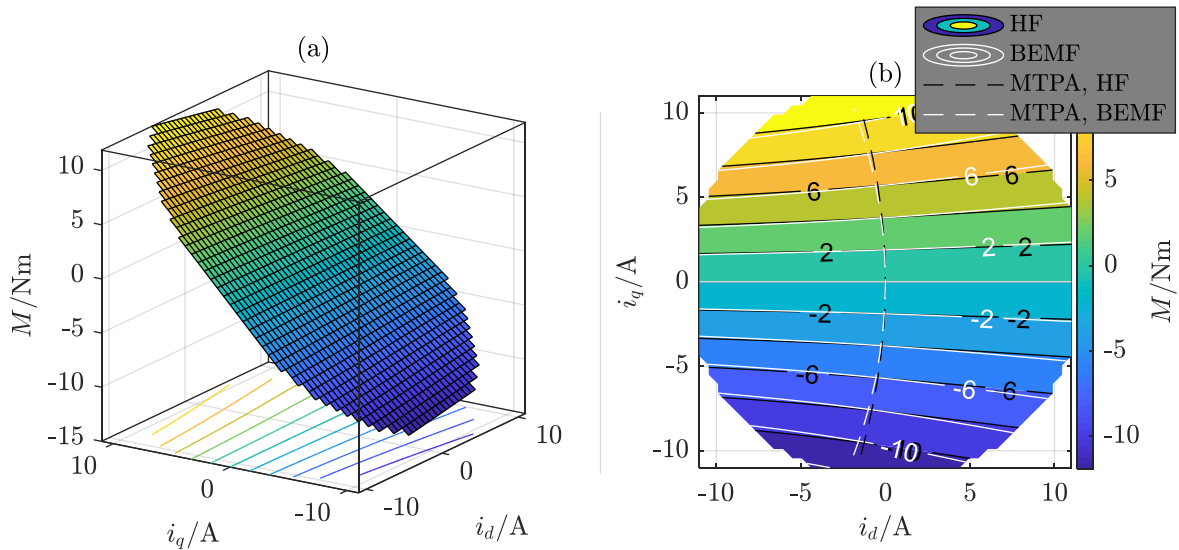


Figure 6.45: Comparison of SPMSM torque maps obtained from optimized HF (black and colored) and BEMF (white) measurements

In Figure 6.46 (a), we see that the iron effects lead to angle errors of the MTPA trajectory of almost  $-2.5^\circ$ . In consequence, the corresponding torque is reduced by around  $-1.2$  to  $-1.7\%$ . When relying on the HF torque measurements, the expected torque along the MTPA trajectory is up to  $0.7\%$  smaller than we would expect from the BEMF measurements.

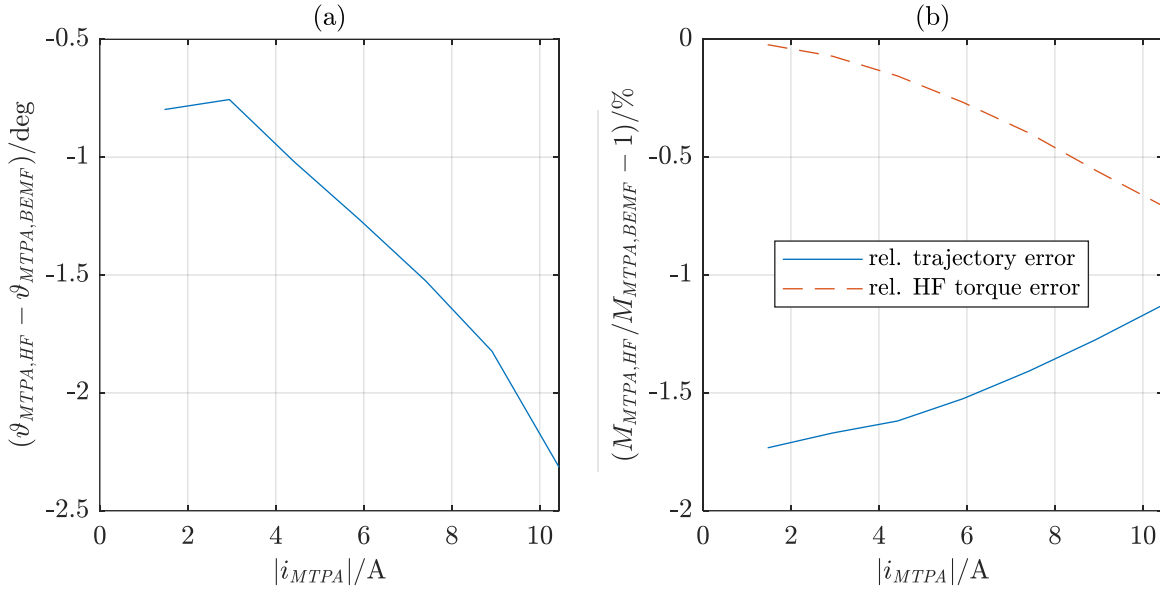


Figure 6.46: Angular differences between (a) and relative torque errors along (b) MTPA trajectories obtained from corrected SPMSM BEMF and HF measurements

In contrast to both PM machines, we find larger differences between the HF and BEMF torque maps of the SynRM as shown in Figure 6.47. While around the origin the differences are small, they grow fast with increasing current vector magnitudes. The already observed strong magnetic hysteresis effects in the unsaturated ferromagnetic material of the SynRM are the most likely explanations for these errors. The resulting smaller inductance measurements cumulate during the integration process towards the border regions of the measured area.

Nevertheless, we can see that the resulting torque errors are comparably symmetrical, which leads to very similar MTPA trajectories. In Figure 6.48 (a), it is shown that the angular displacement of the HF trajectory is below two degrees. Acc. to subfigure (b), the resulting torque is reduced by less than around  $2\%$ .

The torque along the MTPA trajectory that we would expect from the HF measurements, however, is significantly smaller by around  $20$  to  $22\%$ . In applications, where this is problematic, it is thus advisable to measure the actual torque with BEMF based techniques.

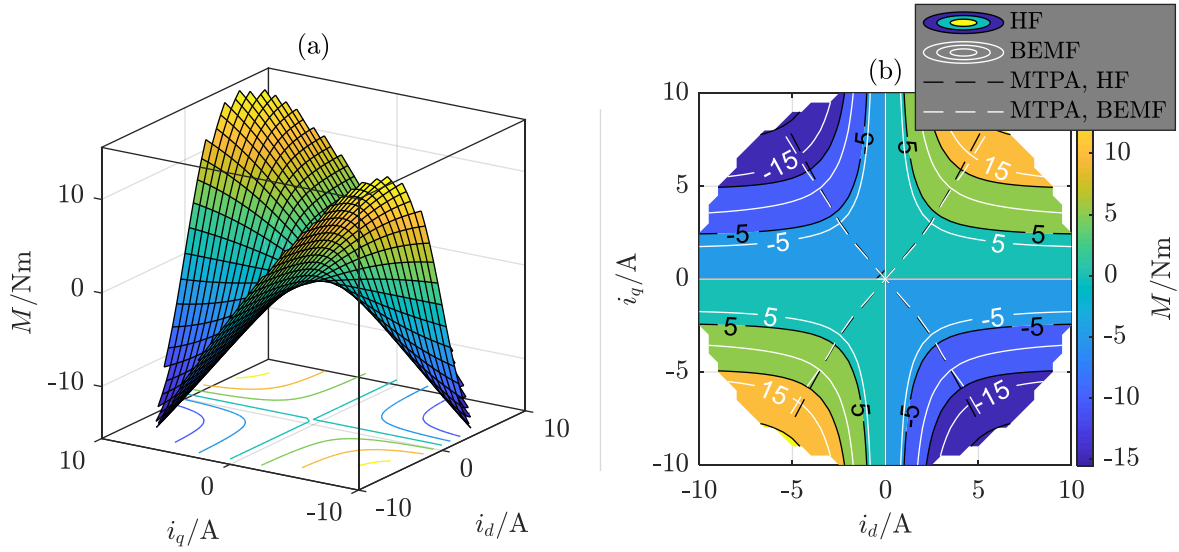


Figure 6.47: Comparison of SynRM torque maps obtained from optimized HF (black and colored) and BEMF (white) measurements

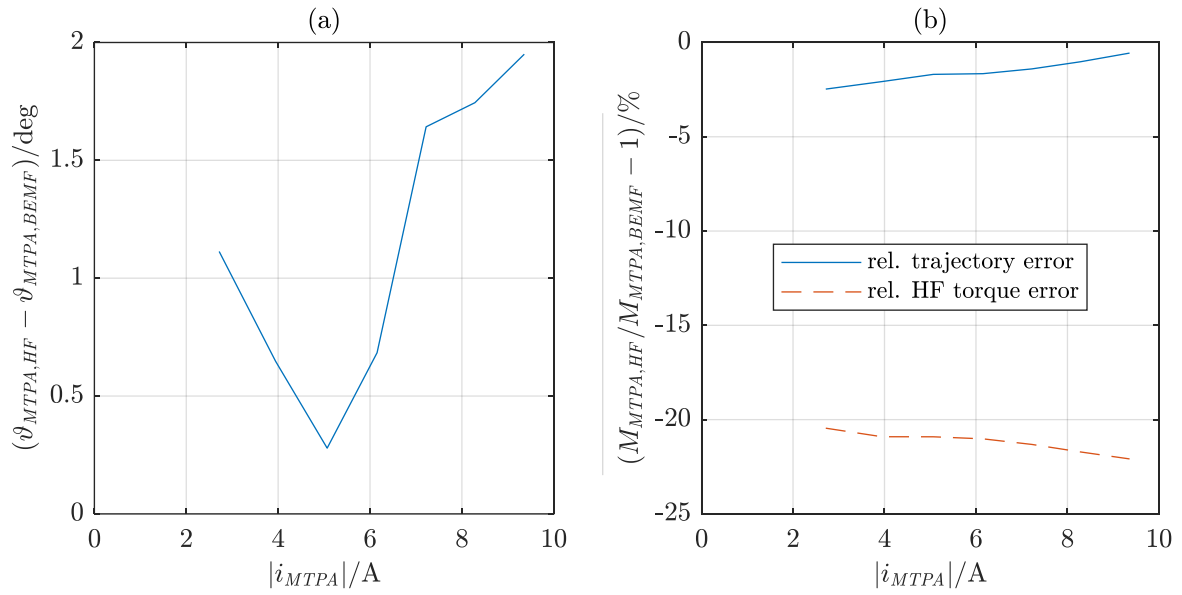


Figure 6.48: Angular differences between (a) and relative torque errors along (b) MTPA trajectories obtained from corrected SynRM BEMF and HF measurements



# CHAPTER 7

---

## Conclusions and Outlook

---

### 7.1 Summary

---

In this work, the issue of accurately modelling and identifying the respective model parameters of synchronous machines under the influence of magnetic saturation is addressed.

The underlying physical processes that cause magnetic saturation as well as magnetic hysteresis in ferromagnetic material are discussed. After transferring the insights from a fundamental, mesoscopic view to a macroscopic view in the form of lumped elements, it is shown that the nonlinearity resulting from magnetic saturation has no influence on the general validity of the widespread space vector theory that is applied to describe, predict and control the behavior of synchronous machines. It is exemplarily discussed that harmonic distortions can occur, which itself can be expressed as harmonic space vectors.

With a SynRM, an IPMSM and an SPMSM, three important types of synchronous machines are discussed. Based on fundamental space vectors, nonlinear models are introduced and subsequently linearized in order to obtain affine models that allow the mathematically efficient approximation of the motor behavior around given operating points.

Two methods to measure the nonlinear relation between currents in the stator windings and the resulting flux linkages are presented and discussed – one method that evaluates the back electromotive force and one that bases on the linearized small-signal model and that evaluates the current responses to high-frequency voltages that are injected to the machine. For both methods, different sources of error are discussed, and appropriate measures are proposed to minimize those errors.

The BEMF method was found to be sensitive to stator voltage errors, to inaccurate stator resistance parameters, to harmonic distortions and, to a limited extent, to iron effects. The

errors in the stator voltages result from their indirect measurement via the DC-link voltage and nonlinear switching characteristics of the IGBTs in the supplying VSI. It is discussed, how these switching effects can be measured and the results being used to eliminate the resulting model errors. The resistance parameter errors can have different sources, such as the frequency dependent proximity effect or heat related effects. The latter are explicitly taken care of in all proposed measurement schemes by heat management via resistance measurements. The problem of harmonic distortions is addressed by selecting measurement intervals that cover integer numbers of rotor turns.

For the proposed HF based measurement scheme, a detailed analysis of linear, time-invariant systems with rotating input signals is performed. This allows to explicitly consider the influence of the stator resistance in HF current responses of synchronous machines, which is generally neglected in literature. Depending on the injection frequency, especially at low frequencies, it is shown that neglecting the resistance leads to errors in the identified anisotropy orientation, which can distort derived flux linkage maps and is also relevant in anisotropy-based sensorless control schemes. Additionally, the LTI system analysis shows that neglecting the BEMF as it is done in several HF-based publications does lead to inductance parameter errors for low to medium injection frequencies.

Besides that, the main sources of error in the HF based measurement scheme are harmonic distortions and iron effects. The former are only partly addressed by measurement intervals covering complete rotor turns and by properly selecting the injection frequencies such that they do not interfere with motor harmonics. The main problem here are the high injection frequencies that go up to half the PWM frequency. The discrete sampling at PWM frequency and the discrete nature of the applied space vector modulation technique make it necessary to consider frequency leakage and aliasing effects. Both effects are analyzed, and appropriate compensation techniques are proposed.

After eliminating the discussed sources of error as good as possible, it can be stated that the remaining errors in both measurement schemes are due to iron effects. Comparing the measurement results allows to better understand their influence on the machine behavior. Additionally, the HF-based measurements at variable injection frequencies allow to further distinguish between the influence of eddy currents and magnetic hysteresis. It is discussed that magnetic hysteresis results in inductance offsets, especially in unsaturated operating points. With increasing levels of magnetic saturation, the influence of magnetic saturation decreases. Eddy currents are causing inductance parameter errors that scale linearly or quadratically with the injection frequency. Additionally, they lead to misorientation of the anisotropy position.

While the BEMF based method measures flux linkages, the HF method identifies inductances. The flux linkage information is needed to identify optimal current trajectories that produce maximal torque while simultaneously considering current and voltage limitations. The inductance parameters are important in anisotropy-based sensorless control schemes. Independent from the measurement scheme, it is thus useful to convert flux linkage maps to inductance maps and vice versa. Differentiating flux linkage maps to obtain inductances is straightforward. Integrating inductance maps that contain measurement errors, however, is

more difficult. Depending on the selected integration paths, we obtain different flux linkage maps. To overcome this problem, an optimization algorithm is proposed that constraints the inductance maps to comply with fundamental physical laws. This guarantees unambiguous flux linkage or even magnetic energy and co-energy maps.

The optimization algorithm is further extended by symmetry constraints. The linear optimization identifies the minimal necessary modifications that enforce both, physical and symmetry constraints. It is shown that the optimization does effectively eliminate the inverter voltage errors and the resistance parameter errors in the BEMF based measurements and reduces the influence of iron effects.

The optimized results of all three synchronous machines are used to discuss the general differences between the machine types. Additionally, the results are discussed in the context of magnetic energy, torque production, the affine model parameters and the motor characteristics in anisotropy-based sensorless control schemes. The aforementioned misorientation of the anisotropy position caused by eddy currents is addressed by a frequency dependent polynomial model. It is shown that in the proposed way, the relatively nonlinear dependency of the position error on the injection frequency can be accurately modelled, while also adequately describing the frequency dependency of the inductance parameters.

Even though the HF measurement scheme is more affected by iron effects, it is shown that the results nevertheless are useful to identify MTPA trajectories for efficient control strategies. For all three machines, we obtain trajectories that differ less than  $2.5^\circ$  from the ideal trajectories. The resulting effective torque reductions remain below 2%. For the PM machines, the predicted torques along the MTPA trajectories are even better with errors below 1%. Only the SynRM shows larger relative errors of more than 20% in the predicted torques due to the strong influence of magnetic hysteresis and due to the absence of permanent magnetic torque components.

Since the HF measurements can also be performed at standstill, they can be a useful alternative, when no load machine is available to control the speed of the motor under test. When the influence of iron effects on sensorless control errors shall be analyzed, the HF method is also preferable over BEMF-based measurements.

## **7.2 Outlook**

---

With magnetic saturation, magnetic hysteresis and eddy currents, this work addresses fundamental problems in basically all control strategies for synchronous machines. It thus provides several potential connecting points with further works, which are addressed in the following.

In the discussion of the results for sensorless control schemes in section 6.5.1, a model describing the influence of iron effects is proposed. Since this will only work for steady injection frequencies, a more general attempt that allows the dynamic analysis of iron effects seems worth further work. One way might be to extend the state-space model of the synchronous machine by additional states that represent eddy currents. In its simplest form, we would add two states for a single eddy current space vector that models the average magnetic repercussions of all

individual eddy current loops. This way, we obtain a model with the same structure as that of an induction machine.

When addressing the issue of identifying the additional model parameters, it can be useful that the particular solution of LTI systems responding to circular inputs is also valid for systems of higher order than two. We would thus need to find a systematic approach to determine those eddy current parameters that let the entries of the particular solution matrix that correlate the stator voltages with the stator currents match those of the BEMF model.

The differences between the particular solution matrix entries obtained from BEMF and HF measurements are exemplarily shown in Figure 7.1. Obviously, the HF results for all motor speeds and all injections amplitudes are very similar and – at least in subfigures (a) to (c) – are clearly distinguishable from the BEMF results. These differences should be modelled by additional eddy current parameters, while the main model parameters obtained from BEMF measurements should remain unchanged.

This approach of dynamically modelling eddy currents might also be advantageous, when dealing with iron losses. In literature, this is typically done by introducing frequency-dependent resistances [21, 111, 112, 116], which does not reflect the physical reality.

Since we end up with a similar model as an induction motor without eddy currents, the presented HF based measurement approach might also be interesting for parameter identification of induction machines.

An open point that could not be completely analyzed within this work are the partially elliptic injection voltages and especially their abrupt changes at low injection frequencies. As mentioned in section 6.4.2.1, oscillations of the motor speed in response to the low injection frequencies might be a reason. Since analyzing speed oscillations would require to introduce the speed as additional state variable, the resulting model would be much more complex to analyze. This remains open for further works.

If it turns out that speed oscillations are not the reason for the elliptic voltages, it might also be useful to work on control schemes that eliminate all negatively rotating voltages or to extend the HF method such that it can handle elliptic injection voltages as well.

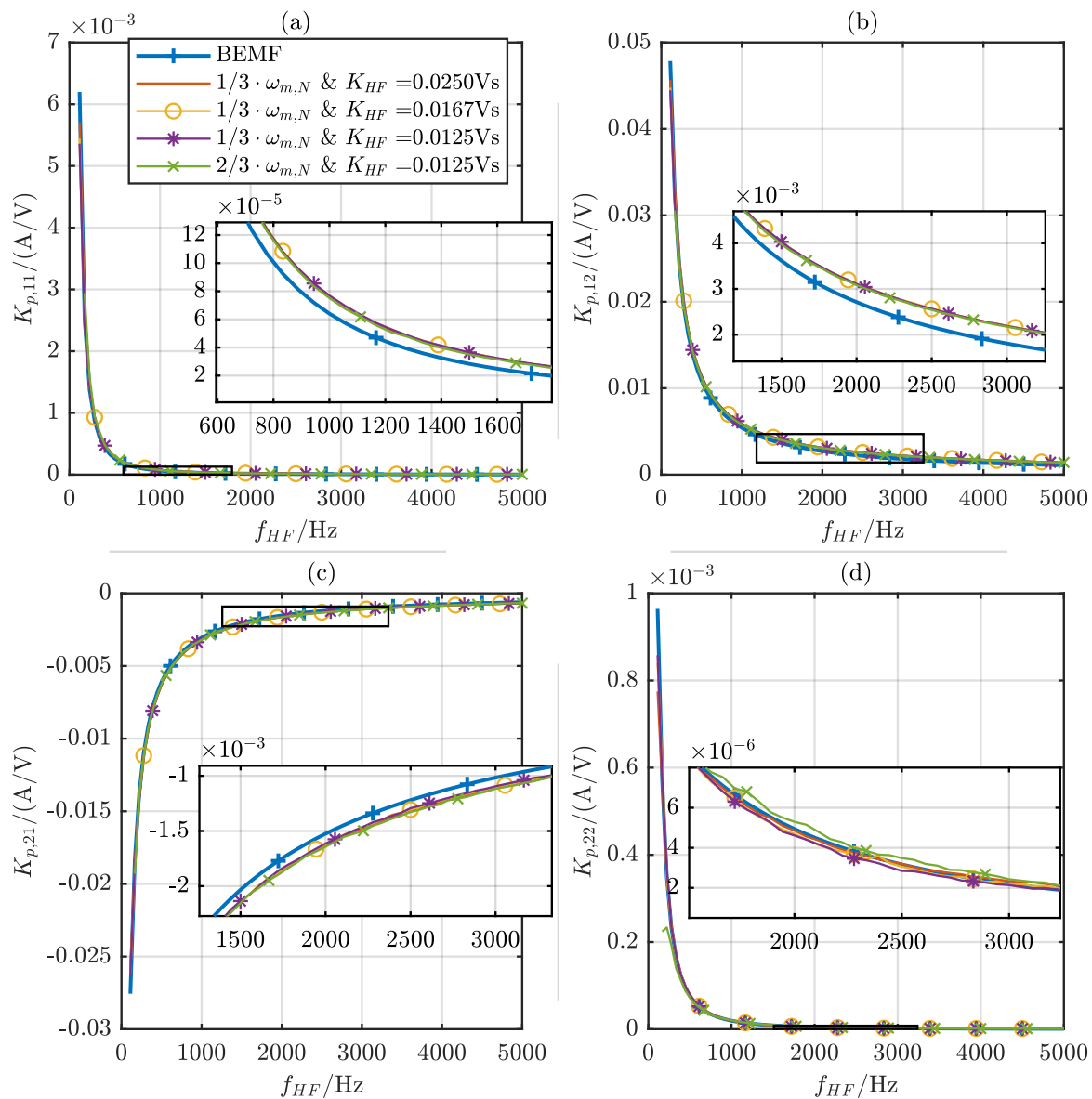


Figure 7.1: Entries of the particular solution matrix for rotating voltage signals of the IPMSM for variable injection frequencies and at different injection amplitudes and motor speeds (legend valid for all subfigures)



# APPENDIX A

## Nomenclature

### A.1 List of Symbols

#### A.1.1 Roman Characters

$a$	A/m	current loading
$A$		system matrix of a state space model
$A^r$		system matrix of a synchronous machine in rotor reference frame
$\bar{B}$	Vs/m <sup>2</sup>	magnetic flux density
$B^r$		input matrix of a synchronous machine in rotor reference frame
$c_1$		scaling factor for fundamental HF signal components
$C$	m	contour line around a surface $S$ (section 2.1)
$C$		stator current and flux linkage space vector trajectory (section 2.2)
$d_{u,v,w}$	1	duty cycles of phases $u, v, w$ in space vector modulation
$D$	$\Omega^4$	denominator of the particular solution matrix $K_p^r$
$D$		diagonal matrix
$d\vec{a}$	m	normal vector of an infinitesimal surface $S$
$d\vec{s}$	m	infinitesimal line segment
$dv$	m <sup>3</sup>	infinitesimal volume
$e_1$	1	unit vector in first dimension of multi-dimensional space
$e_2$	1	unit vector in second dimension of multi-dimensional space
$\vec{E}$	V/m	electric field intensity
$f$	Hz	frequency
$f_{an}$	Hz	$n^{\text{th}}$ alias frequency of a given frequency, $f$
$f_{HF}$	Hz	HF injection frequency
$f_k$	Hz	discrete frequency in Fourier analysis
$f_m$	Hz	mechanical rotor frequency

$f_r$	Hz	electrical rotor frequency
$f_S$	Hz	sampling frequency
$\mathbf{f}^r$		bijjective vector function
$\vec{H}$	A/m	magnetic field intensity
$H_c$	A/m	coercive field intensity
$H_s$	A/m	saturation magnetic field intensity
$i$	A	electrical current
$i_{PM}$	A	permanent magnet equivalent stator current
$\mathbf{i}_s^a$	A	stator current space vector in anisotropy reference frame
$\mathbf{i}_s^r$	A	stator current space vector in rotor reference frame
$\mathbf{i}_s^*$	V	reference input for $\mathbf{i}_s^r$
$\mathbf{i}_s^s$	A	stator current space vector in stator reference frame
$\mathbf{i}_{s,0}^r$	A	stator current space vector in the magnetic origin
$\mathbf{I}$	1	unit matrix
$\vec{j}$	A/m <sup>2</sup>	current density vector
$\vec{j}_f$	A/m <sup>2</sup>	free current density vector in conducting material
$\vec{j}_M$	A/m <sup>2</sup>	magnetizing current density
$\vec{j}_{MS}$	A/m <sup>2</sup>	magnetizing surface current density
$\mathbf{J}$	1	90° rotation matrix
$k_{sat}$	1	saturation factor in space vector modulation
$K_{HF}$	Vs	scaling factor for injection voltage amplitudes over injection frequency
$\mathbf{K}_p^r$	A/V	particular solution matrix of a SM in rotor reference frame
$l$	m	length
$L$	H	inductance of an electric conductor
$L_{dd}$	H	$d$ -axis inductance
$L_{dq}$	H	coupling inductance between $d$ - and $q$ -axis
$L_{qd}$	H	coupling inductance between $q$ - and $d$ -axis
$L_{qq}$	H	$q$ -axis inductance
$L_m$	H	mutual inductance
$L_D$	H	$D$ -axis inductance
$L_Q$	H	$Q$ -axis inductance
$L_{A,\Delta}$	H	anisotropic inductance of the stator windings
$L_s$	H	inductance of the stator windings
$L_\Delta$	H	mean difference inductance of the stator windings
$L_\Sigma$	H	mean (isotropic) inductance of the stator windings
$\mathbf{L}_s^a$	H	inductance matrix of the stator windings in anisotropy reference frame
$\mathbf{L}_s^r$	H	inductance matrix of the stator windings in rotor reference frame
$\mathbf{L}_s^s$	H	inductance matrix of the stator windings in stator reference frame
$M$	Nm	motor torque
$\vec{M}$	A/m	magnetization density
$M_L$	Nm	load torque
$M_r$	A/m	remanent magnetization
$M_s$	A/m	saturation magnetization

$\vec{n}$	1	normal vector
$N_{I+}$	$\Omega^3$	pos. rotating numerator term of $\mathbf{K}_p^r$
$N_{J+}$	$\Omega^3$	pos. rotating 90° numerator term of $\mathbf{K}_p^r$
$N_{I-}$	$\Omega^3$	neg. rotating numerator term of $\mathbf{K}_p^r$
$N_{J-}$	$\Omega^3$	neg. rotating 90° numerator term of $\mathbf{K}_p^r$
$p$	1	number of pole pairs
$\vec{p}$	W/m <sup>2</sup>	power density vector (Poynting vector)
$p_J$	W/m <sup>3</sup>	Joule loss density
$p_\mu$	W/m <sup>3</sup>	magnetic energy density
$P_{mech}$	W	mechanical power
$r_S$	1	saliency ratio
$R$	$\Omega$	electrical resistance
$R_a$	$\Omega$	approximative resistance of stator windings and motor cable
$R_{cal}$	$\Omega$	calibrated resistance of stator windings and motor cable
$R_s$	$\Omega$	resistance of the stator windings
$S$	m <sup>2</sup>	surface area (section 2.1)
$S$		sector number of a space vector (section 2.3)
$\mathbf{S}$	1	double-angle rotation matrix
$t$	s	time
$t_0$	s	active time of zero vector in SVM
$t_l$	s	active time of left vector in SVM
$t_r$	s	active time of right vector in SVM
$T_1$	s	period length of a signal in Fourier analysis
$T_{fi}$	s	filter time constant of current measurements
$T_{fu1,2}$	s	filter time constants of voltage measurements
$T_{meas}$	s	measurement time period
$T_S$	s	sampling time or SVM cycle time
$\mathbf{T}$	1	rotation matrix
$u$	V	voltage
$u_{DC}$	V	DC link voltage
$\mathbf{u}_s^a$	V	stator voltage space vector in anisotropy reference frame
$\mathbf{u}_s^r$	V	stator voltage space vector in rotor reference frame
$\mathbf{u}_s^{r*}$	V	reference input for $\mathbf{u}_s^r$
$\mathbf{u}_s^s$	V	stator voltage space vector in stator reference frame
$\mathbf{u}_s^{s*}$	V	reference input for $\mathbf{u}_s^s$
$\vec{v}$	m/s	velocity vector
$V$	m <sup>3</sup>	volume
$\mathbf{V}$		eigenvector matrix
$w$	J/m <sup>3</sup>	energy density
$w_\mu$	J/m <sup>3</sup>	magnetic energy density
$w_{\mu,co}$	J/m <sup>3</sup>	magnetic co-energy density
$w_{\mu,hyst}$	J/m <sup>3</sup>	hysteretic magnetic co-energy density
$W_{el}$	J	electric energy

$W_\mu$	J	magnetic energy
$W_{\mu,co}$	J	magnetic co-energy
$\mathbf{X}$	1	vertical flip matrix (complex conjugate analogon)

### A.1.2 Greek Characters

$\Gamma_{dd}$	1/H	inverse $d$ -axis inductance
$\Gamma_{dq}$	1/H	inverse coupling inductance between $d$ - and $q$ -axis
$\Gamma_{qd}$	1/H	inverse coupling inductance between $q$ - and $d$ -axis
$\Gamma_{qq}$	1/H	inverse $q$ -axis inductance
$\Gamma_m$	1/H	inverse mutual inductance
$\Gamma_D$	1/H	inverse $D$ -axis inductance
$\Gamma_Q$	1/H	inverse $Q$ -axis inductance
$\Gamma_{A,\Delta}$	1/H	inverse anisotropic inductance of the stator windings
$\Gamma_s$	1/H	inverse inductance of the stator windings
$\Gamma_\Delta$	1/H	inverse mean difference inductance of the stator windings
$\Gamma_\Sigma$	1/H	inverse mean (isotropic) inductance of the stator windings
$\Gamma_s^a$	1/H	inv. inductance matrix of the stator windings in anisotropy reference frame
$\Gamma_s^r$	1/H	inverse inductance matrix of the stator windings in rotor reference frame
$\Gamma_s^s$	1/H	inverse inductance matrix of the stator windings in stator reference frame
$\Delta$		Delta (difference) operator
$\epsilon$	F/m	permittivity
$\epsilon_0$	F/m	permittivity of free space ( $8.854 \cdot 10^{-12}$ F/m)
$\vartheta$	rad	generic angle
$\vartheta_a$	rad	angle between stator and anisotropy reference frame
$\vartheta_A$	rad	angle between rotor and anisotropy reference frame
$\vartheta_r$	rad	electrical rotor angle of a synchronous machine
$\vartheta_m$	rad	mechanical rotor angle of a synchronous machine
$\Theta$	kg m <sup>2</sup>	moment of inertia
$\lambda_i$		$i^{\text{th}}$ eigenvalue of a square matrix
$\mu_0$	H/m	permeability of free space ( $4\pi \cdot 10^{-7}$ H/m)
$\boldsymbol{\mu}$	H/m	permeability matrix
$\boldsymbol{\mu}_r$	1	relative permeability matrix
$\rho$	C/m <sup>3</sup>	charge density
$\sigma$	1/ $\Omega\text{m}$	electrical conductivity
$\tau_i$	s	time constant of a linear system
$\phi_k$	rad	phase of a signal in Fourier analysis
$\chi_{rev}$	1	reversible susceptibility
$\chi_{dif}$	1	differential susceptibility
$\boldsymbol{\chi}$	1	magnetic susceptibility tensor
$\psi$	Vs/A	magnetic flux linkage
$\psi_{PM}$	Vs/A	permanent magnet flux linkage
$\psi_s^a$	Vs	stator flux linkage space vector in anisotropy reference frame
$\psi_s^r$	Vs	stator flux linkage space vector in rotor reference frame

$\bar{\psi}_s^r$	Vs	arithmetic average of $\psi_s^r$
$\psi_s^s$	Vs	stator flux linkage space vector in stator reference frame
$\psi_{s,0}^r$	Vs	stator flux linkage space vector in the magnetic origin
$\psi_{s,c}^s$	Vs	constant of integration of the stator flux linkage space vector
$\omega_k$	rad/s	discrete radial frequency in Fourier analysis
$\omega_m$	rad/s	mechanical angular velocity of the rotor
$\omega_r$	rad/s	electrical angular velocity of the rotor

### A.1.3 Special Characters

$\nabla$	nabla operator
$\ell$	vector norm
$\Re$	real part of a complex number

## A.2 List of Abbreviations

---

AC	Alternating Current
ADC	Analog-to-Digital Converter
BEMF	Back Electromotive Force
CL	Closed-Loop
DC	Direct Current
DTC	Direct Torque Control
EMF	Electromotive Force
EQS	Electroquasistatic
FEA	Finite Element Analysis
FFT	Fast Fourier Transform
FOC	Field Oriented Control
FOH	First Order Hold
HF	High Frequency
HPF	High-Pass Filter
IGBT	Insulated Gate Bipolar Transistor
IO	Input-Output
IPM	Interior Permanent Magnet
IPMSM	Interior Permanent Magnet Synchronous Machine
ISR	Interrupt Service Routine
LHS	Left-Hand-Side
LPF	Low-Pass Filter
LTI	linear, time-invariant
LUT	Look-Up Table
MTPA	Maximum Torque Per Ampere
MTPV	Maximum Torque Per Volts
MQS	Magnetoquasistatic
NdFeB	Neodymium-Iron-Boron
OL	Open-Loop
PC	Personal Computer
PI	Proportional-Integral (type controller)
PM	Permanent Magnet
PMSM	Permanent Magnet Synchronous Machine
PWA	Piece Wise Affine
PWC	Piece Wise Constant
PWM	Pulse Width Modulation
RMS	Root Mean Square
RTP	Real-Time Processor
RHS	Right-Hand-Side
SDRAM	Synchronous Dynamic Random Access Memory
SM	Synchronous Machine
SmCo	Samarium-Cobalt
SNR	Signal-to-Noise Ratio

SPM	Surface Permanent Magnet
SPMSM	Surface Permanent Magnet Synchronous Machine
SR	Saliency Ratio
SVM	Space Vector Modulation
SynRM	Synchronous Reluctance Machine
VSI	Voltage Source Inverter
VFD	Variable Frequency Drive
ZOH	Zero Order Hold



## APPENDIX B

---

### Calculations

---

#### B.1 Energy Balance of Synchronous Machines

---

Starting with the electrical three-phase model (2.43), the power balance can be obtained by multiplication with the phase current vector. Hence,

$$\begin{bmatrix} u_a \\ u_b \\ u_c \end{bmatrix} = R_s \cdot \begin{bmatrix} i_a \\ i_b \\ i_c \end{bmatrix} + \frac{d}{dt} \begin{bmatrix} \psi_a \\ \psi_b \\ \psi_c \end{bmatrix}, \quad (\text{B.1})$$

$$\mathbf{u}_{abc} = R_s \cdot \mathbf{i}_{abc} + \frac{d}{dt} \boldsymbol{\psi}_{abc}, \quad (\text{B.2})$$

$$P_{el} = \mathbf{i}_{abc}^T \cdot \mathbf{u}_{abc} = R_s \cdot \mathbf{i}_{abc}^T \cdot \mathbf{i}_{abc} + \mathbf{i}_{abc}^T \cdot \frac{d}{dt} \boldsymbol{\psi}_{abc}, \quad (\text{B.3})$$

where the vectors are denoted by  $\mathbf{x}_{abc}$  for conciseness.

Transforming (2.97) into space vector notation, when the transformation matrix is denoted by  $\mathbf{A}_{abc2r}$  gives

$$\mathbf{A}_{abc2r} = \frac{2}{3} \begin{bmatrix} 1 & -1/2 & -1/2 \\ 0 & \sqrt{3}/2 & -\sqrt{3}/2 \end{bmatrix} \quad (\text{B.4})$$

$$(\mathbf{A}_{abc2r} \cdot \mathbf{i}_s^s)^T \cdot \mathbf{A}_{abc2r} \cdot \mathbf{u}_s^s = R_s \cdot (\mathbf{A}_{abc2r} \cdot \mathbf{i}_s^s)^T \cdot \mathbf{A}_{abc2r} \cdot \mathbf{i}_s^s + (\mathbf{A}_{abc2r} \cdot \mathbf{i}_s^s)^T \cdot \frac{d}{dt} \mathbf{A}_{abc2r} \cdot \boldsymbol{\psi}_s^s, \quad (\text{B.5})$$

$$\mathbf{i}_s^{sT} \cdot \mathbf{A}_{abc2r}^T \cdot \mathbf{A}_{abc2r} \cdot \mathbf{u}_s^s = R_s \cdot \mathbf{i}_s^{sT} \cdot \mathbf{A}_{abc2r}^T \cdot \mathbf{A}_{abc2r} \cdot \mathbf{i}_s^s + \mathbf{i}_s^{sT} \cdot \mathbf{A}_{abc2r}^T \cdot \frac{d}{dt} \mathbf{A}_{abc2r} \cdot \boldsymbol{\psi}_s^s \quad (\text{B.6})$$

With  $\mathbf{A}_{abc2r}^T \cdot \mathbf{A}_{abc2r} = \frac{3}{2} \begin{bmatrix} 1 & 0 \\ 0 & 1 \end{bmatrix}$ , (2.97) can be rewritten as

$$P_{el} = \frac{3}{2} \mathbf{i}_s^{sT} \cdot \mathbf{u}_s^s = \frac{3}{2} \left( R_s \cdot \mathbf{i}_s^{sT} \cdot \mathbf{i}_s^s + \mathbf{i}_s^{sT} \cdot \frac{d}{dt} \boldsymbol{\psi}_s^s \right). \quad (\text{B.7})$$

Transforming the space vectors in (B.7) into rotor coordinates gives

$$P_{el} = \frac{3}{2} \mathbf{i}_s^r T \mathbf{u}_s^r = \frac{3}{2} \left( R_s \mathbf{i}_s^r T \mathbf{i}_s^r + \omega \mathbf{i}_s^r T \mathbf{J} \boldsymbol{\psi}_s^r + \mathbf{i}_s^r T \frac{d}{dt} \boldsymbol{\psi}_s^r \right). \quad (\text{B.8})$$

Finally, the energy balance can be obtained by integrating (2.97) over a time interval,  $\Delta t$ . Hence,

$$W_{el} = \int_{\Delta t} \frac{3}{2} \mathbf{i}_s^r T \mathbf{u}_s^r dt = \frac{3}{2} \int_{\Delta t} (R_s \mathbf{i}_s^r T \mathbf{i}_s^r + \omega \mathbf{i}_s^r T \mathbf{J} \boldsymbol{\psi}_s^r) dt + \frac{3}{2} \int_C \mathbf{i}_s^r T d\boldsymbol{\psi}_s^r, \quad (\text{B.9})$$

where  $C$  is the integration path along the trajectory of currents and flux linkages during the given time interval.

## B.2 Alternative Machine Model in Stator Coordinates

In section 2.2.3.1, the machine model in stator coordinates (2.54) was transformed into rotor coordinates in order to account for the nonlinear magnetic characteristics,  $\boldsymbol{\psi}_s^r = \mathbf{f}^r(\mathbf{i}_s^r)$ , which can be described best in rotor coordinates. The result was

$$\mathbf{u}_s^r = R_s \mathbf{i}_s^r + \omega_r \mathbf{J} \boldsymbol{\psi}_s^r + \mathbf{L}_s^r \frac{d}{dt} \mathbf{i}_s^r, \quad (\text{B.10})$$

where

$$\mathbf{L}_s^r = \begin{bmatrix} \frac{\partial \psi_d}{\partial i_d} & \frac{\partial \psi_d}{\partial i_q} \\ \frac{\partial \psi_q}{\partial i_d} & \frac{\partial \psi_q}{\partial i_q} \end{bmatrix} = \begin{bmatrix} L_{dd} & L_{dq} \\ L_{qd} & L_{qq} \end{bmatrix}. \quad (\text{B.11})$$

In an attempt to maintain this description of the magnetic characteristics and at the same time have a model with directly measurable inputs and variables, we transform (B.10) back into stator coordinates. Therefore, we rewrite the time derivative in the third term on the RHS of (B.10) as

$$\frac{d}{dt} \mathbf{i}_s^r = \frac{d}{dt} (\mathbf{T}(-\vartheta_r) \mathbf{i}_s^s) = -\omega_r \mathbf{J} \mathbf{T}(-\vartheta_r) \mathbf{i}_s^s + \mathbf{T}(-\vartheta_r) \frac{d\mathbf{i}_s^s}{dt}. \quad (\text{B.12})$$

By multiplying (B.10) with  $\mathbf{T}(\vartheta_r)$  and substituting the time rate of change of the current acc. to (B.12) into (B.10), we obtain

$$\mathbf{u}_s^s = R_s \mathbf{i}_s^s + \omega_r \mathbf{J} \boldsymbol{\psi}_s^s + \mathbf{T}(\vartheta_r) \mathbf{L}_s^r \left( -\omega_r \mathbf{J} \mathbf{T}(-\vartheta_r) \mathbf{i}_s^s + \mathbf{T}(-\vartheta_r) \frac{d\mathbf{i}_s^s}{dt} \right), \quad (\text{B.13})$$

which, when considering the fact that  $\mathbf{J}$  is also a rotational matrix and that those matrices commute with each other, can be further simplified to

$$\mathbf{u}_s^s = R_s \mathbf{i}_s^s + \omega_r (\mathbf{J} \boldsymbol{\psi}_s^s - \mathbf{L}_s^s \mathbf{J} \mathbf{i}_s^s) + \mathbf{L}_s^s \frac{d\mathbf{i}_s^s}{dt}, \quad (\text{B.14})$$

where

$$\mathbf{L}_s^s = \begin{bmatrix} \frac{\partial \psi_\alpha}{\partial i_\alpha} & \frac{\partial \psi_\alpha}{\partial i_\beta} \\ \frac{\partial \psi_\beta}{\partial i_\alpha} & \frac{\partial \psi_\beta}{\partial i_\beta} \end{bmatrix} = \mathbf{T}(\vartheta_r) \mathbf{L}_s^r \mathbf{T}(-\vartheta_r). \quad (\text{B.15})$$

### B.3 Rotational Transformations of Matrices

Rotational coordinate transformations as in the former section B.2 lead to matrix expressions of the following form,

$$\mathbf{K}^a = \mathbf{T}(\vartheta) \mathbf{K}^b \mathbf{T}(-\vartheta), \quad (\text{B.16})$$

where  $\mathbf{K}^a$  is a  $2 \times 2$  matrix in coordinate system  $a$  and  $\mathbf{K}^b$  is the respective matrix in coordinate system  $b$  with  $\vartheta$  being the angle between the axes of abscissae of both systems (from  $a$  to  $b$ ) and  $\mathbf{T}(\vartheta)$  being the rotational matrix as defined in (2.38).

When performing the transformation, we get

$$\begin{aligned} \mathbf{T}(\vartheta) \mathbf{K}^b \mathbf{T}(-\vartheta) &= \begin{bmatrix} \cos(\vartheta) & -\sin(\vartheta) \\ \sin(\vartheta) & \cos(\vartheta) \end{bmatrix} \begin{bmatrix} k_{11} & k_{12} \\ k_{21} & k_{22} \end{bmatrix} \begin{bmatrix} \cos(\vartheta) & \sin(\vartheta) \\ -\sin(\vartheta) & \cos(\vartheta) \end{bmatrix} \\ &= \begin{bmatrix} \cos(\vartheta) k_{11} - \sin(\vartheta) k_{21} & \cos(\vartheta) k_{12} - \sin(\vartheta) k_{22} \\ \sin(\vartheta) k_{11} + \cos(\vartheta) k_{21} & \sin(\vartheta) k_{12} + \cos(\vartheta) k_{22} \end{bmatrix} \begin{bmatrix} \cos(\vartheta) & \sin(\vartheta) \\ -\sin(\vartheta) & \cos(\vartheta) \end{bmatrix} \\ &= \begin{bmatrix} \cos^2(\vartheta) k_{11} - \sin(\vartheta) \cos(\vartheta) k_{21} - \sin(\vartheta) \cos(\vartheta) k_{12} + \sin^2(\vartheta) k_{22} \\ \sin(\vartheta) \cos(\vartheta) k_{11} + \cos^2(\vartheta) k_{21} - \sin^2(\vartheta) k_{12} - \sin(\vartheta) \cos(\vartheta) k_{22} \\ \sin(\vartheta) \cos(\vartheta) k_{11} - \sin^2(\vartheta) k_{21} + \cos^2(\vartheta) k_{12} - \sin(\vartheta) \cos(\vartheta) k_{22} \\ \sin^2(\vartheta) k_{11} + \sin(\vartheta) \cos(\vartheta) k_{21} + \sin(\vartheta) \cos(\vartheta) k_{12} + \cos^2(\vartheta) k_{22} \end{bmatrix} \\ &= \begin{bmatrix} \cos^2(\vartheta) k_{11} - \sin(\vartheta) \cos(\vartheta) (k_{21} + k_{12}) + \sin^2(\vartheta) k_{22} \\ \sin(\vartheta) \cos(\vartheta) (k_{11} - k_{22}) + \cos^2(\vartheta) k_{21} - \sin^2(\vartheta) k_{12} \\ \sin(\vartheta) \cos(\vartheta) (k_{11} - k_{22}) - \sin^2(\vartheta) k_{21} + \cos^2(\vartheta) k_{12} \\ \sin^2(\vartheta) k_{11} + \sin(\vartheta) \cos(\vartheta) (k_{21} + k_{12}) + \cos^2(\vartheta) k_{22} \end{bmatrix}. \end{aligned}$$

With the trigonometric identities [58 pp. 81–83]

$$\sin^2(\vartheta) = \frac{1}{2}(1 - \cos(2\vartheta)), \quad (\text{B.17})$$

$$\cos^2(\vartheta) = \frac{1}{2}(1 + \cos(2\vartheta)), \quad (\text{B.18})$$

and

$$\sin(\vartheta) \cos(\vartheta) = \frac{1}{2} \sin(2\vartheta), \quad (\text{B.19})$$

we can further simplify above calculations to

$$\begin{aligned} \mathbf{T}(\vartheta) \mathbf{K}^b \mathbf{T}(-\vartheta) &= \frac{1}{2} \begin{bmatrix} (1 + \cos(2\vartheta))k_{11} - \sin(2\vartheta)(k_{21} + k_{12}) + (1 - \cos(\vartheta))k_{22} \\ \sin(2\vartheta)(k_{11} - k_{22}) + (1 + \cos(2\vartheta))k_{21} - (1 - \cos(\vartheta))k_{12} \\ \sin(2\vartheta)(k_{11} - k_{22}) - (1 - \cos(\vartheta))k_{21} + (1 + \cos(2\vartheta))k_{12} \\ (1 - \cos(\vartheta))k_{11} + \sin(2\vartheta)(k_{21} + k_{12}) + (1 + \cos(2\vartheta))k_{22} \end{bmatrix} \\ &= \frac{1}{2} \left( \begin{bmatrix} (1 + \cos(2\vartheta))k_{11} + (1 - \cos(\vartheta))k_{22} & \sin(2\vartheta)(k_{11} - k_{22}) \\ \sin(2\vartheta)(k_{11} - k_{22}) & (1 - \cos(\vartheta))k_{11} + (1 + \cos(2\vartheta))k_{22} \end{bmatrix} \right. \\ &\quad \left. + \begin{bmatrix} -\sin(2\vartheta)(k_{21} + k_{12}) & -(1 - \cos(\vartheta))k_{21} + (1 + \cos(2\vartheta))k_{12} \\ (1 + \cos(2\vartheta))k_{21} - (1 - \cos(\vartheta))k_{12} & \sin(2\vartheta)(k_{21} + k_{12}) \end{bmatrix} \right) \\ &= \frac{1}{2} \left( \begin{bmatrix} k_{11} + k_{22} + \cos(2\vartheta)(k_{11} - k_{22}) & \sin(2\vartheta)(k_{11} - k_{22}) \\ \sin(2\vartheta)(k_{11} - k_{22}) & k_{11} + k_{22} + \cos(2\vartheta)(-k_{11} + k_{22}) \end{bmatrix} \right. \\ &\quad \left. + \begin{bmatrix} -\sin(2\vartheta)(k_{21} + k_{12}) & k_{12} - k_{21} + \cos(\vartheta)(k_{21} + k_{12}) \\ k_{21} - k_{12} + \cos(2\vartheta)(k_{21} + k_{12}) & \sin(2\vartheta)(k_{21} + k_{12}) \end{bmatrix} \right) \\ &= \frac{1}{2} \left( (k_{11} + k_{22}) \begin{bmatrix} 1 & 0 \\ 0 & 1 \end{bmatrix} + (k_{11} - k_{22}) \begin{bmatrix} \cos(2\vartheta) & \sin(2\vartheta) \\ \sin(2\vartheta) & -\cos(2\vartheta) \end{bmatrix} + (k_{21} - k_{12}) \begin{bmatrix} 0 & -1 \\ 1 & 0 \end{bmatrix} \right. \\ &\quad \left. + (k_{21} + k_{12}) \begin{bmatrix} -\sin(2\vartheta) & \cos(2\vartheta) \\ \cos(2\vartheta) & \sin(2\vartheta) \end{bmatrix} \right). \end{aligned}$$

With the definition of  $\mathbf{S}(\vartheta)$  as

$$\mathbf{S}(\vartheta) = \begin{bmatrix} \cos(2\vartheta) & \sin(2\vartheta) \\ \sin(2\vartheta) & -\cos(2\vartheta) \end{bmatrix}, \quad (\text{B.20})$$

we can write

$$\mathbf{T}(\vartheta) \mathbf{K}^b \mathbf{T}(-\vartheta) = \frac{1}{2} \left( (k_{11} + k_{22}) \mathbf{I} + (k_{11} - k_{22}) \mathbf{S}(\vartheta) + (k_{21} - k_{12}) \mathbf{J} + (k_{21} + k_{12}) \mathbf{J} \mathbf{S}(\vartheta) \right) \quad (\text{B.21})$$

and finally

$$\mathbf{T}(\vartheta) \mathbf{K}^b \mathbf{T}(-\vartheta) = \frac{1}{2} \left( (k_{11} + k_{22}) \mathbf{I} + (k_{21} - k_{12}) \mathbf{J} + ((k_{11} - k_{22}) \mathbf{I} + (k_{21} + k_{12}) \mathbf{J}) \mathbf{S}(\vartheta) \right), \quad (\text{B.22})$$

where

$$\mathbf{I} = \mathbf{T}(0) = \begin{bmatrix} 1 & 0 \\ 0 & 1 \end{bmatrix}, \quad (\text{B.23})$$

and

$$\mathbf{J} = \mathbf{T}\left(\frac{\pi}{2}\right) = \begin{bmatrix} 0 & -1 \\ 1 & 0 \end{bmatrix}. \quad (\text{B.24})$$

### B.4 Eigenvalues and Eigenvectors of a (2×2) Matrix

A square ( $n \times n$ ) matrix,  $\mathbf{A}$ , has  $n$  eigenvalues,  $\lambda_i$ , that can be found from

$$\det(\mathbf{A} - \lambda_i \mathbf{I}) = 0. \quad (\text{B.25})$$

For  $n = 2$ , we can write

$$\det \begin{bmatrix} a_{11} - \lambda_i & a_{12} \\ a_{21} & a_{22} - \lambda_i \end{bmatrix} = 0 \quad (\text{B.26})$$

Solving (B.26) for  $\lambda_i$  is straightforward and gives:

$$\begin{aligned} (a_{11} - \lambda_i)(a_{22} - \lambda_i) - a_{12}a_{21} &= 0 \\ a_{11}a_{22} - a_{11}\lambda_i - a_{22}\lambda_i + \lambda_i^2 - a_{12}a_{21} &= 0 \\ \lambda_i^2 - (a_{11} + a_{22})\lambda_i + a_{11}a_{22} - a_{12}a_{21} &= 0 \\ \lambda_i &= \frac{a_{11} + a_{22}}{2} \pm \sqrt{\left(\frac{a_{11} + a_{22}}{2}\right)^2 - a_{11}a_{22} + a_{12}a_{21}} \\ \lambda_i &= \frac{a_{11} + a_{22}}{2} \pm \frac{1}{2} \sqrt{a_{11}^2 + 2a_{11}a_{22} + a_{22}^2 - 4a_{11}a_{22} + 4a_{12}a_{21}} \end{aligned}$$

Simplifying the root expression finally gives

$$\lambda_i = \frac{a_{11} + a_{22}}{2} \pm \sqrt{\left(\frac{a_{11} - a_{22}}{2}\right)^2 + a_{12}a_{21}}. \quad (\text{B.27})$$

When substituting (B.27) into the eigenvalue problem, we can determine the components of the corresponding eigenvectors,  $\mathbf{x}_i$ :

$$(\mathbf{A} - \lambda_i \mathbf{I})\mathbf{x}_i = \mathbf{0} \quad (\text{B.28})$$

For  $n = 2$ , (B.28) is a set of two equations, namely

$$\begin{bmatrix} a_{11} - \lambda_i & a_{12} \\ a_{21} & a_{22} - \lambda_i \end{bmatrix} \begin{bmatrix} x_{i1} \\ x_{i2} \end{bmatrix} = \mathbf{0}. \quad (\text{B.29})$$

When solving both equations separately for the first component of  $\mathbf{x}_i$ , we get:

1)

$$\begin{aligned} (a_{11} - \lambda_i)x_{i1} + a_{12}x_{i2} &= 0 \\ x_{i1} &= -\frac{a_{12}}{a_{11} - \lambda_i}x_{i2} \\ x_{i1} &= -\frac{a_{12}}{a_{11} - \frac{a_{11} + a_{22}}{2} \mp \sqrt{\left(\frac{a_{11} - a_{22}}{2}\right)^2 + a_{12}a_{21}}}x_{i2} \\ x_{i1} &= \frac{a_{12}}{-\frac{a_{11} - a_{22}}{2} \pm \sqrt{\left(\frac{a_{11} - a_{22}}{2}\right)^2 + a_{12}a_{21}}}x_{i2} \end{aligned} \quad (\text{B.30})$$

2)

$$\begin{aligned}
 a_{21}x_{i1} + (a_{22} - \lambda_i)x_{i2} &= 0 \\
 x_{i1} &= -\frac{a_{22} - \lambda_i}{a_{21}}x_{i2} \\
 x_{i1} &= -\frac{a_{22} - \frac{a_{11} + a_{22}}{2} \mp \sqrt{\left(\frac{a_{11} - a_{22}}{2}\right)^2 + a_{12}a_{21}}}{a_{21}}x_{i2} \\
 x_{i1} &= \frac{\frac{a_{11} - a_{22}}{2} \pm \sqrt{\left(\frac{a_{11} - a_{22}}{2}\right)^2 + a_{12}a_{21}}}{a_{21}}x_{i2}
 \end{aligned} \tag{B.31}$$

The length of eigenvectors is usually not interesting. Often, they are normalized to one. The orientation, however, contains their relevant information. We can express it in terms of the angle  $\vartheta$  between the axis of abscissae and the respective eigenvector:

From 1)

$$\vartheta_i = \text{atan} \left( \frac{x_{i2}}{x_{i1}} \right) = \text{atan} \left( \frac{-\frac{a_{11} - a_{22}}{2} \pm \sqrt{\left(\frac{a_{11} - a_{22}}{2}\right)^2 + a_{12}a_{21}}}{a_{12}} \right) \tag{B.32}$$

From 2)

$$\vartheta_i = \text{atan} \left( \frac{x_{i2}}{x_{i1}} \right) = \text{atan} \left( \frac{a_{21}}{\frac{a_{11} - a_{22}}{2} \pm \sqrt{\left(\frac{a_{11} - a_{22}}{2}\right)^2 + a_{12}a_{21}}} \right) \tag{B.33}$$

When we assume that  $\mathbf{A}$  is *symmetric* and by comparing (B.32) and (B.33) to the definitions of the atan2 function (B.40) and (B.43) in the following section B.5, we can also write in both cases

$$\vartheta_i = \frac{1}{2} \text{atan2} \left( \pm a_{12}, \pm \frac{a_{11} - a_{22}}{2} \right) \tag{B.34}$$

## B.5 Definition of atan2(y,x)

---

The atan2 function shall give us the angle,  $\vartheta$ , of a point in Cartesian coordinates  $(x, y)$  with respect to the axis of ordinate in all four quadrants of that coordinate system, i.e. in the interval  $-\pi < \vartheta \leq \pi$ . We thus define

$$\text{atan2}(y, x) = \vartheta, \tag{B.35}$$

where the coordinates are given by

$$(x, y) = (r \cos \vartheta, r \sin \vartheta), \tag{B.36}$$

with

$$r = \sqrt{x^2 + y^2}. \tag{B.37}$$

The tangent half-angle formula is known to be [58 p. 82]

$$\tan\left(\frac{\vartheta}{2}\right) = \frac{\sin \vartheta}{1 + \cos \vartheta}. \quad (\text{B.38})$$

Substituting (B.36) into (B.38) and subsequently solving for  $\vartheta/2$  gives us:

$$\begin{aligned} \tan\left(\frac{\vartheta}{2}\right) &= \frac{y/r}{1 + x/r} \\ \tan\left(\frac{\vartheta}{2}\right) &= \frac{y}{r + x} \\ \frac{\vartheta}{2} &= \text{atan} \frac{y}{\sqrt{x^2 + y^2} + x} \end{aligned} \quad (\text{B.39})$$

Finally, substituting (B.39) into (B.35) gives us the solution:

$$\text{atan2}(y, x) = 2 \text{atan} \frac{y}{\sqrt{x^2 + y^2} + x} \quad (\text{B.40})$$

An alternative solution can be found analogously, when using the other half-angle formula [58 p. 82]:

$$\tan\left(\frac{\vartheta}{2}\right) = \frac{1 - \cos \vartheta}{\sin \vartheta}. \quad (\text{B.41})$$

$$\frac{\vartheta}{2} = \text{atan} \frac{\sqrt{x^2 + y^2} - x}{y} \quad (\text{B.42})$$

$$\text{atan2}(y, x) = 2 \text{atan} \frac{\sqrt{x^2 + y^2} - x}{y} \quad (\text{B.43})$$

## B.6 Response of Linear State Space Models to Rotating Input Signals

---

The particular solution of a linear, time-invariant system in state-space notation,

$$\frac{d}{dt} \mathbf{x} = \mathbf{A}\mathbf{x} + \mathbf{B}\mathbf{u}, \quad (\text{B.44})$$

is given by

$$\mathbf{x}_p(t) = \int_{t_0}^t \exp(\mathbf{A}(t - \tau)) \mathbf{B}\mathbf{u}(\tau) d\tau, \quad (\text{B.45})$$

where  $\mathbf{x}$  is the vector of state variables,  $\mathbf{u}$  is the input vector and  $\mathbf{A}$  and  $\mathbf{B}$  are the corresponding system and input matrices [74 pp. 706–707].

When we consider the special case of a rotational input signal, we can define

$$\mathbf{u}(t) = u \begin{bmatrix} \cos(\omega t + \phi) \\ \sin(\omega t + \phi) \end{bmatrix} = u \mathbf{T}(\omega t + \phi) \mathbf{e}_1, \quad (\text{B.46})$$

where  $u$  is the magnitude of the signal rotating at a frequency of  $\omega$  with an initial phase of  $\phi$ .

We thus have two input dimensions. With  $n$  state variables, the input matrix has the size  $n \times 2$ , whereas the system matrix is a  $n \times n$  square matrix. The latter can be decomposed into

$$\mathbf{A} = \mathbf{V}\mathbf{D}\mathbf{V}^{-1}, \quad (\text{B.47})$$

where  $\mathbf{D}$  is a diagonal matrix containing the  $n$  eigenvalues of  $\mathbf{A}$  and  $\mathbf{V}$  is a square matrix, whose columns are the eigenvectors of  $\mathbf{A}$  [65 p. 113]. Analogously, the matrix exponential in (B.45) can be decomposed into ([65 pp. 108–109])

$$\exp(\mathbf{A}(t - \tau)) = \mathbf{V} \exp(\mathbf{D}(t - \tau)) \mathbf{V}^{-1}, \quad (\text{B.48})$$

where

$$\exp(\mathbf{D}(t - \tau)) = \begin{bmatrix} \exp \lambda_1(t - \tau) & 0 & 0 \\ 0 & \ddots & 0 \\ 0 & 0 & \exp \lambda_n(t - \tau) \end{bmatrix}. \quad (\text{B.49})$$

It is easy to see that (B.49) can be rewritten as the product of two diagonal matrix exponentials, i.e.

$$\exp(\mathbf{D}(t - \tau)) = \exp(\mathbf{D}t) \exp(-\mathbf{D}\tau). \quad (\text{B.50})$$

Since  $\mathbf{V}$  is constant and also the time,  $t$ , is independent from the integration variable,  $\tau$ , we can substitute (B.48) into (B.45) and rewrite the result as

$$\mathbf{x}_p(t) = \mathbf{V} \exp(\mathbf{D}t) \int_{t_0}^t \exp(-\mathbf{D}\tau) \mathbf{V}^{-1} \mathbf{B}\mathbf{u}(\tau) d\tau. \quad (\text{B.51})$$

The product of inverse eigenvector matrix and input matrix is a constant  $n \times 2$  matrix,

$$\mathbf{K} = \mathbf{V}^{-1} \mathbf{B}. \quad (\text{B.52})$$

When substituting the rotational input signal acc. to (B.46) into (B.51) and determining the vector elements in the integral on the RHS of (B.51), we obtain scalar expressions in the form of

$$x_{int,n} = u \int_{t_0}^t \exp(-\lambda_n \tau) (K_{n1} \cos(\omega\tau + \phi) + K_{n2} \sin(\omega\tau + \phi)) d\tau, \quad (\text{B.53})$$

where  $K_{n1}$  and  $K_{n2}$  are the elements of the first and second columns of  $\mathbf{K}$  in row  $n$ .

With the known integral solutions [58 p. 1103]

$$\int \exp(\lambda\tau) \cos(\omega\tau + \phi) d\tau = \frac{\exp(\lambda\tau)}{\lambda^2 + \omega^2} (\lambda \cos(\omega\tau + \phi) + \omega \sin(\omega\tau + \phi)), \quad (\text{B.54})$$

$$\int \exp(\lambda\tau) \sin(\omega\tau + \phi) d\tau = \frac{\exp(\lambda\tau)}{\lambda^2 + \omega^2} (\lambda \sin(\omega\tau + \phi) - \omega \cos(\omega\tau + \phi)), \quad (\text{B.55})$$

we can rewrite (B.53) as

$$x_{int,n} = u \left[ \frac{\exp(-\lambda_n \tau)}{\lambda_n^2 + \omega^2} (K_{n1}(-\lambda_n \cos(\omega\tau + \phi) + \omega \sin(\omega\tau + \phi)) + K_{n2}(-\lambda_n \sin(\omega\tau + \phi) - \omega \cos(\omega\tau + \phi))) \right]_{t_0}^t, \quad (\text{B.56})$$

which can be further simplified to

$$x_{int,n} = u \left[ \frac{\exp(-\lambda_n \tau)}{\lambda_n^2 + \omega^2} (\cos(\omega\tau + \phi) (-K_{n1}\lambda_n - K_{n2}\omega) + \sin(\omega\tau + \phi) (K_{n1}\omega - K_{n2}\lambda_n)) \right]_{t_0}^t. \quad (\text{B.57})$$

When substituting this elementwise solution of the integral into the matrix expression (B.51), we obtain

$$\mathbf{x}_p(t) = \mathbf{V} \exp(\mathbf{D}t) [(\mathbf{D}^2 + \omega^2 \mathbf{I})^{-1} \exp(-\mathbf{D}\tau) (-\omega \mathbf{KJ} - \mathbf{DK}) \mathbf{u}(\tau)]_{t_0}^t, \quad (\text{B.58})$$

and, after substituting (B.52) and the definite integral boundaries,

$$\mathbf{x}_p(t) = \mathbf{V} \exp(\mathbf{D}t) (\mathbf{D}^2 + \omega^2 \mathbf{I})^{-1} \left( \exp(-\mathbf{D}t) (-\omega \mathbf{V}^{-1} \mathbf{BJ} - \mathbf{DV}^{-1} \mathbf{B}) \mathbf{u}(t) - \exp(-\mathbf{D}t_0) (-\omega \mathbf{V}^{-1} \mathbf{BJ} - \mathbf{DV}^{-1} \mathbf{B}) \mathbf{u}(t_0) \right). \quad (\text{B.59})$$

Further simplification of (B.59) leads to

$$\mathbf{x}_p(t) = \mathbf{V} (\mathbf{D}^2 + \omega^2 \mathbf{I})^{-1} \left( (-\omega \mathbf{V}^{-1} \mathbf{BJ} - \mathbf{DV}^{-1} \mathbf{B}) \mathbf{u}(t) - \exp(\mathbf{D}(t - t_0)) (-\omega \mathbf{V}^{-1} \mathbf{BJ} - \mathbf{DV}^{-1} \mathbf{B}) \mathbf{u}(t_0) \right), \quad (\text{B.60})$$

and, by transforming the diagonal eigenvalue matrices and matrix exponentials acc. to (B.48) and (B.49) back into their system matrix representation, we obtain

$$\mathbf{x}_p(t) = (\mathbf{A}^2 + \omega^2 \mathbf{I})^{-1} \left( (-\omega \mathbf{BJ} - \mathbf{AB}) \mathbf{u}(t) - \exp(\mathbf{A}(t - t_0)) (-\omega \mathbf{BJ} - \mathbf{AB}) \mathbf{u}(t_0) \right). \quad (\text{B.61})$$

When rearranging (B.61) and introducing the particular response matrix,

$$\mathbf{K}_p = -(\mathbf{A}^2 + \omega^2 \mathbf{I})^{-1} ((\mathbf{AB} + \omega \mathbf{BJ})), \quad (\text{B.62})$$

we end up with

$$\mathbf{x}_p(t) = -\exp(\mathbf{A}(t - t_0)) \mathbf{K}_p \mathbf{u}(t_0) + \mathbf{K}_p \mathbf{u}(t). \quad (\text{B.63})$$

We can see that the particular response of a linear system to rotating input signals consists of an exponential component depending on the initial input  $\mathbf{u}(t_0)$  and a linear component depending on  $\mathbf{K}_p$  and the rotating input signal.

---

## B.7 Current Response of Synchronous Machines to Rotating Voltages

---

In the previous section, the particular response matrix of linear systems with rotating inputs was found to be

$$\mathbf{K}_p = -(\mathbf{A}^2 + \omega^2 \mathbf{I})^{-1} ((\mathbf{AB} + \omega \mathbf{BJ})). \quad (\text{B.64})$$

The system and input matrices of synchronous machines linearized at a given operating point are given by

$$\mathbf{A} = -\mathbf{L}_{s,op}^r{}^{-1}(\mathbf{R}_s\mathbf{I} + \omega_{r,op}\mathbf{J}\mathbf{L}_{s,op}^r) \quad (\text{B.65})$$

and

$$\mathbf{B} = \mathbf{L}_{s,op}^r{}^{-1}. \quad (\text{B.66})$$

Substituting (B.65) and (B.66) into (B.64) results in

$$\mathbf{K}_p = -\left(\left(-\mathbf{L}_{s,op}^r{}^{-1}(\mathbf{R}_s\mathbf{I} + \omega_{r,op}\mathbf{J}\mathbf{L}_{s,op}^r)\right)^2 + \omega^2\mathbf{I}\right)^{-1}\left(\left(-\mathbf{L}_{s,op}^r{}^{-1}(\mathbf{R}_s\mathbf{I} + \omega_{r,op}\mathbf{J}\mathbf{L}_{s,op}^r)\mathbf{L}_{s,op}^r{}^{-1} + \omega\mathbf{L}_{s,op}^r{}^{-1}\mathbf{J}\right)\right), \quad (\text{B.67})$$

which can be rewritten as

$$\mathbf{K}_p = \left(\left(\mathbf{R}_s^2\mathbf{I} + \omega_{r,op}\mathbf{R}_s\mathbf{L}_{s,op}^r\mathbf{J} + \omega_{r,op}\mathbf{R}_s\mathbf{J}\mathbf{L}_{s,op}^r + \omega_{r,op}^2\mathbf{L}_{s,op}^r\mathbf{J}\mathbf{L}_{s,op}^r\right) + \omega^2\mathbf{L}_{s,op}^r{}^2\right)^{-1}\left(\mathbf{R}_s\mathbf{I} - (\omega - \omega_{r,op})\mathbf{L}_{s,op}^r\mathbf{J}\right). \quad (\text{B.68})$$

With

$$\mathbf{J}\mathbf{J} = -\mathbf{I} \quad (\text{B.69})$$

and

$$\mathbf{L}_{s,op}^r\mathbf{J} + \mathbf{J}\mathbf{L}_{s,op}^r = \mathbf{L}_\Sigma\mathbf{J}, \quad (\text{B.70})$$

we can obtain

$$\mathbf{K}_p = \left(\mathbf{R}_s^2\mathbf{I} + 2\omega_{r,op}\mathbf{R}_s\mathbf{L}_\Sigma\mathbf{J} + (\omega^2 - \omega_{r,op}^2)\mathbf{L}_{s,op}^r{}^2\right)^{-1}\left(\mathbf{R}_s\mathbf{I} - (\omega - \omega_{r,op})\mathbf{L}_{s,op}^r\mathbf{J}\right). \quad (\text{B.71})$$

In order to further simplify this expression, we need to apply the following equations:

$$(\mathbf{X} + \mathbf{Y})^{-1} = \frac{1}{\det(\mathbf{X} + \mathbf{Y})}(\text{adj}(\mathbf{X}) + \text{adj}(\mathbf{Y})) \quad (\text{a})$$

$$\text{adj}(\mathbf{I}) = \mathbf{I} \quad (\text{b})$$

$$\text{adj}(\mathbf{J}) = -\mathbf{J} \quad (\text{c})$$

$$\text{adj}(\mathbf{L}_{s,op}^r{}^2) = -\mathbf{J}\mathbf{L}_{s,op}^r{}^2\mathbf{J} \quad (\text{d})$$

$$\det(x\mathbf{I} + y\mathbf{J} + z\mathbf{S}(\vartheta)) = x^2 + y^2 - z^2 \quad (\text{e}) \quad (\text{B.72})$$

$$\mathbf{L}^r = \mathbf{L}_\Sigma\mathbf{I} + \mathbf{L}_{A,\Delta}\mathbf{S}(\vartheta_A) \quad (\text{f})$$

$$\mathbf{L}^r\mathbf{J} = \mathbf{J}\left(\mathbf{L}_\Sigma\mathbf{I} - \mathbf{L}_{A,\Delta}\mathbf{S}(\vartheta_A)\right) \quad (\text{g})$$

$$\mathbf{L}^r{}^2 = (\mathbf{L}_\Sigma^2 + \mathbf{L}_{A,\Delta}^2)\mathbf{I} + 2\mathbf{L}_\Sigma\mathbf{L}_{A,\Delta}\mathbf{S}(\vartheta_A) \quad (\text{h})$$

$$\mathbf{J}\mathbf{L}^r{}^2\mathbf{J} = -(\mathbf{L}_\Sigma^2 + \mathbf{L}_{A,\Delta}^2)\mathbf{I} + 2\mathbf{L}_\Sigma\mathbf{L}_{A,\Delta}\mathbf{S}(\vartheta_A) \quad (\text{i})$$

With (B.72) (a), we can rewrite the inverse term in (B.71) and obtain

$$\mathbf{K}_p = \frac{(\text{adj}(\mathbf{R}_s^2\mathbf{I}) + \text{adj}(2\omega_{r,op}\mathbf{R}_s\mathbf{L}_\Sigma\mathbf{J}) + \text{adj}((\omega^2 - \omega_{r,op}^2)\mathbf{L}_{s,op}^r{}^2))(\mathbf{R}_s\mathbf{I} - (\omega - \omega_{r,op})\mathbf{L}_{s,op}^r\mathbf{J})}{\det(\mathbf{R}_s^2\mathbf{I} + 2\omega_{r,op}\mathbf{R}_s\mathbf{L}_\Sigma\mathbf{J} + (\omega^2 - \omega_{r,op}^2)\mathbf{L}_{s,op}^r{}^2)} \quad (\text{B.73})$$

The denominator term in (B.73) can be rewritten by means of (B.72) (e) and (h) as

$$D = \left( R_s^2 + (\omega^2 - \omega_{r,op}^2)(L_\Sigma^2 + L_{A,\Delta}^2) \right)^2 + (2R_s\omega_{r,op}L_\Sigma)^2 - (2(\omega^2 - \omega_{r,op}^2)L_\Sigma L_{A,\Delta})^2. \quad (\text{B.74})$$

After expanding the squared terms and rearranging the results, we end up with

$$D = R_s^2 \left( R_s^2 + 2 \left( (\omega^2 + \omega_{r,op}^2)L_\Sigma^2 + (\omega^2 - \omega_{r,op}^2)L_{A,\Delta}^2 \right) \right) + (\omega^2 - \omega_{r,op}^2)^2 (L_\Sigma^2 - L_{A,\Delta}^2)^2. \quad (\text{B.75})$$

In the numerator term of (B.73), we can rewrite the adjugate expressions by means of (B.72) (b) – (d) and obtain

$$N = (R_s^2 \mathbf{I} - 2R_s\omega_{r,op}L_\Sigma \mathbf{J} - (\omega^2 - \omega_{r,op}^2) \mathbf{J} L_{s,op}^r \mathbf{J}) (R_s \mathbf{I} - (\omega - \omega_{r,op}) L_{s,op}^r \mathbf{J}). \quad (\text{B.76})$$

Substituting the inductance equations (B.72) (g) and (i) leads to

$$N = \left( R_s^2 \mathbf{I} - 2R_s\omega_{r,op}L_\Sigma \mathbf{J} + (\omega^2 - \omega_{r,op}^2) \left( (L_\Sigma^2 + L_{A,\Delta}^2) \mathbf{I} + 2L_\Sigma L_{A,\Delta} \mathbf{S}(\vartheta_A) \right) \right) \left( R_s \mathbf{I} - (\omega - \omega_{r,op}) \mathbf{J} (L_\Sigma \mathbf{I} - L_{A,\Delta} \mathbf{S}(\vartheta_A)) \right). \quad (\text{B.77})$$

We can see that the numerator only contains terms of scalars that are multiplied with  $\mathbf{I}$ ,  $\mathbf{J}$ ,  $\mathbf{S}(\vartheta_A)$  or  $\mathbf{J}\mathbf{S}(\vartheta_A)$ . We thus expand (B.77) and afterwards factor out the respective matrices. The resulting numerator terms of  $\mathbf{K}_p$  are

$$N_I = R_s \left( R_s^2 + (\omega - \omega_{r,op}) \left( L_\Sigma^2 (\omega - \omega_{r,op}) + L_{A,\Delta}^2 (\omega + \omega_{r,op}) \right) \right) \mathbf{I}, \quad (\text{a})$$

$$N_J = - \left( (\omega + \omega_{r,op}) L_\Sigma \left( R_s^2 + (\omega - \omega_{r,op})^2 (L_\Sigma^2 - L_{A,\Delta}^2) \right) \right) \mathbf{J}, \quad (\text{b})$$

$$N_S = -2R_s L_\Sigma L_{A,\Delta} \omega (\omega - \omega_{r,op}) \mathbf{S}(\vartheta_A), \quad (\text{c})$$

$$N_{JS} = \left( (\omega - \omega_{r,op}) L_{A,\Delta} \left( R_s^2 - (\omega^2 - \omega_{r,op}^2) (L_\Sigma^2 - L_{A,\Delta}^2) \right) \right) \mathbf{J}\mathbf{S}(\vartheta_A). \quad (\text{d})$$

With (B.75) and (B.78), we thus found a clearly arranged form of  $\mathbf{K}_p$ , i.e.

$$\mathbf{K}_p = \frac{N_I + N_J + N_S + N_{JS}}{D}. \quad (\text{B.79})$$

## B.8 Fourier Analysis of Piecewise Constant Vector Functions

Given a piecewise constant vector function with  $m$  segments,

$$\mathbf{u}(t) = \begin{cases} \mathbf{u}_1, & t_0 \leq t < t_1 \\ \mathbf{u}_i, & t_{i-1} \leq t < t_i \\ \mathbf{u}_m, & t_{m-1} \leq t < t_m \end{cases}, \quad (\text{B.80})$$

where

$$\mathbf{u}_i = \begin{bmatrix} u_{\alpha i} \\ u_{\beta i} \end{bmatrix}, \quad (\text{B.81})$$

we can determine its Fourier components acc.to (2.143) by

$$\mathbf{u}_k = u_k \mathbf{T}(\phi_k) \mathbf{e}_1 = \frac{1}{T_1} \int_{t_0}^{t_0+T_1} \mathbf{T}(-\omega_k t) \mathbf{u}(t) dt, \quad (\text{B.82})$$

where  $T_1$  is the period time of  $\mathbf{u}(t)$ ,

$$T_1 = t_m - t_0. \quad (\text{B.83})$$

In order to account for the piecewise nature of  $\mathbf{u}(t)$ , we compute the integral segment by segment and obtain

$$\mathbf{u}_k = \frac{1}{T_1} \sum_{i=1}^m \left( \int_{t_{i-1}}^{t_i} \mathbf{T}(-\omega_k t) \mathbf{u}_i dt \right). \quad (\text{B.84})$$

When solving the integrals, we need to remind the definition of  $\omega_k$  acc. to (2.138), i.e.

$$\omega_k = 2\pi \frac{k}{T_1}. \quad (\text{B.85})$$

For  $k = 0$ , we obtain

$$\mathbf{u}_0 = \frac{1}{T_1} \sum_{i=1}^m ((t_i - t_{i-1}) \mathbf{u}_i), \quad (\text{B.86})$$

while in any other case, the solution is

$$\mathbf{u}_k = \frac{1}{T_1} \sum_{i=1}^m \left( \left[ \frac{1}{\omega_k} \mathbf{J} \mathbf{T}(-\omega_k t) \right]_{t_{i-1}}^{t_i} \mathbf{u}_i \right), \quad \forall k \neq 0. \quad (\text{B.87})$$

When considering the trigonometric difference equations acc. to [58 p. 82], i.e.

$$\cos(\phi_1) - \cos(\phi_2) = -2 \sin\left(\frac{\phi_1 + \phi_2}{2}\right) \sin\left(\frac{\phi_1 - \phi_2}{2}\right), \quad (\text{a}) \quad (\text{B.88})$$

$$\sin(\phi_1) - \sin(\phi_2) = 2 \cos\left(\frac{\phi_1 + \phi_2}{2}\right) \sin\left(\frac{\phi_1 - \phi_2}{2}\right), \quad (\text{b})$$

we can find that

$$\mathbf{T}(\phi_1) - \mathbf{T}(\phi_2) = 2 \sin\left(\frac{\phi_1 - \phi_2}{2}\right) \mathbf{J} \mathbf{T}\left(\frac{\phi_1 + \phi_2}{2}\right). \quad (\text{B.89})$$

When applying (B.89), we can rewrite (B.87) as

$$\mathbf{u}_k = \frac{2}{\omega_k T_1} \sum_{i=1}^m \left( \sin\left(\frac{\omega_k}{2}(t_i - t_{i-1})\right) \mathbf{T}\left(-\frac{\omega_k}{2}(t_i + t_{i-1})\right) \mathbf{u}_i^s \right), \quad \forall k \neq 0, \quad (\text{B.90})$$

and, when substituting (B.85), we get

$$\mathbf{u}_k = \frac{1}{k\pi} \sum_{i=1}^m \left( \sin\left(\frac{k\pi}{T_1}(t_i - t_{i-1})\right) \mathbf{T}\left(-\frac{k\pi}{T_1}(t_i + t_{i-1})\right) \mathbf{u}_i^s \right), \quad \forall k \neq 0. \quad (\text{B.91})$$

# APPENDIX C

---

## Related Works

---

### C.1 Advised Student Thesis

---

- Jianneng Cai, “Methods for Determining Inductances in Permanent Magnetic Synchronous Machines Considering Cross-Coupling Effects”, Hauptseminar, 31.03.2012
- Hamza Mili, “Parameter Identification of a Synchronous Reluctance Machine by using a Synchronous PI Current Regulator at Standstill”, Studienarbeit, 23.12.2012
- Michael Heidingsfelder, “Aufbau eines Messboards zur Strom- und Spannungsmessung mittels FPGA“, Forschungspraxis, 21.06.2013
- Michael Heidingsfelder, “Vergleich von verschiedenen Modellen zur Approximation von magnetischen Sättigungseffekten in Synchronmaschinen“, Hauptseminar, 12.11.2013
- Tim Huber, “Regelungsprüfstand – Messwertverarbeitung mittels FPGA“, Bachelorarbeit, 26.02.2014
- Michael Heidingsfelder, „Vergleich von verschiedenen Modellen zur Approximation von Sättigungseinflüssen in Synchronmaschinen“, Masterarbeit, 20.06.2014
- Shuang Ma, “Modeling of Magnetic Saturation Effects to Compensate Angle Estimation Errors in Sensorless Control”, Hauptseminar, 26.06.2015

### C.2 List of Publications

---

The following list includes all peer-reviewed publications, written during the time of the author’s studies at the institute.

- S. Bolognani, R. Kennel, S. Kuehl, and G. Paccagnella, “Speed and Current Model Predictive Control of an IPM Synchronous Motor Drive,” in *Proc. IEEE International Electric Machines & Drives Conference (IEMDC)*, Niagara Falls, Canada, 2011, pp. 1623–1628.

- J. Stumper, S. Kuehl and R. Kennel, "Robust deadbeat control for synchronous machines rejecting noise and uncertainties by predictive filtering," in *Proc. 8th International Conference on Power Electronics - ECCE Asia*, Jeju, Korea (South), 2011, pp. 1378-1385, doi: 10.1109/ICPE.2011.5944416.
- S. Kuehl, P. Landsmann and R. M. Kennel, "Bivariate polynomial approximation of cross-saturated flux curves in synchronous machine models," in *Proc. IEEE International Energy Conference and Exhibition (ENERGYCON)*, Florence, Italy, 2012, pp. 219-224, doi: 10.1109/EnergyCon.2012.6347756
- S. Kuehl, P. Landsmann and R. M. Kennel, "Compensating angle estimation errors caused by magnetic saturation in anisotropy-based sensorless control schemes," in *Proc. 3rd IEEE International Symposium on Sensorless Control for Electrical Drives (SLED 2012)*, Milwaukee, USA, 2012, pp. 1-6, doi: 10.1109/SLED.2012.6422803.
- J. Stumper, V. Hagenmeyer, S. Kuehl and R. Kennel, "Flatness-based deadbeat control revisited: Robust and high-performance design for electrical drives," in *Proc. American Control Conference*, Washington, USA, 2013, pp. 1822-1827, doi: 10.1109/ACC.2013.6580100.
- J. Stumper, S. Kuehl and R. Kennel, "Predictive torque control for AC drives: Improvement of parametric robustness using two-degree-of-freedom control," in *Proc. IEEE Energy Conversion Congress and Exposition*, Denver, USA, 2013, pp. 1170-1175, doi: 10.1109/ECCE.2013.6646837.
- D. Paulus, P. Landsmann, S. Kuehl and R. Kennel, "Arbitrary injection for permanent magnet synchronous machines with multiple saliencies," in *Proc. IEEE Energy Conversion Congress and Exposition*, Denver, USA, 2013, pp. 511-517, doi: 10.1109/ECCE.2013.6646744.
- S. Kuehl and R. Kennel, „Measuring Magnetic Properties of Synchronous Machines by Applying Angle Estimation Techniques Known from Sensorless Control”, in *Proc. IEEE-Energy Conversion Congress and Exposition*, Denver, USA, 2013, pp. 5026-5033, doi: 10.1109/ECCE.2013.6647379
- S. Kuehl and R. M. Kennel, "Measuring Magnetic Characteristics of Synchronous Machines by Applying Position Estimation Techniques," in *IEEE Transactions on Industry Applications*, vol. 50, no. 6, pp. 3816-3824, Nov.-Dec. 2014, doi: 10.1109/TIA.2014.2322137.
- J. Stumper, V. Hagenmeyer, S. Kuehl and R. Kennel, "Deadbeat Control for Electrical Drives: A Robust and Performant Design Based on Differential Flatness," in *IEEE Transactions on Power Electronics*, vol. 30, no. 8, pp. 4585-4596, Aug. 2015, doi: 10.1109/TPEL.2014.2359971.

## BIBLIOGRAPHY

---

- [1] D. Schröder, *Elektrische Antriebe - Grundlagen*, 4th ed. Berlin, Heidelberg: Springer Berlin Heidelberg, 2009.
- [2] \_\_\_\_\_, *Elektrische Antriebe - Regelung von Antriebssystemen*, 3rd ed. Berlin, Heidelberg: Springer Berlin Heidelberg, 2009.
- [3] S. Bolognani, R. Kennel, S. Kuehl, and G. Paccagnella, “Speed and Current Model Predictive Control of an IPM Synchronous Motor Drive,” in *Proc. IEMDC*, Niagara Falls, Canada, 2011, pp. 1623–1628.
- [4] J. Stumper, A. Dotlinger, J. Jung, and R. Kennel, “Predictive control of a permanent magnet synchronous machine based on real-time dynamic optimization,” in *Proc. Proceedings of the 14th European Conference on : Power Electronics and Applications (EPE)*, 2011, pp. 1–8.
- [5] J.-F. Stumper, “Flatness-based predictive and optimal control for electrical drives,” Dissertation, Technische Universität München, München, 2013.
- [6] J.-F. Stumper, S. Kuehl, and R. Kennel, “Robust deadbeat control for synchronous machines rejecting noise and uncertainties by predictive filtering,” in *Proc. 8th International Conference on Power Electronics - ECCE Asia*, Jeju, Korea (South), 2011, pp. 1378–1385.
- [7] A. Consoli, G. Scarcella, and A. Testa, “Industry application of zero-speed sensorless control techniques for PM synchronous motors,” (en), *IEEE Trans. on Ind. Applicat*, vol. 37, no. 2, pp. 513–521, 2001.
- [8] R. Bojoi, M. Pastorelli, J. Bottomley, P. Giangrande, and C. Gerada, “Sensorless control of PM motor drives — A technology status review,” in *Proc. 2013 IEEE Workshop on Electrical Machines Design, Control and Diagnosis (WEMDCD 2013)*, Paris, pp. 168–182.
- [9] M. J. Corley and R. D. Lorenz, “Rotor position and velocity estimation for a salient-pole permanent magnet synchronous machine at standstill and high speeds,” (en), *IEEE Trans. on Ind. Applicat*, vol. 34, no. 4, pp. 784–789, 1998.

- [10] P. L. Jansen and R. D. Lorenz, "Transducerless position and velocity estimation in induction and salient AC machines," (en), *IEEE Trans. on Ind. Applicat*, vol. 31, no. 2, pp. 240–247, 1995.
- [11] Ji-Hoon Jang, Seung-Ki Sul, Jung-Ik Ha, Kozo Ide, and M. Sawamura, "Sensorless drive of surface-mounted permanent-magnet motor by high-frequency signal injection based on magnetic saliency," (en), *IEEE Trans. on Ind. Applicat*, vol. 39, no. 4, pp. 1031–1039, 2003.
- [12] Joohn Sheok Kim and Seung Ki Sul, "New stand-still position detection strategy for PMSM drive without rotational transducers," in *Proc. ASPEC*, Orlando, FL, 1994, pp. 363–369.
- [13] Jung-Ik Ha, K. Ide, T. Sawa, and Seung-Ki Sul, "Sensorless rotor position estimation of an interior permanent-magnet motor from initial states," (en), *IEEE Trans. on Ind. Applicat*, vol. 39, no. 3, pp. 761–767, 2003.
- [14] M. Schroedl, "Sensorless control of AC machines at low speed and standstill based on the "INFORM" method," in *Proc. IAS Annual Meeting*, San Diego, CA, USA, 1996, pp. 270–277.
- [15] S. Shinnaka, "A New Speed-Varying Ellipse Voltage Injection Method for Sensorless Drive of Permanent-Magnet Synchronous Motors With Pole Saliency — New PLL Method Using High-Frequency Current Component Multiplied Signal," (en), *IEEE Trans. on Ind. Applicat*, vol. 44, no. 3, pp. 777–788, 2008.
- [16] M. Seilmeier and B. Piepenbreier, "Sensorless Control of PMSM for the Whole Speed Range Using Two-Degree-of-Freedom Current Control and HF Test Current Injection for Low-Speed Range," (en), *IEEE Trans. Power Electron*, vol. 30, no. 8, pp. 4394–4403, 2015.
- [17] D. Paulus, "Beliebige Injektion für permanent erregte Synchronmaschinen," Dissertation, Technische Universität München, München, 2015.
- [18] Z. Q. Zhu, Y. Li, D. Howe, C. M. Bingham, and D. Stone, "Influence of Machine Topology and Cross-Coupling Magnetic Saturation on Rotor Position Estimation Accuracy in Extended Back-EMF Based Sensorless PM Brushless AC Drives," in *Proc. IAS Annual Meeting*, New Orleans, LA, USA, 2007, pp. 2378–2385.
- [19] Yi Li, Z. Q. Zhu, D. Howe, C. M. Bingham, and D. A. Stone, "Improved Rotor-Position Estimation by Signal Injection in Brushless AC Motors, Accounting for Cross-Coupling Magnetic Saturation," (en), *IEEE Trans. on Ind. Applicat*, vol. 45, no. 5, pp. 1843–1850, 2009.
- [20] P. Sergeant, F. de Belie, and J. Melkebeek, "Effect of Rotor Geometry and Magnetic Saturation in Sensorless Control of PM Synchronous Machines: Magnetics, IEEE Transactions on," (en), *IEEE Trans. Magn*, vol. 45, no. 3, pp. 1756–1759, 2009.

- 
- [21] L. Alberti, N. Bianchi, M. Morandin, and J. Gyselinck, "Finite-Element Analysis of Electrical Machines for Sensorless Drives With High-Frequency Signal Injection," (en), *IEEE Trans. on Ind. Applicat*, vol. 50, no. 3, pp. 1871–1879, 2014.
- [22] N. Bianchi, S. Bolognani, Ji-Hoon Jang, and Seung-Ki Sul, "Comparison of PM Motor Structures and Sensorless Control Techniques for Zero-Speed Rotor Position Detection," (en), *IEEE Trans. Power Electron*, vol. 22, no. 6, pp. 2466–2475, 2007.
- [23] N. Bianchi, S. Bolognani, and A. Faggion, "Predicted and measured errors in estimating rotor position by signal injection for salient-pole PM synchronous motors," in *Proc. IEMDC*, Miami, FL, USA, 2009, pp. 1565–1572.
- [24] N. Bianchi, E. Fornasiero, and S. Bolognani, "Effect of Stator and Rotor Saturation on Sensorless Rotor Position Detection," (en), *IEEE Trans. on Ind. Applicat*, vol. 49, no. 3, pp. 1333–1342, 2013.
- [25] L. M. Gong and Z. Q. Zhu, "Improved rotating carrier signal injection method for sensorless control of PM brushless AC motors, accounting for cross-saturation effect," in *Proc. ECCE Asia (ICPE 2011- ECCE Asia)*, Jeju, Korea (South), pp. 1132–1139.
- [26] P. Guglielmi, M. Pastorelli, and A. Vagati, "Cross-Saturation Effects in IPM Motors and Related Impact on Sensorless Control," (en), *IEEE Trans. on Ind. Applicat*, vol. 42, no. 6, pp. 1516–1522, 2006.
- [27] H. W. de Kock, M. J. Kamper, and R. M. Kennel, "Anisotropy Comparison of Reluctance and PM Synchronous Machines for Position Sensorless Control Using HF Carrier Injection," (en), *IEEE Trans. Power Electron*, vol. 24, no. 8, pp. 1905–1913, 2009.
- [28] R. Morales-Caporal and M. Pacas, "Suppression of Saturation Effects in a Sensorless Predictive Controlled Synchronous Reluctance Machine Based on Voltage Space Phasor Injections," (en), *IEEE Transactions on Industrial Electronics*, vol. 58, no. 7, pp. 2809–2817, 2011.
- [29] D. D. Reigosa, P. Garcia, D. Raca, F. Briz, and R. D. Lorenz, "Measurement and Adaptive Decoupling of Cross-Saturation Effects and Secondary Saliencies in Sensorless Controlled IPM Synchronous Machines," (en), *IEEE Trans. on Ind. Applicat*, vol. 44, no. 6, pp. 1758–1767, 2008.
- [30] M. Seilmeier and B. Piepenbreier, "Impact of iron losses and parameter errors on back-EMF based sensorless control of PMSM," in *Proc. IECON 2014 - 40th Annual Conference of the IEEE Industrial Electronics Society*, Dallas, TX, USA, pp. 634–640.
- [31] J. C. Maxwell, "A Dynamical Theory of the Electromagnetic Field," (en), *Philosophical Transactions of the Royal Society of London*, vol. 155, no. 0, pp. 459–512, 1865.
- [32] H. A. Haus and J. R. Melcher, *Electromagnetic Fields and Energy*, Massachusetts Institute of Technology: MIT OpenCourseWare, Available: <http://ocw.mit.edu> (2015, May. 22), License: Creative Commons Attribution-NonCommercial-Share Alike.

- [33] A. J. Schwab, *Field Theory Concepts: Electromagnetic Fields Maxwell's Equations grad, curl, div. etc. Finite-Element Method Finite-Difference Method Charge Simulation Method Monte Carlo Method*. Berlin, Heidelberg: Springer Berlin Heidelberg, 1988.
- [34] S. F. Bart, T. A. Lober, R. T. Howe, J. H. Lang, and M. F. Schlecht, "Design considerations for micromachined electric actuators," (da), *Sensors and Actuators*, vol. 14, no. 3, pp. 269–292, 1988.
- [35] Coey, J. M. D, *Magnetism and magnetic materials*. Cambridge, New York: Cambridge University Press, 2009.
- [36] C. van der Togt, "The Equivalence of Magnetic and Kinetic Energy," (en), *Galilean Electrodynamics*, vol. 17, no. 6, pp. 110–114, <http://www.gsjournal.net/Science-Journals/Research%20Papers/View/1179>, 2006.
- [37] G. S. Ohm, *Die galvanische Kette, mathematisch bearbeitet*, 1827.
- [38] H.-G. Herzog, "Grundzüge der elektromechanischen Energiewandlung: Skriptum zur Vorlesung," Fachgebiet Energiewandlungstechnik, Technische Universität München, München, 2008.
- [39] N. Ida, *Engineering Electromagnetics*. New York, NY: Springer New York, 2000.
- [40] T. Miyazaki and H. Jin, *The physics of ferromagnetism*. Berlin, New York: Springer, 2012.
- [41] S. Chikazumi and C. D. Graham, *Physics of ferromagnetism*, 2nd ed. Oxford, New York: Oxford University Press, 1997.
- [42] D. C. Jiles, "Dynamics of Domain Magnetization and the Barkhausen Effect," (en), *Czechoslovak Journal of Physics*, vol. 50, no. 8, pp. 893–924, 2000.
- [43] C. S. Helrich, *The classical theory of fields: Electromagnetism*. Heidelberg, New York: Springer-Verlag Berlin Heidelberg, 2012.
- [44] Du Trémolet de Lacheisserie, Etienne, D. Gignoux, and M. Schlenker, *Magnetism*. New York: Springer Science+Business Media, 2005.
- [45] D. C. Jiles and D. L. Atherton, "Theory of ferromagnetic hysteresis," (af), *J. Appl. Phys*, vol. 55, no. 6, p. 2115, 1984.
- [46] D. C. Jiles, "Frequency dependence of hysteresis curves in conducting magnetic materials," (af), *J. Appl. Phys*, vol. 76, no. 10, p. 5849, 1994.
- [47] R. M. Bozorth, *Ferromagnetism*. Piscataway, N.J.: Wiley-IEEE Press, 1993.
- [48] Lacheisserie, Étienne du Trémolet, D. Gignoux, and M. Schlenker, *Magnetism: II- Materials and Applications*. Boston, MA: Springer US, 2002.
- [49] J. Reinert, A. Brockmeyer, and De Doncker, R. W. AA, "Calculation of losses in ferro- and ferrimagnetic materials based on the modified Steinmetz equation," (en), *Industry Applications, IEEE Transactions on*, vol. 37, no. 4, pp. 1055–1061, 2001.

- 
- [50] C. D. Graham, “Physical origin of losses in conducting ferromagnetic materials (invited),” (af), *J. Appl. Phys.*, vol. 53, no. 11, p. 8276, 1982.
- [51] G. E. Fish, “Soft magnetic materials,” *Proceedings of the IEEE*, vol. 78, no. 6, pp. 947–972, 1990.
- [52] G. Bertotti, “General properties of power losses in soft ferromagnetic materials,” (af), *IEEE Trans. Magn.*, vol. 24, no. 1, pp. 621–630, 1988.
- [53] G. Bertotti and M. Pasquale, “Physical interpretation of induction and frequency dependence of power losses in soft magnetic materials,” (en), *IEEE Trans. Magn.*, vol. 28, no. 5, pp. 2787–2789, 1992.
- [54] J. J. Becker, “Magnetization Changes and Losses in Conducting Ferromagnetic Materials,” (en), *J. Appl. Phys.*, vol. 34, no. 4, p. 1327, 1963.
- [55] J. Cordier, P. Landsmann, and R. Kennel, “The influence of magnetic hysteresis on HF injection based inductance calculation,” in *Proc. ECCE*, Phoenix, AZ, USA, 2011, pp. 638–645.
- [56] R. H. Pry and C. P. Bean, “Calculation of the Energy Loss in Magnetic Sheet Materials Using a Domain Model,” (en), *J. Appl. Phys.*, vol. 29, no. 3, p. 532, 1958.
- [57] I. Wolff, *Grundlagen der Elektrotechnik: Einführung in die elektrischen und magnetischen Felder und die Grundlagen der Netzwerktheorie*, 6th ed. Aachen: Nellissen-Wolff, 1997.
- [58] I. N. Bronstein and K. A. Semendjajew, *Taschenbuch der Mathematik*, 7th ed. Frankfurt am Main: Deutsch, 2008.
- [59] A. Binder, *Elektrische Maschinen und Antriebe*. Berlin, Heidelberg: Springer Berlin Heidelberg, 2012.
- [60] Gustav Robert Kirchhoff, “Ueber den Durchgang eines elektrischen Stromes durch eine Ebene, insbesondere durch eine kreisförmige,” (de), *Annalen der Physik*, no. LXIV, pp. 497–514, <http://gallica.bnf.fr/ark:/12148/bpt6k151490/f509>, 1845.
- [61] T. N. Matzen, “Sensorless Control of Permanent Magnet Synchronous Machines,” Dissertation, Department of Energy Technology, Aalborg University, Aalborg, Denmark, 2010.
- [62] M. Frank, P. van Habelt, P. Kummeth, P. Masek, W. Nick, H. Rothfischer, H. Schmidt, B. Wacker, H.-W. Neumuller, G. Nerowski, J. Fraunhofer, R. Hartig, and W. Rzdki, “High-Temperature Superconducting Rotating Machines for Ship Applications,” (en), *IEEE Trans. Appl. Supercond.*, vol. 16, no. 2, pp. 1465–1468, 2006.
- [63] Martin Doppelbauer, “Elektrische Antriebe für hybride und vollelektrische Fahrzeuge, Teil 1,” *ETG-Mitgliederinformation*, no. 2, pp. 39–42, 2015.
- [64] R. M. Crowder, *Electric drives and electromechanical systems*. Oxford: Elsevier, 2006.
- [65] C. Voigt and J. Adamy, *Formelsammlung der Matrizenrechnung*. München [u.a.]: Oldenbourg, 2007.

- [66] P. Vas, *Sensorless Vector and Direct Torque Control*. New York: Oxford University Press, 1998.
- [67] H. Abu-Rub, A. Iqbal, and J. Guzinski, *High Performance Control of AC Drives with MATLAB/Simulink Models*. Chichester, UK: John Wiley & Sons, Ltd, 2012.
- [68] W. Gerke, *Elektrische Maschinen und Aktoren: Eine anwendungsorientierte Einführung*. München: Oldenbourg, 2012.
- [69] E. Clarke, *Circuit analysis of A-C power systems; symmetrical and related components*. New York: Wiley, 1943.
- [70] S. Skogestad and I. Postlethwaite, *Multivariable Feedback Control - Analysis and Design*, 2nd ed.: John Wiley & Sons, Ltd, 2005.
- [71] Charles P. Steinmetz, *Theory and Calculation of Alternating Current Phenomena*, 3rd ed. New York: Electrical World and Engineer, 1900.
- [72] B. R. Oswald, *Berechnung von Drehstromnetzen: Berechnung stationärer und nichtstationärer Vorgänge mit symmetrischen Komponenten und Raumzeigern*, 1st ed. Wiesbaden: Vieweg + Teubner, 2009.
- [73] J. Holtz, “Pulsewidth modulation for electronic power conversion,” *Proc. IEEE*, vol. 82, no. 8, pp. 1194–1214, 1994.
- [74] H. Lutz and W. Wendt, *Taschenbuch der Regelungstechnik: Mit MATLAB und Simulink*, 10th ed. Haan-Gruiten: Verl. Europa-Lehrmittel, 2014.
- [75] S. L. Kellner and B. Piepenbreier, “General PMSM d,q-model using optimized interpolated absolute and differential inductance surfaces,” in *Proc. IEMDC*, Niagara Falls, Canada, 2011, pp. 212–217.
- [76] M. Seilmeier and B. Piepenbreier, “Identification of steady-state inductances of PMSM using polynomial representations of the flux surfaces,” in *Proc. IECON*, Vienna, Austria, 2013, pp. 2899–2904.
- [77] S. J. Underwood and I. Husain, “Online Parameter Estimation and Adaptive Control of Permanent-Magnet Synchronous Machines,” (en), *IEEE Trans. Ind. Electron.*, vol. 57, no. 7, pp. 2435–2443, 2010.
- [78] S.-H. Hwang, J.-M. Kim, and J.-W. Ahn, “Parameter Identification of a Synchronous Reluctance Motor by using a Synchronous PI Current Regulator at a Standstill,” (en), *Journal of Power Electronics*, vol. 10, no. 5, pp. 491–497, 2010.
- [79] A. Kilthau and J. M. Pacas, “Parameter-measurement and control of the synchronous reluctance machine including cross saturation,” in *Proc. Conference Record of the 2001 IEEE Industry Applications Conference. Thirty-Sixth IAS Annual Meeting*, 2001, pp. 2302–2309.
- [80] N. Bianchi, S. Bolognani, A. Consoli, T. M. Jahns, R. D. Lorenz, E. C. Lovelace, S. Morimoto, and A. Vagati, *Design, Analysis and Control of Interior PM Synchronous Machines*. Padova: CLEUP, 2004.

- 
- [81] P. Landsmann, “Sensorless Control of Synchronous Machines by Linear Approximation of Oversampled Current,” Dissertation, Fakultät für Elektrotechnik und Informationstechnik, Technische Universität München, Munich, 2014.
- [82] M. Linke, R. Kennel, and J. Holtz, “Sensorless speed and position control of synchronous machines using alternating carrier injection,” in *Proc. IEMDC*, Madison, 2003, pp. 1211–1217.
- [83] \_\_\_\_\_, “Sensorless position control of permanent magnet synchronous machines without limitation at zero speed,” in *Proc. IEEE 28th Annual Conference of the Industrial Electronics Society*, 2002, pp. 674–679.
- [84] D. Paulus, P. Landsmann, and R. Kennel, “Sensorless field- oriented control for permanent magnet synchronous machines with an arbitrary injection scheme and direct angle calculation,” in *Proc. SLED*, Birmingham, United Kingdom, 2011, pp. 41–46.
- [85] S. Kuehl, P. Landsmann, and R. M. Kennel, “Compensating Angle Estimation Errors Caused by Magnetic Saturation in Anisotropy-Based Sensorless Control Schemes,” in *Proc. SLED*, Milwaukee, WI, USA, 2012, pp. 1–6.
- [86] W. Hammel, P. Landsmann, and R. M. Kennel, “Operating point dependent anisotropies and assessment for position-sensorless control,” in *Proc. 2016 18th European Conference on Power Electronics and Applications (EPE'16 ECCE Europe)*, Karlsruhe, 2016, pp. 1–10.
- [87] F. Preisach, “Über die magnetische Nachwirkung,” *Z. Physik (Zeitschrift für Physik)*, vol. 94, no. 5-6, pp. 277–302, 1935.
- [88] I. Takahashi and T. Noguchi, “A New Quick-Response and High-Efficiency Control Strategy of an Induction Motor,” *IEEE Trans. on Ind. Applicat*, vol. IA-22, no. 5, pp. 820–827, 1986.
- [89] M. Depenbrock, “Direct self-control (DSC) of inverter-fed induction machine,” *IEEE Trans. Power Electron*, vol. 3, no. 4, pp. 420–429, 1988.
- [90] Jean Baptiste Joseph Fourier, *Théorie Analytique de la Chaleur*. Paris: Imprimerie de Firmin Didot, 1822.
- [91] \_\_\_\_\_, *Analytical Theory of Heat*. London: Cambridge University Press, 1878.
- [92] H. J. Uwe Kiencke, *Signale und Systeme, 5, überarbeitete Auflage*: Oldenbourg Wissenschaftsverlag.
- [93] V. A. Kotelnikov, “On the capacity of the 'ether' and cables in electrical communication: English Translation,” in *Proc. Procs. of the first All-Union Conference on the technological reconstruction of the communications sector and low-current engineering*, Moscow, 1933.
- [94] F. Zach, *Leistungselektronik: Ein Handbuch*. Wien: Springer, 2010.
- [95] Hyun-Soo Kim, Hyung-Tae Moon, and Myung-Joong Youn, “On-line dead-time compensation method using disturbance observer,” *IEEE Trans. Power Electron*, vol. 18, no. 6, pp. 1336–1345, 2003.

- [96] Nicola Bedetti, Sandro Calligaro, Roberto Petrella, “Self-Commissioning of Inverter Dead-Time Compensation by Multiple Linear Regression based on a Physical Model,” in *Proc. ECCE*, Pittsburgh, PA, USA, 2014.
- [97] V. Manzolini and S. Bolognani, “On the Rotor Position Self-sensing Capability of Reluctance and IPM Synchronous Motors,” *IEEE Trans. on Ind. Applicat.*, vol. 56, no. 4, pp. 3755–3766, 2020.
- [98] N. Bianchi and S. Bolognani, “Magnetic models of saturated interior permanent magnet motors based on finite element analysis,” in *Proc. Conference record of the 1998 IEEE Industry Applications Conference: Thirty-third IAS Annual Meeting : 12-15 October 1998, St. Louis, Missouri, USA*, St. Louis, MO, USA, 1998, pp. 27–34.
- [99] D. Mingardi, M. Morandini, S. Bolognani, and N. Bianchi, “On the Proprieties of the Differential Cross-Saturation Inductance in Synchronous Machines,” *IEEE Trans. on Ind. Applicat.*, vol. 53, no. 2, pp. 991–1000, 2017.
- [100] J. Löfberg, “YALMIP: A Toolbox for Modeling and Optimization in MATLAB,” in *Proc. CACSD*, Taipei, Taiwan, 2004, pp. 284–289.
- [101] J. Holtz, “Sensorless control of induction motor drives,” *Proc. IEEE*, vol. 90, no. 8, pp. 1359–1394, 2002.
- [102] E. Armando, R. I. Bojoi, P. Guglielmi, G. Pellegrino, and M. Pastorelli, “Experimental Identification of the Magnetic Model of Synchronous Machines,” (en), *IEEE Trans. on Ind. Applicat.*, vol. 49, no. 5, pp. 2116–2125, 2013.
- [103] Gianmario Pellegrino, Barbara Boazzo, and Thomas M. Jahns, “Magnetic Model Self-Identification for PM Synchronous Machine Drives,” in *Proc. OPTIM*, Bran, Romania, 2014, pp. 252–260.
- [104] J.J.R. Melgoza, G. T. Heydt, A. Keyhani, B. L. Agrawal, and D. Selin, “Synchronous machine parameter estimation using the Hartley series,” *IEEE Trans. Energy Conversion*, vol. 16, no. 1, pp. 49–54, 2001.
- [105] K.M. Rahman and S. Hiti, “Identification of Machine Parameters of a Synchronous Motor,” (af), *IEEE Trans. on Ind. Applicat.*, vol. 41, no. 2, pp. 557–565, 2005.
- [106] S. Kuehl and R. Kennel, “Measuring magnetic properties of synchronous machines by applying angle estimation techniques known from sensorless control,” in *Proc. 2013 IEEE Energy Conversion Congress and Exposition (ECCE)*, Denver, CO, USA, pp. 5026–5033.
- [107] S. Kuehl and R. M. Kennel, “Measuring Magnetic Characteristics of Synchronous Machines by Applying Position Estimation Techniques,” *IEEE Trans. on Ind. Applicat.*, vol. 50, no. 6, pp. 3816–3824, 2014.
- [108] B. Stumberger, G. Stumberger, D. Dolinar, A. Hamler, and M. Trlep, “Evaluation of Saturation and Cross-Magnetization Effects in Interior Permanent-Magnet Synchronous Motor,” (en), *IEEE Trans. on Ind. Applicat.*, vol. 39, no. 5, pp. 1264–1271, 2003.

- [109] S. Ebersberger and B. Piepenbreier, “Identification of differential inductances of permanent magnet synchronous machines using test current signal injection,” in *Proc. SPEEDAM*, Sorrento, Italy, 2012, pp. 1342–1347.
- [110] H. Peter and I. Hahn, “Determination of differential inductances of permanent magnet synchronous machines for sensorless control,” in *Proc. IEMDC*, Niagara Falls, Canada, 2011, pp. 1579–1584.
- [111] M. Seilmeier, A. Boehm, I. Hahn, and B. Piepenbreier, “Identification of time-variant high frequency parameters for sensorless control of PMSM using an internal model principle based high frequency current control,” in *Proc. ICEM*, Marseille, France, 2012, pp. 987–993.
- [112] M. Seilmeier, S. Ebersberger, and B. Piepenbreier, “Identification of high frequency resistances and inductances for sensorless control of PMSM,” in *Proc. 2013 IEEE International Symposium on Sensorless Control for Electrical Drives and Predictive Control of Electrical Drives and Power Electronics (SLED/PRECEDE)*, München, Germany, pp. 1–8.
- [113] T. L. Vandoorn, F. M. de Belie, T. J. Vyncke, J. A. Melkebeek, and P. Lataire, “Generation of Multisinusoidal Test Signals for the Identification of Synchronous-Machine Parameters by Using a Voltage-Source Inverter,” *IEEE Trans. Ind. Electron*, vol. 57, no. 1, pp. 430–439, 2010.
- [114] Wei Xu and R.D. Lorenz, Eds, *High frequency injection-based stator flux linkage and torque estimation for DB-DTFC implementation on IPMSMs considering cross-saturation effects*. Energy Conversion Congress and Exposition (ECCE), 2013 IEEE, 2013.
- [115] The MathWorks, Inc, *MATLAB and Symbolic Math Toolbox*. Natick, Massachusetts, United States: The MathWorks, Inc, 2019.
- [116] N. Limsuwan, T. Kato, C.-Y. Yu, J. Tamura, D. D. Reigosa, K. Akatsu, and R. D. Lorenz, “Secondary Resistive Losses With High-Frequency Injection-Based Self-Sensing in IPM Machines,” (en), *IEEE Trans. on Ind. Applicat*, vol. 49, no. 4, pp. 1499–1507, 2013.